Development of novel nanomaterials for multimodal biomedical imaging

Sandiford, Lydia Grace

Awarding institution:
King's College London

Development of novel nanomaterials for multimodal biomedical imaging

By

Lydia Grace Sandiford

A thesis submitted in partial satisfaction of the
requirements for the degree of
Doctor of Philosophy

in the

Division of Imaging Sciences and Biomedical Engineering

King's College London

2015

Abstract

This thesis focuses on the development of novel nanomaterials for biomedical imaging using both iron oxide nanoparticles and cadmium based quantum dots, and two different coating methods. The first approach involved a coating ligand consisting of the stealth molecule polyethylene glycol, and a bisphosphonate enabling strong binding to the nanoparticle surface. This polymer conjugate was chosen in order to reduce undesirable reticuloendothelial system uptake, and hence increase blood circulation times allowing for efficient delivery of particles to specific *in vivo* vascular targets. The second route employed a naturally occurring amphiphilic protein, hydrophobin, as an encapsulation agent affording water solubility of nanomaterials and potential for bioconjugation.

The first part of the study involved the synthesis of novel iron oxide nanomaterials of small size distribution and a near-zero surface charge resulting in dispersions that were stable in solution for several months. Both longitudinal (r_1) and transverse (r_2) relaxivity measurements were performed at a clinically relevant magnetic field of 3 T, revealing a low r_2/r_1 ratio of 2.97 showing the particles to have optimal properties for efficient T_1-weighted magnetic resonance imaging. The strong T_1 effect was validated *in vivo*, revealing a long blood circulation time and a 6-fold enhancement of its signal, allowing for high resolution visualisation of vessels and vascularised organs. The low reticuloendothelial system uptake observed was confirmed by radiolabelling the particles, hence affording dual-modality contrast, and performing *in vivo* single photon emission computed tomography. From this study, the blood half-life was calculated to be 2.97 h. *In vitro* targeting studies using three different cardiovascular/cancer biomarkers (VCAM-1, PSMA, and p32) were conducted, showing specific uptake of the targeted particles to relevant cell lines.

The second section examines the potential for applying the polyethylene glycol-bisphosphonate coating to other inorganic nanomaterials. CdZnSeS alloyed quantum dots were successfully synthesised, with the resulting particles exhibiting red emission ($\sim$604.0 nm) and no significant shift after phase transfer into aqueous solution. Preliminary *in vitro* cell studies revealed particle emission at the expected wavelength.

Finally, the synthesised nanoparticles were successfully coated with the amphiphilic protein (hydrophobin). The resulting nanoparticles exhibited no change in core size or morphology

as determined by transmission electron microscopy, as well as no shift in emission ($\sim$627.0 nm). *In vitro* studies were performed allowing for visualisation of the quantum dots in a biological environment after incubation at physiological temperature. In addition, particles were injected intratumourly into a live mouse model, with emission detected up to 24 h post injection. Lastly, radiolabelling with iodine-131 was achieved; confirming the possibility of utilising exposed residues on the protein to further functionalise the surface.

In conclusion, the described methods and nanoparticles synthesised represent a promising platform for the development of targeted agents for multimodal medical imaging and other bio-applications.

Acknowledgements

Firstly, a massive thanks goes to Prof. Mark Green (I'm extremely grateful for the use of your office and printer during my writing up time) and Dr. Rafael Torres Martin de Rosales for their great support and encouragement throughout my PhD.

Many thanks go to Andrew Cakebread for running my many ICP-MS samples over the years, and to Dr. Gema Vizcay-Barrena for assistance with TEM.

I would like to thank Dr. Andrea Protti, Dr. Alkystis Phinikaridou, Prof. Yves Gossuin, Dr. Arunkumar Panneerselvam, Dr. Xianjin Cui, Dr. Florian Kampmeier, Dr. Dylan Owen, Dr. Gilbert Fruhwirth, Dr. Nick Gaddum, Dr. Levente Meszaros, Dr. Ehsan Sharif-Paghaleh, Dr. Maya Thanou, Dr. Lea Ann Dailey, Raha Ahmadkhanbeigi, and Thais Fedatto Abelha for their help with experimental work and collaborations.

Thanks go to the lab group for keeping me company during long experiments and providing many laughs, in particular Jennifer Williams, Julia Blower, Michelle Ma, Mary Burkitt-Gray and Evren Kemal.

I'd like to show my appreciation to the Department of Physics for the support they have given me during this time, especially Julia Kilpatrick who has always looked after me, and Dr. Chris Lorenz for solving all my LaTeX problems!

I would also like to thank all my friends in both Physics and Imaging Sciences for helping me enjoy the past four years so much!

And lastly, I want to thank my family for their continued love and support.

To Mum, Dad and Emily.

Contents

List of Figures

List of Tables

Abbreviations

General abbreviations

ζ-potential	Zeta potential
AKI	Acute kidney injury
ATR	Attenuated total reflection
AUC	Analytical ultracentrifugation
CSI	Chemical shift imaging
CT	Computed tomography
D_H	Hydrodynamic diameter
DLS	Dynamic light scattering
D_M	Core size (as determined from a hysteresis curve)
D_TEM	Core size (as determined by transmission electron microscopy)
DVT	Deep venous thrombosis
EDX	Energy-dispersive X-ray spectroscopy
EM	Electromagnetic
FACS	Fluorescence-activated cell sorting
fcc	Face-centered cubic
FDA	Food and Drug Administration
FMT	Fluorescence molecular tomography
FOT	Fluorescence optical tomography
FWHM	Full width at half maximum
GI	Gastrointestinal
H_C	Coercive field
HPLC	High performance liquid chromatography
HRTEM	High resolution transmission electron microscopy
ICP-MS	Inductively coupled plasma mass spectrometry
IR	Infra-red
IS	Inner sphere
LD50	Lethal dose for 50 %
MR	Magnetic resonance
MRI	Magnetic resonance imaging
M_r	Remanent field
M_S	Saturation magnetisation
MWCO	Molecular weight cut-off
NC	Nanocrystal
NIR	Near-infrared
NMR	Nuclear magnetic resonance
NMRD	Nuclear magnetic relaxation dispersion
NP	Nanoparticle
NSCLC	Non-small cell lung cancer
NSF	Nephrogenic systemic fibrosis
OCT	Optical coherence tomography

OS	Outer sphere
PDI	Polydispersity index
PDT	Photodynamic therapy
PEG	Polyethylene glycol
PET	Positron emission tomography
PSMA	Prostate-specific membrane antigen
QD	Quantum dot
r_1	Longitudinal relaxivity
r_2	Transverse relaxivity
R_1	Longitudinal relaxation rate
R_2	Transverse relaxation rate
RES	Reticuloendothelial system
Rf	Retention factor
RF	Radio frequency
scFv	Single chain variable fragment
SIMS	Secondary-ion mass spectrometry
SPECT	Single photon emission computed tomography
SPIO	Superparamagnetic iron oxide nanoparticle
T_1	Longitudinal relaxation time
T_2	Transverse relaxation time
TE	Transmission electron
TEM	Transmission electron microscopy
TGA	Thermogravimetric analysis
TLC	Thin layer chromatograph
USPIO	Ultrasmall superparamagnetic iron oxide nanoparticle
VCAM-1	Vascular cell adhesion protein 1
XPS	X-ray photoelectron spectroscopy
XRD	X-ray diffraction

Chemical compound abbreviations

ATP	Adenosine triphosphate
BDP	Beclomethasone dipropionate
BP	Bisphophonate
BSA	Bovine serum albumin
$CDCl_3$	Deuterated chloroform
Cho/NAA	Choline/N-acetylaspartate
DPA-ale	Dipicolylamine-alendronate
DTT	Dithiothreitol
EDTA	Ethylenediaminetetraacetic acid
FDG	Fluorodeoxyglucose
$Fe(acac)_3$	Iron(III) acetylacetonate
HDA	Hexadecylamine
mal	Maleimide
MDP	Methylene diphosphonate
MET	Methionine
MSA	Mercaptosuccinic acid
OA	Oleic acid
OAm	Oleylamine
PEG	Polyethylene glycol
PFC	Perfluorocarbon
PTFE	Polytetrafluoroethylene

SAMSA	5-((2-(and-3)-S-(acetylmercapto) succinoyl) amino)
SDS	Sodium dodecyl sulfate
TAMRA	Carboxytetramethylrhodamine
TOP	Trioctylphosphine
TOPO	Trioctylphosphine oxide

Chapter 1

Introduction

1.1   Introduction and thesis outline

This thesis focuses on the development of novel nanomaterials for biomedical imaging using both iron oxide nanoparticles (NPs) and cadmium based quantum dots (QDs).

Chapter one gives an introduction to the main concepts of the thesis, and provides a background on current imaging techniques and contrast materials. Firstly, the principles behind clinically used diagnostic imaging will be presented, as well as the rationale behind the recent interest in the combination of different molecular imaging techniques. This will be followed by a summary of different imaging probes available, and the reasoning behind the use of NPs. Finally, the properties of magnetite and semiconductor particles will be described, concluding with an outline of available coating molecules coordinated to the surface of these nanocrystals (NCs) in order to provide stabilisation.

Chapter two concentrates on the development of targeted bimodal contrast agents, with low reticuloendothelial system (RES) uptake *in vivo*, based on magnetite NPs for use in positron emission tomography/single photon emission computed tomography-magnetic resonance (PET/SPECT-MR) imaging. The synthesis of novel iron oxide nanomaterials based in a polyethylene glycol-bisphosphonate (PEG-BP) coating will be described. In addition, full characterisation of the water soluble NPs is shown, including transmission electron microscopy (TEM), dynamic light scattering (DLS), infra-red (IR) spectroscopy, X-ray diffraction (XRD), and relaxivity measurements. Analysis of *in vivo* MR and SPECT imaging will then be presented, and finally the results from *in vitro* targeting studies of three different biomarkers will be detailed.

Chapter three describes the work undertaken on applying the previously mentioned PEG-BP coating to CdZnSeS alloyed QDs. The optical properties of the semiconductor NCs before and after surface ligand exchange is presented, followed by preliminary results from an *in vitro* macrophage study.

Chapter four focuses on applying amphiphilic proteins called hydrophobins as a method of phase transferring inorganic NPs. Optical analysis and size characterisation before and after encapsulation is given, followed by details of *in vitro*/*in vivo* studies involving ovarian and breast cancer cells, in addition to HeLa cells. This chapter concludes with results from functionalisation of the protein coated QDs using the radioactive isotope iodine-131

(^{131}I).

Chapter five describes future work.

Chapter six outlines the experimental procedures used in chapters two, three and four.

Appendices present the DLS number distributions for chapters two, three and four.

1.2   Imaging techniques

1.2.1   General introduction to *in vivo* imaging

Medical imaging techniques allow us to look inside the human body and detect diseased tissue without the need of surgery [1–3]. Two clinically available imaging techniques are single photon emission computed tomography and positron emission tomography. These modalities rely on the properties of radionuclides [4]. Other routinely used techniques include computed tomography (CT) which relies on the attenuation of X-rays to give anatomical information, and magnetic resonance imaging (MRI) in which magnetic fields are used to detect water molecules in different tissue environments [5,6]. In addition, optical imaging techniques such as optical coherence tomography (OCT) allow for high resolution and functional imaging of biological tissues [7].

In the following sections, the theory behind each of these techniques as well as their strengths and weaknesses will be briefly described.

1.2.2   Computed tomography

Basic principles behind computed tomography

Modern day CT instruments comprise of one X-ray source mounted opposite to several detectors, as shown in figure 1.1. Once the X-ray photons have passed through the body, they are detected by the detector system producing electrical signals. As both the radiation source and detectors rotate, the patient is moved through the scanner at a steady rate,

allowing for a rapid 3D image acquisition [8, 9].
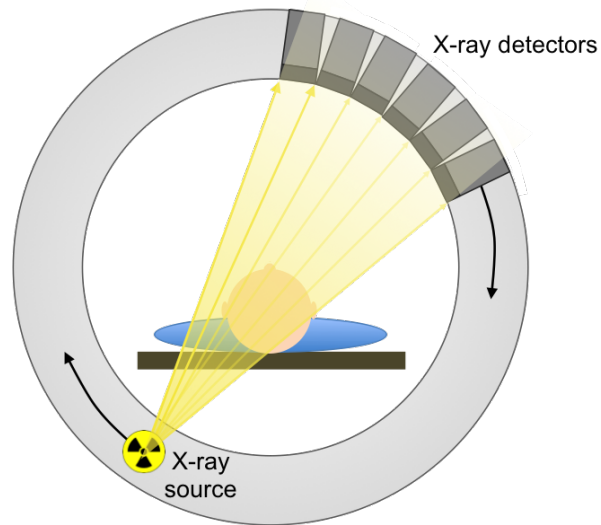
Figure 1.1: Schematic representation of a CT scanner.

Advantages and disadvantages of computed tomography

There are several benefits to using CT as a diagnostic tool, including the previously mentioned short scan times [10, 11]. When comparing against the first X-ray techniques implemented which involved one photographic plate detecting the X-ray beam, it is clear that CT significantly minimises (i) detail lost when superimposing 3D structural information on to a 2D film display, (ii) the noise-to-signal ratio which is high due to radiation scattering from the patient, and (iii) the difficulty in distinguishing between certain biological tissues [12, 13]. One particular area where CT is an accomplished diagnostic approach is in cardiac imaging where it provides important evaluation of disease of large vessels, as well as in abnormal coronary arteries [10].

As with any imaging procedure there are disadvantages, the main one being the exposure to ionising radiation. However, in most cases the diagnostic advantages outweigh the possible harmful effects from the X-ray beam [13]. Secondly, the temporal resolution of the images acquired is impaired due to collecting data from several rotations [14]. In addition, the imaging agents occasionally administered to enhance the contrast of the scan can exacerbate kidney function in patients with renal disease [10].

1.2.3   Magnetic resonance imaging

Basic principles behind magnetic resonance imaging

MRI (scanner shown in figure 1.2) works using the principles of nuclear magnetic resonance (NMR), whereby protons are aligned in an external magnetic field and disturbed when electromagnetic (EM) radiation of a certain frequency is applied. Once this EM wave has been removed, these protons relax back to the original alignment. In relation to MRI, this means the image acquired is essentially a representation of the relaxation times of water protons in tissues [15, 16]. Other biologically relevant nuclei, for example ^{13}C, ^{19}F and ^{31}P, are MRI responsive, however their lower sensitivities and tissue concentrations present difficulties for imaging applications [17].
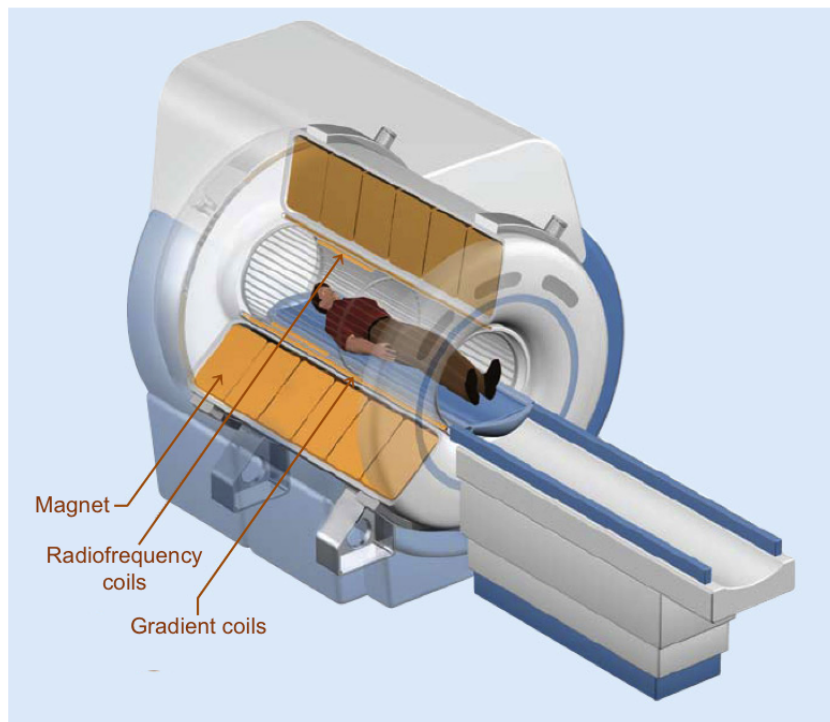
Figure 1.2: Schematic representation of an MRI machine [18].

There are two different types of relaxation times, and in order to explain these in slightly more detail, it is important to note some fundamental physics principles. All protons possess a positive electric charge and a spin, and hence induce a small magnetic field. Therefore, when an external magnetic field is applied, it is possible for these protons to align with it in two directions - parallel or anti-parallel to the field, with a slightly higher proportion aligning with the lower energy state (as demonstrated in figure 1.3a). In addition, the

protons will precess along the external magnetic field lines with a frequency, known as the Larmor frequency, given by equation 1.1 (depicted in figure 1.3b) [19].

(a) (b)
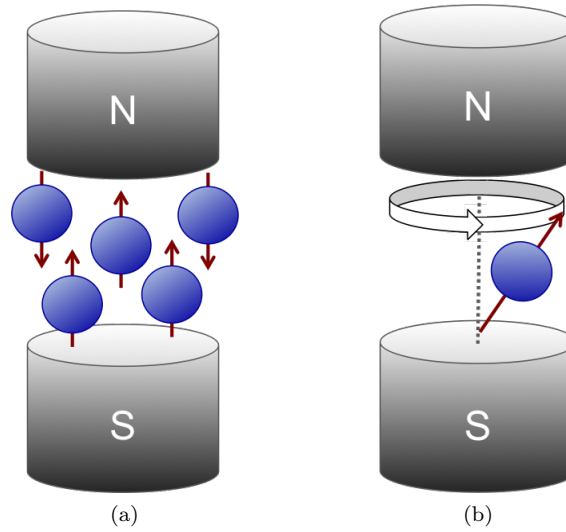
Figure 1.3: (a) Alignment of protons both parallel and anti-parallel to an external magnetic field; (b) Precession of protons in an external magnetic field.

$$\omega_0 = \gamma B_0 \qquad (1.1)$$

where ω_0 = Larmor frequency (Hz)

γ = gyro-magnetic ratio

B_0 = external magnetic field strength (T)

When a radio frequency (RF) pulse is applied to the system, some protons will move up an energy level, *i.e.* from parallel to the field to anti-parallel, hence decreasing the longitudinal magnetisation vector (orange arrow) as illustrated in figure 1.4. The time taken for the protons to realign with the external magnetic field once this RF pulse has been removed is known as the longitudinal, or spin-lattice, relaxation time (T_1) [19]. During this process, protons emit thermal energy to the surrounding lattice [15]. Figure 1.6a gives an example of the intensity variation of a vial of water during a T_1 sequence. In addition, the RF pulse causes all the protons to precess in phase, as shown in figure 1.5, initiating the formation of a transverse magnetisation vector (purple arrow). Once the pulse is withdrawn, the protons lose phase coherence, and this is the transverse, or spin-spin (as protons exchange energy with other nuclei during this time), relaxation time (T_2) [15, 16]. Figure 1.6b shows how the intensity of a vial of water changes during a T_2 sequence.
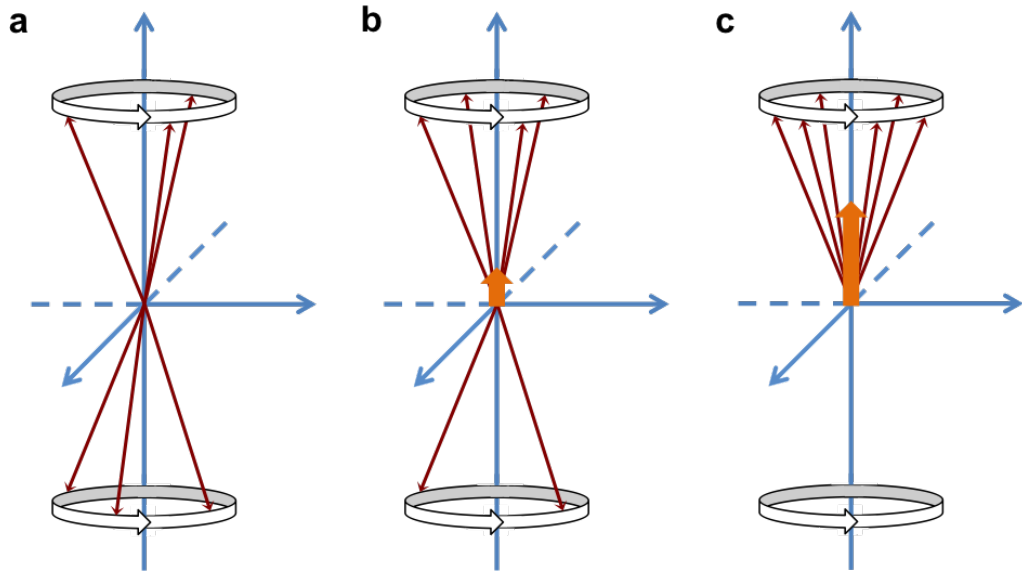
Figure 1.4: Schematic representation of longitudinal relaxation with only the protons aligned parallel to the external magnetic field shown: (a) the RF pulse is applied moving some protons up to a higher energy level, *i.e.* anti-parallel alignment, (b) the RF pulse is removed and the protons begin to relax, in turn increasing the longitudinal magnetisation vector, and (c) all protons have relaxed back down to the lower energy state, *i.e.* parallel alignment.
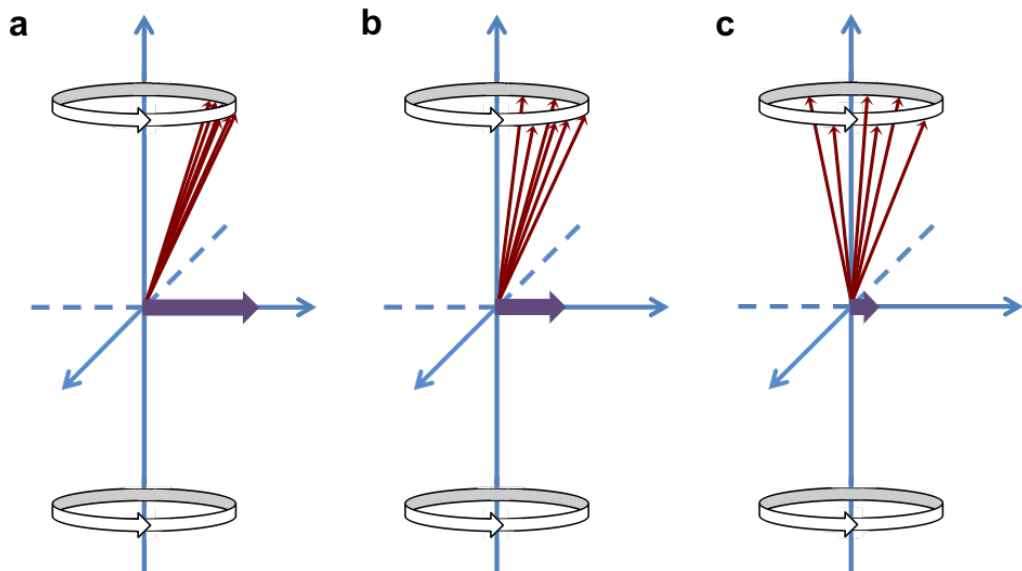
Figure 1.5: Schematic representation of transverse relaxation with only the protons aligned parallel to the external magnetic field shown: (a) the RF pulse is applied causing all protons to precess in phase, initiating the formation of a transverse magnetisation vector, (b) the RF pulse is removed and the protons begin to lose phase coherence, in turn decreasing the transverse magnetisation vector, and (c) most protons have relaxed out of phase.

15 ms   35 ms   95 ms   165 ms   295 ms   495 ms

(a)

1 ms   2.5 ms   5 ms   7.5 ms   10 ms   15 ms

(b)
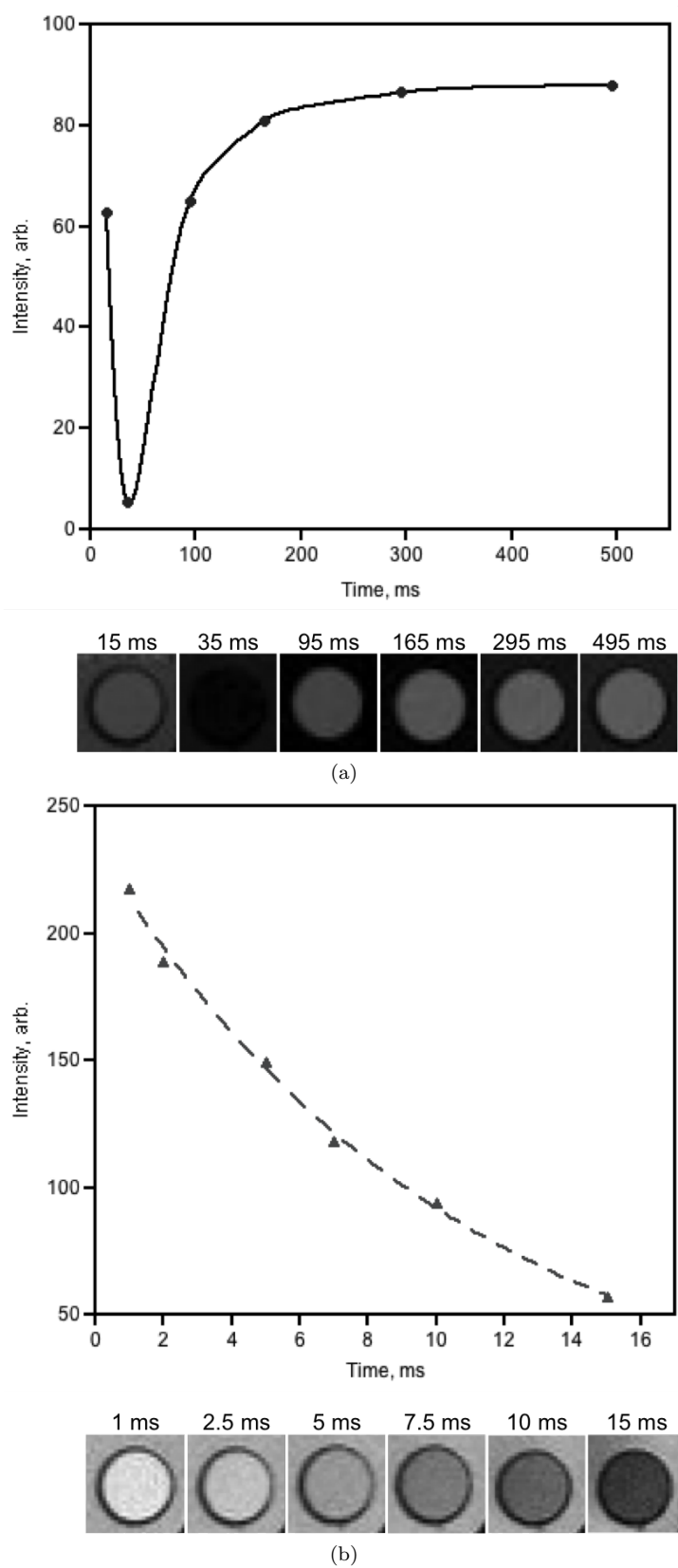
Figure 1.6: Variation of the measured intensity of a vial of water during a (a) T_1 sequence, and (b) T_2 sequence.

Advantages and disadvantages of magnetic resonance imaging

There are several advantages to using MR as an imaging technique. It allows for the acquisition of soft tissue images with high three-dimensional spatial resolution (<0.1 cm), and can be considered as a non-invasive procedure delivering no ionising radiation dose [20, 21]. Additionally, the intensity of the signal, and hence contrast of the image, can be determined by several parameters. Firstly, intrinsic properties such as both the longitudinal and transverse relaxation rates, as well as the proton density. Secondly, instrumental factors including magnetic field strength and the sequencing technique used. Altering these can emphasise differences between tissues. The fact that there are many parameters influencing the overall contrast of the image allows for very different images of the same region to be captured [21, 22].

Although there are clear advantages for the use of MRI it does have its limitations. Perhaps the main limitation is its low sensitivity when using contrast agents, which limits its potential for molecular imaging. The low signal intensity per mole has to be compensated for by the use of large amounts of an agent [20]. For example, the dose of Magnevist (described fully in a later section; figure 1.19) for a 60 kg adult contains 11 g of the contrast agent, which includes 2 g of the toxic metal gadolinium. However, it should be noted that contrast agent material available for MRI is considered safer than iodinated agents utilised in CT [10, 23]. In addition, long scanning times combined with loud noises in a confined space make the imaging procedure uncomfortable for the patient [10].

1.2.4 Positron emission tomography and single photon emission computed tomography

Basic principles behind positron emission tomography

For PET, a radioactive nuclide undergoing beta decay due to an inadequate number of neutrons, resulting in the release of a positron (e^+) is required. This radioisotope, for example fluorine-18 (^{18}F), is injected into the patient prior to imaging. The theory behind this technique is once the emitted positron has lost a sufficient amount of its kinetic energy, it interacts with an electron (e^- – located in the patients tissue) producing two annihilation photons (γ). These photons travel in opposite directions, each with an energy of 511 keV.

Detectors placed approximately 180 ° from each other (figure 1.7) will only register a valid event if both photons are detected coincidently [24].
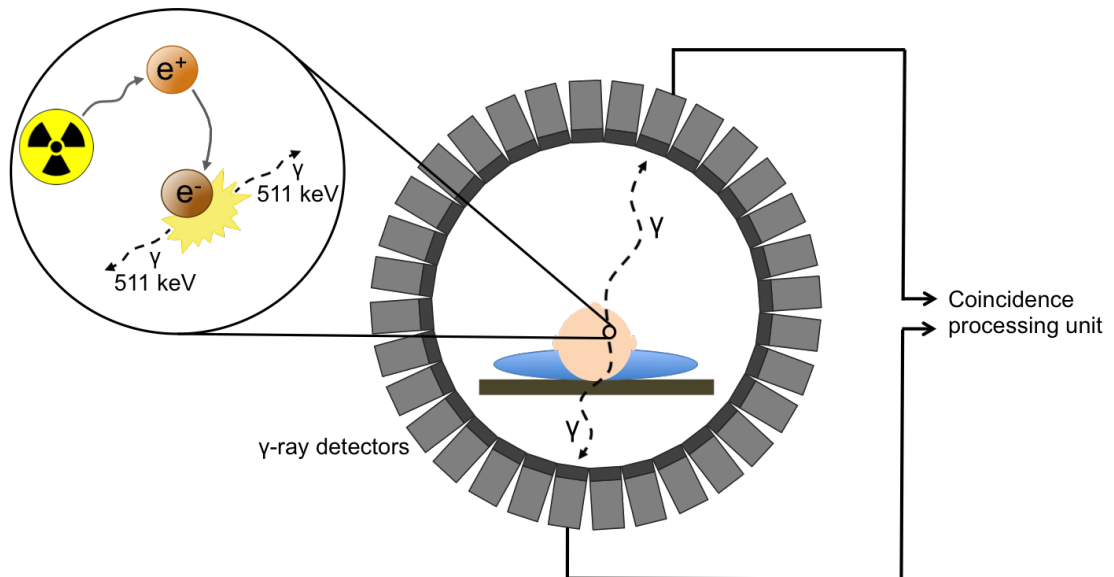
Figure 1.7: Schematic representation of a PET scanner.

The spatial resolution of this radionuclide imaging technique is dependent on instrumental factors and the distance travelled by the emitted positron before a sufficient amount of energy has been lost allowing annihilation to occur, known as the positron range (figure 1.8). Although this distance varies slightly between different radioactive isotopes, the maximum possible resolution is $\sim$4-5 mm, with $\sim$1.2 mm achieved in small animal imaging [1, 25, 26].
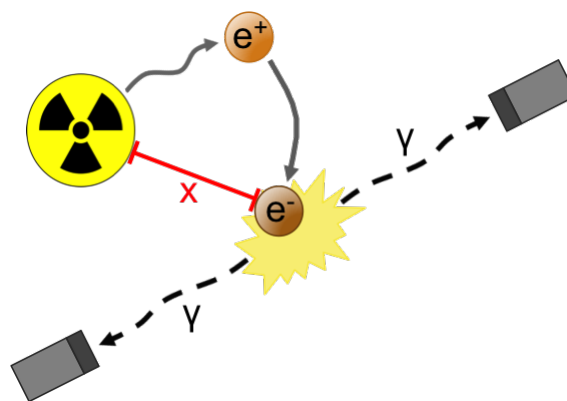
Figure 1.8: Dependence of PET resolution on the positron range (represented by x).

Basic principles behind single photon emission computed tomography

SPECT works on the same basis as PET in that a radioisotope is injected into the patient initially and imaging is through the detection of gamma rays. The difference with this

technique is the radiotracer injected decays emitting gamma radiation. As can be seen in figure 1.9, it is these photons that are recorded by the detectors which rotate around the patient (in contrast to the ring of detectors used in PET scanning) [27].
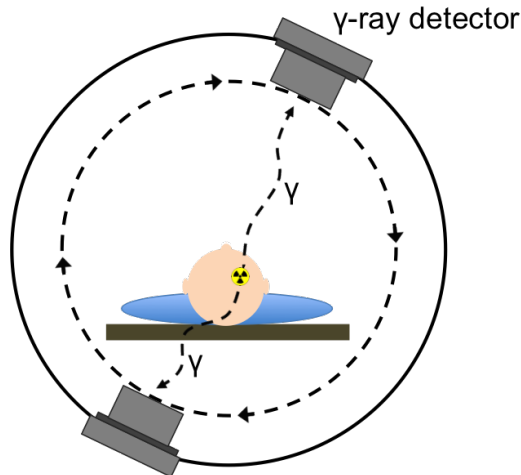
Figure 1.9: Schematic representation of a SPECT scanner.

Comparison of positron emission tomography and single photon emission computed tomography

In comparison with nuclides required for PET, most SPECT isotopes have longer half-lives allowing for *in vivo* biological processes which occur over several hours or days, for example cell division or endogenous processes, to be observed [28]. In addition, SPECT tracers can be produced at a more economical cost and it should be noted that the radiation-absorbed dose per decay event is generally lower for gamma emitters than for positron emitters [29]. However, the collimators used in clinical SPECT imaging significantly reduce the number of emitted photons reaching the detector [27]. This reduces the intensity of the signal by approximately two to three orders of magnitude, and as a result the spatial resolution of 8-15 mm is lower than that of PET [1, 26, 30]. Furthermore, this loss of signal increases the time needed per scan due to a lower signal-to-noise ratio, therefore implying PET is the most effective technique. The shorter scans required for PET also allow for multiple fields of view to be examined in a feasible length of time. This is particularly important in fields such as clinical oncology [30]. In addition, when compared to the most commonly used clinical SPECT isotope, technetium-99m (^{99m}Tc), PET has a larger tissue penetration depth and improved quantification due to the higher energy gamma rays emitted (511 keV in comparison to 140 keV for ^{99m}Tc) [24, 29].

Advantages and disadvantages of positron emission tomography/single photon emission computed tomography

PET and SPECT imaging techniques are used to obtain metabolic and molecular information. This is advantageous over anatomical imaging techniques, such as MRI, for the reason that disease is a biomolecular process. This means it can be studied throughout its evolution allowing for diagnosis, as well as development and monitoring of therapies [31]. For example, using PET/SPECT imaging in cancer allows for the early identification of disease in all organs, and to distinguish between malignant and benign lesions. Compared to techniques such as CT and MRI, PET/SPECT has an 8-43 % higher diagnostic accuracy, and changes treatment in 20-40 % of cases [32–42]. For instance, it has been reported that when staging non-small cell lung cancer (NSCLC), PET has an accuracy of $\sim$83 % compared to $\sim$64 % for CT [43, 44]. In addition, Changlai *et al.* detailed a study whereby the staging of patients with NSCLC were re-evaluated using PET rather than conventional techniques, revealing a total of 37 % of cases being reclassified from resectable to unresectable or vice versa [45].

Another main advantage is the higher signal intensity per mole of PET/SPECT imaging agents when compared to agents used in MRI. Thus, for a typical PET or SPECT procedure only nano- to micrograms are injected into the patient, whereas for MRI gram quantities are needed. As a consequence, in general, there are fewer toxicity issues associated with the use of radiopharmaceuticals.

Again, there are disadvantages associated with this procedure. First is the potential harmful effects of handling radioactivity, although this is manageable and closely monitored by medical physics/radiation protection teams. In addition, large amounts of radioactivity may be required during synthesis to accommodate for radioactive decay as well as the possible low radiolabelling yields. Furthermore, synthesis of suitable imaging agents is highly specialised due to the need for facilities suitably equipped for radiolabelling procedures [46]. Furthermore, as was mentioned previously, the spatial and temporal resolution of these techniques is lower in comparison with MR imaging.

1.2.5 Optical

Optical imaging is a rapidly emerging modality in disease and therapy due to the ability to investigate both structural and functional changes with a high spatial resolution [47]. There are two main optical imaging techniques implemented in *in vivo* applications, bioluminescence imaging and fluorescence imaging [48]. The principles behind each approach are briefly described below.

Basic principles behind bioluminescence imaging

This imaging technique (figure 1.10) depends on the enzymatic generation of visible light by living organisms, and for animal tumour model purposes this is primarily based on the luciferase system derived from the North American firefly *Photinus pyralis* [49]. The oxidation of luciferin (a small-molecule substrate responsible for bioluminescence, in this case it is firefly luciferin) by luciferase (the enzyme catalysing the oxidation reaction) in the presence of adenosine triphosphate (ATP, a nucleoside triphosphate responsible for transportation of chemical energy within cells for metabolism) and molecular oxygen forms an electronically excited oxy-luciferin species [50], which then emits light in the region of 530 nm following relaxation to its ground state [51,52]. In order for luciferase to be expressed, cells can be be transfected or transduced *in vitro* prior to *in vivo* implantation, alternatively, bioluminescent transgenic tumour models may be generated via introduction of reporter gene expression through the germline [50].

Basic principles behind fluorescence imaging

Fluorescence imaging is illustrated in figure 1.11 and is based on the simultaneous absorption and re-emission of light by a substance [53]. A fluorescent imaging probe is exogenously administered into the subject, excited at a specific wavelength and the consequent red-shifted light is detected by an optical device [54].

Advantages and disadvantages of optical imaging

One main advantage of optical imaging is the high sensitivity of the contrast molecules used, the lower limits of detection may require as little as femtomolar concentrations of an optical reporter [55]. However, there is a major shortcoming with this imaging technique. Tissue
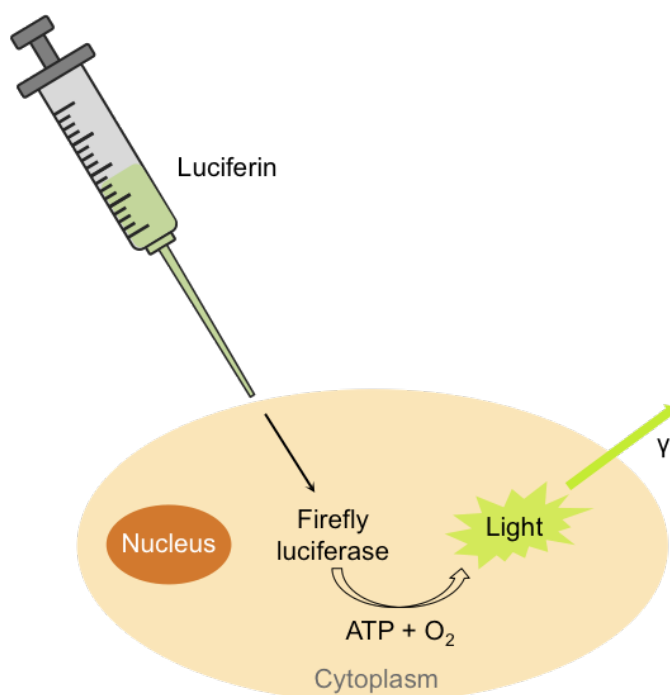
Figure 1.10: Schematic representation of bioluminescence imaging involving the production of light photons from the oxidation of the substrate luciferin in the presence of luciferase expressed by engineered cells, ATP and oxygen.
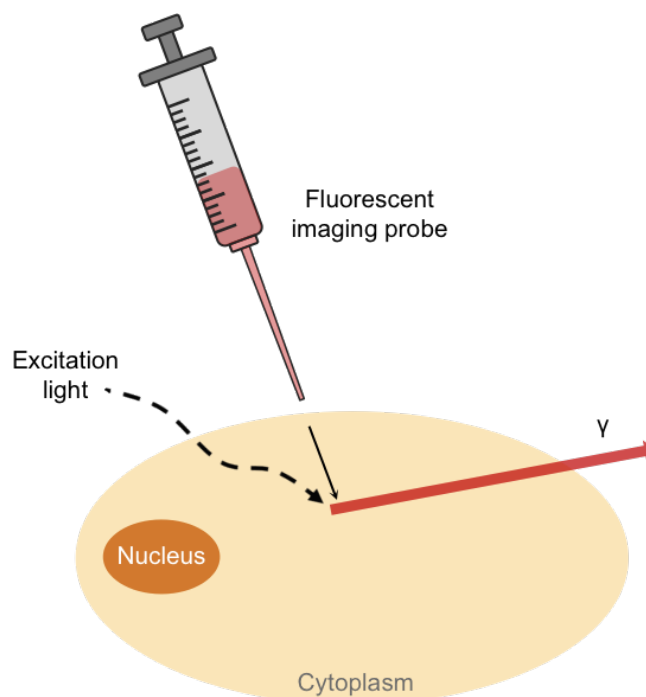
Figure 1.11: Schematic representation of fluorescence imaging involving the production of light photons by excitation of a fluorescent imaging probe at a particular wavelength.

autofluorescence coupled with the attenuation and scattering of light in the visible region by haemoglobin, lipids and other molecules significantly reduces optical signals, in some cases by as much as 10-fold per centimetre of tissue [56–58]. An approach to overcome this problem is the use of near-infrared (NIR) imaging agents which emit below a wavelength of 900 nm, in order to minimise absorption of light by water molecules, with the optimal emission wavelength being at approximately 800 nm [59–61]. In this region of the spectrum, the aforementioned processes are reduced resulting in a considerable improvement in the signal-to-background ratio a point comparable to or exceeding that of other molecular techniques [48]. This increase in sensitivity opens up the possibility of detecting tomographic optical signals at significantly lower depths than currently possible [62]. A second disadvantage is related to quantification of the detected signal. As the differential absorption of light skews imaging toward the contrast probes accumulated near the surface of the subject, it is only currently possible to obtain relative quantification rather than absolute as with radionuclide imaging, although developments in 3D imaging and analysis techniques such as fluorescence molecular tomography (FMT) are improving this limitation [63]. Finally, optical imaging techniques are non-ionising, non-invasive, allow for near real-time acquisition of results as well as utilising portable and economical equipment [47].

1.2.6 Combining imaging modalities

The development of instruments capable of imaging more than one modality is beneficial in gaining both anatomical and physiological information simultaneously about a region of interest. Not only does this reduce the overall scanning time, but it also allows for the more accurate superimposition of images due to the lack of temporal changes and other factors such as the involuntary movement of internal organs [64].

Positron emission tomography/single photon emission computed tomography-computed tomography

PET/SPECT-CT instruments have become conventional in the clinical environment. CT gives anatomical information whilst metabolic information is gained from PET/SPECT. Although software fusion of these two modalities is possible, there are several advantages to fusion of hardware. Inaccuracy in the information obtained due to change in the patients position (usually occurring during the moving from one instrument to the other) is reduced

[65], registration accuracy is improved with no further alignment required, and transmission scans are unnecessary due the relevant data needed for attenuation correction being available from the CT acquisition [66, 67].

Significant improvements in the clinical information gained for oncology patients from PET-CT scanners have been reported from various studies, leading to enhanced diagnosis and staging of cancer [68–70]. Furthermore, response to therapy can be monitored shortly after treatment has begun, allowing for ineffective therapeutics to be identified early [71].

An example illustrating how PET-CT is an improvement upon the comparison between separate PET and CT scans, and how this has contributed to the care of oncology patients, is shown in figure 1.12. In this case, the patient had a history of colon cancer and an initial PET scan (figure 1.12a) revealed the presence of recurrent lesions in the right abdomen. However, two difficulties arise from using this single scanning mode: (i) they would be assumed to be either serosal or nodal, with the possibility of resection, and (ii) identifying their exact locations would be challenging. Fusing PET with CT (figure 1.12c) clearly locates the lesions to the right psoas and iliacus muscles and classifies them as unresectable, therefore altering the patients treatment [72].

Figure 1.12: PET-CT images of a patient being restaged for colon cancer. (a) PET image shows ^{18}F-FDG uptake consistent with recurrence (dashed circle) but localisation of cancerous tumour is not possible, (b) CT and (c) fusion images indicate intraabdominal cancerous region (arrow), as well as psoas and iliacus muscle lesions (arrowheads). Lesser activity elsewhere is physiologic bowel uptake [72].

Although the combination of PET with CT offers advantages over using the techniques individually, there are some associated disadvantages. The first being the increase in radiation dose received by the patient, which can be 5 to 10 times greater than the average annual exposure from naturally occurring radiation sources ($\sim$25 mSv for a ^{18}F-fluorodeoxyglucose, ^{18}F-FDG, PET-CT [73]). This is accommodated for by using lower energy settings for the CT scan, resulting in poorer quality images. In addition, PET-CT may not be suitable for some procedures such as those using iodinated contrast agents, which may cause artefacts when reconstructing the PET images due to absorbance of the lower energy X-

rays [72].

Positron emission tomography/single photon emission computed tomography-magnetic resonance imaging

The combination of PET/SPECT with MRI will give both highly sensitive quantifiable metabolic information and high resolution anatomical information in any orientation leading to enhanced diagnostic precision, particularly in identifying cancerous cells. Regions of interest can be established using PET/SPECT, which can then be examined in closer detail using the high resolution of MRI. This then reduces (i) the amount of tissue to be scanned, and (ii) the time it takes to run when compared to sequential scans [74,75]. There are several reasons why using MRI rather than CT to obtain structural information in a bimodal system is beneficial. MRI is viewed as the initial imaging procedure for diagnosis in oncological examinations regarding tumours in the brain or neck region due to the clear differentiation between closely neighbouring anatomical structures such lymph nodes, mucosa and blood vessels [76,77]. In addition, MR can provide some functional information, such as perfusion and spectroscopy used in the management of stroke patients, however the sensitivity of this technique is lower than for PET/SPECT ($\sim 10^{-5}$ mol/L for MRI vs. $\sim 10^{-12}$ mol/L for PET/SPECT) making the radionuclide component essential. The combination of functional information from two modalities can provide complimentary data which can aid diagnosis of disease and hence treatment [78]. Secondly, with PET/SPECT-MRI there is the possibility to acquire both image datasets simultaneously. This opens up the possibility of performing motion correction of the PET image reducing artefacts which results in better resolution and activity quantification [79, 80]. On top of this, when compared to current bimodal systems such as PET-CT, the patient will acquire a lower dose of radiation [81]. Finally, it has been reported that in a magnetic field, the distance travelled by a positron before annihilation with an electron is reduced, leading to an improvement in the resolution PET images acquired with PET-MRI scanners. This loss of resolution is proportional to the strength of the magnetic field, for instance, when comparing 0 T and 4 T there is narrowing of the positron range full width at half maximum (FWHM) by a factor of 1.22 [82].

An example demonstrating the limitations of PET-CT in comparison to PET-MRI is illustrated in figure 1.13 which shows the scans of a patient with a peripheral sarcoma. The degree of invasion into adjacent muscles can be more accurately determined on PET-MRI (figure 1.13b) than on PET-CT (figure 1.13d). However, the functional information gained

by using the PET component is of limited use in this case [83]. A second case where the PET and MRI combination provided essential information is shown in figure 1.14. These images are of a patient with brain gliomatosis admitted for a tumour biopsy. The contrast-enhanced T_1-weighted MRI in figure 1.14a revealed no enhancement of the tumour was indicated, suggesting a low-grade carcinoma. However, carbon-11-methionine (^{11}C-MET) PET imaging and chemical shift imaging (CSI) mapping of choline/N-acetylaspartate (Cho/NAA) displayed hot spots in the basal frontal lobe on the left side and in the right insular region respectively. As a result, biopsies were performed in both locations revealing anaplastic glioma in the left frontal region and low-grade glioma in the right insular region [84].
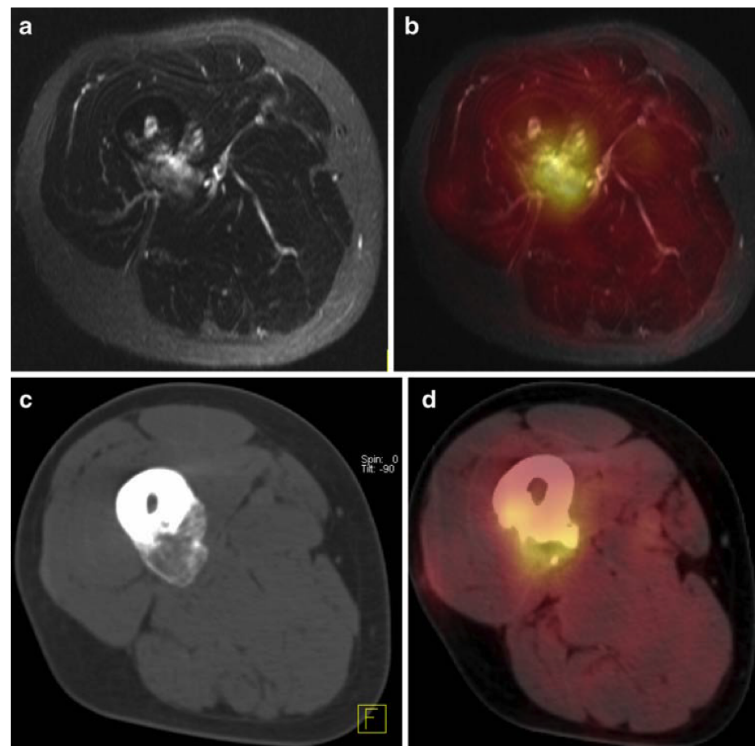
Figure 1.13: PET-CT and PET-MRI comparison for imaging of peripheral osseous sarcoma. (a) MRI, and (b) PET-MRI (retrospectively fused image) allows for clear assessment of the tumour within the bone and adjacent muscles when compared with (c) CT, and (d) PET-CT [83].

Again, as with any imaging technique and modality combination, there are some drawbacks. As discussed previously, the examination times associated with MRI are significantly longer (ranging from 20 min to 60 min for a whole-body scan) which varies between imaging protocols depending on the number and type of sequences used [83]. Another challenge facing PET-MRI are the higher running costs causing problems in procuring approval for new imaging tests with regulatory agencies [85]. Additionally, on account of MRI contrast being dependent on water content of tissues, it is not suitable for imaging of bone and the

T_1-weighted MRI   CSI Cho/NAA   PET ^{11}C-MET
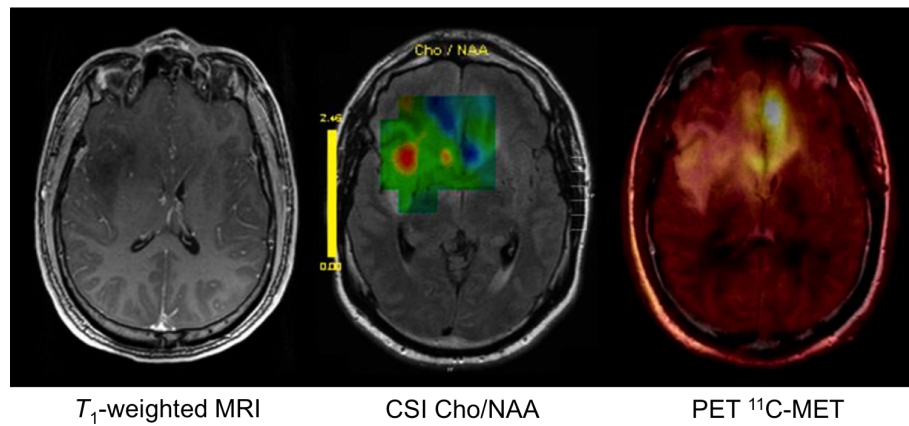
Figure 1.14: Standard contrast-enhanced T_1-weighted MRI (left) of brain gliomatosis indicated a low-grade tumour due to no contrast enhancement, chemical shift imaging (CSI) (echo time = 135 ms, centre) of choline/N-acetylaspartate (Cho/NAA) quotient revealed a hot spot in the right insular region, and PET-MRI with ^{11}C-methionine (right) displayed uptake in the basal frontal lobe on left side. Due to this discrepancy, biopsy was performed in locations suggested by CSI and PET-MRI revealing anaplastic glioma (World Health Organisation grade III) in the frontal left region and low-grade glioma (World Health Organisation grade II) in the right insular region [84].

lungs where CT is still the favoured technique [79]. Finally, despite the fact that research into PET-MRI commenced at the same time as PET-CT, due to the challenging engineering as well as the economical issues, the development of instruments capable of both PET and MRI has been delayed [75]. There are two main difficulties to overcome when designing a PET-MRI system. First, the magnetic-sensitive photomultiplier technology used to detect gamma photons in the PET/SPECT set-up needs to be replaced by compact, solid state silicon photo sensors - avalanche photodiodes - that are not susceptible to magnetic fields and minimise potential interference with MR gradients or radio frequencies [86]. Secondly, new procedures for PET attenuation correction need to be developed to be based on MRI data alone [84].

Although there are technological and economical obstacles to overcome in the development of PET-MRI, there are several preclinical and clinical applications where this combination of modalities into a single instrument could prove invaluable. Focussing firstly on preclinical studies, the lower radiation dose of PET-MRI compared to that of PET-CT is important when imaging small animals due to the lower LD50 value (lethal dose for 50 %) for rodents. For a typical whole-body mouse CT scan, the dose received is ∼0.6 Gy (equating to ∼5 % of the LD50) and several studies have shown that a dose as low as 0.075 Gy can induce changes in expression of some small proteins [87, 88]. With regards to clinical usage, simultaneous mapping of MRI spectroscopy and functional changes could be of particular use in neurology,

where it could lead to new insight into brain activation [89], and in pediatric patients. Musculoskeletal imaging will be an area of particular clinical interest owing to false negative results occurring in some cases of small metastases when using current PET-CT imaging. Due to radiotracer uptake of normal bone and CT unable to visualise changes in bone architecture in early stage tumours, MRI is required as it can be used to image bone marrow with higher sensitivity and specificity [90–92]. In addition, there is potential for studying the tumour response to new drugs and as result, treatment strategies may be optimised [93].

The focus of the above section has been to identify the potential of PET-MRI and to show how this has already been proved possible in preclinical research. It should be noted however, that these systems are now becoming a reality in the clinical environment with two instruments in the UK based at St Thomas' Hospital and University College Hospital.

Magnetic resonance imaging-optical

The fusing of MRI with optical imaging is advantageous as it allows for the acquisition of fluorescence based histology and anatomical evaluations simultaneously [94]. An example of where this has been proven to aid the diagnosis of cancerous cells was demonstrated by Rodriguez *et al.* using fluorescently tagged magnetic NPs. T_2-weighted MRI was used to locate a prostate cancer xenograft alongside fluorescence microscopy to create histology sections, which clearly showed particles embedded in the tumour tissue, confirming the diagnosis of the cancerous nature of the cells (figure 1.15) [95]. In addition, it could be possible to use the external magnetic field to physically manipulate the location of the fluorescent particles [96].
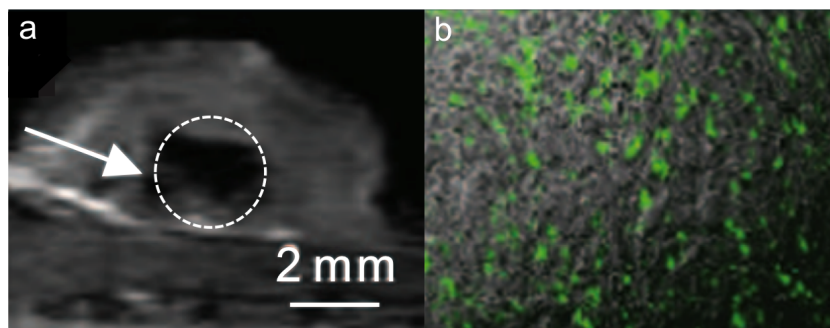
Figure 1.15: (a) T_2-weighted imaging of mouse prostate xenograft; (b) Frozen tumour section imaged by confocal microscopy [95].

Positron emission tomography/single photon emission computed tomography-optical

Simultaneous radionuclide and optical imaging has the potential to provide complementary information as well as for the tight correlation between both sets of contrast data [97]. For example, during a drug delivery study fluorescence optical tomography (FOT) can be used to monitor tumour response to therapy, with PET quantifying the distribution of the drug throughout the subject [98]. Current research has demonstrated the feasibility of the combination PET/SPECT and optical systems, indicating the potential for this bimodal technique to become a dynamic tool for a multitude of real-time imaging applications [99].

1.3 Imaging agents

1.3.1 General introduction to use of contrast agents

Imaging agents are used as a means to increase the signal of an imaging technique at an area of interest. This is achieved by the accumulation of the probe at a desired region, sometimes followed by the interaction of the agent with the target, improving the contrast of the image [100]. Although many groups have researched the hardware aspect of multimodal imaging in order to exploit this technique, imaging agents capable of being used for two techniques simultaneously are also of interest.

When developing a contrast medium there are several initial stages to consider which include identifying a suitable diagnostic opportunity and how the agent will be used in order to determine the performance metrics required. In addition, once these factors have been established chemical synthesis optimisation is necessary followed by preclinical and clinical studies [101]. Figure 1.16 gives a more detailed summary of the development process [101]. Additional requirements that need to be addressed include the biocompatibility of the probe, excretion time and route, solubility and stability in aqueous conditions, and the osmotic potential when in solution [102,103]. Moreover, the costs of bringing an imaging agent from the laboratory to the commercial market is substantial, it's estimated to be in the range of $100 million to $200 million [104].
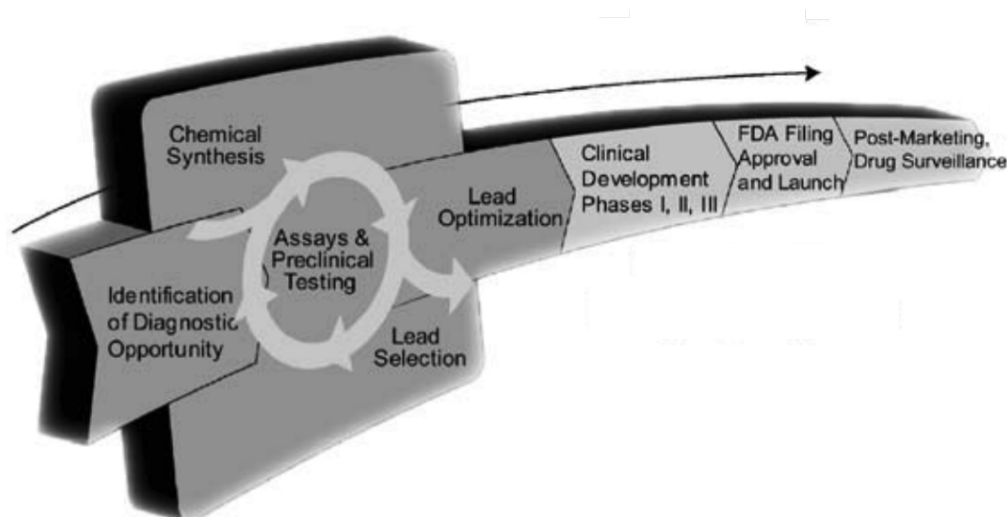
Figure 1.16: Discovery and development of diagnostic imaging agents [101].

The following section will outline current agents available for individual modality imaging that have overcome the above mentioned development and economic issues, as well as the mechanisms behind how they enhance contrast. Furthermore, the current preclinical outcomes of combining several modalities into one probe will be described.

1.3.2 Magnetic resonance imaging

Relaxation theory of magnetic resonance imaging agents

MRI contrast agents have the ability to change relaxation times, the amount by which is characterised by the relaxivity values, r_1 ($s^{-1}mM^{-1}$; the capacity to adjust the longitudinal relaxation time) and r_2 ($s^{-1}mM^{-1}$; the capacity to adjust the transverse relaxation time). As a particular material will affect both T_1 and T_2, it is the ratio of r_2 to r_1 which determines whether an agent can be used as a T_1 agent or a T_2 agent. T_1 contrast agents (positive contrast agents) brighten areas of uptake whereas T_2 (negative contrast agents) darken these areas [16], an example of which is shown in figure 1.17 [105]. Contrast agents for MR imaging are based on paramagnetic metals such as gadolinium and iron.

The three main contributions to the relaxation effects of MR imaging agents are inner sphere (IS) relaxation, outer sphere (OS) relaxation, and diamagnetic relaxation, as shown in equation 1.2. The latter being the relaxation of the solvent in the absence of a paramagnetic species.

Figure 1.17: MR imaging showing T_1 (left) and T_2 (right) sagittal complete spine stitch imaged using the Discovery MR750 3.0 T developed by GE Healthcare [105].

$$R_{1,2} = R_{1,2}^{\text{IS}} + R_{1,2}^{\text{OS}} + R_{1,2}^{0} \tag{1.2}$$

where $\quad R_{1,2}$ = measured relaxation

$\qquad R_{1,2}^{\text{IS}}$ = inner sphere relaxation

$\qquad R_{1,2}^{\text{OS}}$ = outer sphere relaxation

$\qquad R_{1,2}^{0}$ = diamagnetic relaxation

Inner sphere relaxation is described by the Soloman-Bloembergen-Morgan theory, equations 1.3 and 1.4 [106–108], and arises from the exchange between water molecules coordinated directly to the metal centre and surrounding bulk water [22, 109].

$$R_1^{\text{IS}} = \frac{q}{55.56(T_{1\text{M}} + \tau_{\text{M}})} \tag{1.3}$$

$$T_{1\text{m}} = f(\tau_{\text{M}}, \tau_{\text{R}}, T_{ie}, r) \tag{1.4}$$

where q = number of water molecules coordinated to the metal ion

T_{1M} = longitudinal relaxation time of coordinated water molecules

τ_M = mean residence lifetime of coordinated water molecules

τ_R = rotational correlation time of the complex

T_{ie} (i = 1, 2) = longitudinal and transverse electron spin relaxation times

r = distance between the metal ion and the protons of the coordinated water molecules

Outer sphere relaxation is outlined by the Freed theory [110,111] and is induced by the diffusion of water molecules within the magnetic field gradients surrounding the paramagnetic hydrated ion [109]. The dominant parameters influencing the OS relaxation are the minimum distance of approach between non-bound water molecules and the metal ion, and the sum of the water and paramagnetic diffusion coefficients as shown in equation 1.5 [22].

$$\tau_D = \frac{a^2}{D} \tag{1.5}$$

where τ_D = diffusional correlation time

a = distance of closest approach of water molecules

D = relative diffusion coefficient of solute and solvent

Both inner sphere and outer sphere relaxation are dependent on the concentration of the paramagnetic species [112]. In most cases, the IS contribution tends to be larger because (1) the distance between the metal based complex and a coordinated water molecule is on average smaller than that between the hydrated ion and a diffusing water molecule, (2) the diffusion time is often shorter than the residence time on the binding site [109]. However, in the absence of water exchange, for instance with nanoparticle based agents, the OS process controls relaxation [113].

Figure 1.18 gives a summary of the principle physical properties mentioned above that affect the relaxivity of imaging probes and should be considered when designing an MRI contrast agent.
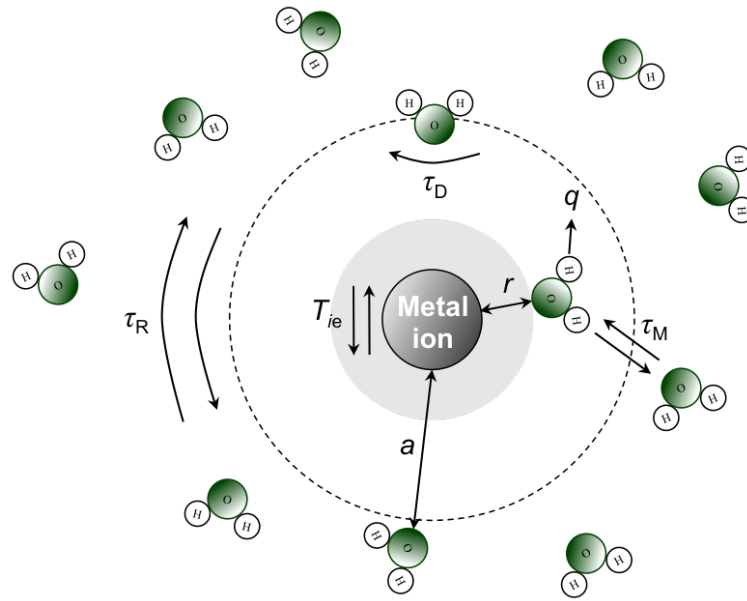
Figure 1.18: Schematic representation of the principle parameters contributing to the relaxation effects of MR imaging probes.

Currently available agents

There are several agents commercially available for imaging, both consisting of iron oxide (Fe_3O_4) nanoparticles and gadolinium-based agents. The lanthanide ion Gd(III) is generally the ion of choice for T_1 MR imaging probes because it has a high magnetic moment ($\mu^2 = 63\ \mu_B^2$) [22], whereas iron oxide is routinely used for T_2-weighted imaging. One example of a gadolinium based agent is Magnevist (Bayer Schering Pharma AG, Germany), figure 1.19. This is a paramagnetic ion based agent containing the N-methylglucamine salt of the gadolinium complex of diethylenetriamine pentaacetic acid [114]. It is used primarily to image lesions with abnormal vascularity in the brain and the rest of the body [115]. At a field strength of 3.0 T (in aqueous solution) it is found to have a r_1 of 3.29 s^{-1}mM^{-1}, a r_2 of 4.8 s^{-1}mM^{-1} and hence a r_2/r_1 of 1.46, therefore allowing this probe to be used in T_1 weighted imaging [116].
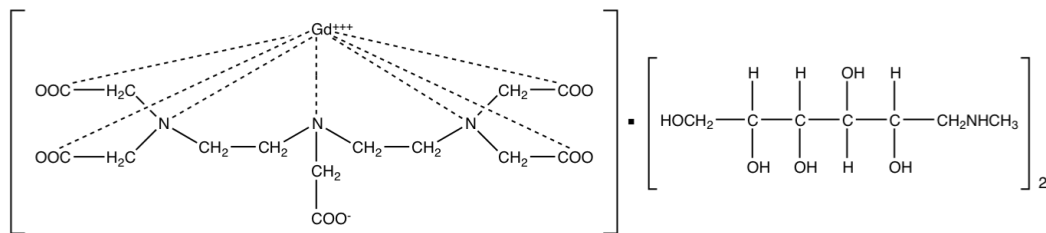
Figure 1.19: General structure of Magnevist.

An example of a clinically available oral iron oxide nanoparticle is Lumirem (Guerbet, France), which is used primarily for T_2-weighted imaging of the gastrointestinal (GI) tract [117]. This imaging agent consists of superparamagnetic iron oxide crystals with a core size of approximately 10 nm, which are siloxane-coated increasing the overall diameter to *ca.* 300 nm [118,119]. The relaxivities have been found to be r_1 of 3.2 s^{-1}mM^{-1} and r_2 of 72 s^{-1}mM^{-1} (at 0.47 T in aqueous solution), yielding an overall r_2/r_1 of 22.5 [120,121].

1.3.3 Positron emission tomography and single photon emission computed tomography

Compared to agents for MR imaging, there are several more available for PET/SPECT. A clinically used PET imaging agent is ^{18}F-FDG used for the imaging of tumours as demonstrated in figure 1.20a. As cancerous cells have an increased consumption of glucose and because ^{18}F-FDG cannot be metabolised by cells, the activity in these areas will be larger and therefore the signal intensity will be higher [122]. Due to the short half-life of the radioisotope (110 min), this agent is usually prepared on-site. A commonly used class of SPECT radiopharmaceuticals are ^{99m}Tc-labelled phosphonates, which bind well to metabolically active bone. As a consequence, ^{99m}Tc conjugated to phosphonates, such as methylene diphosphonate (MDP), is routinely used in the SPECT imaging of bone metastases, as illustrated in figure 1.20b [20,123].

1.3.4 Optical

A frequent dye used in fluorescence imaging applications is Cy5.5, the structure of which is illustrated in figure 1.21 [126]. The excitation and emission maxima of this dye are 675 nm and 695 nm respectively, and hence the dye will perform optimally in the red region of the spectrum [60]. It has previously been shown that this molecule can be conjugated to antibodies in order to demonstrate the use of fluorescence imaging to detect cancerous tumours in animal models [127]. However, due to a reduction in performance in the NIR, it is best to use this dye in applications requiring a lower sensitivity [60].

(a)   (b)
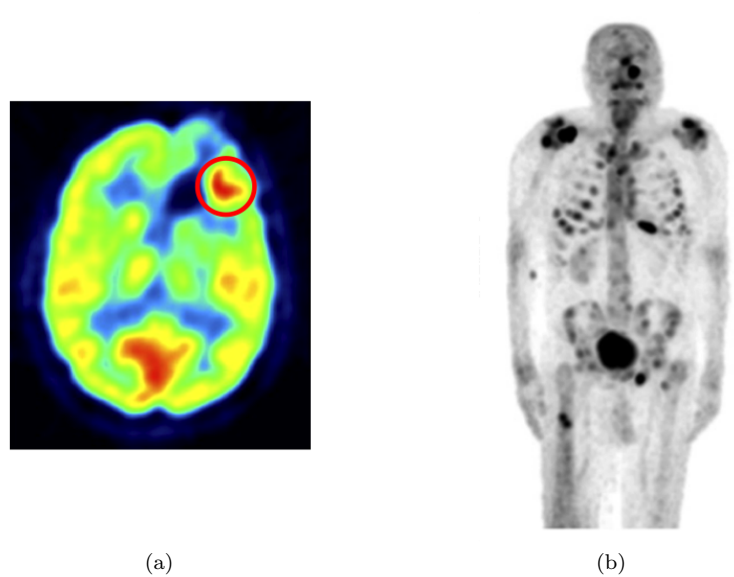
Figure 1.20: (a) ^{18}F-FDG PET image showing a transaxial slice of the brain, the red circled region shows the location of a tumour [124]; (b) ^{99m}Tc-labelled MDP multiple-field-of-view SPECT image showing multiple bone metastases [125].
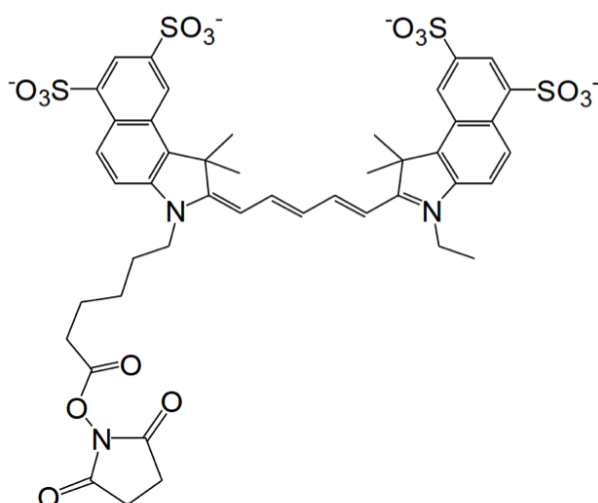
Figure 1.21: General structure of a Cy5.5 *N*-Hydroxysuccinimide (NHS) ester [126].

1.3.5 Why focus on nanoparticles

This work will focus on using NPs as a platform for the development of bimodal imaging probes, and the following section will detail the reasons behind this. First, it should be noted that nanomaterials have recently been defined as 'a natural, incidental or manufactured material containing particles, in an unbound state or as an aggregate or as an agglomerate and where, for 50 % or more of the particles in the number size distribution, one or more external dimensions is in the size range 1 nm to 100 nm' by the European Commission [128]. Interest in the field of nanomedicine has grown exponentially in the past few years, increasing from ten articles per year in the latter half of the 1980's to over 1,200 in 2004, figure 1.22. As can be seen from figure 1.23, the majority of these publications focus on drug delivery aspects (76 %) with only 4 % concentrating on imaging applications. This figure is further implemented when examining the commercial efforts represented in table 1.1 [129].
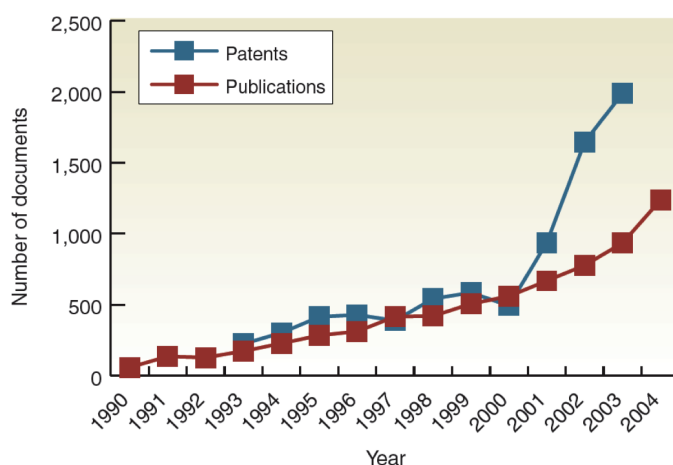
Figure 1.22: Nanomedicine publications and patents worldwide. Sources: Science Citation Index, VDI Technologiezentrum GmbH, Düsseldorf, Germany and EPODOC patent database, European Patent Office, Rijswijk, The Netherlands [129].
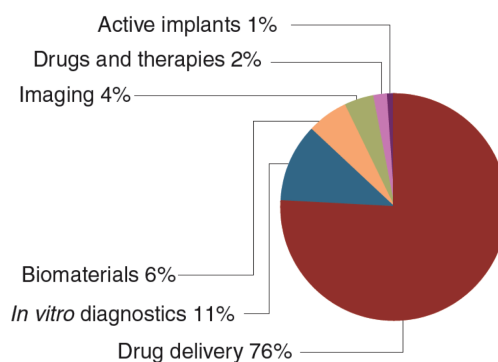
Figure 1.23: Sectorial breakdown of nano medicine publications. Source: Science Citation Index, 1984-2004, VDI Technologiezentrum GmbH, Düsseldorf, Germany [129].

Healthcare sector	Product pipeline				
	Number of products	Sales ($ billions)	Total	Advanced stages[b]	Companies
Drug delivery	23	5.4	98	9	113
Biomaterials	9	0.07	9	6	32
In vivo imaging	3	0.02	8	2	13
In vitro diagnostics	2	0.78	30	4	35
Active implants	1	0.65	5	1	7
Drugs & therapy	0	0	7	1	7
Total	38	6.8	157	23	207

Table 1.1: Commercial efforts in nanomedicine[a]. Source: VDI Technologiezentrum GmbH, Düsseldorf, Germany. [a]Sales numbers of nanomedicines are estimates for the year 2004. [b]Drugs where the product is in clinical phase 2/3 or 3 and for all other products where market introduction is expected within two years [129].

The use of NPs as a basis for contrast agent design is preferable to other types of imaging agents, such as small molecules or engineered protein/peptides, due to the ability to adjust their properties by controlling characteristics such as size, structure and surface properties which can influence their in *in vivo* function and biodistribution [130]. Moreover, the large surface area to volume ratio (modified by altering the size of the particles) is advantageous as it allows for optimisation of the functionalisation of the NPs, which is particularly important in imaging applications involving drug delivery. Additionally, the complexities arising due to conformation/unfolding of molecules or proteins are eliminated due to the solid surface of the NPs, improving the degree of control over the design of the imaging probe [131]. Incorporation of various materials can produce NPs with several different features, for example magnetic and luminescence properties [132–138]. Functionalisation of the NP surface allows for the inclusion of addition modalities or of targeting to a specific region providing maximum enhancement of a particular area, whilst not significantly altering the properties of the NP [139,140]. For instance, Kyle *et al.* describe the potential use of ligand-directed perfluorocarbon (PFC) NPs in monitoring the therapeutic response of patients with cardiovascular diseases such as stroke [141], whereas Kiessling *et al.* detailed the benefits offered by NPs over molecular agents in the labelling of implants and grafts to review function over time and depict potential failure [142]. Another example examines the use of Au NPs as photodynamic therapy (PDT) drug delivery vectors for aqueous insoluble molecules providing promise for future applications utilising drugs currently unavailable due to hydrophobicity issues [131]. This feature of functionalisation is not easy with currently available contrast agents, for example Gd^{3+} chelates. Other issues facing these molecular complex agents include quick removal by the renal system and short accumulation times.

There are drawbacks to the use of NPs with the main disadvantage being that they are quickly recognised and sequestered by circulating macrophages and Kupffer cells of the RES

present in the liver and spleen. The process by which this occurs is known as opsonisation, whereby xenobiotic materials are tagged with opsonin proteins to initiate association with circulating/stationary macrophages as illustrated in figure 1.24 [143].
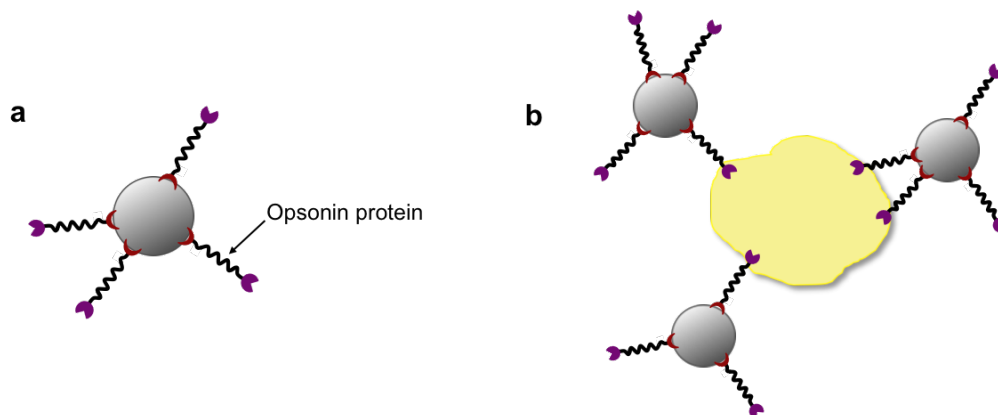
Figure 1.24: Schematic representation of (a) an opsonin tagged iron oxide NP, and (b) association of opsonin tagged iron oxide NPs with a macrophage.

This uptake depends on several factors including size [144], geometry [145–147], overall charge, and functional groups conjugated to the surface [148,149]. Secondly, they are prone to forming aggregates with large diameters that can be irreversibly trapped in the capillaries of the lungs [150]. These two effects represent a potential toxicity threat for the patient and also results in short circulation times and failure to reach the intended target. In addition, the NPs need to be non-toxic or be excreted as fast as possible after the procedure. During the past decade, a number of toxicity reports have highlighted some risks to biological systems exposed to nanomaterials, and more research is needed in order to fully understand the processes taking place [151,152]. However, toxicity is a problem faced by all pharmaceuticals, whether it be a small molecule, a genetically engineered protein or a nanoparticle.

1.3.6 Ultrasmall superparamagnetic iron oxide nanoparticles

The most successful NP platform for *in vivo* imaging to date is based on iron oxide materials, in particular superparamagnetic iron oxide nanoparticles (SPIOs). SPIOs are classified by a hydrodynamic diameter larger than ∼60 nm, with some having overall sizes of up to 150 nm [119]. Most iron oxide nanomaterials are quickly recognised by the macrophages of the RES, making them useful for imaging of the spleen and liver. However, for alternative imaging applications it is desirable to extend their circulation time by minimising this RES uptake. A well-established strategy for doing this is to use ultrasmall SPIOs (USPIOs),

which are SPIOs with a hydrodynamic diameter of less than 40 nm [113].

Structure

The iron oxide focused on here is magnetite, Fe_3O_4, a ferrimagnetic material which has an inverse spinel crystal structure with the unit cell ($a = 0.839$ nm) comprising of 32 oxygen atoms in a face-centred cubic (fcc) arrangement as illustrated in figure 1.25a [153]. The octahedral sites are occupied alternately by Fe^{2+} and Fe^{3+} ions, with only Fe^{3+} ions located in the tetrahedral sites [113, 154]. Due to superexchange oxygen-mediated coupling, the magnetic moments of the iron ions occupying the tetrahedral and octahedral sites are aligned in opposite directions [155] (figure 1.25b), meaning the Fe^{3+} ions compensate for each other and the magnetic properties of magnetite arise due to uncompensated octahedral Fe^{2+} [113].

Magnetic properties

Iron oxide crystals consist of multiple regions, within which the magnetic dipoles interact and align together, known as Weiss domains. Ordered bulk magnetite will exhibit a zero magnetic moment when no external magnetic field is applied due to the negating effect of the magnetically random orientation of the Weiss domains [156]. This is indicated by point **1** of the top hysteresis curve in figure 1.26. Once an external magnetic field $\vec{H}$ is applied, the Weiss domains begin to align with the field increasing the net magnetisation moment until a saturation point, M_S (defined as the maximum magnetisation in a sufficiently large magnetic field [162]), is reached when all dipoles are oriented in the same direction as the applied field (as illustrated by point **2** of the top diagram in figure 1.26) [156]. When the external field is then removed, the Weiss domains will attempt to return to their original randomly orientated states. However, a frictional force arising between the domains will be encountered preventing this, and as a result, the material will retain a remanent field, M_r, corresponding to point **3** on the top hysteresis curve in figure 1.26. Point **4** gives the opposing coercive field, H_C, required to return the material to its initial zero-sum magnetic moment state [156].
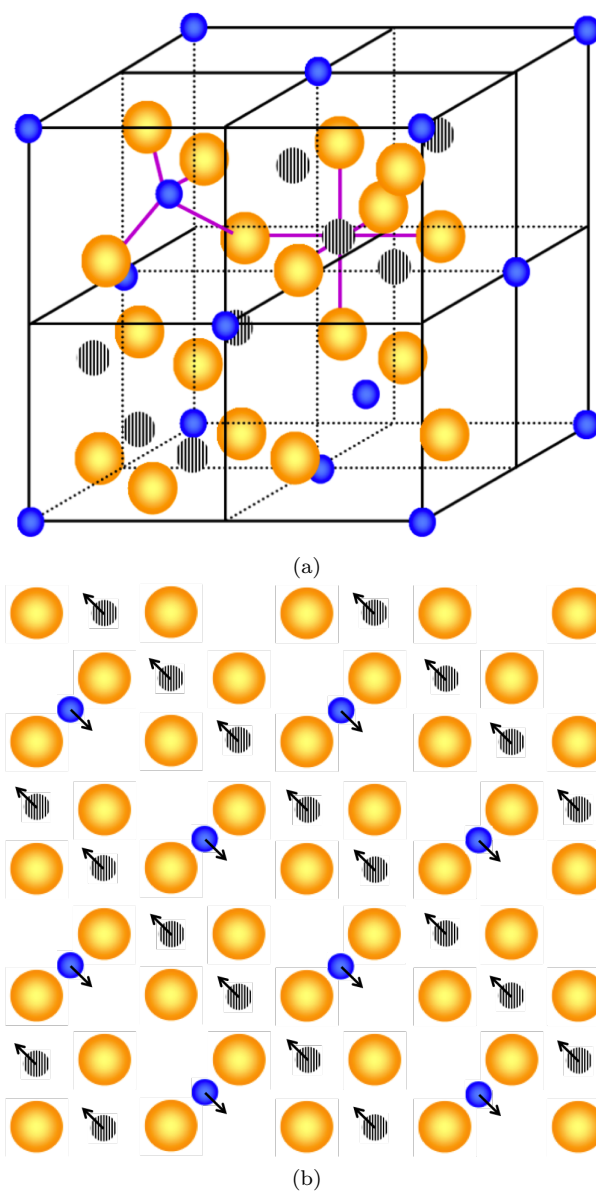
Figure 1.25: Schematic diagram for (a) a unit cell of magnetite (Fe_3O_4) [153], and (b) ferrimagnetic organisation in magnetite (illustration of [1,1,1] plane) [113]. Blue circles = Fe^{3+} (tetrahedral coordination), black/white striped circles = Fe^{2+}/Fe^{3+} (octahedral coordination), and yellow circles = oxygen.
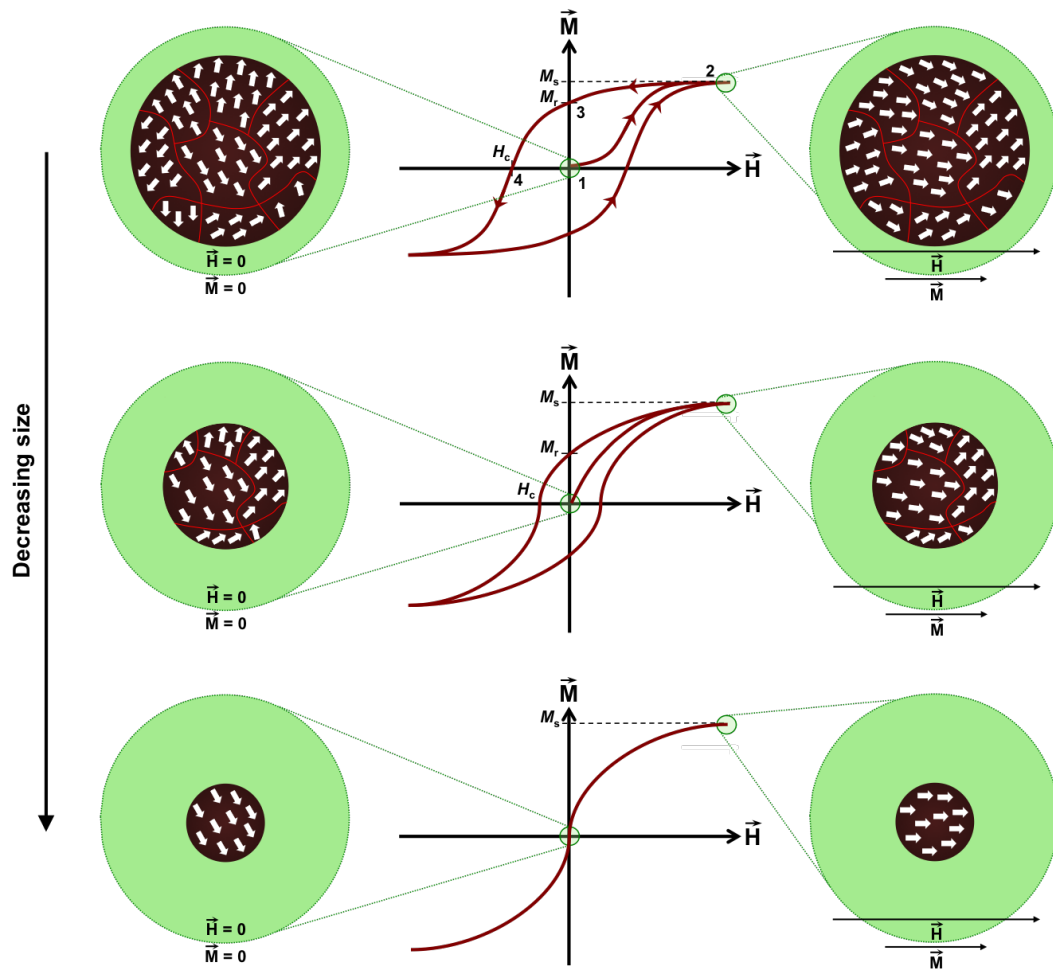
Figure 1.26: Schematic representation of size dependency of magnetic properties of iron oxide crystals on size. A larger crystal (top diagram) will contain multiple Weiss domains, the number of which decreases with crystal size, in turn increasing the M_S [156].

As the size of an iron oxide nanocrystal decreases, so does the number of Weiss domain boundaries (shown by the second diagram in figure 1.26). This decreases the measure of resistance to the recovery of the original random orientation, therefore decreasing M_r and H_C. When the size of the nanocrystal is below the size of a single Weiss domain ($\sim$10-50 nm), all magnetic dipoles within the crystal will be parallel, and hence there will be no remanent magnetic field or coercive field (third hysteresis curve in figure 1.26) [156]. It should be noted that although at $\vec{H} = 0$ all magnetic dipoles are aligned in parallel resulting in a non-zero magnetic moment, the energy required to alter the dipole orientation is lower than the thermal energy absorbed from the environment. As a consequence, the orientation oscillates rapidly (known as Néel relaxation [157]), leading to an average zero-sum magnetic state. When an external field is applied, this oscillation remains present but points preferentially in the direction of the applied field. This is termed superparamagnetism, and results in materials with large saturation magnetisations [156].

There are several parameters affecting superparamagnetism, these including particle size. As the size of the particle decreases, the surface to volume ratio increases, and hence the number of the total atoms in the NP becoming surface atoms increases, which in turn means the influence of surface and interface effects becomes greater [158]. For example, in the case of ionic compounds, the orientation of the magnetic moment per surface atom can become altered which may result in a reduced average net moment in comparison to the bulk material [159–161]. In addition, shape anisotropy, composition and assembly can be used to tailor the magnetic properties of UPSIOs [130]. Furthermore, surface modification has an effect on the saturation magnetisation. It has been reported that steric stabilisation reduces the M_S of SPIOs which is most probably due to the interaction between anchors and surface bound iron ions [163, 164]. Amstad *et al.* have recently shown through EPR studies that these strong coordinations lead to magnetically decoupled Fe^{3+} ions at the nanoparticle surface [163].

Preparation

There are several methods of USPIO fabrication. The first main synthesis procedure is via coprecipitation whereby magnetite is either precipitated from a basic aqueous solution of ferric and ferrous salts [165], or ferrous hydroxide suspensions are partially oxidised using oxidising agents [166]. An early example implementing this method was performed by Sugimoto *et al.* using iron(II) sulfate ($FeSO_4$) and potassium hydroxide (KOH) in the presence

of nitrate ions (this being the oxidant) [167]. Despite the ease of this type of synthesis and the ability to produce large quantities of NPs, the resulting particles lack consistency in size and morphology, and there has been limited success in controlling parameters such as pH and reactant concentrations to tailor these properties [168].

A second synthetic route is thermal decomposition of iron containing compounds such as iron carboxylate salts and iron(III) chloride hexahydrate ($FeCl_3 \cdot 6\,H_2O$) at high temperatures in the presence of surfactants, which has been shown to produce monodispersed particles with high crystallinity [169–171]. Although this method is favourable due to control of size and NP morphology, as well as the yield being high and scalable, there is major drawback in that the subsequent particles are only dispersible in organic solvents, and additional surface modification is required to allow for solubility in an aqueous phase [169, 172].

A third technique is the use of a microemulsion, an isotropic and thermodynamically stable dispersion of two immiscible liquids [173], whereby it is possible to control the average size and composition of the resulting particles to a certain degree due to the ability to measure the exact amount of the metal containing compound in each droplet, as demonstrated by Okoli *et al.* [174, 175].

Finally, the sol-gel method, roughly defined as the formation of an inorganic solid from a precursor solution by chemical means including hydroylsis and polycondensation [176, 177], can be used to synthesis spherical magnetite particles with a narrow size distribution [178]. This process generates homogeneous NPs with a high purity, however cannot be applied to large-scale and economic production, because they require expensive and often toxic reagents and complicated synthetic steps [179].

Advantages over Gd as an MR imaging probe

Although a major problem with many particles is toxicity, Fe_3O_4 NPs have the added benefit of dissolving to form Fe^{3+} ions, which join the body's natural iron storage (for an adult human this is in the range of 3-5 g of iron) [75, 180]. This increase in iron is negligible meaning the NPs are biocompatible [119, 181–183] as has been shown by cytotoxicity studies resulting in cell viability remaining above 91 % after incubation with USPIOs [184–186]. Iron oxide NPs received Food and Drug Administration (FDA) approval and have been used clinically for many years, for example in the treatment of anaemia, hence it is well known that

there are no associated harmful effects. When considering the hurdles of getting a material approved for biomedical use, this is a major advantage. NPs containing Gd complexes have been studied but the synthesis involved is elaborate and the outcome tends to be an agent with a less dramatic enhancement effect. In addition, dissociation of Gd(III) can cause toxic effects due to irreversible association with Ca(II) binding sites, more often with a higher affinity owing to its greater charge/radius ratio, and as a result Ca(II) mediated signalling becomes disrupted [16, 112, 187]. As an example, Gd_2O_3 NPs have been synthesised with relaxivities necessary for T_1-weighted images but on account of toxicity, the concentrations needed are too high for use *in vivo* [130, 188, 189], particularly in patients with pre-existing kidney conditions because of the significant increase in the risk of acute kidney injury (AKI) and nephrogenic systemic fibrosis (NSF) [190, 191]. Furthermore, given the low number of MRI contrast agents approved to date, particles containing potentially toxic metals such as Gd, Co or Mn with favourable magnetic properties [192] may find difficulty in obtaining clinical approval [193].

Each USPIO contains a high number of magnetic ions, this improves MR contrast due to each vectorised particle exhibiting a large magnetic moment when compared to a single gadolinium ion, and in turn decreases the bodies burden of agent required for a given effect [113, 194]. In addition, the efficiency of gadolinium is limited at high magnetic fields due to its magnetic moment not reaching saturation [113]. SPIOs, however, remain relatively unaffected by increasing magnetic fields. Furthermore, paramagnetic ion relaxation effects are highly reliant on the proximity of protons with sufficient exchange rates, whereas USPIOs disturb the magnetic field independent of environment and hence can be used anywhere within a supporting matrix [195].

Low toxicity, larger relaxation effects for a single particle in comparison to a single paramagnetic ion and economical advantages (due to the inexpensive of iron metals [196]) means incorporation of iron into MR contrast agents is favourable over the gadolinium counterpart.

Benefits in using ultrasmall superparamagnetic iron oxide nanoparticles in medical applications

There are several applications which benefit from contrast enhanced by USPIOs compared to gadolinium agents due to uptake by macrophages (other than those present in the RES)

combined with higher relaxivities and an intravascular distribution [197]. It has been reported that iron oxide particles hold advantages in vascular imaging, in particular in the imaging of the portal venous system [198] and deep venous thrombosis (DVT) [199, 200] owing to the non-specificity of the vascular enhancement resulting in both the arteries and veins displaying an increase in signal [197]. A second cardiovascular application is in the evaluation of inflammatory processes. Areas of inflammation are known to be associated with escalated macrophage activity, and as it is well known that iron oxide particles are readily taken up by macrophages of the RES, uptake by macrophages of other parts of the body is also conceivable [197]. Couple this to the intravascular nature of USPIOs, monitoring of cardiac transplant rejection is possible [201].

1.3.7 Quantum dots

Another category of nanoparticle also utilised in imaging applications, specifically optical imaging, are semiconductor nanocrystals, known as quantum dots. These particles are made from a variety of materials, such as cadmium selenide and cadmium telluride, and are used to absorb and emit at particular wavelengths of light which depends on size, shape and composition [202, 203]. In recent years, these particles have been preferred as biomarkers for research purposes over conventional organic dyes and proteins for several reasons, for instance the broad range of tuneable fluorescing properties of QDs covers both the visible and near-infrared parts of the spectrum [100, 204, 205]. In addition they exhibit unique features including large absorption coefficients, and multicolour capability under single source excitation which is possible due to their broad absorption profiles and narrow emission spectra [100, 206–208]. Furthermore, they display enhanced chemical and metabolic stability, and increased solubility, as well as a higher photobleaching threshold which has been demonstrated by Maysinger *et al.* using *in vivo* imaging techniques over several days [209–211].

Applications

One of the most successful applications of QDs in biology is in immunofluorescence labelling of cells and tissues, fundamental work of which was performed by Alivisatos *et al.* [212] and Chan and Nie [213], and this success is primarily due to the small number of particles needed to produce a signal [214, 215]. An example of this is in the diagnosis and staging of

cancerous tumours, where multiplexed molecular profiling is required due to the need for a panel of biomarkers to accurately classify the progression of the disease [216]. Secondly, it has been shown that QDs can be used to label and track membrane proteins on living cells, allowing for further understanding of cellular dynamics [204].

1.4 Nanoparticle coatings

1.4.1 General introduction to importance of correct coating

Nanoparticles are coated in order to improve several properties, including biocompatibility, and to modulate interactions both between the particles and with other biological molecules [188, 217]. Dispersant molecules are divided into two components: the anchor and the spacer. Ideally, anchors need to have a high binding affinity and low desorption rate in order to irreversibly conjugate the spacer to the NP surface. In addition, it is necessary for the chosen coating molecule to have the ability to replace the hydrophobic surfactants normally used during synthesis [217]. Furthermore, it is essential that spacers provide sufficient steric stabilisation to prevent aggregation of particles in an aqueous phase by overcoming attractive van der Waals and magnetic potentials (as shown in figure 1.27a), as well as allowing for further functionalisation [100, 217]. It is also preferable that the chosen surface ligand provides *in vivo* stability and an extended blood circulation time by reducing the opsonisation process (the mechanism by which is illustrated in figure 1.27b) to allow for use in biomedical applications [218]. The most successful strategy to minimise aggregation and RES uptake, is to coat the NP surface with hydrophilic polymers, and below details some of the most commonly used coatings.

1.4.2 Anchors

Carboxylic acids

Carboxylic acids have been used as surfactants for decades, with oleic acid coated magnetite NPs being reported as far back as 1973 [219]. Binding to the NP surface occurs via the hydroxyl group, however it has been shown that in some cases involving oleic acid coordination

Increased polymer concentration

(a)   (b)
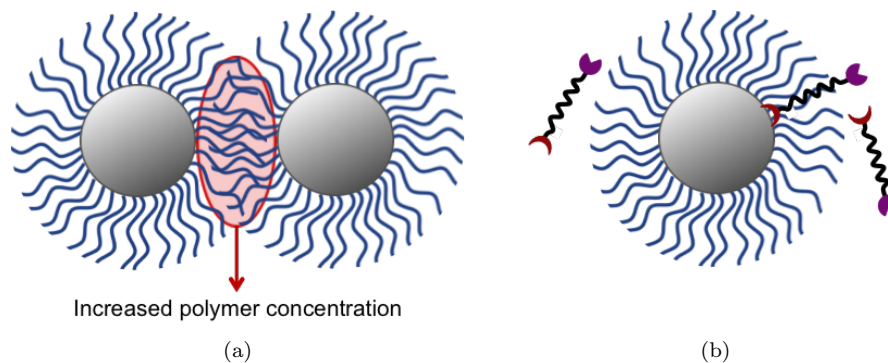
Figure 1.27: Schematic representation illustrating the mechanism behind hydrophilic polymers reducing (a) aggregation of particles, and (b) the opsonisation process.

can take place through the double bond in the alkyl chain [220]. These molecules have been shown to be effective stabilisers for both magnetic and luminescent materials, and for oleic acid, its solubility in both polar and non-polar solvents makes it highly versatile [221]. However, due to their poor stability, coatings utilising this anchor are only useful as temporary coatings rather than for long-term applications.

Catechols

Catechols (figure 1.28) have recently been investigated as anchor groups in the stabilisation of Fe_3O_4 NPs. These molecules are well known to bind very strongly to iron oxides and other materials. In fact, catechols are the active groups in the glue proteins that mussels use to stick to surfaces. Catechol bonding to the metallic surface occurs through two adjacent hydroxyl groups, and their vicinal positions in the aromatic ring which results in a high dispersant packing density, as well as improved stability in physiological conditions [222, 223]. While the strong bonding to metallic surface is a major advantage, catechols may react through a redox mechanism with the surface of iron oxide nanoparticles in protic environments, leading to decomposition and precipitation of the nanoparticles [224].
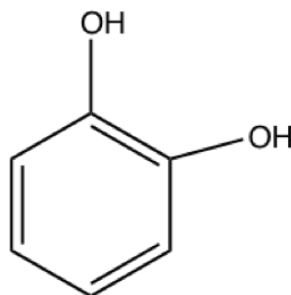
Figure 1.28: General structure of a catechol.

Bisphosphonates

A recent and yet unexplored approach to coat iron oxide NPs is the use of bisphosphonates (BPs). BPs (figure 1.29 with R_1 and R_2 being an alkyl or functional group) are well known molecules in the osteoporosis and oncology fields due to the fact that they bind avidly to the calcium in hydroxyapatite (the main mineral component of bone) at the surface of metabolically-active bone [225, 226]. Recently, BPs have begun to be incorporated into coatings for use on iron oxide nanomaterials due to their particularly strong binding to metallic surfaces, which can stabilise particles in solution for at least one month [227–234]. In this study, a BP was chosen as the anchor due to this strong binding to the iron oxide surface and stability both *in vitro* and *in vivo* [81]. In addition, our group has recently shown that bifunctional BPs can be radiolabled with no detrimental effect to the *in vivo* binding to bone [235]. This will allow for the radionuclide modality to be easily incorporated into the coating of the USPIOs without effecting the ability of the BP to bind to the NP surface, a concept that has been demonstrated in our group using ^{64}Cu and a dextran coated iron oxide particle [79].
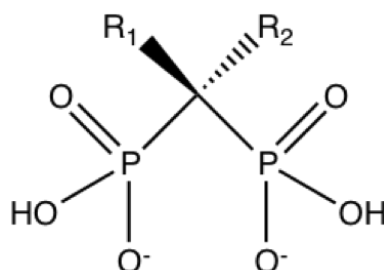
Figure 1.29: General structure of a bisphosphonate.

1.4.3 Coatings

Dextran

Dextran, figure 1.30, is a polymer of anhydroglucose. It interacts with the metal surface via the hydroxyl groups and although a single bond is weak, the large number of hydroxyl groups per molecule available for bonding to the iron oxide increases the overall stability of the coating [236]. However, the high numbers of anchoring groups of dextran results in aggregation of several nanocrystals, increasing the hydrodynamic diameter of the particles/aggregates to up to 150 nm [236, 237]. The advantages of using dextran is its high biocompatibility and

relatively ease of functionalisation via standard bioconjugation techniques. Its weakness, however, is that the non covalent NP-dextran binding is weak and may result in lack of stability *in vivo* [238]. This dissociation may be overcome by crosslinking the dextran shell for example with epichlorohydrin, yet this may then result in particles that are less suitable for biological applications due to the toxicity of the crosslinking agent [239, 240].
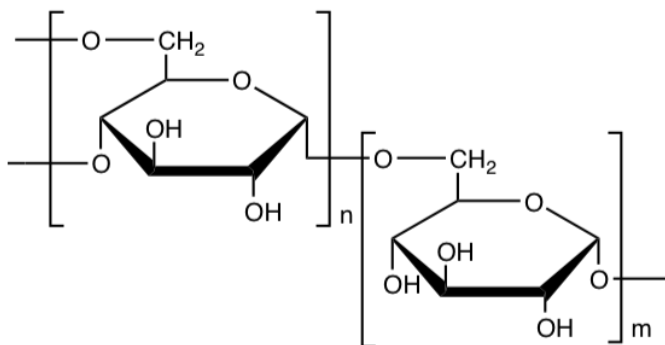
Figure 1.30: General structure of dextran.

Polyethylene glycol

Polyethylene glycol (PEG) is a coating molecule that has been used to successfully provide a non-ionic hydrophilic layer around various inorganic nanoparticle materials such as metal oxides and silica [241–245]. A wide range of molecular weights of PEG can be synthesised (400 Da up to 50 kDa) with a small distribution of molecular sizes [246–248]. The main reason behind the preference of a PEG as a coating for a NP designed for biomedical applications is due to its stealth behaviour, which has been shown to reduce RES uptake and prolong blood circulation times by up to 10 times [249, 250]. Furthermore, a PEG coating adjusts the overall charge of the particle in such a way as to lessen protein adsorption on to the NP surface [150]. The solubility of PEG in organic solvents allows for facile modification of end groups, whilst its high solubility in water, low toxicity, and immunogenicity combined with desirable excretion kinetics make it ideally suited for biological applications [251–256]. Moreover, this polymer has received FDA approval, and has been used in several pharmaceutical applications, such as organ storage and in the conjugation to proteins in order to improve pharmacokinetics [257–259]. Not only this, but PEG is a frequent component in a variety of cosmetics from toothpaste and shampoos to fragrances and make-up [260, 261]. Finally, in addition to the biocompatibility of PEG, it also has the benefit of being low-cost [262].
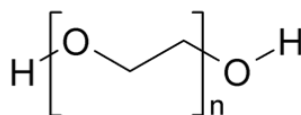
Figure 1.31: General structure of polyethylene glycol.

Hydrophobins

Hydrophobins are amphiphilic proteins that have received recent interest for coating inorganic nanomaterials due to their ability to self-assemble into monolayers on hydrophobic materials [263, 264]. They have a molecular mass below 20 kDa with a diameter of *ca.* 1.2 nm and consist of approximately 100 amino acids characteristic of filamentous fungi [265–267]. These proteins comprise of eight cysteine residues, forming four intramolecular disulphide bonds, specifically ordered creating a hydrophilic region which contributes to the hydrophobin's distinguishing features and structural robustness, whilst the hydrophobic area arises due to aliphatic side-chains in the loop region of the protein, yielding an amphiphilic structure [263, 268–270]. There are two principle classifications of hydrophobins categorised by their hydropathy and the distance between cysteine residues [271]. Class I hydrophobins (figure 1.32a [272]) have a high stability in harsh solvents and conditions, for example the protein remains intact after boiling in a 2 % sodium dodecyl sulfate (SDS) for a short period of time. Formic acid and trifluoroacetic acid being the only chemicals capable of dissociation. Class II hydrophobins (figure 1.32b [273]) however, have a far lower stability and can readily be dissolved by SDS [270]. Due to their potential biocompatibility combined with resistance against pH and ionic salts arising in biological environments, hydrophobins have recently become of interest as coatings for nanoparticles [274]. Several groups have reported successfully phase transfers into aqueous solution with various nanomaterials, notably hybrid nanostructures formed from single-walled carbon nanotubes bound to gold nanoparticles [275], graphene sheets [276], and silicon particles [277, 278]. Furthermore, the exposed amino acid residues on the protein allow for additional functionalisation for use *in vivo* applications, for example targeted imaging. Whilst hydrophobins have traditionally been difficult to obtain, new advances in recombinant processing have made hydrophobins a realistic option for use in phase transfer.

(a)   (b)
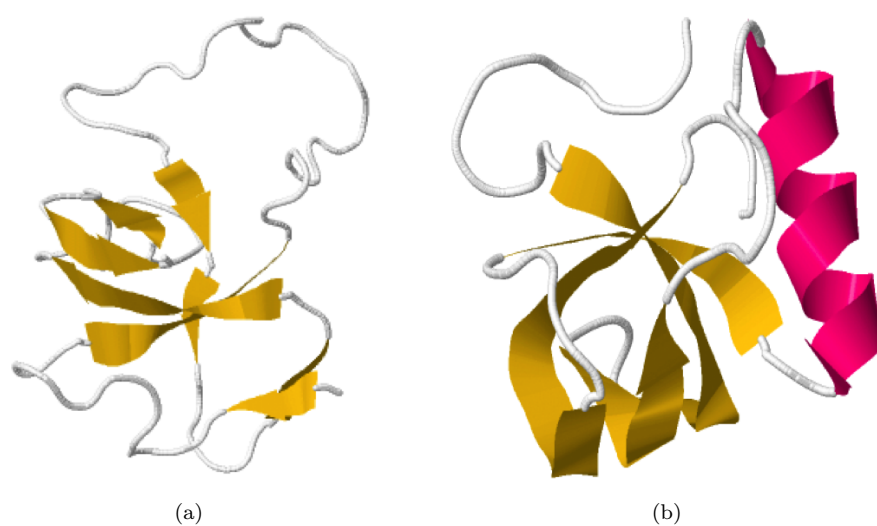
Figure 1.32: General structure of a (a) class-I hydrophobin [272], and (b) class-II hydrophobin [273].

Bibliography

[1] A. Signore, S. J. Mather, G. Piaggio, G. Malviya, and R. A. Dierckx. Molecular Imaging of Inflammation/Infection: Nuclear Medicine and Optical Imaging Agents and Methods. *Chem. Rev.,* 110: 3112–3145, **2010**.

[2] T. J. Wadas, E. H. Wong, G. R. Weisman, and C. J. Anderson. Coordinating Radiometals of Copper, Gallium, Indium, Yttrium, and Zirconium for PET and SPECT Imaging of Disease. *Chem. Rev.,* 110: 2858–2902, **2010**.

[3] S. Achilefu. Introduction to Concepts and Strategies for Molecular Imaging. *Chem. Rev.,* 110: 2575–2578, **2010**.

[4] P. Zanzonico. Principles of Nuclear Medicine Imaging: Planar, SPECT, PET, Multi-Modality, and Autoradiography Systems. *Radiat. Res.,* 177: 349–364, **2012**.

[5] M. F. Kircher and J. K. Willmann. Molecular Body Imaging: MR Imaging, CT, and US. Part I. Principles. *Radiology,* 263: 633–643, **2012**.

[6] M. F. Kircher and J. K. Willmann. Molecular Body Imaging: MR Imaging, CT, and US. Part II. Applications. *Radiology,* 264: 349–368, **2012**.

[7] A. F. Fercher, W. Drexler, C. K. Hitzenberger, and T. Lasser. Optical Coherence Tomography - Principles and Applications. *Rep. Prog. Phys.,* 66: 239–303, **2003**.

[8] L. W. Goldman. Principles of CT and CT Technology. *J. Nucl. Med. Technol.,* 35: 115–128, **2007**.

[9] J. Hsieh. *Computed Tomography: Principles, Design, Artifacts, and Recent Advances.* SPIE Press, **2003**.

[10] R. Y. Kwong and E. K. Yucel. Computed Tomography Scan and Magnetic Resonance Imaging. *Circulation,* 108: e104–e106, **2003**.

[11] F. Earnest 4th, H. L. Jr. Baker, D. B. Kispert, and E. R. Jr. Laws. Magnetic Resonance Imaging vs. Computed Tomography: Advantages and Disadvantages. *Clin. Neur.,* 32: 540–573, **1985**.

[12] N. Hassani, R. Khomeini, and R. Bard. Principles of Computerized Tomography. *J. Natl. Med. Assoc.,* 68: 110–112, **1976**.

[13] R. A. Robb. X-Ray Computed Tomography: From Basic Principles to Applications. *Annu. Rev. Biophys. Bio.,* 11: 177–201, **1982**.

[14] A. F. Kopp, K. Klingenbeck-Regn, M. Heuschmid, A. Küttner, B. Ohnesorge, T. Flohr,

S. Schaller, and C. D. Claussen. Multislice Computed Tomography: Basic Principles and Clinical Applications. *Electromedica*, 68: 94–105, **2000**.

[15] H. H. Schild. *MRI Made Easy.* Schering AG, **1990**.

[16] M. Bottrill, L. Kwok, and N. J. Long. Lanthanides in Magnetic Resonance Imaging. *Chem. Soc. Rev.*, 35: 557–571, **2006**.

[17] I. L. Pykett, J. H. Newhouse, F. S. Buonanno, T. J. Brady, M. R. Goldman, J. P. Kistler, and G. M. Pohost. Principles of Nuclear Magnetic Resonance Imaging. *Radiology*, 143: 157–168, **1982**.

[18] Scientia.   http://www.scientia.ro/tehnologie/39-cum-functioneaza-lucrurile/1392-rezonanta-magnetica-nucleara-pe-intelesul-tuturor.html, March 2015.

[19] Y. Gossuin, A. Hocq, P. Gillis, and Q. L. Vuong. Physics of Magnetic Resonance Imaging: From Spin to Pixel. *J. Phys. D Appl. Phys.*, 43: 213001, **2010**.

[20] R. T. M. de Rosales, R. Tavaré, A. Glaria, G. Varma, A. Protti, and P. J. Blower. ^{99m}Tc-Bisphosphonate-Iron Oxide Nanoparticle Conjugates for Dual-Modality Biomedical Imaging. *Bioconjugate Chem.*, 22: 455–465, **2011**.

[21] P. Caravan. Strategies for Increasing the Sensitivity of Gadolinium Based MRI Contrast Agents. *Chem. Soc. Rev.*, 35: 512–523, **2006**.

[22] L. Frullano and T. J. Meade. Multimodal MRI Contrast Agents. *J. Biol. Inorg. Chem.*, 12: 939–949, **2007**.

[23] K. M. Hasebroock and N. J. Serkova. Toxicity of MRI and CT Contrast Agents. *Expert Opin. Drug. Metab. Toxicol.*, 5: 403–416, **2009**.

[24] M. E. Raichle. Positron Emission Tomography. *Annu. Rev. Neurosci.*, 6: 249–267, **1983**.

[25] M. E. Phelps. *PET: Physics, Intrumentation, and Scanners.* Springer-Verlag New York, 1 edition, **2006**.

[26] S. A. Eshuis. *Radiotracer Imaging in PD.* PhD thesis, Rijksuniversiteit Groningen, Groningen, The Netherlands, **2009**.

[27] G. F. Knoll. Single-Photon Emission Computed Tomography. *Pr. Inst. Electr. Elect.*, 71: 320–329, **1983**.

[28] S. R. Meikle, P. Kench, M. Kassiou, and R. B. Banati. Small Animal SPECT and its Place in the Matrix of Molecular Imaging Technologies. *Phys. Med. Biol.*, 50: R45–R61, **2005**.

[29] R. T. M. de Rosales, E. Ärstad, and P. J. Blower. Nuclear Imaging of Molecular Processes in Cancer. *Targ. Oncol.*, 4:183–197, **2009**.

[30] A. Rahmim and H. Zaidi. PET versus SPECT: Strengths, Limitations and Challenges. *Nucl. Med. Commun.*, 29:193–207, **2008**.

[31] M. E. Phelps. PET: The Merging of Biology and Imaging into Molecular Imaging. *J. Nucl. Med.*, 41:661–681, **2000**.

[32] M. E. Phelps. Positron Emission Tomography Provides Molecular Imaging of Biological Processes. *P. Natl. Acad. Sci. USA*, 97:9226–9233, **2000**.

[33] P. E. Valk, T. R. Pounds, R. D. Tesar, D. M. Hopkins, and M. K. Haseman. Cost-Effectiveness of PET Imaging in Clinical Oncology. *Nucl. Med. Biol.*, 23:737–743, **1996**.

[34] J. V. Vitola, D. Delbeke, M. P. Sandler, M. G. Campbell, T. A. Powers, J. K. Wright, W. C. Chapman, and C. W. Pinson. Positron Emission Tomography to Stage Suspected Metastatic Colorectal Carcinoma to the Liver. *Am. J. Surg.*, 171:21–26, **1996**.

[35] G. Beets, F. Penninckx, C. Schiepers, L. Filez, L. Mortelmans, R. Kerremans, R. Aerts, and M. De Roo. Clinical Value of Whole-Body Positron Emission Tomography with [18F]Fluorodeoxyglucose in Recurrent Colorectal Cancer. *Brit. J. Surg.*, 81:1666–1670, **1994**.

[36] D. T. Lai, M. Fulham, M. S. Stephen, K. M. Chu, M. Solomon, J. F. Thompson, D. M. Sheldon, and D. W. Storey. The Role of Whole-Body Positron Emission Tomography with [^{18}F]Fluorodeoxyglucose in Identifying Operable Colorectal Cancer Metastases to the Liver. *Arch. Surg.*, 131:703–707, **1996**.

[37] P. E. Valk, E. Abella-Columna, M. K. Haseman, T. R. Pounds, R. D. Tesar, R. W. Myers, H. B. Greiss, and G. A. Hofer. Whole-Body PET Imaging with [^{18}F]Fluorodeoxyglucose in Management of Recurrent Colorectal Cancer. *Arch. Surg.*, 134:503–511, **1999**.

[38] O. A. Ogunbiyi, F. L. Flanagan, F. Dehdashti, B. A. Siegel, D. D. Trask, E. H. Birnbaum, J. W. Fleshman, T. E. Read, G. W. Philpott, and I. J. Kodner. Detection of Recurrent and Metastatic Colorectal Cancer: Comparison of Positron Emission Tomography and Computed Tomography. *Ann. Surg. Oncol.*, 4:613–620, **1997**.

[39] D. L. Damian, M. J. Fulham, E. Thompson, and J. F. Thompson. Positron Emission Tomography in the Detection and Management of Metastatic Melanoma. *Melanoma Res.*, 6:325–329, **1996**.

[40] D. Rinne, R. P. Baum, G. Hör, and R. Kaufmann. Primary Staging and Follow-Up

of High Risk Melanoma Patients with Whole-Body ^{18}F-Fluorodeoxyglucose Positron Emission Tomography: Results of a Prospective Study of 100 Patients. *Cancer*, 82: 1664–1671, **1998**.

[41] K. D. M. Stumpe, M. Urbinelli, H. C. Steinert, C. Glanzmann, A. Buck, and G. K. von Schulthess. Whole-Body Positron Emission Tomography Using Fluorodeoxyglucose for Staging of Lymphoma: Effectiveness and Comparison with Computed Tomography. *Eur. J. Nucl. Med.*, 25: 721–728, **1998**.

[42] F. Moog, M. Bangerter, C. G. Diederichs, A. Guhlmann, E. Merkle, N. Frickhofen, and S. N. Reske. Extranodal Malignant Lymphoma: Detection with FDG PET versus CT. *Radiology*, 206: 475–481, **1998**.

[43] E. M. Marom, H. P. McAdams, J. J. Erasmus, P. C. Goodman, D. K. Culhane, R. E. Coleman, J. E. Herndon, and E. F. Jr. Patz. Staging Non-Small Cell Lung Cancer by Whole-Body PET. *Radiology*, 212: 803–809, **1999**.

[44] P. E. Valk, T. R. Pounds, D. M. Hopkins, M. K. Haseman, G. A. Hofer, H. B. Greiss, R. W. Myers, and C. L. Lutrin. Staging Non-Small Cell Lung Cancer by Whole-Body Positron Emission Tomographic Imaging. *Ann. Thorac. Surg.*, 60: 1573–1581, **1995**.

[45] S-P. Changlai, S-C. Tsai, M-C. Chou, Y-J. Ho, and C-H. Kao. Whole Body 18F-2-deoxyglucose Positron Emission Tomography to Restage Non-Small Cell Lung Cancer. *Oncol. Rep.*, 8:337–339, **2001**.

[46] J. S. Fowler and A. P. Wolf. Working against Time: Rapid Radiotracer Synthesis and Imaging the Human Brain. *Acc. Chem. Res.*, 30: 181–188, **1997**.

[47] C. Balas. Review of Biomedical Optical Imaging - A Powerful, Non-Invasive, Non-Ionizing Technology for Improving *In Vivo* Diagnosis. *Meas. Sci. Technol.*, 20: 104020, **2009**.

[48] G. D. Luker and K. E. Luker. Optical Imaging: Current Applications and Future Directions. *J. Nucl. Med.*, 49: 1–4, **2008**.

[49] C. W. G. M. Lowik, M. G. Cecchini, A. Maggi, and G. van der Pluijm. Noninvasive Real-Time *In Vivo* Bioluminescent Imaging of Gene Expression and of Tumor Progression and Metastasis. *Ernst Schering Res. Found. Workshop*, pages 193–227, **2005**.

[50] K. O'Neill, S. K. Lyons, W. M. Gallagher, K. M. Curran, and A. T. Byrne. Bioluminescent Imaging: A Critical Tool in Pre-Clinical Oncology Research. *J. Pathol.*, 220: 317–327, **2010**.

[51] T. Nakatsu, S. Ichiyama, J. Hiratake, A. Saldanha, N. Kobashi, K. Sakata, and

H. Kato. Structural Basis for the Spectral Difference in Luciferase Bioluminescence. *Nature*, 440: 372–376, **2006**.

[52] P. Naumov, Y. Ozawa, K. Ohkubo, and S. Fukuzumi. Structure and Spectroscopy of Oxyluciferin, the Light Emitter of the Firefly Bioluminescence. *J. Am. Chem. Soc.*, 131: 11590–11605, **2009**.

[53] M. R. Young. Principles and Technique of Fluorescence Microscopy. *Q. J. Microsc. Sci.*, 102: 419–449, **1961**.

[54] F. Leblond, S. C. Davis, P. A. Valdés, and B. W. Pogue. Pre-Clinical Whole-Body Fluorescence Imaging: Review of Instruments, Methods and Applications. *J. Photoch. Photobiol. B*, 98: 77–94, **2010**.

[55] A. S. K. Dzik-Jurasz. Molecular Imaging *In Vivo*: An Introduction. *Brit. J. Radiol.*, 76: S98–S109, **2003**.

[56] C. H. Contag, P. R. Contag, J. I. Mullins, S. D. Spilman, D. K. Stevenson, and D. A. Benaron. Photonic Detection of Bacterial Pathogens in Living Hosts. *Mol. Microbiol.*, 18(4): 593–603, **1995**.

[57] B. J. Tromberg, N. Shah, R. Lanning, A. Cerussi, J. Espinoza, T. Pham, L. Svaasand, and J. Butler. Non-Invasive In Vivo Characterization of Breast Tumors Using Photon Migration Spectroscopy. *Neoplasia*, 2: 26–40, **2000**.

[58] J. V. Frangioni. *In Vivo* Near-Infrared Fluorescence Imaging. *Curr. Opin. Chem. Biol.*, 7: 626–634, **2003**.

[59] D. J. Hawrysz and E. M. Sevick-Muraca. Developments Toward Diagnostic Breast Cancer Imaging Using Near-Infrared Optical Measurements and Fluorescent Contrast Agents. *Neoplasia*, 2: 388–417, **2000**.

[60] J. L. Kovar, M. A. Simpson, A. Schutz-Geschwender, and D. M. Olive. A Systematic Approach to the Development of Fluorescent Contrast Agents for Optical Imaging of Mouse Cancer Models. *Anal. Biochem.*, 367: 1–12, **2007**.

[61] M. Gurfinkel, S. Ke, X. Wen, C. Li, and E. M. Sevick-Muraca. Near-Infrared Fluorescence Optical Imaging and Tomography. *Dis. Markers*, 19: 107–121, **2003-2004**.

[62] R. Weissleder and V. Ntziachristos. Shedding Light onto Live Molecular Targets. *Nat. Med.*, 9: 123–128, **2003**.

[63] X. Montet, V. Ntziachristos, J. Grimm, and R. Weissleder. Tomographic Fluorescence Mapping of Tumor Targets. *Cancer Res.*, 65: 6330–6336, **2005**.

[64] D. W. Townsend. Dual-Modality Imaging: Combining Anatomy and Function. *J. Nucl. Med.*, 49: 938–955, **2008**.

[65] S. R. Cherry. Multimodality Imaging: Beyond PET/CT and SPECT/CT. *Semin. Nucl. Med.*, 39: 348–353, **2009**.

[66] D. W. Townsend, J. P. J. Carney, J. T. Yap, and N. C. Hall. PET/CT Today and Tomorrow. *J. Nucl. Med.*, 45: 4S–14S, **2004**.

[67] T. Beyer, G. Antoch, S. Müller, T. Egelhof, L. S. Freudenberg, J. Debatin, and A. Bockisch. Acquisition Protocol Considerations for Combined PET/CT Imaging. *J. Nucl. Med.*, 45: 25S–35S, **2004**.

[68] D. Lardinois, W. Weder, T. F. Hany, E. M. Kamel, S. Korom, B. Seifert, G. K. von Schulthess, and H. C. Steinert. Staging of Non-Small-Cell Lung Cancer with Integrated Positron-Emission Tomography and Computed Tomography. *New Engl. J. Med.*, 348: 2500–2507, **2003**.

[69] R. Bar-Shalom, N. Yefremov, L. Guralnik, D. Gaitini, A. Frenkel, A. Kuten, H. Altman, Z. Keidar, and O. Israel. Clinical Performance of PET/CT in Evaluation of Cancer: Additional Value for Diagnostic Imaging and Patient Management. *J. Nucl. Med.*, 44: 1200–1209, **2003**.

[70] J. Czernin and H. Schelbert. PET/CT Imaging: Facts, Opinions, Hopes, and Questions. *J. Nucl. Med.*, 45: 1S–3S, **2004**.

[71] A. H. Maurer. Combined Imaging Modalities: PET/CT and SPECT/CT. *Health Phys.*, 95: 571–576, **2008**.

[72] L. K. Griffeth. Use of PET/CT Scanning in Cancer Patients: Technical and Practical Considerations. *BUMC Proceedings*, 18: 321–330, 10 **2005**.

[73] G. Brix, U. Lechel, G. Glatting, S. I. Ziegler, W. Münzing, S. P. Müller, and T. Beyer. Radiation Exposure of Patients Undergoing Whole-Body Dual-Modality ^{18}F-FDG PET/CT Examinations. *J. Nucl. Med.*, 46: 608–613, **2005**.

[74] L. E. Jennings and N. J. Long. 'Two is Better than One' - Probes for Dual-Modality Molecular Imaging. *Chem. Commun.*, pages 3511–3524, **2009**.

[75] A. Louie. Multimodality Imaging Probes: Design and Challenges. *Chem. Rev.*, 110: 3146–3195, **2010**.

[76] A. Drzezga, M. Souvatzoglou, M. Eiber, A. J. Beer, S. Fürst, A. Martinez-Möller, S. G. Nekolla, S. Ziegler, C. Ganter, E. J. Rummeny, and M. Schwaiger. First Clinical Experience with Integrated Whole-Body PET/MR: Comparison to PET/CT in

Patients with Oncologic Diagnoses. *J. Nucl. Med*, 53: 845–855, **2012**.

[77] D. J. Loeffelbein, M. Souvatzoglou, V. Wankerl, A. Martinez-Moller, J. Dinges, M. Schwaiger, and A. J. Beer. PET-MRI Fusion in Head-and-Neck Oncology: Current Status and Implications for Hybrid PET/MRI. *J. Oral Maxil. Surg.*, 70: 473–483, **2012**.

[78] J. A. Disselhorst, I. Bezrukov, A. Kolb, C. Parl, and B. J. Pichler. Principles of PET/MR Imaging. *J. Nucl. Med.*, 55: 2S–10S, **2014**.

[79] R. T. M. de Rosales. Potential Clinical Applications of Bimodal PET-MRI or SPECT-MRI Agents. *J. Labelled Compd. Rad.*, 57: 298–303, **2014**.

[80] B. Pichler, H. F. Wehrl, A. Kolb, and M. S. Judenhofer. PET/MRI: The Next Generation of Multi-Modality Imaging. *Semin. Nucl. Med.*, 38: 199–208, **2008**.

[81] R. T. M. de Rosales, R. Tavaré, R. L. Paul, M. Jauregui-Osoro, A. Protti, A. Glaria, G. Varma, I. Szanda, and P. J. Blower. Synthesis of ^{64}Cu(II)–Bis(dithiocarbamatebisphosphonate) and Its Conjugation with Superparamagnetic Iron Oxide Nanoparticles: *In Vivo* Evaluation as Dual-Modality PET–MRI Agent. *Angew. Chem. Int. Ed.*, 50: 5509–5513, **2011**.

[82] B. E. Hammer, N. L. Christensen, and B. G. Heil. Use of a Magnetic Field to Increase the Spatial Resolution of Positron Emission Tomography. *Med. Phys.*, 21: 1917–1920, **1994**.

[83] G. Antoch and A. Bockisch. Combined PET/MRI: A New Dimension in Whole-Body Oncology Imaging? *Eur. J. Nucl. Med. Mol. I.*, 36 (Suppl. 1): S113–S20, **2009**.

[84] B. J. Pichler, A. Kolb, T. Nägele, and H-P. Schlemmer. PET/MRI: Paving the Way for the Next Generation of Clinical Multimodality Imaging Applications. *J. Nucl. Med.*, 51: 333–336, **2010**.

[85] W. A. Weber. PET/MR Imaging: A Critical Appraisal. *J. Nucl. Med.*, 55: 56S–58S, **2014**.

[86] M. S. Judenhofer, H. F. Wehrl, D. F. Newport, C. Catana, S. B. Siegel, M. Becker, A. Thielscher, M. Kneilling, M. P. Lichy, M. Eichner, K. Klingel, G. Reischl, S. Widmaier, M. Röcken, R. E. Nutt, H-J. Machulla, K. Uludag, S. R. Cherry, C. D. Claussen, and B. J. Pichler. Simultaneous PET-MRI: A New Approach for Functional and Morphological Imaging. *Nat. Med.*, 14: 459–465, **2008**.

[87] B. J. Pichler, M. S. Judenhofer, and C. Pfannenberg. *Molecular Imaging I.* Springer Berlin Heidelberg, **2008**.

[88] X-D. Liu, S-M. Ma, and S-Z. Liu. Effects of 0.075 Gy X-Ray Irradiation on the Expression of IL-10 and IL-12 in Mice. *Phys. Med. Biol.*, 48: 2041–2049, **2003**.

[89] T. Beyer. PET: Speed Dating CT or MRI? *J. Nucl. Med.*, 48: 331, **2007**.

[90] H-P. Schlemmer, B. J. Pichler, R. Krieg, and W-D. Heiss. An Integrated MR/PET System: Prospective Applications. *Abdom. Imaging*, 34: 668–674, **2009**.

[91] N. Ghanem, M. Uhl, I. Brink, O. Schäfer, T. Kelly, E. Moser, and M. Langer. Diagnostic Value of MRI in Comparison to Scintigraphy, PET, MS-CT and PET/CT for the Detection of Metastases of Bone. *Eur. J. Radiol.*, 55: 41–55, **2005**.

[92] G. K. von Schulthess and H-P. Schlemmer. A Look Ahead: PET/MR versus PET/CT. *Eur. J. Nucl. Med. Mol. I.*, 36 (Suppl. 1): S3–S9, **2009**.

[93] M. Zaman, N. Fatima, Z. Sajjad, and U. Zaman. Whole Body Simultaneous PET/MRI: One-Stop-Shop? *J. Pak. Med. Assoc.*, 64: 201–204, **2014**.

[94] J-H. Lee, J-W. Kim, and J. Cheon. Magnetic Nanoparticles for Multi-Imaging and Drug Delivery. *Mol. Cells*, 35: 274–284, **2013**.

[95] O. Rodriguez, S. Fricke, C. Chien, L. Dettin, J. VanMeter, E. Shapiro, H-N. Dai, M. Casimiro, L. Ileva, J. Dagata, M. D. Johnson, M. P. Lisanti, A. Koretsky, and C. Albanese. Contrast-Enhanced *In Vivo* Imaging of Breast and Prostate Cancer Cells by MRI. *Cell Cycle*, 5: 113–119, **2006**.

[96] P. Howes, M. Green, A. Bowers, D. Parker, G. Varma, M. Kallumadil, M. Hughes, A. Warley, A. Brain, and R. Botnar. Magnetic Conjugated Polymer Nanoparticles as Bimodal Imaging Agents. *J. Am. Chem. Soc.*, 132: 9833–9842, **2010**.

[97] J. Culver, W. Akers, and S. Achilefu. Multimodality Molecular Imaging with Combined Optical and SPECT/PET Modalities. *J. Nucl. Med.*, 49: 169–172, **2008**.

[98] C. Li, Y. Yang, G. S. Mitchell, and S. R. Cherry. Simultaneous PET and Multispectral 3-Dimensional Fluorescence Optical Tomography Imaging System. *J. Nucl. Med.*, 52: 1268–1275, **2011**.

[99] M. Solomon, R. E. Nothdruft, W. Akers, W. B. Edwards, K. Liang, B. Xu, G. P. Suddlow, H. Deghani, Y-C. Tai, A. T. Eggebrecht, S. Achilefu, and J. P. Culver. Multimodal Fluorescence-Mediated Tomography and SPECT/CT for Small-Animal Imaging. *J. Nucl. Med.*, 54: 639–646, **2013**.

[100] E. C. Cho, C. Glaus, J. Chen, M. J. Welch, and Y. Xia. Inorganic Nanoparticle-Based Contrast Agents for Molecular Imaging. *Trends Mol. Med.*, 16: 561–573, **2010**.

[101] E. D. Agdeppa and M. E. Spilker. A Review of Imaging Agent Development. *AAPS J.*, 11: 286–299, **2009**.

[102] S. Aime, M. Fasano, and E. Terreno. Lanthanide(III) Chelates for NMR Biomedical Applications. *Chem. Soc. Rev.*, 27: 19–29, **1998**.

[103] S. Aime, M. Botta, and E. Terreno. Gd(III)-Based Contrast Agents for MRI. *Adv. Inorg. Chem.*, 57: 173–237, **2005**.

[104] A. D. Nunn. The Cost of Developing Imaging Agents for Routine Clinical Use. *Invest. Radiol.*, 41: 206–212, **2006**.

[105] GE Healthcare. http://www3.gehealthcare.com/en/Products/Categories/Magnetic_ Resonance_Imaging/Discovery_MR750_3-0T, February 2015.

[106] N. Bloembergen. Proton Relaxation Times in Paramagnetic Solutions. *J. Chem. Phys.*, 27: 572–573, **1957**.

[107] N. Bloembergen and L. O. Morgan. Proton Relaxation Times in Paramagnetic Solutions. Effects of Electron Spin Relaxation. *J. Chem. Phys.*, 34: 842–850, **1961**.

[108] I. Solomon. Relaxation Processes in a System of Two Spins. *Phys. Rev.*, 99: 559–565, **1955**.

[109] Y. Gossuin, A. Roch, R. N. Muller, and P. Gillis. An Evaluation of the Contributions of Diffusion and Exchange in Relaxation Enhancement by MRI Contrast Agents. *J. Magn. Reson.*, 158: 36–42, **2002**.

[110] J. H. Freed. Dynamic Effects of Pair Correlation Functions on Spin Relaxation by Translational Diffusion in Liquids. II. Finite Jumps and Independent T1 Processes. *J. Chem. Phys.*, 68: 4034–4037, **1978**.

[111] M. Botta. Second Coordination Sphere Water Molecules and Relaxivity of Gadolinium(III) Complexes: Implications for MRI Contrast Agents. *Eur. J. Inorg. Chem.*, 2000: 399–407, **2000**.

[112] P. Caravan, J. J. Ellison, T. J. McMurry, and R. B. Lauffer. Gadolinium(III) Chelates as MRI Contrast Agents: Structure, Dynamics, and Applications. *Chem. Rev.*, 99: 2293–2352, **1999**.

[113] Y. Gossuin, P. Gillis, A. Hocq, Q. L. Vuong, and A. Roch. Magnetic Resonance Relaxation Properties of Superparamagnetic Particles. *Nanomed. Nanobiotechnol.*, 1: 299–310, **2009**.

[114] Magnetic Resonance Technology Information Portal. http://www.mr-

tip.com/serv1.php?type=db1&dbs=magnevist, March 2015.

[115] Radiology Bayer HealthCare. http://www.radiologysolutions.bayer.com/products/mr/contrast/magnevist, March 2015.

[116] C. Kalavagunta and G. J. Metzger. A Field Comparison of r_1 and r_2^* Relaxivities of Gd-DTPA in Aqueous Solution and Whole Blood: 3 T versus 7 T. *Proc. Intl. Soc. Mag. Reson. Med.*, 18: 4990, **2010**.

[117] P. F. Hahn, D. D. Stark, J. M. Lewis, S. Saini, G. Elizondo, R. Weissleder, C. J. Fretz, and J. T. Ferrucci. First Clinical Trial of a New Superparamagnetic Iron Oxide for Use as an Oral Gastrointestinal Contrast Agent in MR Imaging. *Radiology*, 175: 695–700, **1990**.

[118] Guerbet. http://www.guerbet.com/en/our-products/mri-contrast-agents.html, March 2015.

[119] Y. X. J. Wang, S. M. Hussain, and G. P. Krestin. Superparamagnetic Iron Oxide Contrast Agents: Physicochemical Characteristics and Applications in MR Imaging. *Eur. Radiol.*, 11: 2319–2331, **2001**.

[120] J. F. Debatin and M. A. Patak. MRI of the Small and Large Bowel. *Eur. Radiol.*, 9: 1523–1534, **1999**.

[121] C. W. Jung and P. Jacobs. Physical and Chemical Properties of Superparamagnetic Iron Oxide MR Contrast Agents: Ferumoxides, Ferumoxtran, Ferumoxsil. *Magn. Reson. Imaging*, 13: 661–674, **1995**.

[122] R. Boellaard, M. J. O'Doherty, W. A. Weber, F. M. Mottaghy, M. N. Lonsdale, S. G. Stroobants, W. J. G. Oyen, J. Kotzerke, O. S. Hoekstra, J. Pruim, P. K. Marsden, K. Tatsch, C. J. Hoekstra, E. P. Visser, B. Arends, F. J. Verzijlbergen, J. M. Zijlstra, E. F. I. Comans, A. A. Lammertsma, A. M. Paans, A. T. Willemsen, T. Beyer, A. Bockisch, C. Schaefer-Prokop, D. Delbeke, R. P. Baum, A. Chiti, and B. J. Krause. FDG PET and PET/CT: EANM Procedure Guidelines for Tumour PET Imaging: Version 1.0. *Eur. J. Nucl. Med. Mol. I.*, 37: 181–200, **2010**.

[123] S. Vallabhajosula. *Molecular Imaging: Radiopharmaceuticals for PET and SPECT*. Springer, Berlin, **2009**.

[124] E. Prieto, J. M. Martí-Climent, I. Domínguez-Prado, P. Garrastachu, R. Díez-Valle, S. Tejada, J. J. Aristu, I. Peñuelas, and J. Arbizu. Voxel-Based Analysis of Dual-Time-Point ^{18}F-FDG PET Images for Brain Tumor Identification and Delineation. *J. Nucl. Med.*, 52: 865–872, **2011**.

[125] F. D. Grant, F. H. Fahey, A. B. Packard, R. T. Davis, A. Alavi, and S. T. Treves.

Skeletal PET with ^{18}F-Fluoride: Applying New Technology to an Old Tracer. *J. Nucl. Med.*, 49: 68–78, **2008**.

[126] Y. Ye and X. Chen. Integrin Targeting for Tumor Optical Imaging. *Theranostics*, 1: 102–126, **2011**.

[127] K. Licha and C. Olbrich. Optical imaging in drug discovery and diagnostic applications. *Adv. Drug Deliv. Rev.*, 57: 1087–1108, **2005**.

[128] Commission Recommendation of 18 October 2011 on the Definition of Nanomaterial (Text with EEA relevance; 2011/696/EU). OJ L 275, 20.10.2011, p. 38–40.

[129] V. Wagner, A. Dullaart, A-K. Bock, and A. Zweck. The Emerging Nanomedicine Landscape. *Nat. Biotechnol.*, 24: 1211–1217, **2006**.

[130] F. Hu, Q. Jia, Y. Li, and M. Gao. Facile Synthesis of Ultrasmall PEGylated Iron Oxide Nanoparticles for Dual-Contrast T1- and T2-Weighted Magnetic Resonance Imaging. *Nanotechnology*, 22: 245604, **2011**.

[131] T. L. Doane and C. Burda. The Unique Role of Nanoparticles in Nanomedicine: Imaging, Drug Delivery and Therapy. *Chem. Soc. Rev.*, 41: 2885–2911, **2012**.

[132] D. L. J. Thorek, A. K. Chen, J. Czupryna, and A. Tsourkas. Superparamagnetic Iron Oxide Nanoparticle Probes for Molecular Imaging. *Ann. Biomed. Eng.*, 34: 23–38, **2006**.

[133] E. V. Shashkov, M. Everts, E. I. Galanzha, and V. P. Zharov. Quantum Dots as Multimodal Photoacoustic and Photothermal Contrast Agents. *Nano Lett.*, 8: 3953–3958, **2008**.

[134] R. A. Farrer, F. L. Butterfield, V. W. Chen, and J. T. Fourkas. Highly Efficient Multiphoton-Absorption-Induced Luminescence from Gold Nanoparticles. *Nano Lett.*, 5: 1139–1142, **2005**.

[135] E. Dulkeith, T. Niedereichholz, T. A. Klar, J. Feldmann, G. von Plessen, D. I. Gittins, K. S. Mayya, and F. Caruso. Plasmon Emission in Photoexcited Gold Nanoparticles. *Phys. Rev. B*, 70: 205424, **2004**.

[136] R. Popovtzer, A. Agrawal, N. A. Kotov, A. Popovtzer, J. Balter, T. E. Carey, and R. Kopelman. Targeted Gold Nanoparticles Enable Molecular CT Imaging of Cancer. *Nano Lett.*, 8: 4593–4596, **2008**.

[137] X. Qian, X-H. Peng, D. O. Ansari, Q. Yin-Goen, G. Z. Chen, D. M. Shin, L. Yang, A. N. Young, M. D. Wang, and S. Nie. *In Vivo* Tumor Targeting and Spectroscopic Detection with Surface-Enhanced Raman Nanoparticle Tags. *Nat. Biotechnol.*, 26: 83–

90, **2008**.

[138] P-C. Li, C-R. C. Wang, D-B. Shieh, C-W. Wei, C-K. Liao, C. Poe, S. Jhan, A-A. Ding, and Y-N. Wu. *In Vivo* Photoacoustic Molecular Imaging with Simultaneous Multiple Selective Targeting Using Antibody-Conjugated Gold Nanorods. *Opt. Express*, 16: 18605–18615, **2008**.

[139] A. K. Iyer, G. Khaled, J. Fang, and H. Maeda. Exploiting the Enhanced Permeability and Retention Effect for Tumor Targeting. *Drug Discov. Today*, 11: 812–818, **2006**.

[140] P. Ghosh, G. Han, M. De, C. K. Kim, and V. M. Rotello. Gold Nanoparticles in Delivery Applications. *Adv. Drug Deliver. Rev.*, 60: 1307–1315, **2008**.

[141] S. Kyle and S. Saha. Nanotechnology for the Detection and Therapy of Stroke. *Adv. Healthc. Mater.*, 3: 1703–1720, **2014**.

[142] F. Kiessling, M. E. Mertens, J. Grimm, and T. Lammers. Nanoparticles for Imaging: Top or Flop? *Radiology*, 273: 10–28, **2014**.

[143] C. J. Czuprynski. *Opsonization and Phagocytosis*. Springer Berlin Heidelberg, **2005**.

[144] H. S. Choi, W. Liu, P. Misra, E. Tanaka, J. P. Zimmer, B. I. Ipe, M. G. Bawendi, and J. V. Frangioni. Renal Clearance of Quantum Dots. *Nat. Biotech.*, 25: 1165–1170, **2007**.

[145] G. Zhang, Z. Yang, W. Lu, R. Zhang, Q. Huang, M. Tian, L. Li, D. Liang, and C. Li. Influence of Anchoring Ligands and Particle Size on the Colloidal Stability and *In Vivo* Biodistribution of Polyethylene Glycol-Coated Gold Nanoparticles in Tumor-Xenografted Mice. *Biomaterials*, 30: 1928–1936, **2009**.

[146] T. Niidome, M. Yamagata, Y. Okamoto, Y. Akiyama, H. Takahashi, T. Kawano, Y. Katayama, and Y. Niidome. PEG-Modified Gold Nanorods with a Stealth Character for *In Vivo* Applications. *J. Controlled Release*, 114: 343–347, **2006**.

[147] J. Chen, C. Glaus, R. Laforest, Q. Zhang, M. Yang, M. Gidding, M. J. Welch, and Y. Xia. Gold Nanocages as Photothermal Transducers for Cancer Treatment. *Small*, 6: 811–817, **2010**.

[148] C. Chouly, D. Pouliquen, I. Lucet, J. J. Jeune, and P. Jallet. Development of Superparamagnetic Nanoparticles for MRI: Effect of Particle Size, Charge and Surface Nature on Biodistribution. *J. Microencapsul.*, 13: 245–255, **1996**.

[149] M. L. Schipper, G. Iyer, A. L. Koh, Z. Cheng, Y. Ebenstein, A. Aharoni, S. Keren, L. A. Bentolila, J. Li, J. Rao, X. Chen, U. Banin, A. M. Wu, R. Sinclair, S. Weiss, and S. S. Gambhir. Particle Size, Surface Coating, and PEGylation Influence the

Biodistribution of Quantum Dots in Living Mice. *Small*, 5: 126–134, **2009**.

[150] J. V. Jokerst, T. Lobovkina, R. N. Zare, and S. S. Gambhir. Nanoparticle PEGylation for Imaging and Therapy. *Nanomedicine*, 6: 715–728, **2011**.

[151] V. L. Colvin. The Potential Environmental Impact of Engineered Nanomaterials. *Nat. Biotechnol.*, 21: 1166–1170, 10 **2003**.

[152] A. A. Shvedova, V. Castranova, E. R. Kisin, D. Schwegler-Berry, A. R. Murray, V. Z. Gandelsman, A. Maynard, and P. Baron. Exposure to Carbon Nanotube Material: Assessment of Nanotube Cytotoxicity Using Human Keratinocyte Cells. *J. Toxicol. Env. Heal. A*, 66: 1909–1926, **2003**.

[153] B. Y. Yu and S-Y. Kwak. Assembly of Magnetite Nanocrystals into Spherical Mesoporous Aggregates with a 3-D Wormhole-Like Pore Structure. *J. Mater. Chem.*, 20: 8320–8328, **2010**.

[154] M. Mohapatra and S. Anand. Synthesis and Applications of Nano-Structured Iron Oxides/Hydroxides – A Review. *Int. J. Eng. Sci Technol.*, 2: 127–146, **2010**.

[155] L. Néel. Antiferromagnetism and Ferrimagnetism. *P. Phys. Soc. Lond. A*, 65: 869–885, **1952**.

[156] L. Cademartiri and G. A. Ozin. *Concepts of Nanochemistry*. Wiley-VCH Verlag GmbH & Co. KGaA, **2009**.

[157] R. J. Deissler, Y. Wu, and M. A. Martens. Dependence of Brownian and Néel Relaxation Times on Magnetic Field Strength. *Med. Phys.*, 41: 012301, **2014**.

[158] P. Tartaj. Superparamagnetic Composites: Magnetism with No Memory. *Eur. J. Inorg. Chem.*, pages 333–343, **2009**.

[159] R. H. Kodama, A. E. Berkowitz, E. J. McNiff, Jr., and S. Foner. Surface Spin Disorder in $NiFe_2O_4$ Nanoparticles. *Phys. Rev. Lett.*, 77: 394–397, **1996**.

[160] N. Moumen and M. P. Pileni. Control of the Size of Cobalt Ferrite Magnetic Fluid. *J. Phys. Chem.*, 100: 1867–1873, **1996**.

[161] M. P. Morales, S. Veintemillas-Verdaguer, M. I. Montero, C. J. Serna, A. Roig, Ll. Casas, B. Martínez, and F. Sandiumenge. Surface and Internal Spin Canting in γ-Fe_2O_3 Nanoparticles. *Chem. Mater.*, 11: 3058–3064, **1999**.

[162] H. M. Lu, W. T. Zheng, and Q. Jiang. Saturation Magnetization of Ferromagnetic and Ferrimagnetic Nanocrystals at Room Temperature. *J. Phys. D Appl. Phys.*, 40: 320–325, **2007**.

[163] E. Amstad, A. U. Gehring, H. Fischer, V. V. Nagaiyanallur, G. Hähner, M. Textor, and E. Reimhult. Influence of Electronegative Substituents on the Binding Affinity of Catechol-Derived Anchors to Fe_3O_4 Nanoparticles. *J. Phys. Chem. C*, 115: 683–691, **2011**.

[164] E. Amstad, H. Fischer, A. U. Gehring, M. Textor, and E. Reimhult. Magnetic Decoupling of Surface Fe^{3+} in Magnetite Nanoparticles upon Nitrocatechol-Anchored Dispersant Binding. *Chem. – Eur. J.*, 17: 7396–7398, **2011**.

[165] P. Majewski and B. Thierry. Functionalized Magnetite Nanoparticles - Synthesis, Properties, and Bio-Applications. *Crit. Rev. Solid State*, 32: 203–215, **2007**.

[166] P. Tartaj, M. D. Morales, S. Veintemillas-Verdaguer, T. González-Carreño, and C. J. Serna. The Preparation of Magnetic Nanoparticles for Applications in Biomedicine. *J. Phys. D Appl. Phys.*, 36: R182–R197, **2003**.

[167] T. Sugimoto and E. Matijević. Formation of Uniform Spherical Magnetite Particles by Crystallization From Ferrous Hydroxide Gels. *J. Colloid Interf. Sci.*, 74: 227–243, **1980**.

[168] M. A. Willard, L. K. Kurihara, E. E. Carpenter, S. Calvin, and V. G. Harris. Chemically Prepared Magnetic Nanoparticles. *Int. Mater. Rev.*, 49: 125–170, **2004**.

[169] D. Ling and T. Hyeon. Chemical Design of Biocompatible Iron Oxide Nanoparticles for Medical Applications. *Small*, 9: 1450–1466, **2013**.

[170] W. W. Yu, J. C. Falkner, C. T. Yavuz, and V. L. Colvin. Synthesis of Monodisperse Iron Oxide Nanocrystals by Thermal Decomposition of Iron Carboxylate Salts. *Chem. Commun.*, pages 2306–2307, **2004**.

[171] Z. Li, Q. Sun, and M. Gao. Preparation of Water-Soluble Magnetite Nanocrystals from Hydrated Ferric Salts in 2-Pyrrolidone: Mechanism Leading to Fe_3O_4. *Angew. Chem. Int. Ed.*, 44: 123–126, **2004**.

[172] P. H-L. Tran, T. T-D. Tran, T. V. Vo, and B-J. Lee. Promising Iron Oxide-Based Magnetic Nanoparticles in Biomedical Engineering. *Arch. Pharm. Res.*, 35: 2045–2061, **2012**.

[173] A. K. Gupta and M. Gupta. Synthesis and Surface Engineering of Iron Oxide Nanoparticles for Biomedical Applications. *Biomaterials*, 26: 3995–4021, **2005**.

[174] S. P. Gubin, Y. A. Koksharov, G. B. Khomutov, and G. Y. Yurkov. Magnetic Nanoparticles: Preparation, Structure and Properties. *Russ. Chem. Rev.*, 74: 489, **2005**.

[175] C. Okoli, M. Sanchez-Dominguez, M. Boutonnet, S. Järåas, C. Civera, C. Solans, and

G. R. Kuttuva. Comparison and Functionalization Study of Microemulsion-Prepared Magnetic Iron Oxide Nanoparticles. *Langmuir*, 28: 8479–8485, **2012**.

[176] M. Niederberger. Nonaqueous Sol–Gel Routes to Metal Oxide Nanoparticles. *Acc. Chem. Res.*, 40: 793–800, **2007**.

[177] A. Tavakoli, M. Sohrabi, and A. Kargari. A Review of Methods for Synthesis of Nanostructured Metals with Emphasis on Iron Compounds. *Chem. Pap.*, 61: 151–170, **2007**.

[178] O. M. Lemine, K. Omri, B. Zhang, L. El Mir, M. Sajieddine, A. Alyamani, and M. Bououdina. Sol–Gel Synthesis of 8 nm Magnetite (Fe_3O_4) Nanoparticles and their Magnetic Properties. *Superlattices Microst.*, 52: 793–799, **2012**.

[179] J. Xu, H. Yang, W. Fu, K. Du, Y Sui, J. Chen, Y. Zeng, M. Li, and G. Zou. Preparation and Magnetic Properties of Magnetite Nanoparticles by Sol–Gel Method. *J. Magn. Magn. Mater.*, 309: 307–311, **2007**.

[180] K. M. Krishnan. Biomedical Nanomagnetics: A Spin Through Possibilities in Imaging, Diagnostics, and Therapy. *IEEE T. Magn.*, 46: 2523–2558, **2010**.

[181] R. Weissleder, P. F. Hahn, D. D. Stark, E. Rummeny, S. Saini, J. Wittenberg, and J. T. Ferrucci. MR Imaging of Splenic Metastases: Ferrite-Enhanced Detection in Rats. *Am. J. Roentgenol.*, 149: 723–726, **1987**.

[182] B. R. Bacon, D. D. Stark, C. H. Park, S. Saini, E. V. Groman, P. F. Hahn, C. C. Compton, and J. T. Jr. Ferrucci. Ferrite Particles: A New Magnetic Resonance Imaging Contrast Agent. Lack of Acute or Chronic Hepatotoxicity After Intravenous Administration. *J. Lab. Clin. Med.*, 110: 164–171, **1987**.

[183] N. Lewinski, V. Colvin, and R. Drezek. Cytotoxicity of Nanoparticles. *Small*, 4: 26–49, **2008**.

[184] A. K. Gupta and S. Wells. Surface-Modified Superparamagnetic Nanoparticles for Drug Delivery: Preparation, Characterization, and Cytotoxicity Studies. *IEEE T. Nanobiosci.*, 3: 66–73, **2004**.

[185] A. K. Gupta and M. Gupta. Cytotoxicity Suppression and Cellular Uptake Enhancement of Surface Modified Magnetic Nanoparticles. *Biomaterials*, 26: 1565–1573, **2005**.

[186] W. W. Yu, E. Chang, C. M. Sayes, R. Drezek, and V. L. Colvin. Aqueous Dispersion of Monodisperse Magnetic Iron Oxide Nanocrystals Through Phase Transfer. *Nanotechnology*, 17: 4483–4487, **2006**.

[187] R. B. Lauffer. Paramagnetic Metal Complexes as Water Proton Relaxation Agents for

NMR Imaging: Theory and Design. *Chem. Rev.*, 87: 901–927, **1987**.

[188] N. Erathodiyil and J. Y. Ying. Functionalization of Inorganic Nanoparticles for Bioimaging Applications. *Acc. Chem. Res.*, 44: 925–935, **2011**.

[189] M-A. Fortin, R. M. Petoral Jr, F. Söderlind, A. Klasson, M Engström, T Veres, P-O. Käll, and K. Uvdal. Polyethylene Glycol-Covered Ultra-Small Gd_2O_3 Nanoparticles for Positive Contrast at 1.5 T Magnetic Resonance Clinical Scanning. *Nanotechnology*, 18: 395501, **2007**.

[190] M. A. Perazella. Current Status of Gadolinium Toxicity in Patients with Kidney Disease. *Clin. J. Am. Soc. Nephrol.*, 4: 461–469, **2009**.

[191] J. G. Penfield and R. F. Reilly Jr. What Nephrologists Need to Know About Gadolinium. *Nat. Clin. Pract. Nephr.*, 3: 654–668, **2007**.

[192] A. Hütten, D. Sudfeld, I. Ennen, G. Reiss, W. Hachmann, U. Heinzmann, K. Wojczykowski, P. Jutzi, W. Saikaly, and G. Thomas. New Magnetic Nanoparticles for Biotechnology. *J. Biotechnol.*, 112: 47–63, **2004**.

[193] J. D. G. Durán, J. L. Arias, V. Gallardo, and A. V. Delgado. Magnetic Colloids as Drug Vehicles. *J. Pharm. Sci.*, 97: 2948–2983, **2008**.

[194] S. H. Koenig and K. E. Kellar. Theory of 1/T1 and 1/T2 NMRD Profiles of Solutions of Magnetic Nanoparticles. *Magn. Reson. Med.*, 34: 227–233, **1995**.

[195] G. M. Lanza, P. M. Winter, S. D. Caruthers, A. M. Morawski, A. H. Schmieder, K. C. Crowder, and S. A. Wickline. Magnetic Resonance Molecular Imaging with Nanoparticles. *J. Nucl. Cardiol.*, 11: 733–743, **2004**.

[196] C. Felton, A. Karmakar, Y. Gartia, P. Ramidi, A. S. Biris, and A. Ghosh. Magnetic Nanoparticles as Contrast Agents in Biomedical Imaging: Recent Advances in Iron- and Manganese-Based Magnetic Nanoparticles. *Drug Metab. Rev.*, 46: 142–154, **2014**.

[197] A. Bjørnerud and L. Johansson. The Utility of Superparamagnetic Contrast Agents in MRI: Theoretical Consideration and Applications in the Cardiovascular System. *NMR Biomed.*, 17: 465–477, **2004**.

[198] F. D. Knollmann, J. C. Böck, S. Teltenkötter, W. Wlodarczyk, A. Mühler, T. J. Vogl, and R. Felix. Evaluation of Portal MR Angiography using Superparamagnetic Iron Oxide. *J. Magn. Reson. Imaging*, 7: 191–196, **1997**.

[199] U. Hoffmann, C. Loewe, C. Bernhard, M. Weber, M. Cejna, C. J. Herold, and W. Schima. MRA of the Lower Extremities in Patients with Pulmonary Embolism Using a Blood Pool Contrast Agent: Initial Experience. *J. Magn. Reson. Imaging*,

15: 429–437, **2002**.

[200] E-M. Larsson, P. Sundén, C-G. Olsson, J. Debatin, A. J. Duerinckx, R. Baum, D. Hahn, and F. Ebner. MR Venography Using an Intravascular Contrast Agent: Results from a Multicenter Phase 2 Study of Dosage. *Am. J. Roentgenol.*, 180: 227–232, **2003**.

[201] L. Johansson, C. Johnsson, E. Penno, A. Bjørnerud, and H. Ahlström. Acute Cardiac Transplant Rejection: Detection and Grading with MR Imaging with a Blood Pool Contrast Agent – Experimental Study in the Rat. *Radiology*, 225: 97–103, **2002**.

[202] S. M. Moghimi, A. C. Hunter, and J. C. Murray. Nanomedicine: Current Status and Future Prospects. *FASEB J.*, 19: 311–330, **2005**.

[203] R. E. Bailey and S. Nie. Alloyed Semiconductor Quantum Dots: Tuning the Optical Properties without Changing the Particle Size. *J. Am. Chem. Soc.*, 125: 7100–7106, **2003**. PMID: 12783563.

[204] A. M. Smith, H. Duan, A. M. Mohs, and S. Nie. Bioconjugated Quantum Dots for *In Vivo* Molecular and Cellular Imaging. *Adv. Drug Deliv. Rev.*, 60: 1226–1240, **2008**.

[205] M. Ryvolova, J. Chomoucka, J. Drbohlavova, P. Kopel, P. Babula, D. Hynek, V. Adam, T. Eckschlager, J. Hubalek, M. Stiborova, J. Kaiser, and R. Kizek. Modern Micro and Nanoparticle-Based Imaging Techniques. *Sensors*, 12: 14792–14820, **2012**.

[206] X. Wu, H. Liu, J. Liu, K. N. Haley, J. A. Treadway, J. P. Larson, N. Ge, F. Peale, and M. P. Bruchez. Immunofluorescent Labeling of Cancer Marker Her2 and Other Cellular Targets with Semiconductor Quantum Dots. *Nat. Biotech.*, 21: 41–46, **2003**.

[207] D. P. Cormode, T. Skajaa, Z. A. Fayad, and W. J. M. Mulder. Nanotechnology in Medical Imaging Probe Design and Applications. *Arterioscler. Throm. Vas.*, 29: 992–1000, **2009**.

[208] M. N. Rhyner, A. M. Smith, X. Gao, H. Mao, L. Yang, and S. Nie. *Nanoparticles in Biomedical Imaging*. Springer New York, **2008**.

[209] J. K. Jaiswal, H. Mattoussi, J. M. Mauro, and S. M. Simon. Long-Term Multiple Color Imaging of Live Cells Using Quantum Dot Bioconjugates. *Nat. Biotechnol.*, 21: 47–51, **2003**.

[210] A. Kumar and V. Kumar. Synthesis and Optical Properties of Guanosine 5-Monophosphate-Mediated CdS Nanostructures: An Analysis of their Structure, Morphology, and Electronic Properties. *Inorg. Chem.*, 48: 11032–11037, **2009**.

[211] D. Maysinger, M. Behrendt, M. Lalancette-Hébert, and J. Kriz. Real-Time Imag-

ing of Astrocyte Response to Quantum Dots: *In Vivo* Screening Model System for Biocompatibility of Nanoparticles. *Nano Lett.*, 7: 2513–2520, **2007**.

[212] M. Bruchez, M. Moronne, P. Gin, S. Weiss, and A. P. Alivisatos. Semiconductor Nanocrystals as Fluorescent Biological Labels. *Science*, 281: 2013–2016, **1998**.

[213] W. C. W. Chan and S. Nie. Quantum Dot Bioconjugates for Ultrasensitive Nonisotopic Detection. *Science*, 281: 2016–2018, **1998**.

[214] M. Green, D. Smyth-Boyle, J. Harries, and R. Taylor. Nucleotide Passivated Cadmium Sulfide Quantum Dots. *Chem. Commun.*, pages 4830–4832, **2005**.

[215] X. Michalet, F. F. Pinaud, L. A. Bentolila, J. M. Tsay, S. Doose, J. J. Li, G. Sundaresan, A. M. Wu, S. S. Gambhir, and S. Weiss. Quantum Dots for Live Cells, *In Vivo* Imaging, and Diagnostics. *Science*, 307: 538–544, **2005**.

[216] Y. Xing and J. Rao. Quantum Dot Bioconjugates for *In Vitro* Diagnostics & *In Vivo* Imaging. *Cancer Biomark.*, 4: 307–319, **2008**.

[217] E. Amstad, M. Textor, and E. Reimhult. Stabilization and Functionalization of Iron Oxide Nanoparticles for Biomedical Applications. *Nanoscale*, 3: 2819–2843, **2011**.

[218] R. Weissleder, A. Bogdanov, E. A. Neuwelt, and M. Papisov. Long-Circulating Iron Oxides for MR Imaging. *Adv. Drug Deliver. Rev.*, 16: 321–334, **1995**.

[219] M. Green. The Nature of Quantum Dot Capping Ligands. *J. Mater. Chem.*, 20: 5797–5809, **2010**.

[220] T. Bala, A. Swami, B. L. V. Prasad, and M. Sastry. Phase Transfer of Oleic Acid Capped Ni(Core)Ag(Shell) Nanoparticles Assisted by the Flexibility of Oleic Acid on the Surface of Silver. *J. Colloid Interface Sci.*, 283: 422–431, **2005**.

[221] A. Prakash, H. Zhu, C. J. Jones, D. N. Benoit, A. Z. Ellsworth, E. L. Bryant, and V. L. Colvin. Bilayers as Phase Transfer Agents for Nanocrystals Prepared in Nonpolar Solvents. *ACS Nano*, 3: 2139–2146, **2009**.

[222] E. Amstad, T. Gillich, I. Bilecka, M. Textor, and E. Reimhult. Ultrastable Iron Oxide Nanoparticle Colloidal Suspensions Using Dispersants with Catechol-Derived Anchor Groups. *Nano Lett.*, 9: 4042–4048, **2009**.

[223] D. Ruiz-Molina, F. Novio, and C. Roscini. *Bio- and Bioinspired Nanomaterials*. Wiley-VCH, **2014**.

[224] M. D. Shultz, J. U. Reveles, S. N. Khanna, and E. E. Carpenter. Reactive Nature of Dopamine as a Surface Functionalization Agent in Iron Oxide Nanoparticles. *J. Am.*

Chem. Soc., 129: 2482–2487, **2007**.

[225] R. G. G. Russell. Bisphosphonates: Mode of Action and Pharmacology. *Pediatrics*, 119 (Suppl 2): S150–62, **2007**.

[226] J. Galezowska and E. Gumienna-Kontecka. Phosphonates, their Complexes and Bio-Applications: A Spectrum of Surprising Diversity. *Coordin. Chem. Rev.*, 256: 105–124, **2012**.

[227] D. Portet, B. Denizot, E. Rump, J. J. Lejeune, and P. Jallet. Nonpolymeric Coatings of Iron Oxide Colloids for Biological Use as Magnetic Resonance Imaging Contrast Agents. *J. Colloid Interface Sci.*, 238: 37–42, **2001**.

[228] W. Gao, L. Dickinson, C. Grozinger, F. G. Morin, and L. Reven. Self-Assembled Monolayers of Alkylphosphonic Acids on Metal Oxides. *Langmuir*, 12: 6429–6435, **1996**.

[229] R. D. Rutledge, C. L. Warner, J. W. Pittman, R. S. Addleman, M. Engelhard, W. Chouyyok, and M. G. Warner. Thiol-Ene Induced Diphosphonic Acid Functionalization of Superparamagnetic Iron Oxide Nanoparticles. *Langmuir*, 26: 12285–12292, **2010**.

[230] Y. Sahoo, H. Pizem, T. Fried, D. Golodnitsky, L. Burstein, C. N. Sukenik, and G. Markovich. Alkyl Phosphonate/Phosphate Coating on Magnetite Nanoparticles: A Comparison with Fatty Acids. *Langmuir*, 17: 7907–7911, **2001**.

[231] S. Mohapatra and P. Pramanik. Synthesis and Stability of Functionalized Iron Oxide Nanoparticles Using Organophosphorus Coupling Agents. *Colloids Surf., A: Physicochem. Eng. Aspects*, 339: 35–42, **2009**.

[232] Y. Lalatonne, C. Paris, J. M. Serfaty, P. Weinmann, M. Lecouvey, and L. Motte. Bisphosphonates-Ultra Small Superparamagnetic Iron Oxide Nanoparticles: A Platform Towards Diagnosis and Therapy. *Chem. Commun.*, pages 2553–2555, **2008**.

[233] F. Benyettou, Y. Lalatonne, O. Sainte-Catherine, M. Monteil, and L. Motte. Superparamagnetic Nanovector with Anti-cancer Properties: γFe_2O_3@Zoledronate. *Int. J. Pharm.*, 379: 324–327, **2009**.

[234] A. Clearfield. Recent Advances in Metal Phosphonate Chemistry II. *Curr. Opin. Solid State Mater. Sci.*, 6: 495–506, **2002**.

[235] R. T. M. de Rosales, C. Finucane, S. J. Mather, and P. J. Blower. Bifunctional Bisphosphonate Complexes for the Diagnosis and Therapy of Bone Metastases. *Chem. Commun.*, pages 4847–4849, **2009**.

[236] S. Laurent, D. Forge, M. Port, A. Roch, C. Robic, L. Vander Elst, and R. N. Muller. Magnetic Iron Oxide Nanoparticles: Synthesis, Stabilization, Vectorization, Physico-chemical Characterizations, and Biological Applications. *Chem. Rev.*, 108: 2064–2110, **2008**.

[237] M. C. Bautista, O. Bomati-Miguel, M. del Puerto Morales, C. J. Serna, and S. Veintemillas-Verdaguer. Surface Characterisation of Dextran-Coated Iron Oxide Nanoparticles Prepared by Laser Pyrolysis and Coprecipitation. *J. Magn. Magn. Mater.*, 293: 20–27, **2005**.

[238] C. Tassa, S. Y. Shaw, and R. Weissleder. Dextran-Coated Iron Oxide Nanoparticles: A Versatile Platform for Targeted Molecular Imaging, Molecular Diagnostics, and Therapy. *Acc. Chem. Res.*, 44: 842–852, **2011**.

[239] L. Josephson, C. H. Tung, A. Moore, and R. Weissleder. High-Efficiency Intracellular Magnetic Labeling with Novel Superparamagnetic-Tat Peptide Conjugates. *Bioconjugate Chem.*, 10: 186–191, **1999**.

[240] P. Wunderbaldinger, L. Josephson, and R. Weissleder. Crosslinked Iron Oxides (CLIO): A New Platform for the Development of Targeted MR Contrast Agents. *Acad. Radiol.*, 9 (Suppl 2):S304–6, **2002**.

[241] H. Xu, F. Yan, E. E. Monson, and R. Kopelman. Room-Temperature Preparation and Characterization of Poly (ethylene glycol)-Coated Silica Nanoparticles for Biomedical Applications. *J. Biomed. Mater. Res. A*, 66: 870–879, **2003**.

[242] D. Dorniani, A. U. Kura, M. Z. B. Hussein, S. Fakurazi, A. H. Shaari, and Z. Ahmad. Controlled-Release Formulation of Perindopril Erbumine Loaded PEG-Coated Magnetite Nanoparticles for Biomedical Applications. *J. Mater. Sci.*, 49: 8487–8497, **2014**.

[243] M. R. Phadatare, V. M. Khot, A. B. Salunkhe, N. D. Thorat, and S. H. Pawar. Studies on Polyethylene Glycol Coating on $NiFe_2O_4$ Nanoparticles for Biomedical Applications. *J. Magn. Magn. Mater.*, 324: 770–772, **2012**.

[244] E. Illés, E. Tombácz, M. Szekeres, I. Y. Tóth, Á. Szabó, and B. Iván. Novel Carboxylated PEG-Coating on Magnetite Nanoparticles Designed for Biomedical Applications. *J. Magn. Magn. Mater.*, 380: 132–139, **2015**.

[245] J. Mendez-Garza, B. Wang, A. Madeira, C. Giorgio, and G. Bossis. Synthesis and Surface Modification of Spindle-Type Magnetic Nanoparticles: Gold Coating and PEG Functionalization. *J. Biomater. Nanobiotechnol.*, 4: 222–228, **2013**.

[246] S. Zalipsky. Functionalized Poly(ethylene glycols) for Preparation of Biologically Relevant Conjugates. *Bioconjugate Chem.*, 6: 150–165, **1995**.

[247] S. Zalipsky. Synthesis of an End-Group Functionalized Polyethylene Glycol-Lipid Conjugate for Preparation of Polymer-Grafted Liposomes. *Bioconjugate Chem.*, 4: 296–299, **1993**.

[248] A. Bar-Ilan and A. Zilkha. Anionic Polymerization of Ethylene Oxide by Anhydrous Potassium Hydroxide. *J. Macromol. Sci. A*, 4: 1727–1741, **1970**.

[249] A. L. Klibanov, K. Maruyama, V. P. Torchilin, and L. Huang. Amphipathic polyethyleneglycols effectively prolong the circulation time of liposomes. *FEBS Lett.*, 268: 235–237, **1990**.

[250] G. Blume and G. Cevc. Liposomes for the Sustained Drug Release *In Vivo*. *BBA - Biomembranes*, 1029: 91–97, **1990**.

[251] K. Knop, R. Hoogenboom, D. Fischer, and U.S. Schubert. Poly(ethylene glycol) in Drug Delivery: Pros and Cons as Well as Potential Alternatives. *Angew. Chem. Int. Ed.*, 49: 6288–6308, **2010**.

[252] J. H. Lee, H. B. Lee, and J. D. Andrade. Blood Compatibility of Polyethylene Oxide Surfaces. *Prog. Polym. Sci.*, 20: 1043–1079, **1995**.

[253] S. J. Sofia, V. Premnath, and E. W. Merrill. Poly(ethylene oxide) Grafted to Silicon Surfaces: Grafting Density and Protein Adsorption. *Macromolecules*, 31: 5059–5070, **1998**.

[254] N. A. Alcantar, E. S. Aydil, and J. N. Israelachvili. Polyethylene Glycol-Coated Biocompatible Surfaces. *J. Biomed. Mater. Res.*, 51: 343–351, **2000**.

[255] S. Dreborg and E. B. Akerblom. Immunotherapy with Monomethoxypolyethylene Glycol Modified Allergens. *Crit. Rev. Ther. Drug*, 6: 315–365, **1990**.

[256] T. Yamaoka, Y. Tabata, and Y. Ikada. Distribution and Tissue Uptake of Poly(ethylene glycol) with Different Molecular Weights after Intravenous Administration to Mice. *J. Pharm. Sci.*, 83: 601–606, **1994**.

[257] I. B. Mosbah, R. Franco-Gou, H. B. Abdennebi, R. Hernandez, G. Escolar, D. Saidane, J. Rosello-Catafau, and C. Peralta. Effects of Polyethylene Glycol and Hydroxyethyl Starch in University of Wisconsin Preservation Solution on Human Red Blood Cell Aggregation and Viscosity. *Transplant Proc.*, 38: 1229–1235, **2006**.

[258] V. G. Kadajji and G. V. Betageri. Water Soluble Polymers for Pharmaceutical Applications. *Polymers*, 3: 1972–2009, **2011**.

[259] D. S. Pisal, M. P. Kosloski, and S. V. Balu-Iyer. Delivery of Therapeutic Proteins. *J. Pharm. Sci.*, 99: 2557–2575, **2010**.

[260] W. Johnson Jr. Final Report on the Safety Assessment of PEG-25 Propylene Glycol Stearate, PEG-75 Propylene Glycol Stearate, PEG-120 Propylene Glycol Stearate, PEG-10 Propylene Glycol, PEG-8 Propylene Glycol Cocoate, and PEG-55 Propylene Glycol Oleate. *Int. J. Toxicol.*, 20 (Suppl. 4): 13–26, **2001**.

[261] C. Fruijtier-Pölloth. Safety Assessment on Polyethylene Glycols (PEGs) and their Derivatives as used in Cosmetic Products. *Toxicology*, 214: 1–38, **2005**.

[262] O. K. Nag and V. Awasthi. Surface Engineering of Liposomes for Stealth Behavior. *Pharmaceutics*, 5: 542–569, **2013**.

[263] M. B. Linder. Hydrophobins: Proteins that Self Assemble at Interfaces. *Curr. Opin. Colloid In.*, 14: 356–363, **2009**.

[264] K. Scholtmeijer, M. I. Janssen, M. B. M. van Leeuwen, T. G. van Kooten, H. Hektor, and H. A. B. Wösten. The Use of Hydrophobins to Functionalize Surfaces. *Biomed. Mater. Eng.*, 14: 447–454, **2004**.

[265] M. B. Linder, G. R. Szilvay, T. Nakari-Setälä, and Penttilä. Hydrophobins: The Protein-Amphiphiles of Filamentous Fungi. *FEMS Microbiol. Rev.*, 29: 877–896, **2005**.

[266] M. Sunde, A. H. Y. Kwan, M. D. Templeton, R. E. Beever, and J. P. Mackay. Structural Analysis of Hydrophobins. *Micron*, 39: 773–784, **2008**.

[267] J. Bayry, V. Aimanianda, J. I. Guijarro, M. Sunde, and J-P. Latgé. Hydrophobins— Unique Fungal Proteins. *PLoS Pathog.*, 8: e1002700, **2012**.

[268] A. H. Kwan, I. Macindoe, P. V. Vukasin, V. K. Morris, I. Kass, R. Gupte, A. E. Mark, M. D. Templeton, J. P. Mackay, and M. Sunde. The Cys3-Cys4 Loop of the Hydrophobin EAS is not Required for Rodlet Formation and Surface Activity. *J. Mol. Biol.*, 382: 708–720, **2008**.

[269] J. G. H. Wessels. Developmental Regulation of Fungal Cell Wall Formation. *Annu. Rev. Phytopathol.*, 32: 413–437, **1994**.

[270] J. G. Wessels. Hydrophobins: Proteins that Change the Nature of the Fungal Surface. *Adv. Microb. Physiol.*, 38: 1–45, **1997**.

[271] W. Wohlleben, T. Subkowski, C. Bollschweiler, B. von Vacano, Y. Liu, W. Schrepp, and U. Baus. Recombinantly Produced Hydrophobins from Fungal Analogues as Highly Surface-Active Performance Proteins. *Eur. Biophys. J.*, 39: 457–468, **2010**.

[272] I. Macindoe, A. H. Kwan, Q. Ren, V. K. Morris, W. Yang, J. P. Mackay, and M. Sunde. Self-Assembly of Functional, Amphipathic Amyloid Monolayers by the Fungal Hydrophobin EAS. *Proc. Natl. Acad. Sci. USA*, 109: E804–E811, **2012**.

[273] J. Hakanpää, G. R. Szilvay, H. Kalijunen, M. Maksimainen, M. Linder, and J. Rouvinen. Two Crystal Structures of Trichoderma Reesei Hydrophobin HFBI - The Structure of a Protein Amphiphile with and without Detergent Interaction. *Protein Sci.*, 15: 2129–2140, **2006**.

[274] H. K. Valo, P. H. Laaksonen, L. J. Peltonen, M. B. Linder, J. T. Hirvonen, and T. J. Laaksonen. Multifunctional Hydrophobin: Toward Functional Coatings for Drug Nanoparticles. *ACS Nano*, 4: 1750–1758, **2010**.

[275] K. Kurppa, H. Jiang, G. R. Szilvay, A. G. Nasibulin, E. I. Kauppinen, and M. B. Linder. Controlled Hybrid Nanostructures through Protein-Mediated Noncovalent Functionalization of Carbon Nanotubes. *Angew. Chem. Int. Ed.*, 46: 6446–6449, **2007**.

[276] P. Laaksonen, M. Kainlauri, T. Laaksonen, A. Shchepetov, H. Jiang, J. Ahopelto, and M. B. Linder. Interfacial Engineering by Proteins: Exfoliation and Functionalization of Graphene by Hydrophobins. *Angew. Chem. Int. Ed.*, 49: 4946–4949, **2010**.

[277] M. P. Sarparanta, L. M. Bimbo, E. M. Mäkilä, J. J. Salonen, P. H. Laaksonen, A. M. K. Helariutta, M. B. Linder, J. T. Hirvonen, T. J. Laaksonen, H. A. Santos, and A. J. Airaksinen. The Mucoadhesive and Gastroretentive Properties of Hydrophobin-Coated Porous Silicon Nanoparticle Oral Drug Delivery Systems. *Biomaterials*, 33: 3353–3362, **2012**.

[278] L. M. Bimbo, E. Mäkilä, J. Raula, T. Laaksonen, P. Laaksonen, K. Strommer, E. I. Kauppinen, J. Salonen, M. B. Linder, J. Hirvonen, and H. A. Santos. Functional Hydrophobin-Coating of Thermally Hydrocarbonized Porous Silicon Microparticles. *Biomaterials*, 32: 9089–9099, **2011**.

Chapter 2

Ultrasmall superparamagnetic iron oxide nanoparticles

2.1   Introduction

This chapter aims to detail the development of a SPECT-MR imaging probe based on USPIOs and BP-anchored coatings. Iron oxide NPs were chosen as the platform for the contrast agent due to their biocompatibility as proved by previous use in the clinic as liver MR imaging agents and also due to the ability to functionalise the NP surface allowing for use in specific applications. The development of the synthesis to produce iron oxide cores, followed by the ligand exchange method used to introduce a biocompatible coating will be described. Characterisation of the particles before and after exchange of surface ligands will be analysed, as will the introduction of a radionuclide allowing for both *in vivo* MRI and SPECT imaging studies to be performed. Finally, the incorporation of a targeting modality into the particle coating will be outlined and the subsequent *in vitro* analysis will be presented.

2.2   Oleylamine coated ultrasmall superparamagnetic iron oxide nanoparticles

2.2.1   Initial synthetic method

The original synthesis used to produce USPIOs involved the primary amine oleylamine (OAm) as the surfactant, figure 2.1, which has previously been shown to be an excellent coating for metallic NPs [1–5]. This choice of using OAm as a capping ligand is a result of the binding to the surface of the Fe_3O_4 NPs via a lone pair on the amine group (figure 2.2). This is preferable to using oleic acid (OA), as used in many iron oxide preparations [6–8] (and has been shown to form a stronger bond to the NP surface [9, 10]), as it results in a weaker bond allowing for easier ligand exchange. OAm and OA share some similar properties. Firstly, washing strategies following NP synthesis become simplified due to the liquid state of OAm/OA at room temperature. The high boiling point allows strong heating conditions to be applied during synthesis [11]. Secondly, it has been reported that the C=C bond in the middle of the molecules may alter the morphology and crystallinity of NPs, as a result of the less restricted coordination to the particle surface [12]. In addition, an important advantage of using OAm over OA and other stabilisers such as trioctylphosphine (TOP) and

trioctylphosphine oxide (TOPO) is its ability to be used as both a reducing and capping agent. Evidence of this has been reported by several groups. Liu *et al.* detailed studies whereby IR spectroscopy was used to show the oxidation of the amine group to an amide group during the reduction of Au(III) to either Au(I) or Au(0) in the formation of gold NPs [13]. A similar effect has also been demonstrated in the formation of hollow fcc cobalt nanoparallelepipeds via thermolysis of solid fcc cobalt oxide NPs in OAm [14]. As has previously been described, iron oxide (magnetite, Fe_3O_4) consists of both Fe(II) and Fe(III), with the ratio of Fe(II)/Fe(III) being 0.5 in stoichiometric magnetite (but this is not normally the case) [15]. This mixture arises due to a proportion of Fe(III) present in the iron(III) acetylacetonate ($Fe(acac)_3$) being reduced to Fe(II) by donation of an electron from the amino group of the oleylamine.
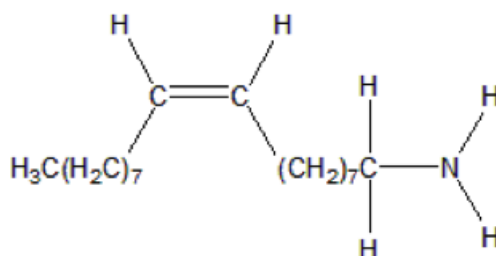
Figure 2.1: General structure of oleylamine.
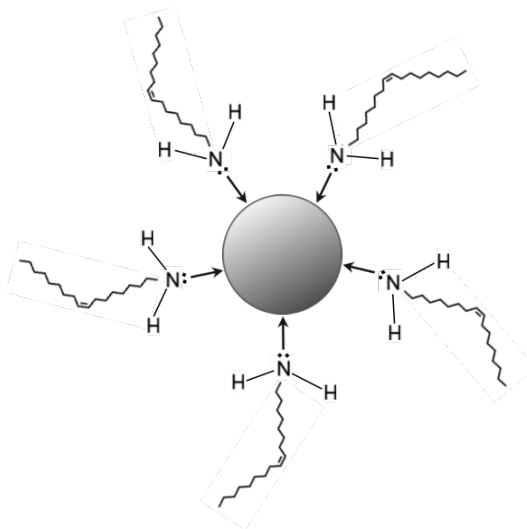
Figure 2.2: Schematic representation of oleylamine binding to a Fe_3O_4 NP via a lone pair on the amine group.

The synthesis of the magnetite NPs was based on a previously reported method involving the thermal decomposition of $Fe(acac)_3$ in benzyl ether and oleylamine, shown in scheme 2.1 [16]. This synthetic route of thermal decomposition of iron containing precursors was the first reported procedure to be an adequate way to synthesise monodispersed Fe_3O_4 NPs

[17,18]. Figure 2.3a shows a transmission electron (TE) micrograph of the NPs synthesised by reproducing the exact method stated by Xu *et al.* [16]. From TEM, it was found that the resulting particles in hexane (note the NPs are also dispersible in other non-polar solvents) had a core size (D_{TEM}) of 4.2 ± 0.7 nm (based on measurement of 41 particles), but it can be seen that large agglomerations had formed.
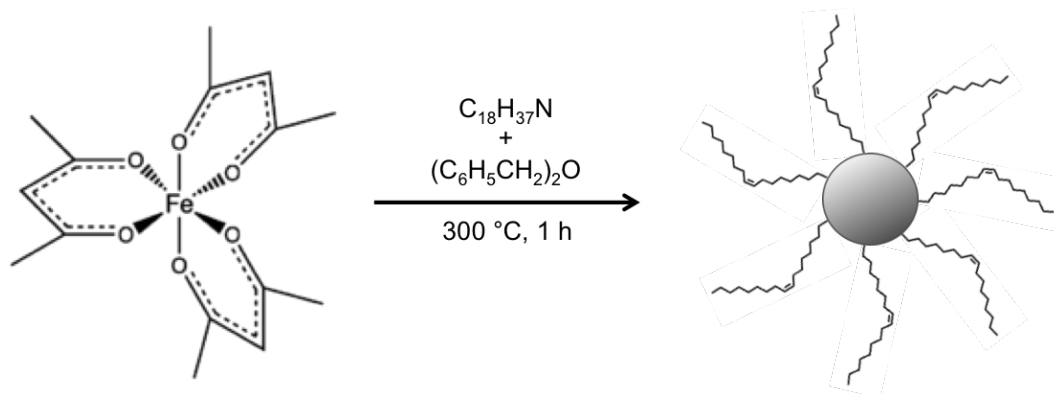
Scheme 2.1: Reaction scheme for the original synthesis of oleylamine coated NPs [16].

| (a) | (b) |
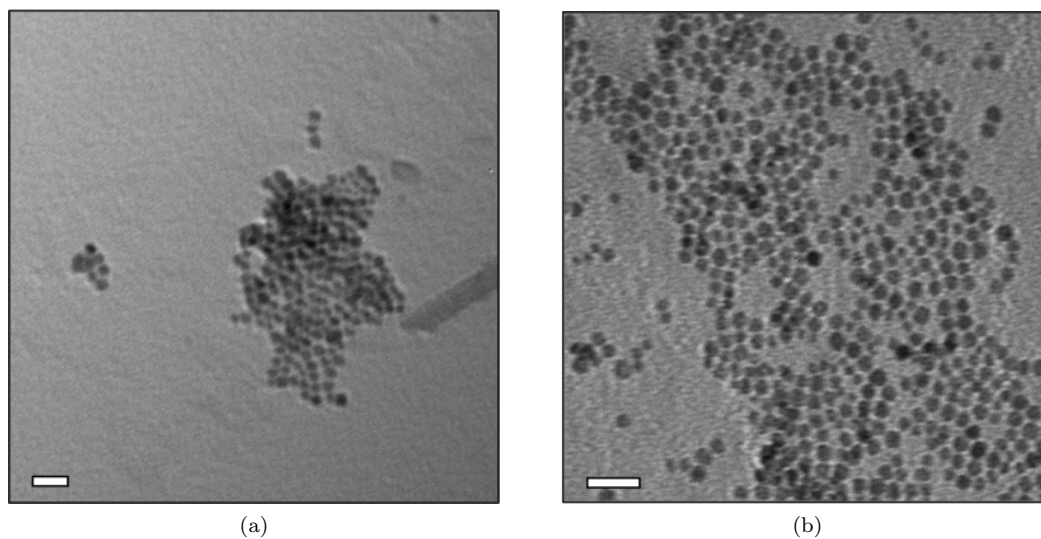
Figure 2.3: Characterisation of oleylamine coated Fe_3O_4 NPs: TEM micrograph of a dispersion (a) in hexane synthesised using the original method shown ($D_{\text{TEM}} = 4.2 \pm 0.7$ nm based on measurement of 41 particles, and (b) in DCM synthesised using an improved method involving heating across three different stages followed by ageing at a lower temperature ($D_{\text{TEM}} = 5.5 \pm 0.6$ nm based on measurement of 200 particles). Scale bars are 20 nm.

After one week in hexane, the particles began precipitating out of solution showing there was a need to develop the synthesis. After several slight modifications to the initial method, it was found that heating across three different stages followed by ageing the particles at a lower temperature for less time enhanced the quality of the sample produced. Figure 2.3b shows a very concentrated monodisperse sample of NPs soluble in dichloromethane

(DCM) with a D_{TEM} of 5.5 ± 0.6 nm based on the measurement of 200 particles, and a hydrodynamic diameter (D_{H}) of 10.0 ± 3.8 nm as determined by DLS. Measuring D_{H} allows for the determination of the overall size when in solution which is not possible with TEM because the sample preparation method causes the coating of the NPs to collapse [19]. In addition, the polydispersity index (PDI) of a sample is calculated as a measurement of the particle size distribution, and was found to be 0.15 for this synthesis. A number of groups have previously reported that a PDI higher than 0.3 indicates a population with a high heterogeneity [20–22]. These results showed a considerable improvement when compared against the TEM for the first sample (figure 2.3a). It should be noted here that as the hydrodynamic diameter measured was less than 40 nm, these particles can be classified as USPIOs (see page 31 of the introduction for a more detailed explanation).

2.2.2 Changing ramping rate

Once the improved synthesis had been established, investigations into parameters controlling the size distribution and regularity of the shape of the NPs was performed. As the intended application of these USPIOs was as a MR contrast agent, it was interesting to identify possible approaches to alter the morphology of the particles in order to optimise the relaxation properties. The first parameter explored was the ramping rate for each heating stage. It is known that ageing at a high temperature increases the particle size due to Oswalt ripening, the process by which dissolved sol particles redeposit on the surface of larger particles [27, 28]. Nakaya *et al.* investigated the effect ageing had on the overall size of iron oxide NPs via thermal decomposition, and found that longer reaction times led to increased particle growth, up until a maximum of 20 nm [29]. Not only does extending the reaction time alter the NP size, it has also been reported to increase the M_{S} of the particles [30]. Hence for this study both decreasing and increasing the time of each heating stage was assessed.

Doubling ramping rate

The synthesis was carried out with the ramping rate for each step doubled, hence halving the time each stage took. The average D_{TEM} remained approximately the same (5.3 ± 1.5 nm measured from 100 particles, figure 2.4a) but the sample was very polydisperse and irregularly shaped.

(a)   (b)
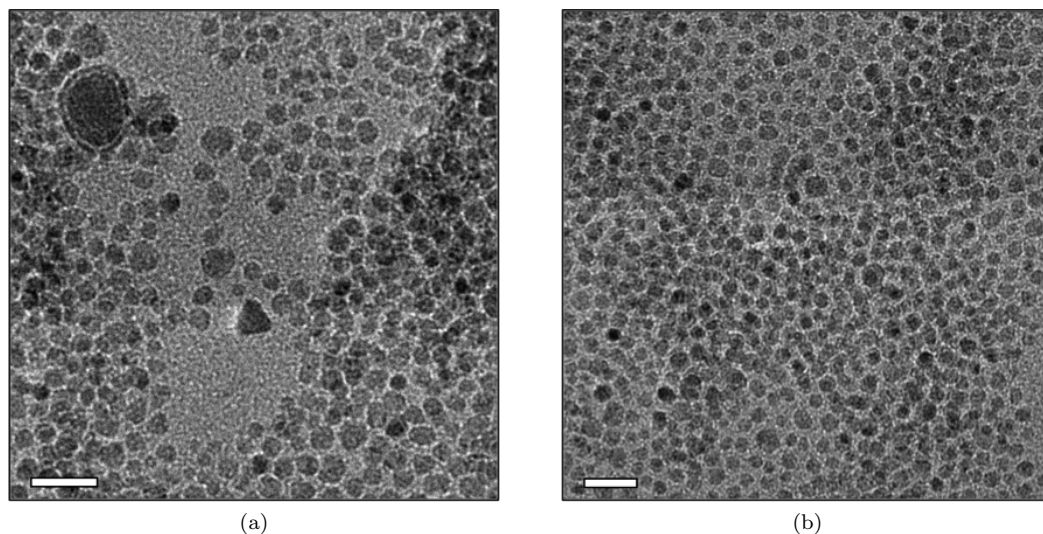
Figure 2.4: Characterisation of oleylamine coated Fe_3O_4 NPs: TEM micrograph of a dispersion in DCM synthesised with (a) the ramping rate doubled ($D_{TEM} = 5.3 \pm 1.5$ nm based on measurement of 100 particles), and (b) the ramping rate halved ($D_{TEM} = 5.0 \pm 0.9$ nm based on measurement of 100 particles). Scale bars are 20 nm.

Halving ramping rate

On this occasion, the procedure was repeated with the ramping rate for each stage halved, consequently doubling the duration of heating. Again, the average D_{TEM} had a similar value of 5.0 ± 0.9 nm (based on the measurement of 100 particles) with an undesirable size distribution and variations in shape as shown in figure 2.4b.

Although it has been reported by several other groups that varying reaction time can significantly alter the size of NPs synthesised, it can be seen from the above results that decreasing/increasing ageing time does not appear to have a beneficial effect for this particular scheme. Rather, it was found that the size distribution of the particles broadened, and the NP shape became less spherical.

2.2.3 Changing precursor ratio

Xu *et al.*, and others, stated that the size of the NPs produced was dependent on the volume ratios of the capping agent and solvent (in this case oleylamine and benzyl ether) used, whilst keeping the total volume constant. To be more precise, the particle size decreases as larger quantities of surfactant are used because it acts as a nucleating agent which favours the formation of a larger number of smaller nuclei [16, 23, 24]. To identify whether this

statement held true for this synthesis, a ratio of 2:1, *i.e.* 20 mL of oleylamine and 10 mL of benzyl ether, was explored in order to observe any difference from a 1:1 ratio. In addition, a reaction involving oleylamine only was attempted as the effect the benzyl ether had on the NPs produced was unknown. Solventless thermal decomposition methods have previously been used to successfully synthesise iron oxide particles [25, 26].

2:1 Oleylamine to benzyl ether

A 2:1 ratio of oleylamine to benzyl ether resulted in NPs with a slightly larger average D_{TEM} of 6.7 ± 1.4 nm, established from the measurement of 100 particles (figure 2.5a). It can also be seen that the acquired sample was polydispersed and irregular in shape.

(a)   (b)
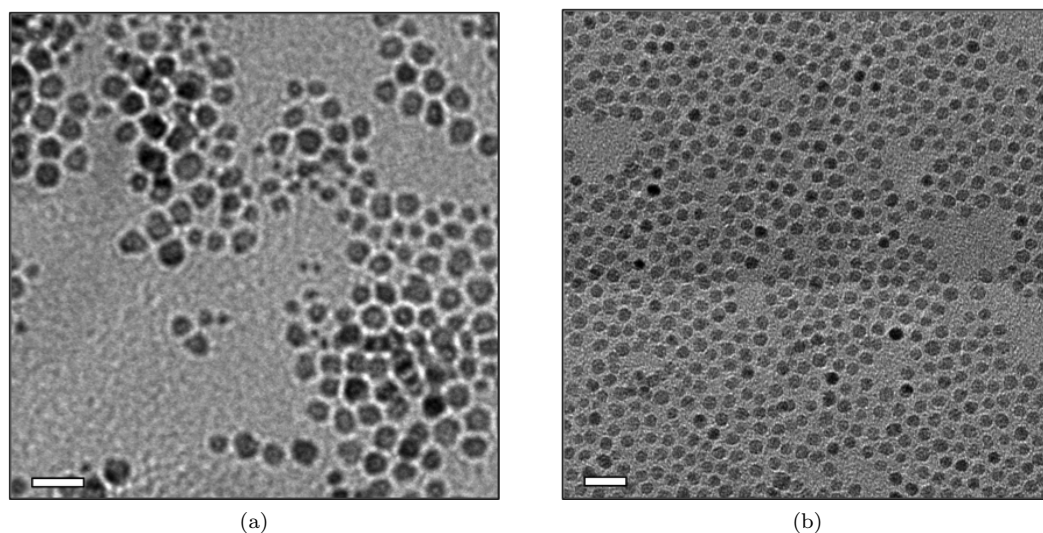
Figure 2.5: Characterisation of oleylamine coated Fe_3O_4 NPs: TEM micrograph of a dispersion in DCM synthesised using (a) a 2:1 ratio of oleylamine to benzyl ether ($D_{\mathrm{TEM}} = 6.7 \pm 1.4$ nm based on measurement of 100 particles), and (b) using oleylamine only ($D_{\mathrm{TEM}} = 5.2 \pm 0.6$ nm based on measurement of 200 particles). Scale bars are 20 nm.

Oleylamine only

The D_{TEM} obtained for the synthesis using oleylamine only was 5.2 ± 0.6 nm (based on 200 particles). Figure 2.5b shows the NPs have a small size distribution and a regular spherical shape.

It can be seen from the above results that higher quality particles are achieved using oleylamine only, hence for the remainder of this study, benzyl ether was removed.

2.2.4 Final synthetic method

The synthetic studies described above allowed for an improved synthesis to be designed that provided USPIOs of consistent quality throughout the remainder of this study. Scheme 2.2 represents the final reaction employed to prepare the iron oxide NPs, which was reliably reproduced a multitude of times with little differences in the particles produced, as determined via TEM and DLS analysis. In order to ensure that the heating rates for each step were consistent each time, equipment was used which allowed for the required ramping rates to be programmed. The plot in figure 2.6 is an example of the programmed heating rate alongside the actual temperatures recorded throughout a synthesis and displays a high degree of accuracy.
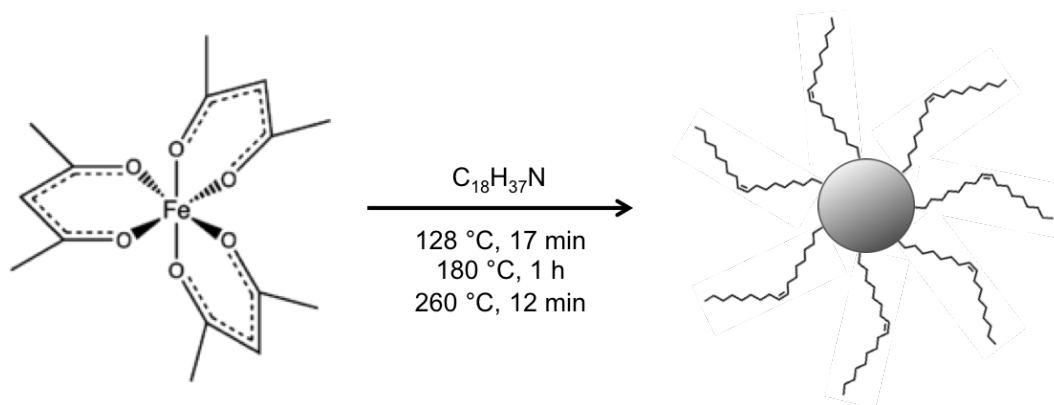
Scheme 2.2: Reaction scheme for the finalised standard synthesis of oleylamine coated NPs.

Volume of oleylamine	30 mL
Volume of benzyl ether	0 mL
Heating stages	25 °C → 128 °C at 363.5 °C/h 128 °C → 180 °C at 52 °C/h 180 °C → 270 °C at 396 °C/h

Table 2.1: Reaction conditions for the final synthetic method for oleylamine coated NPs.

Once this final method had been established, the nature of the synthesised Fe_3O_4 NPs was determined. The D_{TEM} was measured to be 5.2 ± 0.7 (based on the measurement of 100 particles), with a corresponding D_H of 13.0 ± 3.2 and a PDI of 0.23. The USPIOs are shown in figure 2.7 and it can be seen there is a high concentration of particles with some degree of self assembly occurring which may be visible due to the preparation of the TEM grids involving drying the NPs [31].

Further confirmation of the monodispersity of the sample was achieved by performing size-selective precipitation of the USPIOs in DCM. Methanol was used as the cosolvent due to
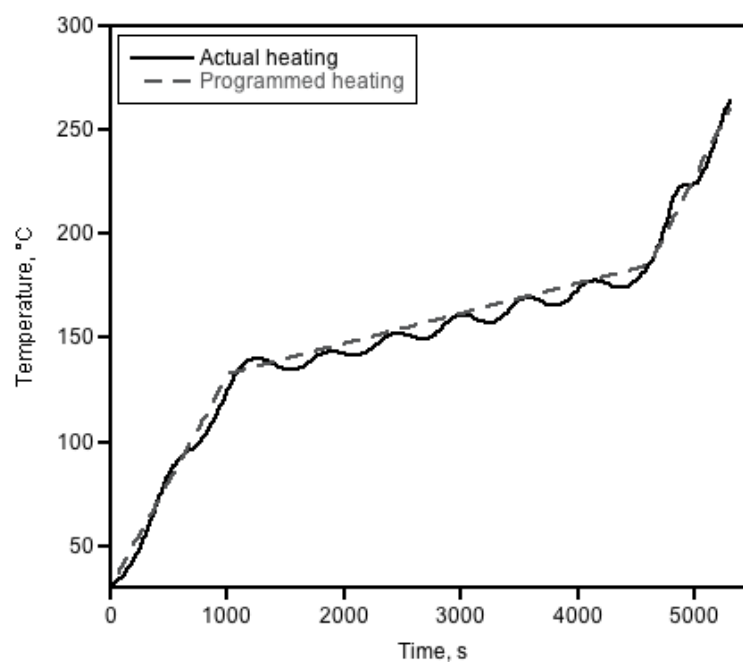
Figure 2.6: Comparison of ramping rates: Graphical representation of programmed heating rate compared to actual heating rate during synthesis of Fe_3O_4 NPs.
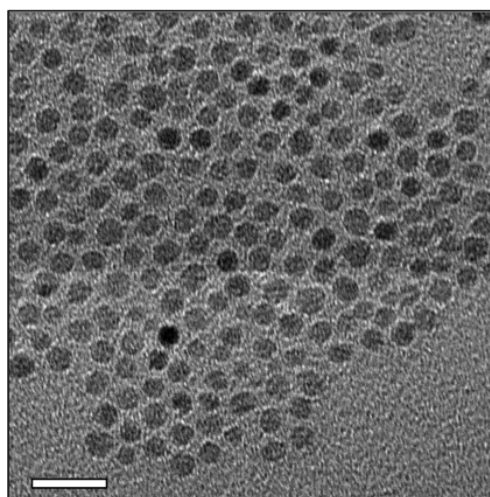
Figure 2.7: Characterisation of oleylamine coated Fe_3O_4 NPs: TEM micrograph of a dispersion in DCM synthesised using the final developed method ($D_{TEM} = 5.2 \pm 0.7$ nm based on measurement of 100 particles). Scale bar is 20 nm.

it being more polar than DCM, and increasing the overall polarity of the solution caused the larger particles/aggregates to precipitate out as they are less stable. It was found that no precipitate formed, suggesting the sample was monodispersed and the particles were of a small size.

2.3 Polyethylene glycol phase transfer of ultrasmall superparamagnetic iron oxide nanoparticles

In order to enhance water solubility of the NPs, the oleylamine coating was replaced with a coating of PEG, a non-ionic hydrophilic polymer which was used to reduce aggregation and hence increase the stability of particles in aqueous solutions. PEG was conjugated to the iron oxide surface via a BP. The rational behind using both these molecules has been described previously in the introduction (see introduction, pages 41 and 40 respectively). The structure of the PEG-BP is given in figure 2.8 and when performing certain studies, for example radiolabelling, various lengths of PEG were explored.
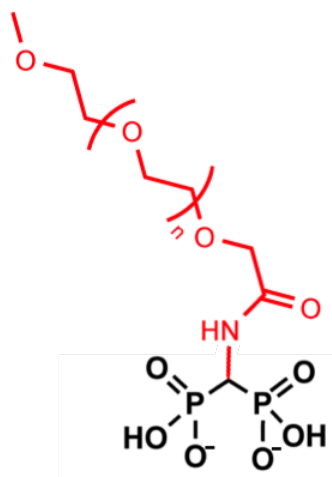
Figure 2.8: General structure of PEG-BP.

2.3.1 Initial synthetic method

The first method investigated for PEGylating the particles involved sonicating the PEG_{2000}-BP (PEG(2)-BP) and oleylamine coated NPs in water until all had evaporated, followed by redispersing in H_2O as shown in scheme 2.3. Although this method seems implausible due

to the particles being coated in a hydrophobic molecule, the ligand exchange occurs rapidly (as observed by the immediate formation of a pale brown solution) which forces the NPs into water. It was found that this method was time consuming due to length of time taken for the evaporation of the water. Furthermore, the particles produced from this approach of ligand exchange appeared to PEGylate in clusters (figure 2.9) resulting in aggregates with large diameters. Additionally, during the water evaporation step it was noticed that some precipitate settled on the bottom of the vial suggesting not all particles were phase transferred. From this, it was determined that the best way to proceed would be to use a more volatile solvent for the first step of dispersing the PEG-BP and USPIOs. It is important to note that due to the *in vivo* application of the USPIOs, selecting the correct PEG chain length is essential in preventing aggregation processes induced by plasma proteins. It has been shown that using a molecular weight of 5000 Da significantly increases the blood half time of coated USPIOs [33,34], thus this was the PEG length used throughout the remainder of this study.
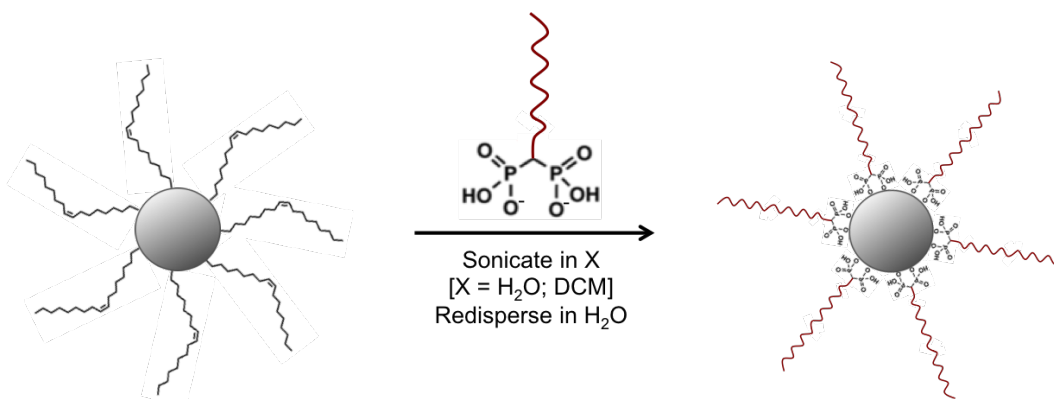
Scheme 2.3: Reaction scheme for the method of PEGylation of iron oxide NPs using water or DCM (represented by X).

2.3.2 Final synthetic method

The final method of PEGylation was kept the same as that shown in scheme 2.3, with the exception of using DCM in place of water. In addition, a lower mass of NPs was used initially as it was found with previous attempts at the phase transfer process, there was a large excess of oleylamine coated Fe_3O_4 remaining once PEGylation was complete. Using an excess of PEG_{5000}-BP (PEG(5)-BP) increased the possibility of maximising the dispersant packing density, which is known to result in particles with a high colloidal stability [19]. This process of functionalisation allowed for high yields to be reached in a short time and at room
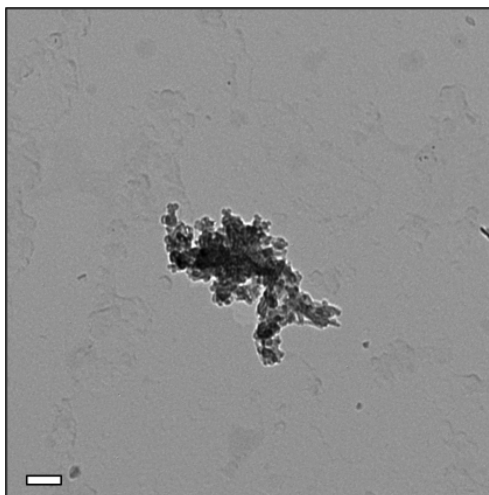
Figure 2.9: Characterisation of PEGylated Fe_3O_4 NPs: TEM micrograph of a dispersion in water phase transferred using the initial method. Scale bar is 100 nm.

temperature, in contrast to other reported methods [32, 34]. For example, Kim *et al.* heated to a temperature of 70 °C for 5 h, whereas Hu *et al.* required 2 days to purify the PEGylated particles (compared to only 1 h of centrifugation needed using this method) [35, 36].

TEM images were collected of the particles after PEGylation in order to ensure no change in the core size and sample dispersity has occurred. Figure 2.10 revealed there was no significant difference in the measured D_{TEM} (5.5 ± 0.7 nm based on the measurement of 200 particles) indicating the BPs do not etch the particle surface which has been shown to occur when using other anchor groups such as mimosine or dopamine derivatives [37, 38]. It is thought that this was due to the stability of complexes formed as a result of the high affinity of some catechols toward Fe^{3+} ions. Furthermore, toxic free radical species have been observed to form at the catechol-iron oxide surfaces [39]. However, it has recently been shown that these adverse effects can be overcome by introducing a strong electron-withdrawing nitro group to the aromatic ring, thus modifying the electronic properties of the anchors [34, 37]. Moreover the monodispersity and spherical shape remained unaffected. It was previously mentioned that a degree of self assembly was observed potentially due to the drying procedure when preparing the TEM grids (figure 2.7), however once the particles are PEGylated, this no longer arises, and the sample remains unclustered. Figure 2.11 shows the phase transfer of the Fe_3O_4 NPs. The vial on the left contains the USPIOs in hexane, and the vial on the right contains the particles in water. This confirms PEG(5)-BP is binding to the surface of the particles.

(a)

(b)
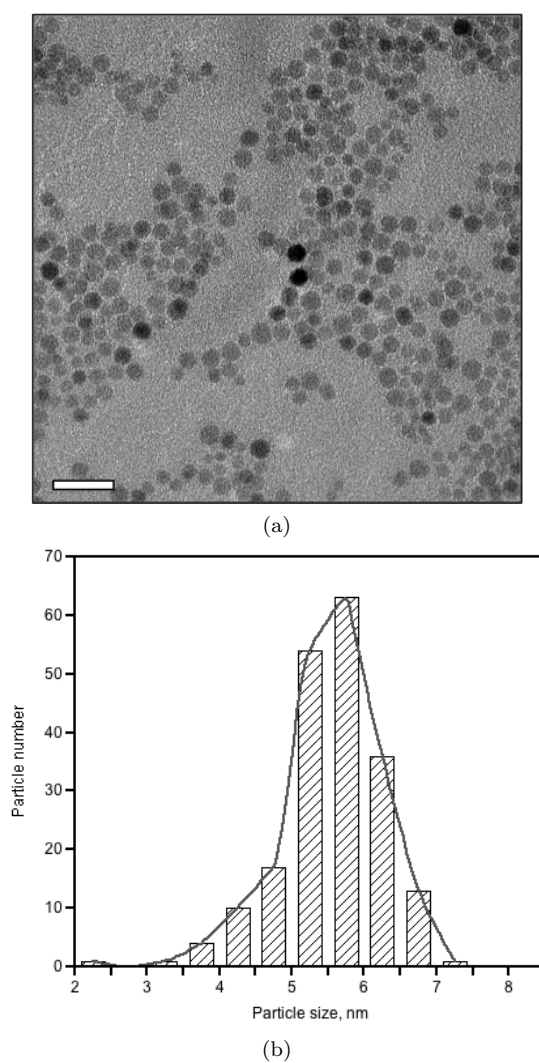
Figure 2.10: Characterisation of PEGylated Fe_3O_4 NPs: (a) TEM micrograph of a dispersion in water phase transferred using the final method ($D_{TEM} = 5.5 \pm 0.7$ nm based on the measurement of 200 particles). Scale bar is 100 nm; (b) Histogram of the diameter distribution of 200 particles.
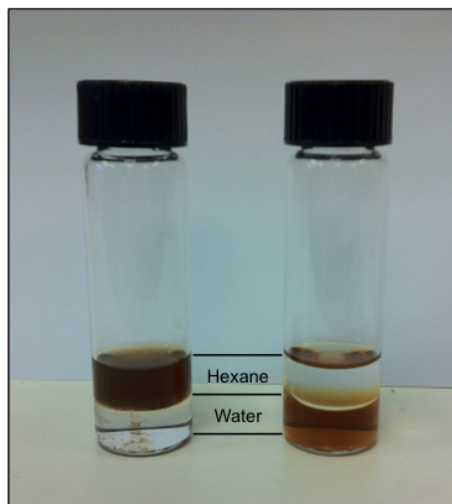
Figure 2.11: Confirmation of PEG-BP binding to the surface of Fe_3O_4 NPs: Phase transfer of a dispersion. The vial on the left contains the particles before PEGylation in hexane (bottom layer is water), and the vial on the right contains the particles after PEGylation in water (top layer is hexane).

It was measured that the average D_H in water after PEGylation was 23.5 ± 6.5 nm (PDI of 0.36), and in saline 23.9 ± 6.4 nm (PDI of 0.36), as shown in figures 2.12a and 2.12b respectively. This was an important result as it demonstrated the stability of the NPs when in the presence of salts which readily come into contact with the USPIO surface in biological environments. This result showed that the particles could still be classified as USPIOs due to the overall diameter remaining below 40 nm.

The size of PEG(5)-BP-USPIO was compared with other reported hydrodynamic diameters of PEG coated Fe_3O_4 NPs (around 50 nm for PEG_{3000} and 60 nm for PEG_{6000} [40]), it could be seen that the hydrodynamic diameter for our PEGylated particles was relatively small. A potential reason for this is that the PEG molecules were not fully extended on the surface of the NPs. An unfolded 5 kDa PEG chain has a length of ∼38 nm, which would result in an overall average particle D_H of 80 nm. Thus, it is believed that the polymers folded to a $^1/_4$ of their extended length forming an expanded coil conformation [41].

The Flory radius, calculated using equation 2.1, is used to describe polymer conformation.

(a)

(b)
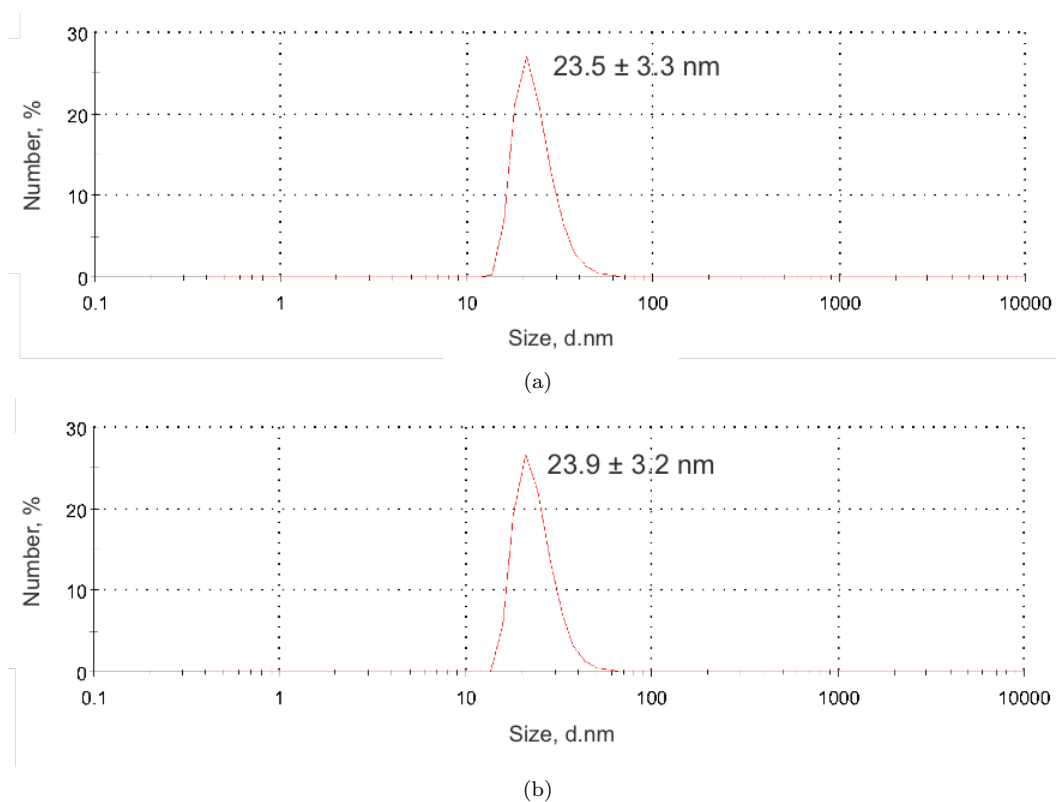
Figure 2.12: Characterisation of PEGylated Fe_3O_4 NPs: DLS number distribution of a dispersion in (a) water ($D_H = 23.5 \pm 6.5$ nm, PDI = 0.36), and (b) saline ($D_H = 23.9 \pm 6.4$ nm, PDI = 0.36).

$$F = \alpha n^{\frac{3}{5}} \tag{2.1}$$

where n = number of monomers per polymer chain

α = length of one monomer (Å)

For PEG_{5000}, $n = 114$ and $\alpha = 3.5$ Å, yielding an F value of 6.0 nm. If the distance between anchors on the surface of the particle is larger than the Flory radius, *i.e.* the packing density is low, then it is expected that the polymers will fold into expanded coils on the particle surface [42]. As this is the polymer conformation implied from the hydrodynamic diameter measured, it suggests there is a low quantity of PEG(5)-BP bound to the USPIO.

2.3.3   Dispersant packing density

By using the amount of non-bound PEG(5)-BP recovered after the synthesis of PEG(5)-BP-USPIO, the PEG(5)-BP packing density on the surface of the USPIOs could be estimated. It should be noted that the below calculations assume the USPIOs were spheres of a fixed diameter of 5.5 nm and were composed of Fe_3O_4.

Calculation of mass of each USPIO and number of Fe atoms/USPIO

The mass of each 5.5 nm USPIO is 4.5 x 10^{-19} g, by using the density of Fe_3O_4 (5.17 g/cm^3).

As the molecular weight of Fe_3O_4 is 232 g/mol, the number of moles can be calculated to be 1.939 x 10^{-21} moles of Fe_3O_4, and the number of Fe_3O_4 units per USPIO is 1.939 x 10^{-21} x N_A = 1168. Hence, the number of Fe atoms/USPIO is 1168 x 3 = 3504 Fe atoms/USPIO.

Calculation of number of PEG molecules bound to USPIOs

Using the mass of the non-bound PEG(5)-BP (obtained from the washings during the purification process following PEGylation) it was found that 2.4 mg of PEG(5)-BP was bound to the USPIOs. Hence, using the average PEG(5)-BP molecular weight value of 5307 g/mol, it was calculated that this corresponds to approximately 2.72 x 10^{17} molecules.

Calculation of number of USPIOs

Method 1. **Using the Fe concentration**

The Fe concentration of the PEG(5)-BP-USPIO dispersion was 26.62 mM (measured using inductively coupled plasma mass spectrometry, ICP-MS) in 300 μL, which corresponds to 7.98 x 10^{-6} moles and 4.81 x 10^{18} Fe atoms. Hence, as it has previously been calculated that there are 3504 Fe atoms/USPIO, it follows that there are 1.37 x 10^{15} USPIOs in total.

Method 2. **Using the thermogravimetric analysis**

From the thermogravimetric analysis (TGA) study (figure 2.13) it could be seen that out of the 2 mg of oleylamine-USPIOs, 19 % corresponds to oleylamine. Hence, 1.6 mg is the weight of the Fe_3O_4 NPs in the oleylamine-USPIOs, and consequently in the PEG(5)-BP-USPIOs (as all USPIOs were capped with PEG(5)-BP and transferred into the aqueous phase). This then corresponds to 3.55 x 10^{15} USPIOs if dividing by the value of 4.5 x 10^{-19} g/USPIO calculated earlier.
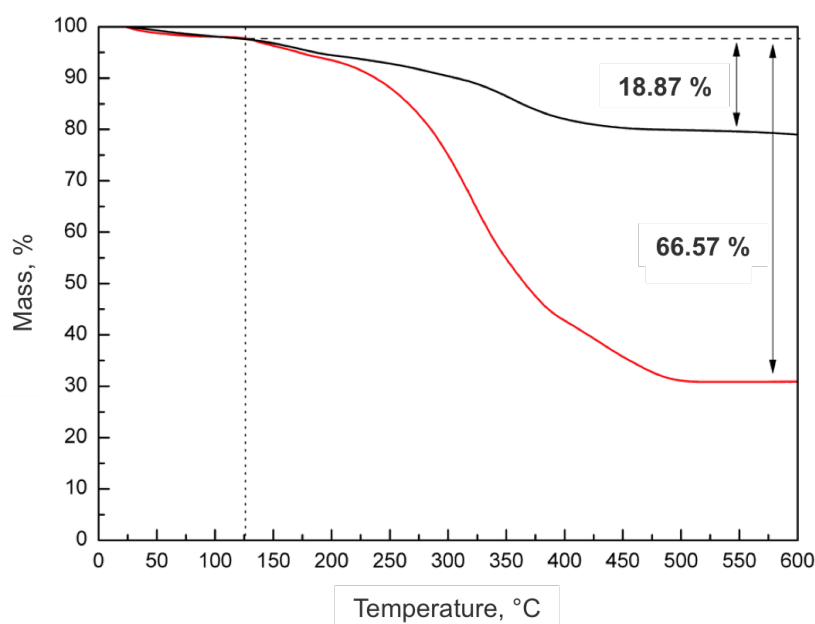
Figure 2.13: TGA study with oleylamine-USPIOs (black line) and PEG(5)-BP-USPIOs (red line). The heating rate was 10 °C/min under a N_2 flow. The vertical line indicates the temperature at which it is considered most of the absorbed water has evaporated (125 °C).

Calculation of number of PEGs/USPIO

Using method 1. 2.72 x 10^{17} PEGs/1.37 x 10^{15} USPIOs = 198 PEGs/USPIO

Using method 2. 2.72 x 10^{17} PEGs/3.6 x 10^{15} USPIOs = 76 PEGs/USPIO

Calculation of theoretical maximum density of BPs/USPIO

The surface area of a 5.5 nm sphere is 95 nm^2 and the footprint of a BP is approximately 0.85 nm^2 (calculated from a computational model using Chem3D, Cambridge Software). Using these values, the theoretical maximum number of BPs that can bind to a 5.5 nm sphere is 112.

Thus, these estimations result in density values that range from 76 to 198 PEGs/USPIO. However, given that the calculations of the theoretical maximum number of BP groups that each 5.5 nm USPIO can accommodate is 112, the true density is likely to be a value in the range between 76 and 112 PEGs/USPIO, which corresponds to a surface density of 68 % to 100 %, or 0.80-1.18 PEGs/nm^2.

TGA measurements (figure 2.13) were carried out to validate these estimations. The results confirm that 67 % of the weight of PEG(5)-BP-USPIO (assuming that the weight loss before 125 °C is due to absorbed water) is due to PEG(5)-BP. This corresponds to 2.68 mg PEG(5)-BP (note that this value is close to the 2.4 mg of non-bound PEG(5)-BP recovered from the reaction). Therefore, it follows that (2.68 x 10^{-3} g/5307 g/mol) x N_A = 304.2 x 10^{15} molecules of PEG(5)-BP. Dividing 304.2 x 10^{15} molecules of PEG(5)-BP by 3.55 x 10^{15} USPIOs obtains the result that each USPIO is bound to 86 PEG(5)-BP molecules, which corresponds to 0.9 PEG/nm^2, using the surface area of a 5.5 nm diameter sphere.

It is important to note that the high density value found is counterintuitive, particularly when the DLS results suggest the PEG chains are likely to be present as folded extended coils that will impact negatively on the density. However, these calculations assume a flat surface area and recent studies have demonstrated that the curvature of USPIOs and other nanomaterials allows for significant higher densities [34]. In addition, sources of error such as the assumption that the particles are homogeneous spheres of 5.5 nm diameter and not taking into account the small variations in diameter/surface areas may also influence the calculations.

This relatively high dispersant packing density may be accounted for by the use of BPs. It has previously been reported by Daou *et al.* that phosphonate coupling agents allow for a higher grafting rate than other common anchors such as carboxylates [43]. It is important to achieve a high density of PEG on the surface of UPSIOs as this inhibits the adsorption

of smaller proteins on to the surface of the particles, which in turn promotes NP clearance [19].

2.4 Further characterisation of polyethylene glycol-coated ultrasmall superparamagnetic iron oxide nanoparticles

2.4.1 Lattice fringe spacing

Further high resolution TEM (HRTEM) was performed in order to determine the interplanar spacing (d) enabling the structure of the iron oxide particles to be confirmed. The images revealed clear lattice fringes indicating a single crystal structure [44] with an average d of 0.261 ± 0.005 nm. This value was slightly higher than the interplanar spacing of bulk magnetite ($d_{311} = 0.2531$ nm; JCPDS file no. 79-0417 [45]), which is most likely explained by the measurement being performed on a different lattice plane as has been observed by several groups [46–48]. Furthermore, it is known that for maghemite (γ-Fe$_2$O$_3$) $d_{311} = 0.2517$ nm (JCPDS file no. 39-1346 [49]), therefore verifying the magnetite nature of the USPIOs.

2.4.2 Zeta potential

The zeta potential (ζ-potential) of the PEGylated Fe$_3$O$_4$ NPs in phosphate buffered saline (PBS) at physiological pH was measured to be -1.24 ± 4.92 mV (figure 2.15) showing that the particles have an approximately neutral surface making them useful for *in vivo* applications. This near zero value is ideal as it has been demonstrated that negative NP surfaces favour uptake by RES macrophages whereas positive NP surfaces result in plasma protein binding, aggregation and uptake in the lungs and liver [50,51]. A near neutral surface charge reduces the protein adsorption process opsonisation and hence prolongs the circulation time of the particles [19].
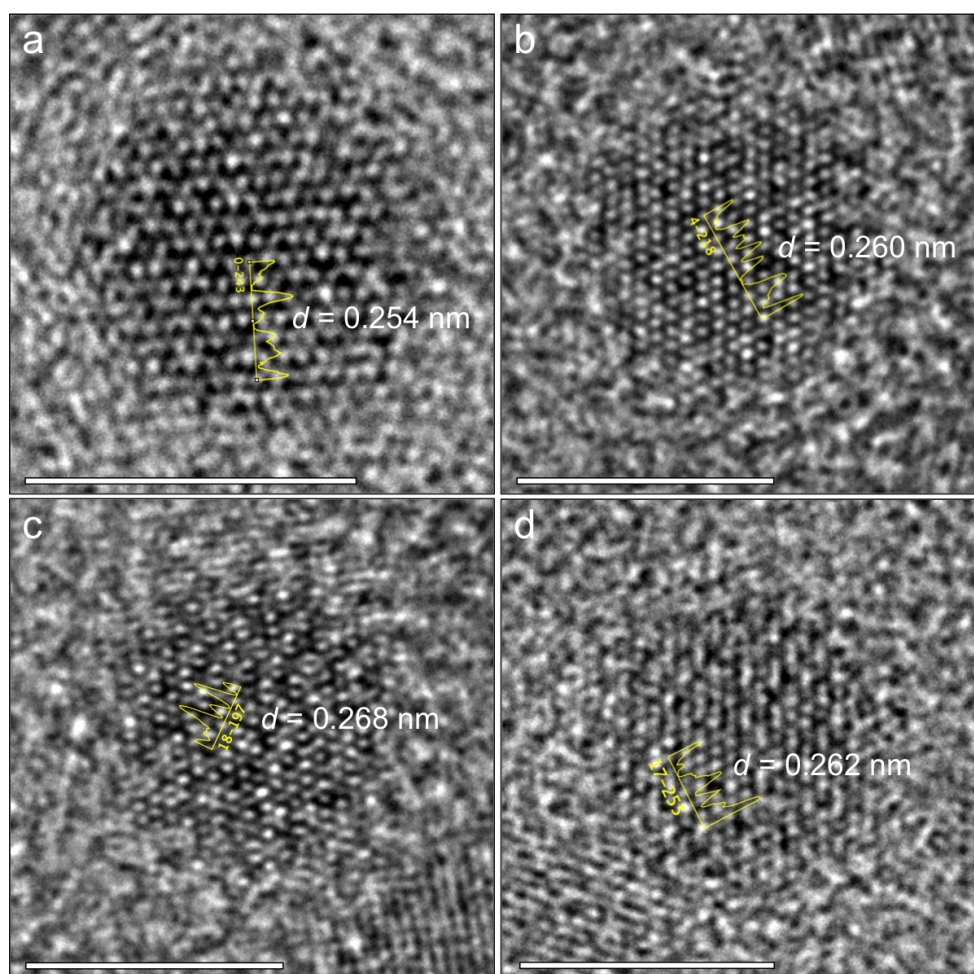
Figure 2.14: Characterisation of PEGylated Fe_3O_4 NPs: HRTEM micrographs of a dispersion in water with (a) $d = 0.254$ nm, (b) $d = 0.260$ nm, (c) $d = 0.268$ nm, and (d) $d = 0.262$ nm. Scale bar is 5 nm.
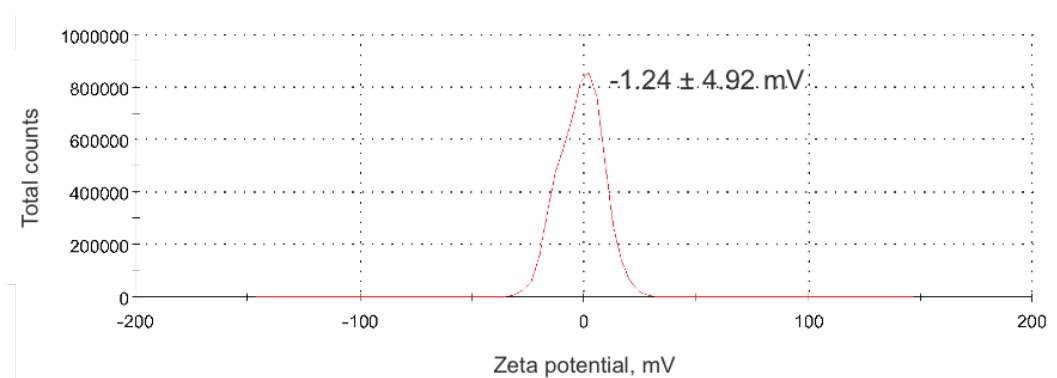
Figure 2.15: Characterisation of PEGylated Fe_3O_4 NPs: Zeta potential distribution of a dispersion in PBS at pH 7.4 (ζ-potential $= -1.24 \pm 4.92$ mV).

2.4.3 Energy-dispersive X-ray spectroscopy

Several techniques were performed in order to confirm that PEG(5)-BP was bound to the surface of the particles, and that all oleylamine had been removed after purification. The first approach was to run energy-dispersive X-ray spectroscopy (EDX) on the PEGylated sample of particles, figure 2.16. The peak representing phosphorus was present in the TEM of the specimen indicating the presence of the BP group.
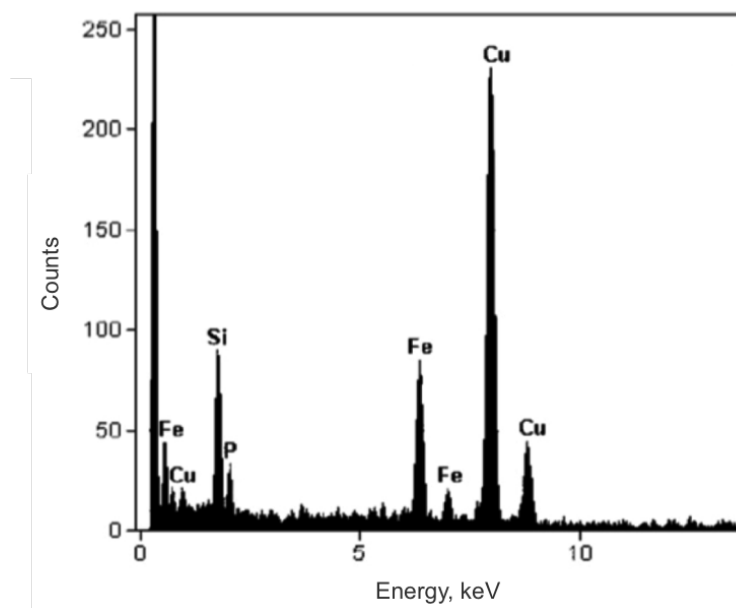
Figure 2.16: Characterisation of PEGylated Fe_3O_4 NPs: EDX spectrum showing presence of iron and phosphorus in PEGylated NP sample.

2.4.4 Infra-red spectroscopy

Infra-red spectroscopy was the second technique used to ensure that the ligand exchange during phase transfer was successful. Figure 2.17 shows the IR spectra of PEG(5)-BP and of the PEGylated NPs. It can be seen there are peaks corresponding to the PEG present in the sample of particles. Vibrations due to the Fe-O bonds in Fe_3O_4 occur around 591 cm^{-1} and hence are not shown in figure 2.17. Sharp peaks are present around 2850 cm^{-1} on all three spectra. On figure 2.17a this represents the C–H bond stretching in oleylamine, whereas on figures 2.17b and 2.17c it is due to the C–H stretching of PEG. The broad peak in the region of 3400 cm^{-1} is assigned to stretching vibrations of N–H bonds and O–H stretching of adsorbed water. Bending vibrations of N–H and C–H are represented by the bands in

the range of 1385 cm^{-1} to 1610 cm^{-1} [52,53]. Confirmation of the success of PEGylation is given by the presence of characteristic PEG vibrations: (ν(C–O) + ρ(–CH$_2$–) = 1096 cm^{-1}; ρ(–CH$_2$–) + τ(–CH$_2$–) = 946 cm^{-1}; τ(–CH$_2$–) + ν(C–O) = 841 cm^{-1}) in the spectrum of PEG(5)-BP-USPIO (figure 2.17c) [54].
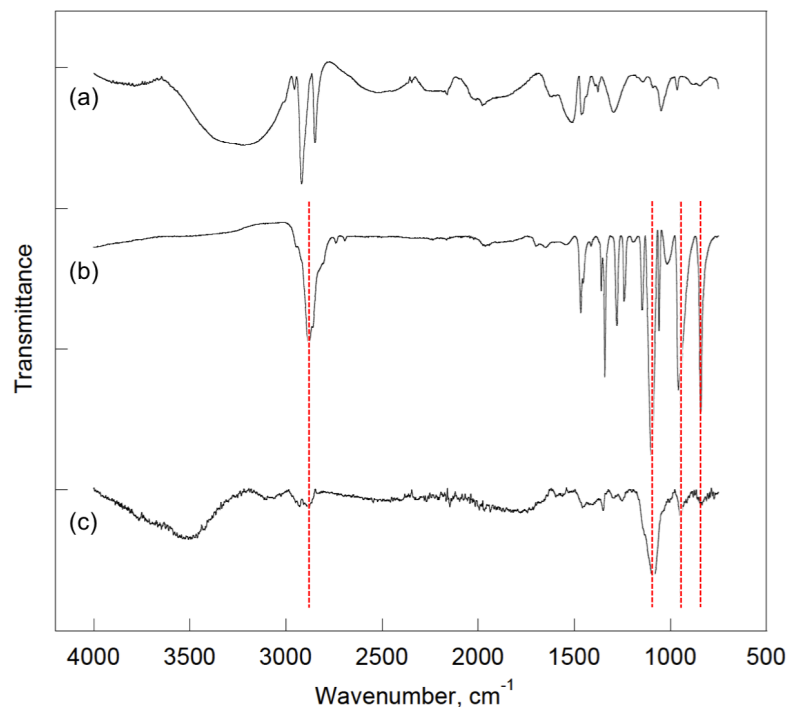
Figure 2.17: Characterisation of PEGylated Fe$_3$O$_4$ NPs: (a) IR spectrum of oleylamine coated NPs; (b) IR spectrum of PEG(5)-BP only; (c) IR spectrum of PEG(5)-BP coated NPs. Drop lines indicate vibrations associated with PEG (ν(C–H) = 2850 cm^{-1}; (ν(C–O) + ρ(–CH$_2$–) = 1096 cm^{-1}; ρ(–CH$_2$–) + τ(–CH$_2$–) = 946 cm^{-1}; τ(–CH$_2$–) + ν(C–O) = 841 cm^{-1}).

Although this result demonstrates PEGylation of the USPIOs has been achieved, it does not confirm complete oleylamine removal. This is despite the high PEG densities accomplished (76 %, *vide supra*) which strongly suggest that at least most oleylamine has been displaced from the dispersion. The expected shift of –PO$_3$ vibrations upon metal binding was not observed due to the overlap with the more intense signals from the PEG methylene groups.

2.4.5 X-ray diffraction

X-ray diffraction studies were used to identify the presence of PEG(5)-BP in the sample after purification, in addition to confirming the removal of oleylamine. Figure 2.18 shows

the characteristic peaks due to iron oxide (30.095 °, 35.422 °, 56.942 ° and 62.525 °; JCPDS file no. 19-0629) [55] as well as PEG(5)-BP (19.2 ° and 23.3 °) [56, 57], which is probably the result of its high density and ordered structure near the surface of the USPIOs.

XRD can also be used to estimate the mean diameter (τ) of the particles using the Scherrer equation (equation 2.2). It was chosen to calculate the average NP size along the (311) direction as this peak did not overlap with any others and measuring the width at half height was simple. The particle size was calculated to be 7.2 nm from the oleylamine-USPIOs curve and 7.1 nm from the PEG(5)-BP-USPIOs curve, as shown in the inset of figure 2.18. These estimations are larger than those indicated by TEM which is due to crystal size not being the only factor contributing to the broadening of diffraction peaks [58].

$$\tau = \frac{K\lambda}{\beta \cos\theta} = \frac{K\lambda}{(b - b_0)\cos\theta} \tag{2.2}$$

where K = shape factor, typically taken to be 0.9

λ = X-ray wavelength (Å)

β = line broadening a half the maximum intensity (rad)

θ = Bragg angle (°)

b = full width at half maximum (FWHM) of the NPs (rad)

b_0 = FWHM of the standard crystal (rad)

Even though this XRD pattern indicated our sample consisted of Fe_3O_4, the structure of γ-Fe_2O_3 gives some similar peaks with comparable intensities, namely at 30.272 °, 35.597 °, 57.166 ° and 62.726 ° (JCPDS file no. 04-0755) [55], making distinguishing between the two difficult. Although there are three additional peaks for γ-Fe_2O_3 (23.836 °, 32.172 ° and 38.783 °; JCPDS file no. 04-0755) [55] due to their low intensities, identification of these peaks is challenging.

2.4.6   X-ray photoelectron spectroscopy

X-ray photoelectron spectroscopy (XPS) was the final technique used to confirm the presence of PEG(5)-BP in the PEGylated NP sample. The full spectrum is given in figure 2.19a and displays dominant C1s (282.2 eV, 283.5 eV and 286.2 eV, figure 2.19b) and O1s (529.7 eV,
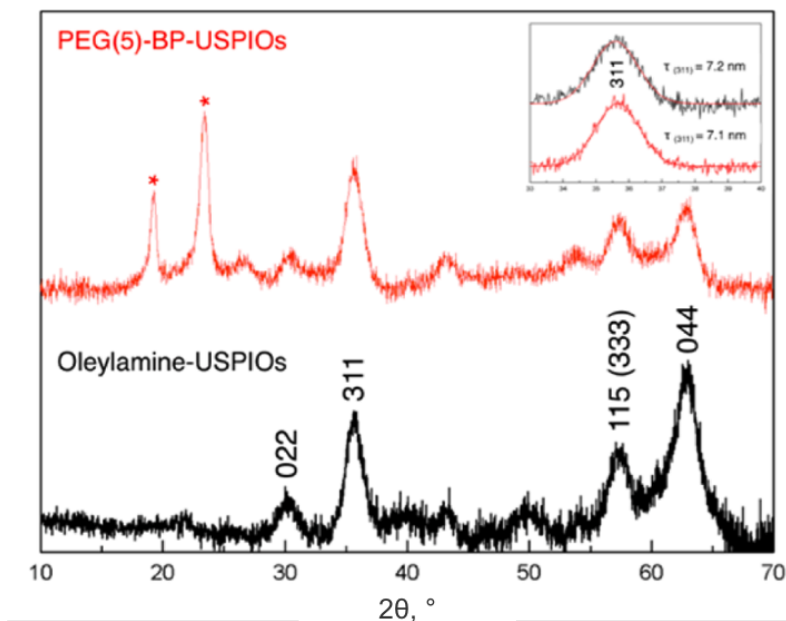
Figure 2.18: Characterisation of PEGylated Fe$_3$O$_4$ NPs: XRD patterns of oleylamine coated USPIOs (bottom, black) and PEGylated USPIOs (top, red). The peaks corresponding to PEG(5)-BP have been labeled with an asterix. The inset shows the peak corresponding to the (311) plane and its mean size ($\tau_{(311)}$).

figure 2.19c) signals from the PEG chain and carbon dioxide adsorbed on the USPIO surface. Additionally, the detectable P2p$_{3/2}$ peak (129.7 eV, figure 2.19e) arising from the BP group further confirms the presence of the PEG(5)-BP. Furthermore, iron displayed a signal at 708 eV (figure 2.19d). The weak signal of the iron and phosphorus was due to the coverage of the PEG chain and the low abundance of P [59, 60]. Similar signals have been observed with other metallic surface-bound bis- and monophosphonates [61, 62].

The combination of EDX, IR, XRD and XPS spectroscopies proved the presence of the PEG(5)-BP on the surface of the USPIO after purification, was well as the removal of the majority, if not all, of the oleylamine. The next step in the analysis of the PEGylated USPIOs was to characterise the magnetic properties.

2.4.7 Magnetic properties

The magnetic properties of both oleylamine coated and PEGylated USPIOs were investigated at 300 K using a SQUID-VSM instrument (figure 2.20) in order to identify any effect of the ligand exchange on the magnetisation of the particles.
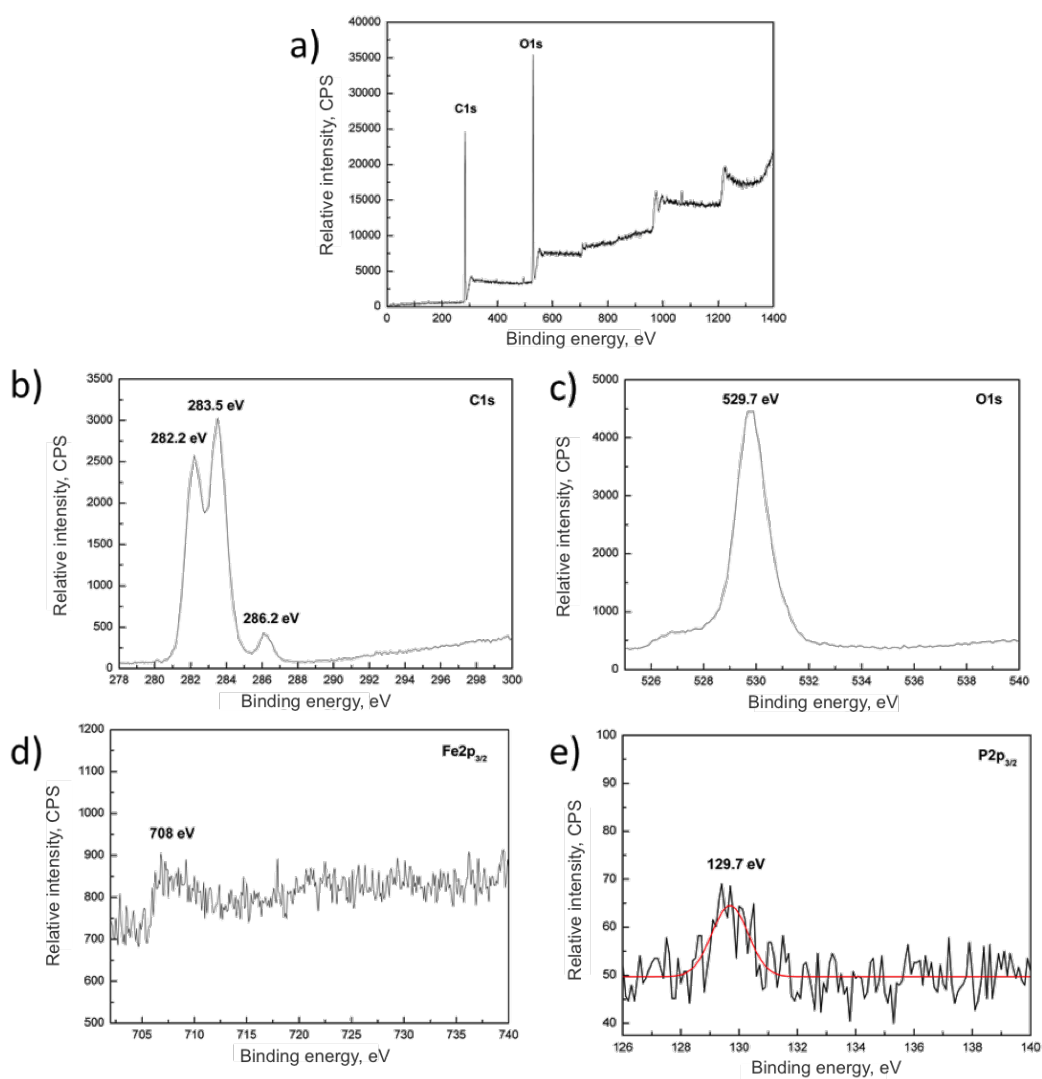
Figure 2.19: Characterisation of PEGylated Fe$_3$O$_4$ NPs: (a) XPS spectrum of PEG(5)-BP coated USPIOs (dominant C1s and O1s displayed); (b) XPS spectrum of carbon (282.2 eV, 283.5 eV and 286.2 eV); (c) XPS spectrum of oxygen (529.7 eV); (d) XPS spectrum of iron (708 eV); (e) XPS spectrum of phosphorus (129.7 eV).
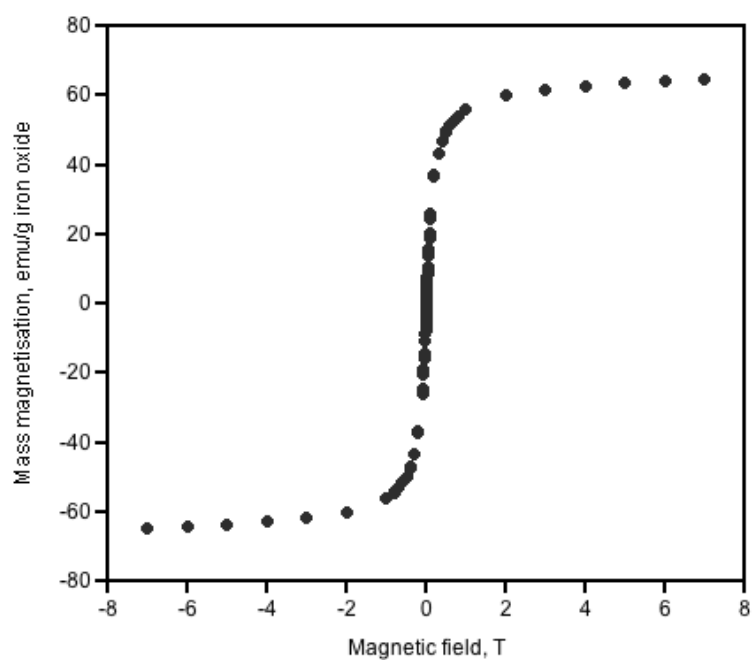
(a)
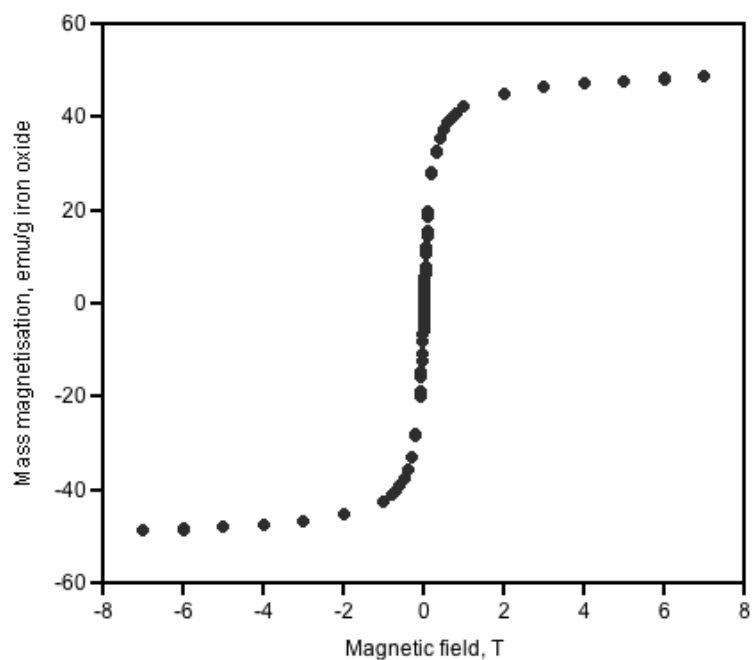
(b)

Figure 2.20: Characterisation of oleylamine coated and PEGylated Fe_3O_4 NPs: (a) Magnetisation at several magnetic fields at 300 K for oleylamine coated USPIOs ($M_S = 65$ emu/g); (b) Magnetisation at several magnetic fields at 300 K for PEG(5)-BP-USPIOs ($M_S = 51$ emu/g). The weight of iron oxide was calculated by subtracting the mass of oleylamine and PEG as calculatedly TGA.

The profiles of both samples clearly demonstrate superparamagnetic behaviour. Before and after PEGylation, the mass magnetisation at saturation was found to be 65 emu/g iron oxide and 51 emu/g iron oxide respectively, as calculated using a Langevin fit. The weight of iron oxide was calculated by subtracting the mass of oleylamine/PEG as calculated by TGA. Both these values are relatively low compared to that of bulk iron oxide (maghemite (γ-Fe$_2$O$_3$, bulk M_S = 74 emu/g) and magnetite (Fe$_3$O$_4$, bulk M_S = 98)), and are consistent with that found with other USPIOs of a similar size [35]. There are two potential reasons as to why the PEG coating has reduced the M_S. Firstly, the functionalisation with the bisphosphonate group may have had an effect. However, it has been stated previously that although this is may be the case for carboxylate molecules, the same is not observed for phosphonate groups [63]. Therefore the second explanation of errors in both the weight measured and the results from TGA analysis are deemed more likely.

2.4.8 Stability studies

In order to ensure the PEGylated NPs did not degrade once in dispersion, studies were performed over time, temperature and washings to explore any change in the hydrodynamic diameter. Several observations confirm the high colloidal stability of the BP-coated USPIOs. Firstly, DLS of the NPs dispersed in both water and saline was performed once again several months later in order to check the stability of the particles over time. It was observed that the particles had a slightly smaller D_H of 21.0 ± 3.0 nm and 22.7 ± 3.0 nm respectively (decrease of 2.5 nm and 1.1 nm). These studies demonstrate that the hydrodynamic diameter of the PEG(5)-BP-USPIOs stored in water or saline for at least 6 months remains unchanged, with no aggregates forming during this time.

Secondly, heating dispersions of PEG(5)-BP-USPIOs in saline to 90 °C for 10 min and at 50 °C for 4 h, figure 2.21, resulted in no change in D_H or aggregation. It is important to note that for the stability study at 50 °C, a different batch of PEG(5)-BP-USPIOs with a slightly larger hydrodynamic diameter was used.

An additional indication of the stability of the PEGylated USPIOs was given by the number of washings that could be performed with large volumes of saline and water using 30 kDa molecular weight cut-off (MWCO) filters without changes in D_H (>8 times). In contrast, USPIOs PEGylated using a PEG(5)-COOH (phase transferred using the same method as
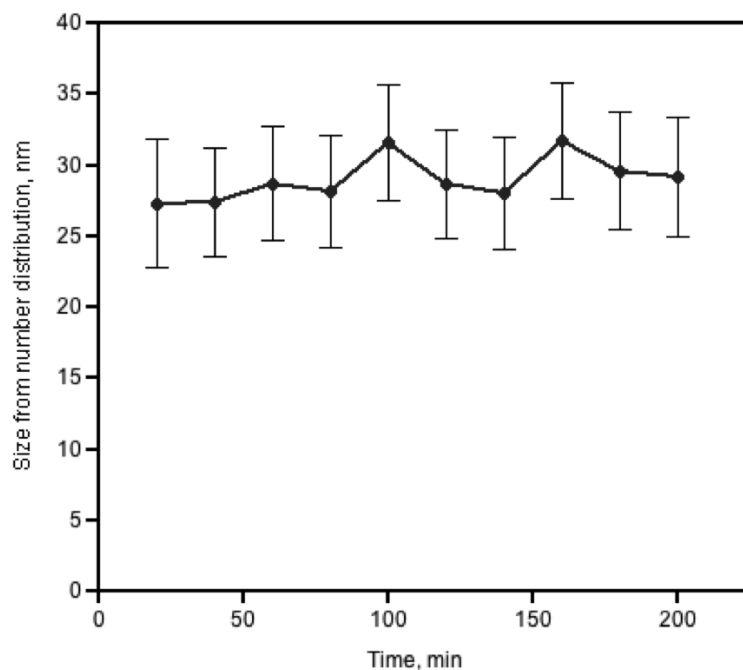
Figure 2.21: Stability of PEGylated Fe$_3$O$_4$ NPs: Temperature stability study over 4 h at 50 °C in saline (note a different batch of PEG(5)-BP-USPIOs with slightly larger D_{H} was used for this study).

with PEG(5)-BP) aggregated entirely after four washings. This aggregation occurred due to the PEG molecules being removed from the retentate containing the particle dispersion into the filtrate after desorption. Hence, inducing the formation of agglomerates. This method has been previously used to evaluate the binding reversibility of several PEG coatings on SPIOs by Amstad *et al*. It was reported that with PEG-COOH and weakly bound PEG-catechols, aggregation occurred between the first and fourth filtration [34]. However, the consistent D_{H} after four filtrations with strongly bound catechol-PEG conjugates indicated irreversible binding. Furthermore, the hydrodynamic diameter of PEG(5)-BP-USPIOs remained constant after repeating the process at various time points during several months. The possibility that the PEG polymer may be binding nonspecifically to the alkyl chains, a method that has been successfully used with other systems [64], is also proved to be unlikely by the lack of binding and stabilisation properties of PEG-COOH to oleylamine USPIOs.

In order for the particles to be useful for *in vivo* imaging, stability in 10 % human serum at 37 °C also had to be confirmed. PEG(5)-BP-USPIOs were incubated for 0 h, 1 h, 24 h, and 48 h and DLS measurements were performed, showing no change in D_{H}. It is important to note that for this stability study a different batch of PEG(5)-BP-USPIOs with a slightly

smaller hydrodynamic diameter was used. This result not only supports the stability of the BP-iron oxide bond, but also indicates that blood serum proteins do not adsorb to the nanoparticle surface. This is believed to be a consequence of a compact and stable PEG coating and the neutral zeta potential achieved.

2.4.9 Comparison with FeraSpin XS

A comparison against a commercially-available preclinical iron oxide nanoparticle, FeraSpin XS (Miltenyi Biotech GmbH), was run. This was chosen as a standard as FeraSpin XS has been designed for use in the *in vivo* MRI of small animals. FeraSpin XS consists of ultra-small superparamagnetic iron oxide nanoparticles coated with carboxydextran (D_{TEM} of 5 nm and D_{H} of 18 nm) which is used to visualise vasculature and to measure steady state blood volume [65]. Figure 2.22 reveals large aggregates of particles, again this is most likely due to drying procedures used in preparation of the TEM grids.
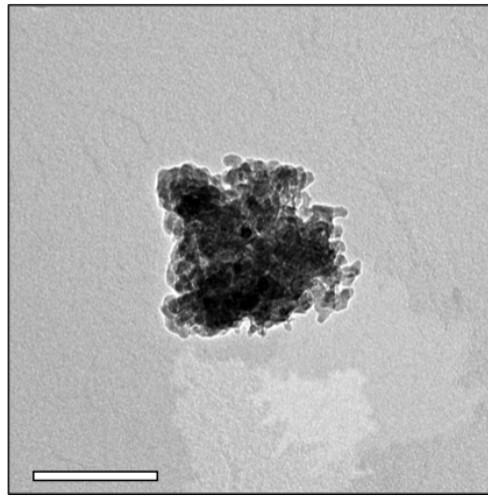
Figure 2.22: Characterisation of FeraSpin XS: TEM micrograph of a dispersion in water ($D_{\text{TEM}} = 5$ nm, $D_{\text{H}} = 18$ nm as given by Miltenyi Biotech GmbH). Scale bar is 200 nm.

In addition, magnetic measurements were acquired and the M_{S} calculated, again using a Langevin fit. This was done in collaboration with Professor Yves Gossuin's group in Biomedical Physics at the University of Mons. Figure 2.23 shows the original experimental measurements (performed on aqueous solutions of USPIOs) alongside data which has been corrected for diamagnetism, a non negligible contribution from water [66]. It was found that the M_{S} is slightly higher than for the PEG(5)-BP-USPIOs at 71.9 emu/g. From this fit, it was also possible to calculate the average particle size (D_{M}). This was found to be 8.2 nm,

somewhat larger than stated by the manufacturers. The most feasible explanation for this is errors in the iron concentration measurement (which was made using ICP-MS) as well as the assumption made during the Langevin fit that the sample is monodispersed, resulting in an over estimation of the particle size.
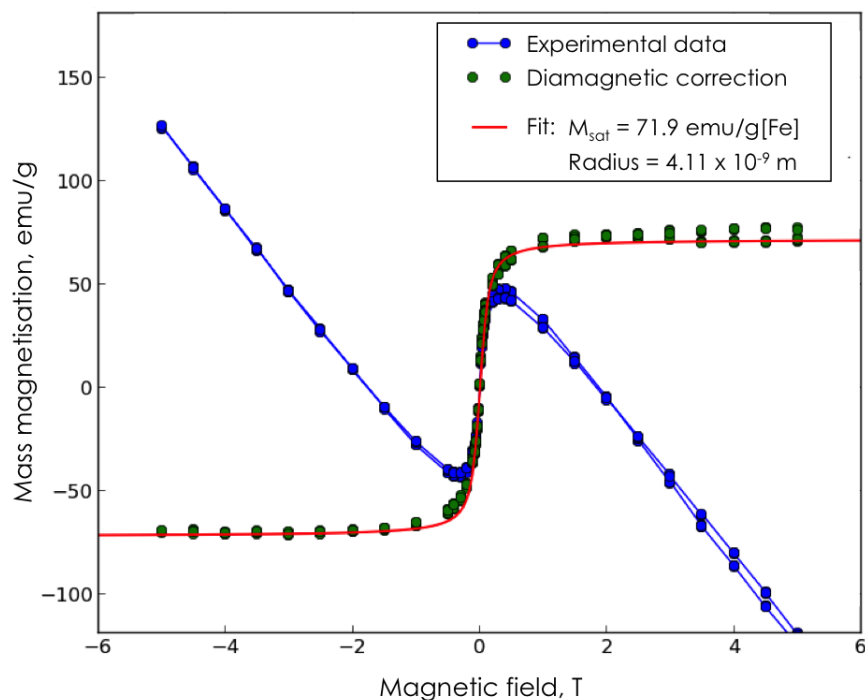
Figure 2.23: Characterisation of FeraSpin XS: Magnetisation at several magnetic fields at 300 K for carboxydextran coated USPIOs (M_S = 71.9 emu/g).

Once the PEG(5)-BP-USPIOs had been fully characterised and FeraSpin XS partially, the next stage was to ascertain the MRI properties of the particles.

2.5 Relaxivity measurements

Experiments were performed in order to investigate the effect of different parameters on the relaxivity values of the water soluble iron oxide.

2.5.1 Changing concentration

The initial parameter explored was the Fe concentration of the sample. Three concentrations were measured at both 0.47 T and 1.41 T. The iron concentrations studied were 0.5 mM,

0.75 mM and 1 mM, which again were measured using ICP-MS.
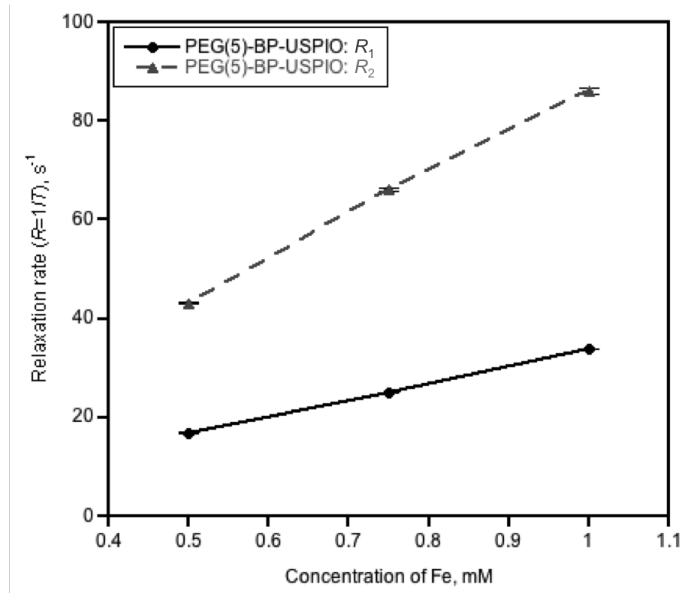
(a)
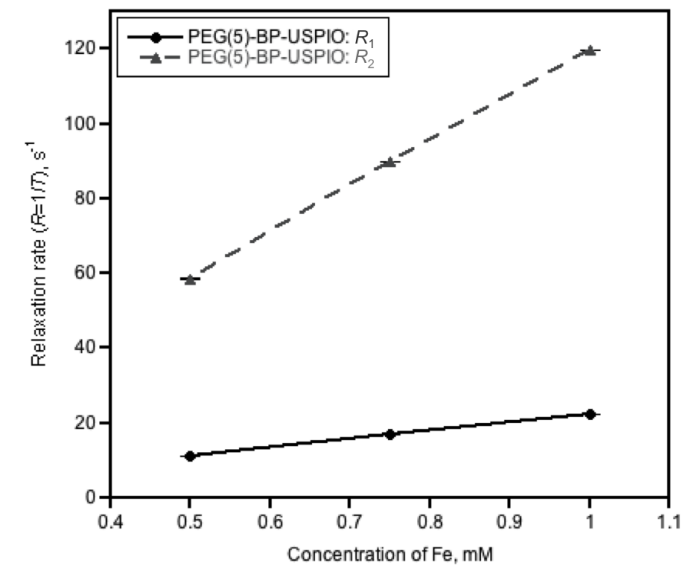
(b)

Figure 2.24: Relaxivity characterisation of PEGylated Fe_3O_4 NPs: Variation of spin-lattice relaxation rate (R_1; solid black line) and spin-spin relaxation rate (R_2; dashed grey line) with concentration for PEG(5)-BP-USPIOs at (a) 0.47 T, and (b) 1.41 T.

The general expression defining the ability of a contrast agent to adjust proton relaxation times is given by equation 2.3 [67].

$$R_{1,2} = R_{1,2}^0 + r_{1,2} \cdot C \tag{2.3}$$

where $R_{1,2}$ = proton relaxation rate in the presence of the contrast agent (s^{-1})

$R_{1,2}^0$ = proton relaxation rate in the absence of the contrast agent (s^{-1})

$r_{1,2}$ = contrast agent relaxivity $(\text{s}^{-1}\text{mM}^{-1})$

C = contrast agent concentration (mM)

It can be seen from the above equation that as the concentration of the contrast agent is increased, there is a direct increase in the proton relaxation rate. Figure 2.24 displays this linear relationship for R_1 and R_2 for both samples.

2.5.2   Changing temperature

The next factor to be investigated was temperature, and the sample (with an iron concentration of 0.5 mM) was measured at 26 °C and 37 °C at 0.66 T in order to observe the effect on the R_1 and R_2 relaxation rates.

Figure 2.25 clearly shows a decrease in the relaxation rate (both longitudinal and transverse) with increasing temperature. Kawaguchi *et al.* suggest that this decrease can be attributed to the increase in motion, and hence an increase in the translation diffusion, of the neighbouring water molecules [68]. It is well established that the superparamagnetic particle effect on relaxation arises from water molecule diffusion in the vicinity of the core [69–71] (more detail is given on page 24 of the introduction).

2.5.3   Longitudinal nuclear magnetic relaxation dispersion profiles

Longitudinal nuclear magnetic relaxation dispersion (NMRD) profiles allow the dependence of the spin-lattice relaxation rate on magnetic field strength to be investigated in detail over a short range of low field strengths. In this case, up to 40 MHz. The concentration used was 2 mM and the measurement was taken at both 25 °C and 37 °C to reconfirm the effect of temperature as seen above.
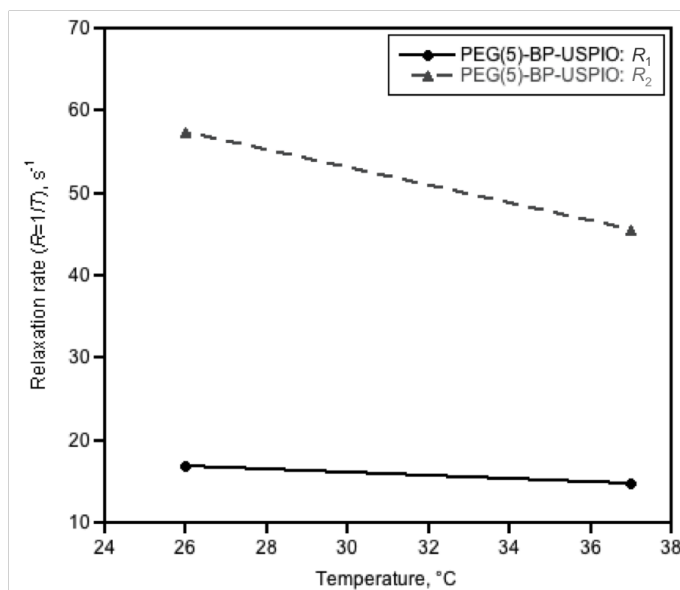
Figure 2.25: Relaxivity characterisation of PEGylated Fe_3O_4 NPs: Variation of spin-lattice relaxation rate (R_1; solid black line) and spin-spin relaxation rate (R_2; dashed grey line) with temperature for PEG(5)-BP-USPIOs.
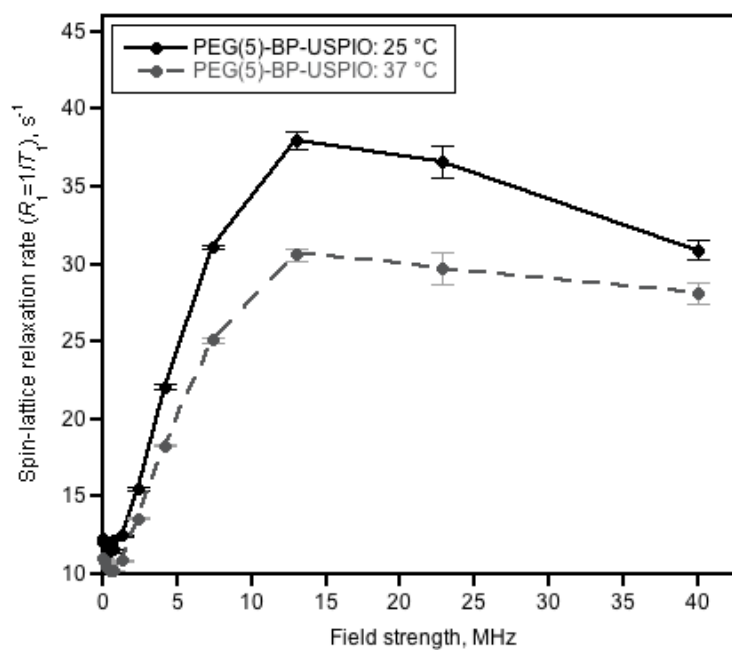
Figure 2.26: Relaxivity characterisation of PEGylated Fe_3O_4 NPs: NMRD profiles of PEG(5)-BP-USPIOs at 25 °C (solid black line) and 37 °C (dashed grey line).

It was found that increasing the field strength led to an initial increase in the spin-lattice relaxation rate for both samples, but was followed by a decrease once the field had reached $\sim$0.47 T (as shown in figure 2.26). This correlates to a statement by Gossuin *et al.* which reports that once the magnetic field strength is large enough, the longitudinal relaxation rate drops to near zero [72]. The explanation for this is complex as the spin-lattice relaxation is dependent on several parameters, one of which is the Néel relaxation time. Other factors affecting the R_1 of a nanoparticle include the core size of the particle, aggregation, and the saturation magnetisation [72]. Again, the same effect of change in temperature was observed as described above.

2.5.4   Changing field strength

The dependence of both the longitudinal and transverse relaxation rates on magnetic field strength were then studied. In this case a larger range of field strengths were investigated: 0.47 T, 0.66 T, 0.92 T, 1.41 T and 7.04 T. All measurements were taken with an iron concentration of 0.5 mM and at a temperature of 37 °C in order to replicate the physiological conditions as much as possible.

Due to the larger field strengths examined, it was clear to see the spin-lattice relaxation rate dropped to zero as expected, figure 2.27a. The general trend of the spin-spin relaxation rates was observed to increase as the magnetic field strength was raised until approximately 6 T where the data appears to plateau, figure 2.27b. This can simply be accounted for by the NP magnetisation increasing from zero to the saturation value [72]. This correlates to the general form of the Langevin function.

Both the spin-lattice and spin-spin relaxation trends that have been observed here have also been noted elsewhere with USPIOs. For example, a significant decrease in r_1 of 15.5 s^{-1}mM^{-1} to 6.6 s^{-1}mM^{-1} (1.5 T and 3 T respectively) with r_2 remaining constant has been reported for Sinerem, dextran coated USPIOs intended for use in detection of metastasis in lymph nodes (Guerbet Group) [73, 74]. Note $r_{1,2}$ is the relaxation rate per mM concentration.
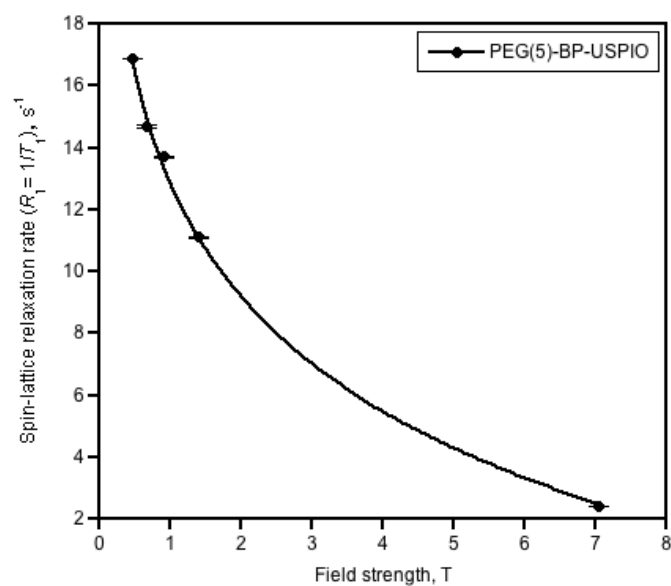
(a)
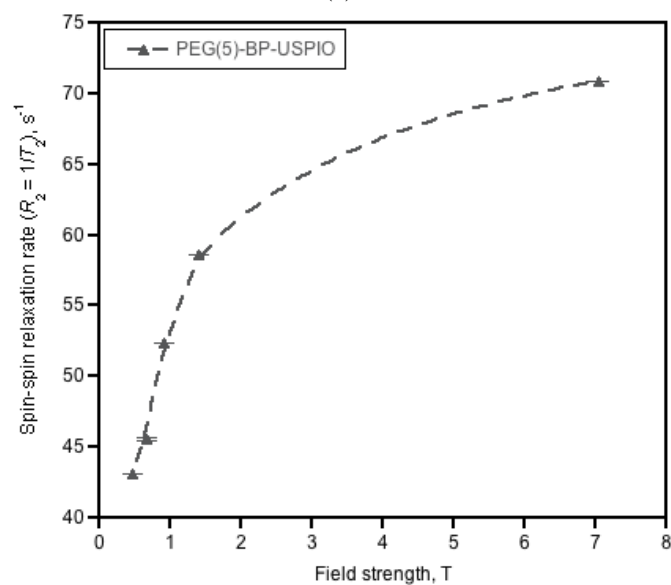
(b)

Figure 2.27: Relaxivity characterisation of PEGylated Fe_3O_4 NPs: Variation of spin-lattice relaxation rate (R_1; solid black line) and spin-spin relaxation rate (R_2; dashed grey line) with magnetic field strength for PEG(5)-BP-USPIOs.

2.5.5 Phantom studies

Phantom studies were then conducted in order to determine the r_1 and r_2 values of the particles. A phantom is a specially designed object that is imaged to allow for analysis and evaluation of various imaging devices. In this case, five vials of PEG(5)-BP-USPIO containing varying concentrations of Fe and one of water were prepared. The longitudinal and transverse relaxivities of the PEGylated USPIOs were then measured at 3 T in order to evaluate at a clinically relevant field. As a result of their improved image resolutions, 3 T MRI scanners are increasingly becoming available in clinics, hence there is an interest of developing USPIOs that retain high T_1 effects at these field strengths. Figure 2.28 shows the Fe concentration against the calculated relaxation rates allowing the r_1 and r_2 to be determined from the gradients. It was found that the particles have an r_1 of 9.5 s^{-1}mM^{-1}, an r_2 of 19.7 s^{-1}mM^{-1} and hence an overall r_2/r_1 of 2.1. For superparamagnetic materials, the higher the r_1 and lower the r_2/r_1 ratio, the more effective the contrast agent will be for use in T_1-weighted imaging. On the other hand, for T_2-weighted imaging high r_2 values and a higher r_2/r_1 ratio is desirable. The substantial T_1 and low T_2 effect induced by the PEG(5)-BP-USPIO was then confirmed by MR imaging of the same phantom samples (figure 2.29).

The values obtained as well as those reported in the literature for other USPIOs at 3 T are listed in table 2.2. This shows that PEG(5)-BP-USPIOs have optimal properties for efficient T_1 contrast, and compare very favourably with other USPIOs approved for clinical use measured under similar conditions. It is thought the strong T_1 effect of the PEG(5)-BP-USPIOs at 3 T is the result of (1) small diameter NP cores of superparamagnetic iron oxide that are known to yield USPIOs with low M_S values and strong T_1 effects [32,35,75,76], (2) a coating composed of two hydrophilic components, PEG and BP, that facilitate diffusion of water molecules to reach the iron oxide surface and allow the relaxation of their protons, and (3) a stable and compact PEG coating, provided by the strong BP-iron oxide bond, that prevents aggregation that would increase r_2 and hence the r_2/r_1 ratio.
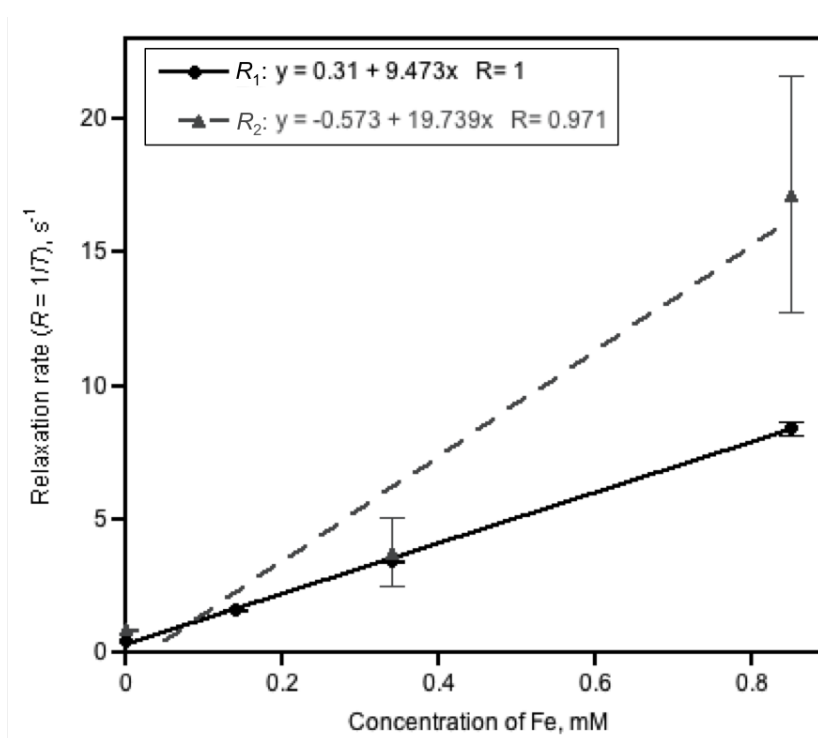
Figure 2.28: *In vitro* MRI studies of PEGylated Fe_3O_4 NPs: Relaxation rates ($R=1/T$) of PEG(5)-BP-USPIOs as a function of Fe concentration at 3 T (r_1 of 9.5 $s^{-1}mM^{-1}$, solid black line, and r_2 of 19.7 $s^{-1}mM^{-1}$, dashed grey line).
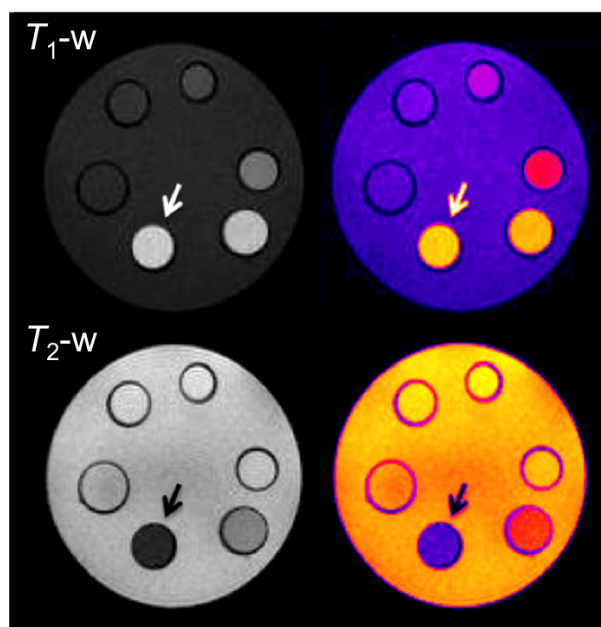
Figure 2.29: Characterisation of PEGylated Fe_3O_4 NPs: MR images of PEG(5)-BP-USPIO phantom showing concentration-dependent effect in T_1- and T_2-weighted sequences. The vial containing the highest Fe concentration (5.3 mM) is indicated by the arrow with concentration decreasing anti-clockwise, the last vial contains water only.

USPIO	D_{TEM}, nm	D_{H}, nm	Coating	r_1, s^{-1}mM^{-1}	r_2, s^{-1}mM^{-1}	r_2/r_1	Medium	T, °C
PEG(5)-BP-USPIOs	5.5	23	PEG-BP	9.5	28.2	2.97	H$_2$O	RT
ESION [35]	2.2	-	PEG-PO	4.8	17.5	3.65	H$_2$O	-
VSOP-C184 [77]	8.6	19	Citrate	8.0	34.0	4.25	H$_2$O	37
ESION [35]	3	15	PEG-PO	4.8	29.2	6.08	H$_2$O	-
Ferucarbotran (Supravist) [78, 79]	3-5	21	Carboxydextran	7.3	57.0	7.81	H$_2$O	37
Ferumoxytol (C7228) [77]	6.7	35	Carboxymethyldextran	7.5	92.0	12.27	H$_2$O	37
Ferumoxtran (Sinerem) [73, 74]	4.5	34	Dextran & citrate	5.0	66.0	13.20	H$_2$O	37
ESION [35]	12	-	PEG-PO	2.4	58.8	24.50	H$_2$O	-

Table 2.2: USPIOs and corresponding nanoparticle size by TEM, DLS, nature of the coating and relaxation properties at 3 T. The entries have been ordered by increasing r_2/r_1.

2.5.6 Comparison with FeraSpin XS

The phantom study was then repeated for the pre-clinical contrast agent, FeraSpin XS. The study yielded a r_1 of 5.4 s^{-1}mM^{-1}, a r_2 of 35.9 s^{-1}mM^{-1}, and hence a r_2/r_1 of 6.6, exhibiting a significant decrease in the T_1-weighted imaging properties. This result was promising as FeraSpin XS has been designed to increase the T_1 effect and have a longer blood half life in contrast to other USPIOs.
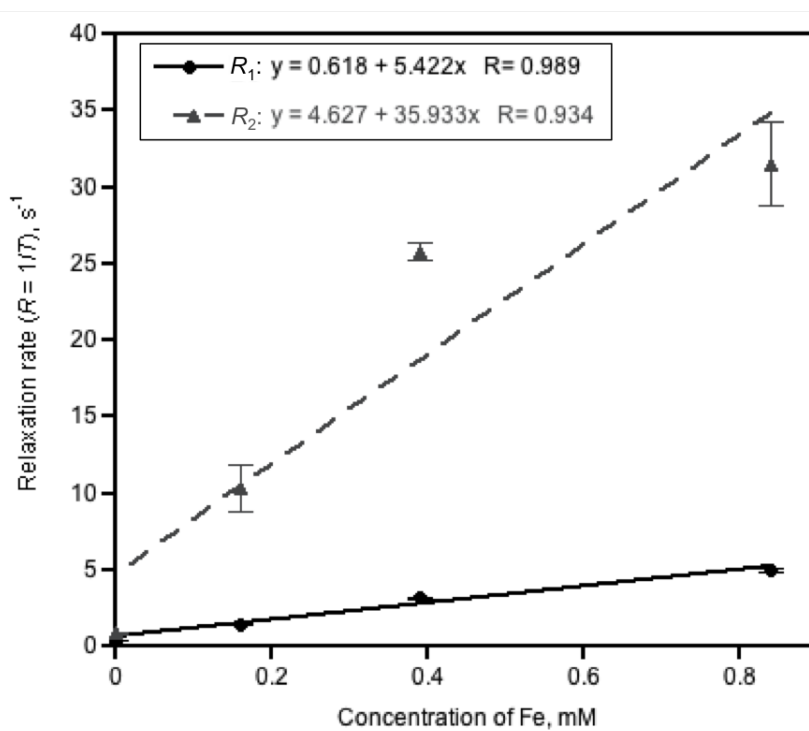
Figure 2.30: *In vitro* MRI studies of FeraSpin XS: Relaxation rates ($R=1/T$) of carboxy-dextran coated USPIOs as a function of Fe concentration at 3 T (r_1 of 5.4 s^{-1}mM^{-1}, solid black line, and r_2 of 35.9 s^{-1}mM^{-1}, dashed grey line).

2.6 Radiolabelling

To radiolabel the Fe$_3$O$_4$ NPs, the bisphosphonate dipicolylamine-alendronate (DPA-ale; figure 2.31) was conjugated to the gamma-emitting isotope ^{99m}Tc which bound to the particle surface. Recent studies in the group have shown that BPs can be used to successfully radio-label the metal ions on the surface of iron oxide nanoparticles with PET or SPECT isotopes without affecting their coatings or surface properties [80,81]. The reason for this is based on the high energy photons emitted providing a strong signal, meaning only small quantities

(micrograms) of BP are required to be radiolabelled [82]. As a consequence, the radiolabelled BPs are present in a much lower quantity than the NPs (and hence coating molecules), therefore in the event that a coating molecule does become displaced, the changes would be so insignificant the colloidal properties would not be affected. DPA-ale has recently been shown to radiolabel iron oxide materials with high stability *in vitro/vivo* [82].
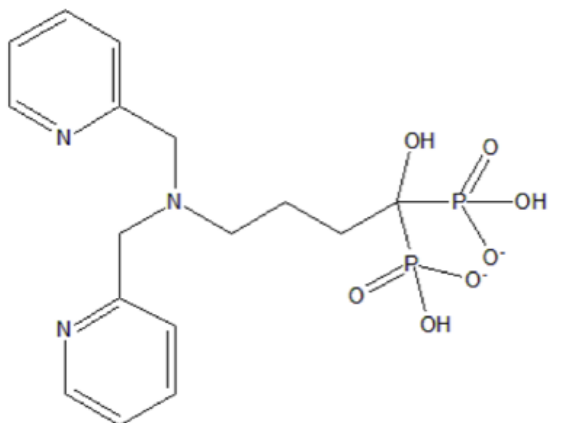
Figure 2.31: General structure of DPA-alendronate.

The radiolabel was produced in two stages. The first being the formation of technetium tricarbonyl, $[^{99m}Tc(CO)_3(OH_2)_3]^+$, and the second being the conjugation of this molecule to DPA-ale. After the initial step, a thin layer chromatography (TLC) plate was run in order to ensure the desired product had been formed. It was expected that there would be a broad peak present at $\sim$30 mm (equivalent to a retention factor - Rf - of $\sim$0.3) if the technetium tricarbonyl had been successfully produced. From figure 2.32 it can be seen there are two regions, the first being the desired product and the second representing a small amount of unreacted starting material, $^{99m}TcO_4^-$. Table 2.3 gives the Rf values for each.

Region	Rf	% Total	% ROI
1	0.392	95.90	98.35
2	0.969	1.60	1.65

Table 2.3: TLC characterisation of $[^{99m}Tc(CO)_3(OH_2)_3]^+$: Rf values for each region of the first TLC plate. Region 1 corresponds to $[^{99m}Tc(CO)_3(OH_2)_3]^+$, region 2 corresponds to unreacted $^{99m}TcO_4^-$.

After the second step, a further TLC plate was then run as before as quality control to ensure the $[^{99m}Tc(CO)_3(OH_2)_3]^+$ had conjugated to the DPA-ale. It was expected that the large broad peak from the previous TLC plate (figure 2.32) would become narrower and shift to the left due to the lower Rf of the radiolabelled bisphosphonate. Figure 2.33 shows the results from the second TLC plate, with table 2.4 giving the relevant values, confirming
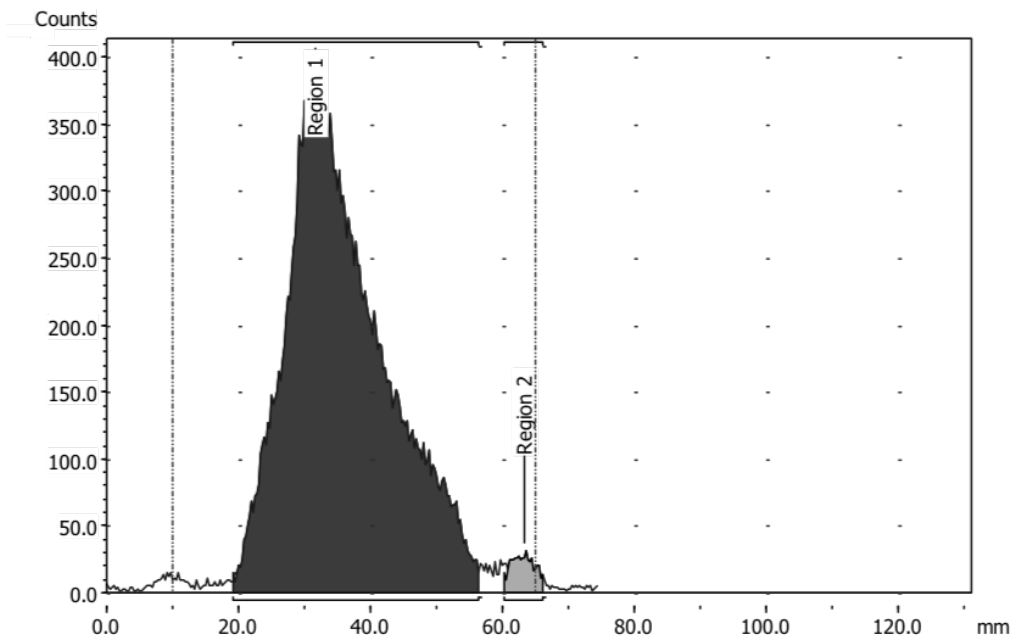
Figure 2.32: TLC characterisation of $[^{99m}Tc(CO)_3(OH_2)_3]^+$: Graphical representation of the first TLC plate. Region 1 corresponds to $[^{99m}Tc(CO)_3(OH_2)_3]^+$, region 2 corresponds to unreacted $^{99m}TcO_4{}^-$.

the reaction was successful. It is thought that the radiolabelled BP appears as two peaks due to the formation of protonated bisphosphonate species as a result of the acid present in the mobile phase (1 % HCl in MeOH; for full details see experimental, page 206). In addition, *in vivo* studies demonstrated that the product of this reaction resulted in bone uptake, suggesting both peaks in the TLC are ^{99m}Tc-DPA-ale.

Region	Rf	% Total	% ROI
1	0.070	45.54	48.89
2	0.229	47.60	41.11

Table 2.4: TLC characterisation of radiolabelled BP: Rf values for each region of the second TLC plate. Regions 1 and 2 correspond to ^{99m}Tc-DPA-ale.

Scheme 2.4 shows how the USPIOs were radiolabelled, with the basic concept being that the ^{99m}Tc-DPA-ale binds to exposed regions on the NP surface. In order to optimise the radiolabelling yield achieved from this procedure, several parameters were explored as well as different methods of purification. To start with it should be noted that reaction pH (6-9) had no affect on the percentage of total activity incorporated into the NP system.
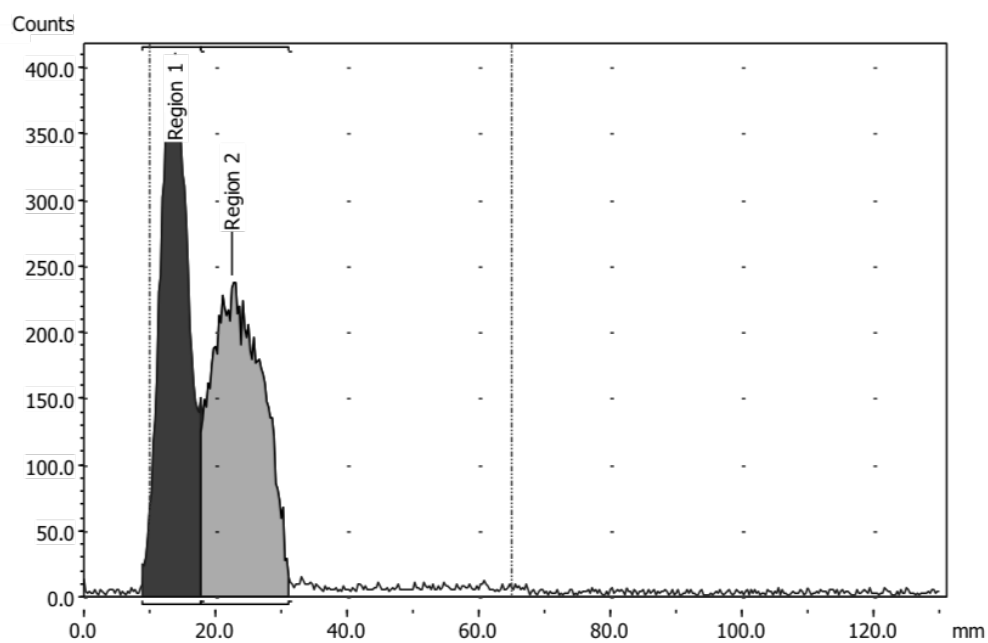
Figure 2.33: TLC characterisation of radiolabelled BP: Graphical representation of the second TLC plate. Regions 1 and 2 correspond to ^{99m}Tc-DPA-ale.
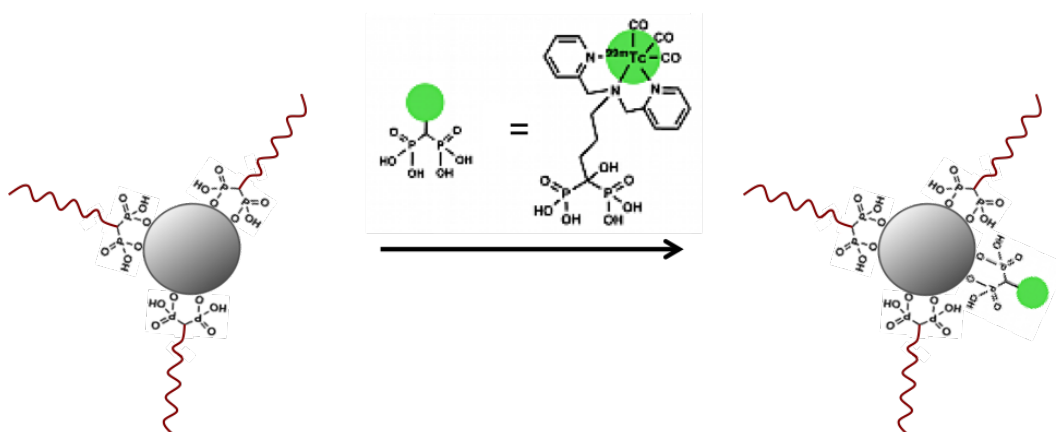
Scheme 2.4: Reaction scheme for radiolabelling PEGylated NPs with ^{99m}Tc-DPA-ale.

2.6.1 Radiolabelling yield dependence on molecular weight and mass of polyethylene glycol

To investigate the effect on the radiolabelling yield of the molecular weight and mass of PEG-BP used in the initial PEGylation of the iron oxide nanoparticles, the following ratios (mass of iron oxide:mass of PEG-BP, in mg) were studied: 0.01:5 of 2 kDa MW (molecular weight), 0.01:13 of 2 kDa MW, 0.01:17 of 5 kDa MW, 0.01:22 of 5 kDa MW and 0.01:57 of 10 kDa MW. Each phase transfer was performed using USPIOs from the same synthesis (labeled USPIO-2), excluding the initial PEGylation which was achieved using a different iron oxide (labeled USPIO-1). All other radiolabelling conditions were kept consistent.

Once the particles had been radiolabelled, unbound ^{99m}Tc-DPA-ale was removed via centrifugation with saline. Figure 2.34 shows how the activity associated with the particles changed during the washing process, with table 2.5 giving the final radiolabelling yield for each sample.
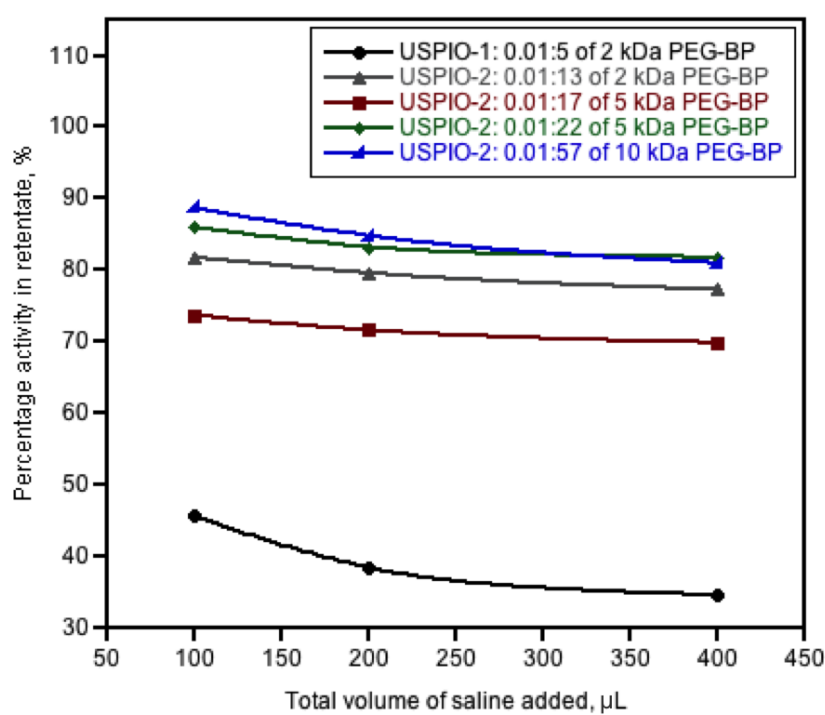
Figure 2.34: Characterisation of radiolabelled NPs: Graphical representation of the centrifugation washings for radiolabelling of various PEG-coated USPIOs.

It can be seen that, in general, as the molecular weight of the PEG is increased, the radiolabelling yield is increased. This is due to longer PEG chains decreasing the coating density

Sample	Final percentage activity in retentate, %
USPIO-1: 0.01:5 of 2 kDa MW	34.6
USPIO-2: 0.01:13 of 2 kDa MW	77.3
USPIO-2: 0.01:17 of 5 kDa MW	69.9
USPIO-2: 0.01:22 of 5 kDa MW	81.8
USPIO-2: 0.01:57 of 10 kDa MW	81.0

Table 2.5: Radiolabelling yields for different PEGylations of USPIOs

meaning there is a larger number of binding sites available for the radiolabel. Although this result seems counterintuitive from the high dispersant packing density previously calculated, the USPIOs investigated here were synthesised using a different method and were coated with oleic acid (USPIO-2) as opposed to oleylamine (USPIO-1). This study was merely used to examine the potential to increase the radiolabelling yield by varying the PEG chain length. As the mass of PEG used to phase transfer the USPIOs is increased, so is the radiolabelling yield. This can be explained in terms of aggregation of the particles. If less PEG is used theres tends to be less surface area exposed to the radiolabel owing to the agglomeration of USPIOs. This is demonstrated in figure 2.35.

(a)   (b)
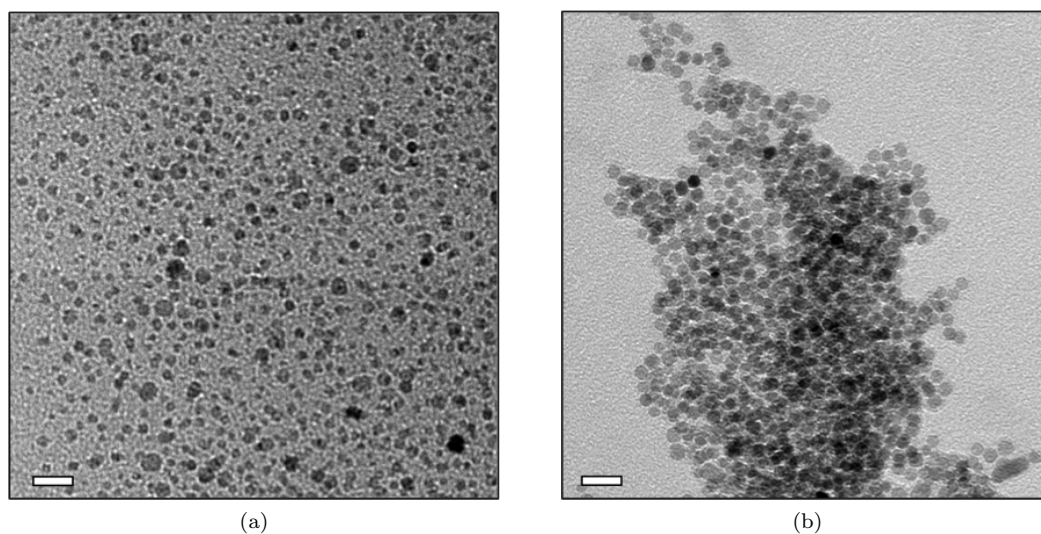
Figure 2.35: Characterisation of PEGylated Fe_3O_4 NPs: TEM micrograph of a dispersion in water PEGylated using a mass iron oxide NP:mass PEG-BP ratio of (a) 0.01:57, and (b) 0.01:17. Scale bars are 20 nm.

2.6.2 Radiolabelling yield dependence on reaction time

The second factor to be studied was the dependence of the radiolabelling yield on the time the USPIOs were reacted with the radiolabelled BP. The amount of bound radioactivity was measured immediately after introducing the radiolabel, and then after 30 min of reacting

at room temperature or 37 °C. It was found that the percentage of the total activity in the retentate was 41.7 % and 42.3 % respectively. This shows that ^{99m}Tc-DPA-ale binds rapidly and almost quantitatively to USPIOs, as has been previously found by de Rosales *et al.* [80].

2.6.3   Radiolabelling yield dependence on heating

In this case, both samples were identical with the exception of the temperature at which the radiolabel was reacted with the USPIOs. In one instance, the temperature heated at was 37 °C and in the other a temperature gradient of 25 °C to 90 °C was used (both heating times were 10 mins). Figure 2.36 show how the radiolabelling changed during the centrifugation process.
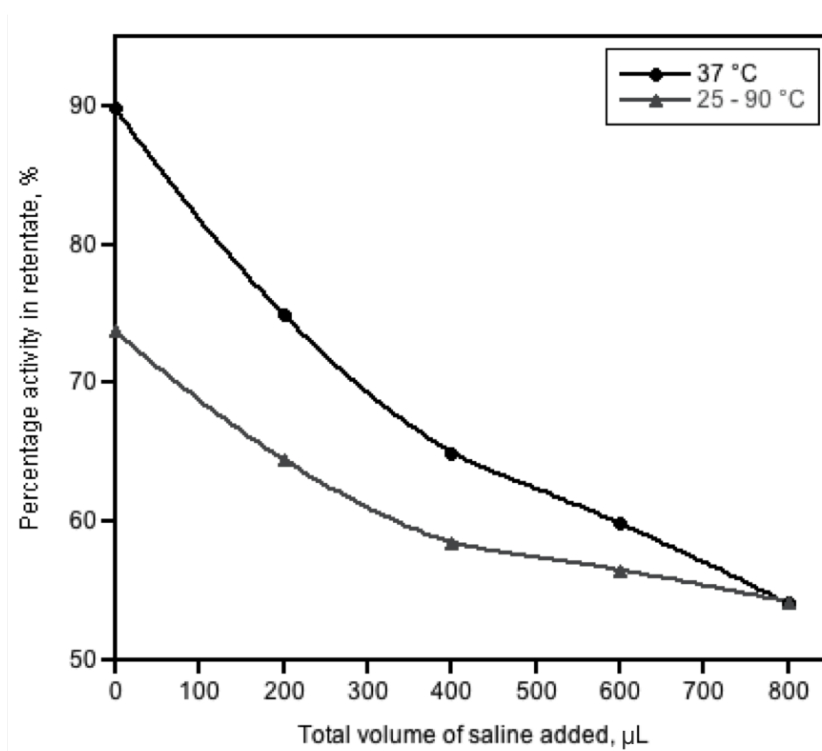
Figure 2.36: Characterisation of radiolabelled NPs: Graphical representation of the centrifugation washings for radiolabelling using different heating conditions.

For the sample heated at 37 °C, the final radiolabelling yield was 24.7 % whereas when the reaction was heated from 25 °C to 90 °C the resulting yield was 46.7 %. It is thought that the PEG will form a barrier limiting the accessibility of the iron oxide surface for the radiolabel. It is therefore presumed that increasing the temperature will increase the

exposure of the less-accessible metallic surface via two mechanisms: (1) ligand exchange on the surface or (2) diffusion of ^{99m}Tc-DPA-ale through the PEG layer to reach exposed gaps of the NP core (represented in scheme 2.4). Referring back to previous calculations of dispersant packing density (approximately 76 % of the USPIO is coated with PEG-BP) and taking into account the strong BP-iron oxide bond [80, 81, 83–90], it is believed that mechanism (2) is most probable. In addition, it was found that using a heating gradient resulted in less non-specifically bound radioactivity in the size exclusion filter.

2.6.4   Radiolabelling yield dependence on filter

Due to the difficulty in removing activity from the centrifugal concentrator used during the washing step, an alternative filter was attempted to see if any difference was noticed. Initially the filter used was a Vivaspin 500 with a 10 kDa MWCO and the second filter investigated was a Vivaspin 2 with a 30 kDa MWCO. Table 2.6 reveals that repeating the experiment with a different filter made no significant difference. The cause of the non-specific binding to the centrifugal concentrator remains unknown.

Sample	Activity in the retentate, %	Radiolabelling yield, %
Vivaspin 500, 10 kDa MWCO	46	34
Vivaspin 2, 30 kDa MWCO	48	31

Table 2.6: Characterisation of radiolabeled NPs: Radiolabelling yields obtained for different centrifugal filters.

2.6.5   Radiolabelling yield dependence on purification method

Due to the problem of the radiolabelled USPIOs non-specifically binding to the size exclusion filter, an alternative route of purification was performed. In this case, once the labeling of the NPs with ^{99m}Tc-DPA-ale had taken place, the reaction solution was passed through a pre-conditioned size exclusion column (PD-10 desalting column, Sephadex G-25 medium). The results of this can be seen in figure 2.37.

The size exclusion column revealed two distinct peaks, the first sharp peak corresponding to the radiolabelled iron oxide NPs (fractions obtained at 1 mL and 1.5 mL) with the second broader peak belonging to the free ^{99m}Tc-DPA-ale. This was the expected result due to the large size of the radiolabelled USPIOs. The activity remaining in the column after
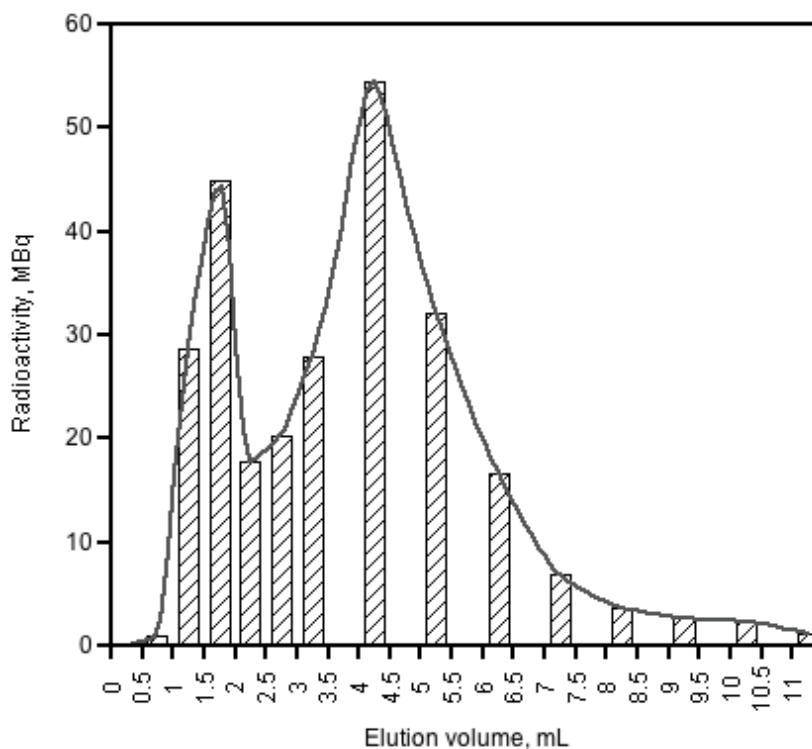
Figure 2.37: Characterisation of radiolabelled NPs: Elution chromatogram of radiolabelled NPs (0.5 mL fractions were collected from 0 to 3 mL, and 1 mL fractions were collected thereafter).

purification was significantly less than for the filter (4.15 MBq compared to 15 MBq), proving only a small amount of non-specific binding to the column matrix occurs. The coelution of the first radioactive peak with PEG(5)-BP-USPIOs shows the association of radiolabel with the particles which are clearly identified visually (inset of figure 2.38a). This demonstrates that size exclusion chromatography is a viable option for the removal of unbound radiolabel. However, although more of the radiolabelled NPs were retrieved, the particle fractions then had to be centrifuged to ensure the small portion of $^{99m}\text{Tc}(\text{CO}_3)$-DPA-ale that eluted with the particles had been removed resulting in a relatively low radiolabelling yield of 25.9 %.

2.6.6   Finalised standard radiolabelling method

The above studies were used to finalise the method of radiolabelling. Firstly, it was established that 10 mg of PEG in the phase transfer would be optimal because, although 20 mg was shown to give a good radiolabelling yield, this is an unnecessarily large excess. As for the heating of the reaction solution, the temperature gradient of 25 °C to 90 °C

was continued with due to the improved removal of the activity after purification. Finally, instead of using a PD-10 column followed by a filter, two PD-10 columns were used. The fractions corresponding the radiolabelled particles collected from the first PD-10 column were passed through the second to ensure all free ^{99m}Tc-DPA-ale had been removed (figure 2.38). This was decided to be an improvement on filtering the fractions from the initial size exclusion column as with centrifugation, unbound ^{99m}Tc-DPA-ale never seemed to be completely removed.

2.6.7 Characterisation of radiolabelled ultrasmall superparamagnetic iron oxide nanoparticles

In order to ensure the radiolabelling procedure was not altering the hydrodynamic diameter of the particles, DLS was run once the radioactivity of the NPs had decayed. It was found that the D_{H} was 24.9 ± 3.5 nm showing no change in size on the addition of the radiolabel to the surface. Furthermore, ^{1}H NMR of the residue after evaporation of the size exclusion and filtration fractions/filtrates did not show any detectable PEG peaks confirming the low, if any, PEG displacement after radiolabelling.

In order to ensure that the radiotracer was stable, a sample of radiolabelled particles was left for 24 hours in PBS, and incubated at 37 °C for 48 h in human serum. These were then centrifuged using a 100 kDa MWCO filter (as serum proteins were below this size, hence ensuring they pass through to the filtrate) and the amount of activity remaining in the retentate and that in the filtrate was measured as shown in tables 2.7 and 2.8. From this the percentage of the radiolabel no longer bound to the iron oxide could be calculated.

	Percentage activity, %
Filtrate	11.4
Retentate and filter	88.6

Table 2.7: Characterisation of radiolabelled NPs: Stability of radiolabelled PEG(5)-BP-USPIOs in PBS after 24 hours at 37 °C.

	Percentage activity, %
Filtrate	6.2
Retentate and filter	93.8

Table 2.8: Characterisation of radiolabelled NPs: Stability of radiolabelled PEG(5)-BP-USPIOs in serum after 48 hours at 37 °C.
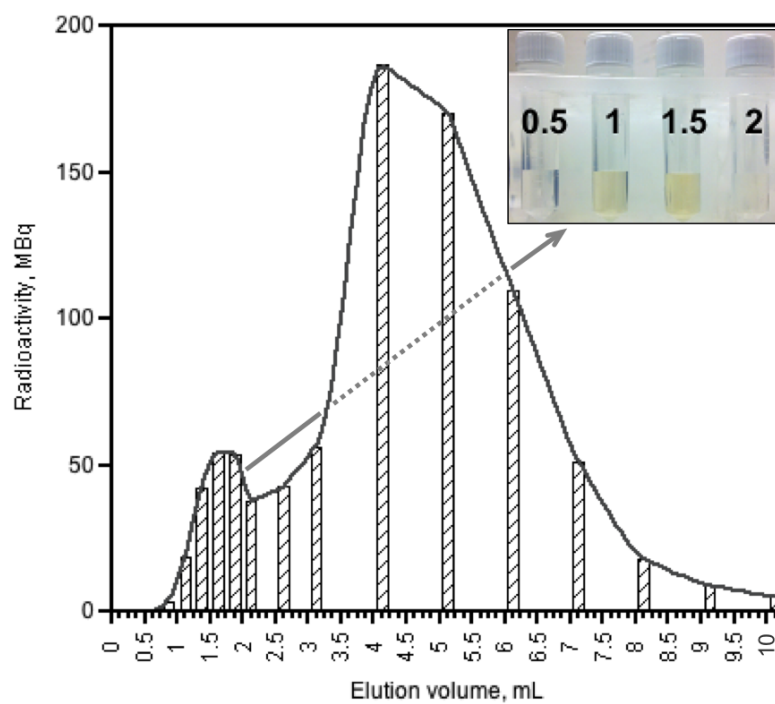
(a)
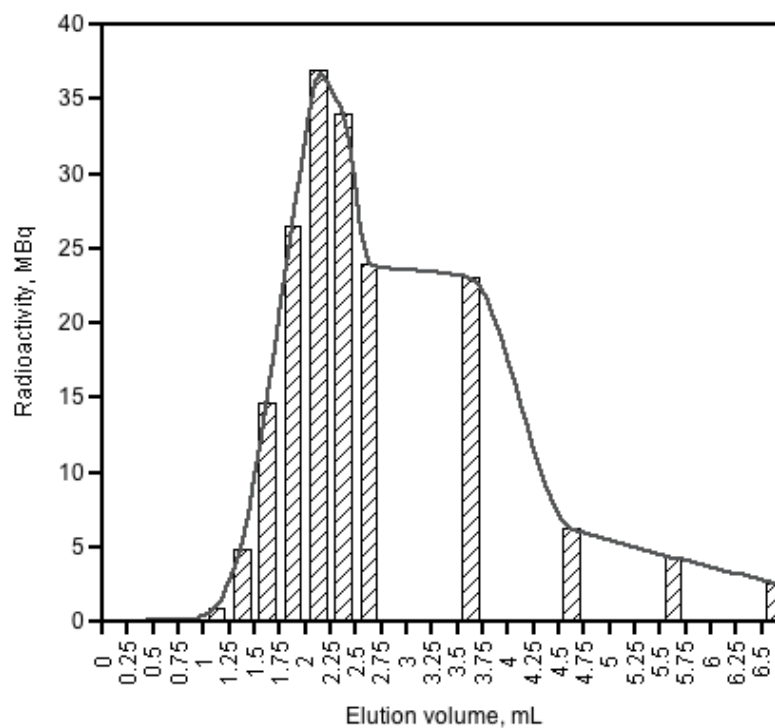
(b)

Figure 2.38: Characterisation of radiolabelled NPs: Results from (a) first (the inset is of the first four fractions collected showing the presence of USPIOs), and (b) second size exclusion column used to purify radiolabelled NPs.

For PBS, it was calculated that the percentage of activity bound to the particles was 88.6 %, and for human serum 93.8 %. This result is consistent with previous findings using dextran-coated SPIOs and other reports that have shown the high stability of the BP-iron oxide bond (more than 4 weeks at pH 7) compared to other anchors such as carboxylates [80, 88]. This suggests these radiolabelled particles are stable in physiological conditions (temperature together with protein and salt concentrations) making them practical for *in vivo* studies.

2.7 *In vivo* imaging

2.7.1 Magnetic resonance imaging

The ability of the PEG(5)-BP-USPIOs to be used as a T_1 contrast agent *in vivo* was then assessed using a 3 T clinical scanner. It was found that the strong T_1 effect demonstrated in the phantom studies was also observed *in vivo*. PEG(5)-BP-USPIOs were injected via the tail vein into a BALB/c mouse leading to a significant increase in the signal intensity from the blood. As can be seen in figure 2.39, this resulted in the vessels, heart compartments and other highly vascularised organs such as the spleen to become clearly visible.

When designing contrast agents, a fundamental consideration is the dose required to obtain signal enhancement. Remarkably, when compared to other USPIOs, PEG-(5)-BP-USPIOs require a very low dose. For MR angiography in human and preclinical studies, a typical dose of USPIOs is 40-70 µmol Fe/kg [35, 91–93]. However, administration of USPIOs at 60 µmol Fe/kg during a recent clinical study was reported to result in detrimental clinical effects [93]. The high r_1 relaxivity and low r_2/r_1 ratio of PEG(5)-BP-USPIOs, however, allow us to obtain high signal enhancement with significantly lower doses. From figure 2.40 it can be seen that the dose of PEG(5)-BP-USPIOs required to obtain a similar signal enhancement to FeraSpin XS was 4 times lower (10 µmol Fe/kg vs 40 µmol Fe/kg). This is believed to be a result of both the optimal relaxation properties and long blood circulation time. T_1-mapping studies of the aorta support this hypothesis. Thus, the normal relaxation rate (R_1) of blood is 0.74 ± 0.05 s^{-1}. Forty minutes after injection of PEG(5)-BP-USPIOs, the rate had increased more than 6-fold to 4.78 ± 1.90 s^{-1}, whereas for FeraSpin XS this value was 2.39 ± 0.33 s^{-1}.
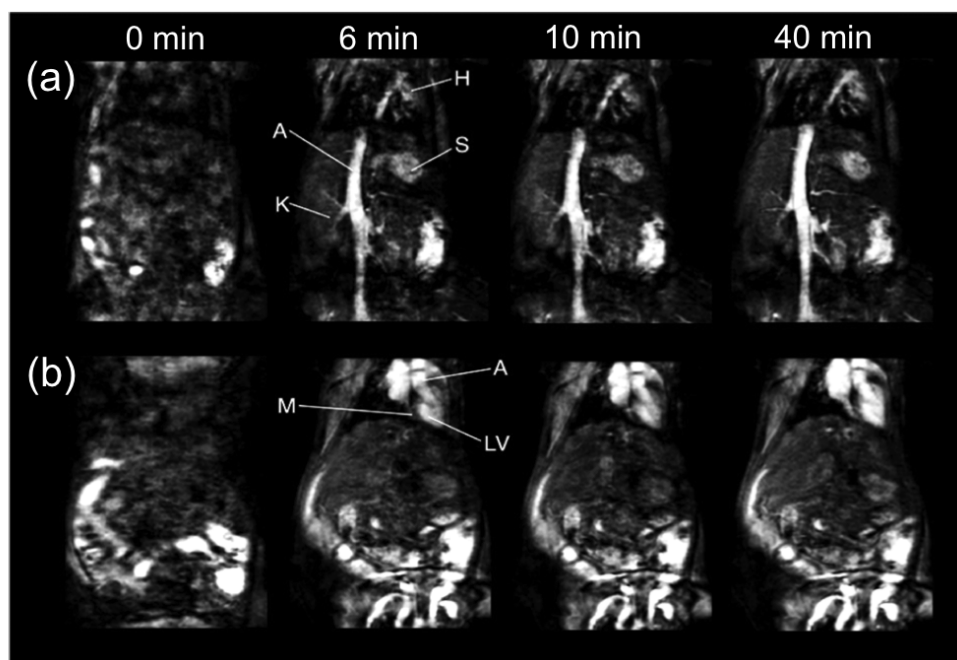
Figure 2.39: *In vivo* T_1-weighted MRI studies of a mouse injected with PEG(5)-BP-USPIO showing the increase in signal from blood in (a) the vessels, and (b) the heart at different time points (t = 0 min, pre-injection). Labels: H = heart, S = spleen, K = kidney, A = aorta, M = myocardium, LV = left ventricle.

Interestingly, throughout the 40 min experiment, the signal intensity in the blood when using PEG(5)-BP-USPIOs remained constant. This is in contrast when using FeraSpin XS, where a substantial decay of approximately 50 % was observed at the end of the 40 min time period (figure 2.40). An important factor for blood pool MRI agents is an extended blood half-life as it allows the acquisition of high-resolution images and could facilitate diagnosis of a series of conditions such as tumour angiogenesis, aneurysms, and internal bleeding [94, 95]. In addition, low RES uptake and extended circulation times are required when using targeted USPIOs that bind to specific receptors.

The excretion route of the particles was examined using a T_2*-weighted gradient echo sequence. This particular sequence was chosen due to the high sensitivity in response to the accumulation and changes in relaxivity of SPIOs in tissues [96]. T_2*-weighted imaging and a mapping sequence were acquired before and 50 min after injection of PEG(5)-BP-USPIOs (figure 2.41). It can be seen that there are indications of liver accumulation, and hence hepatic excretion which is expected for a NP of this D_{H}. Taking into account the high signal from the blood throughout the experiment, liver uptake must be minimal within the first hour after injection. This low level of liver uptake can be attributed to the neutral surface charge of the PEG(5)-BP-USPIOs and the small mean NP diameter (<50 nm) [97,98].
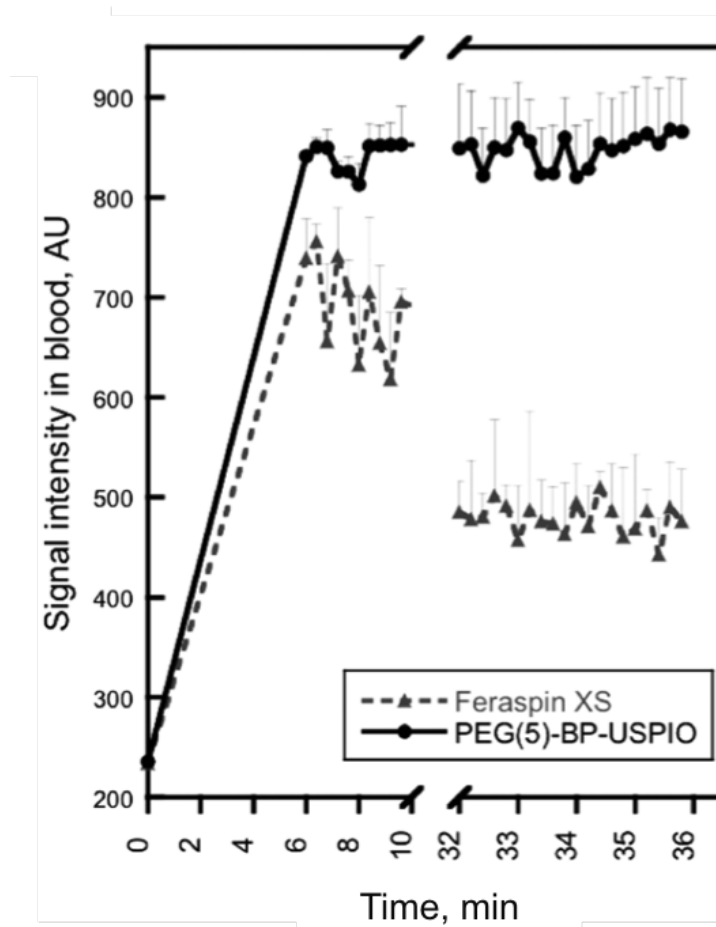
Figure 2.40: Kinetic profile of the MRI signal intensity in blood obtained from PEG(5)-BP-USPIO (black circles, 10 µmol Fe/kg dose) and FeraSpin XS (grey triangles, 40 µmol Fe/kg dose).
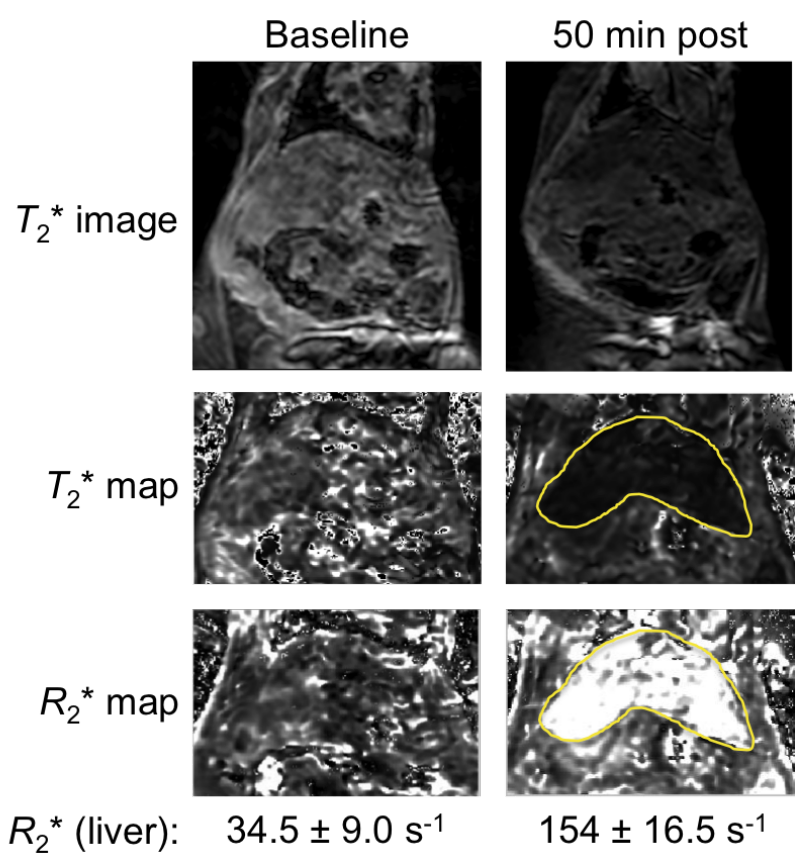
Figure 2.41: T_2* mapping of PEG(5)-BP-USPIOs before (left) and 50 min after (right) showing accumulation of particles in the liver (highlighted area).

2.7.2 Single photon emission computed tomography-computed tomography imaging

The biodistribution of the radiolabelled PEG(5)-BP-USPIOs and the fate of the BP coating was then studied using the high sensitivity of SPECT imaging. Figure 2.42 shows the SPECT-CT imaging of live BALB/c mice 40 min and 200 min post intravenous injection.
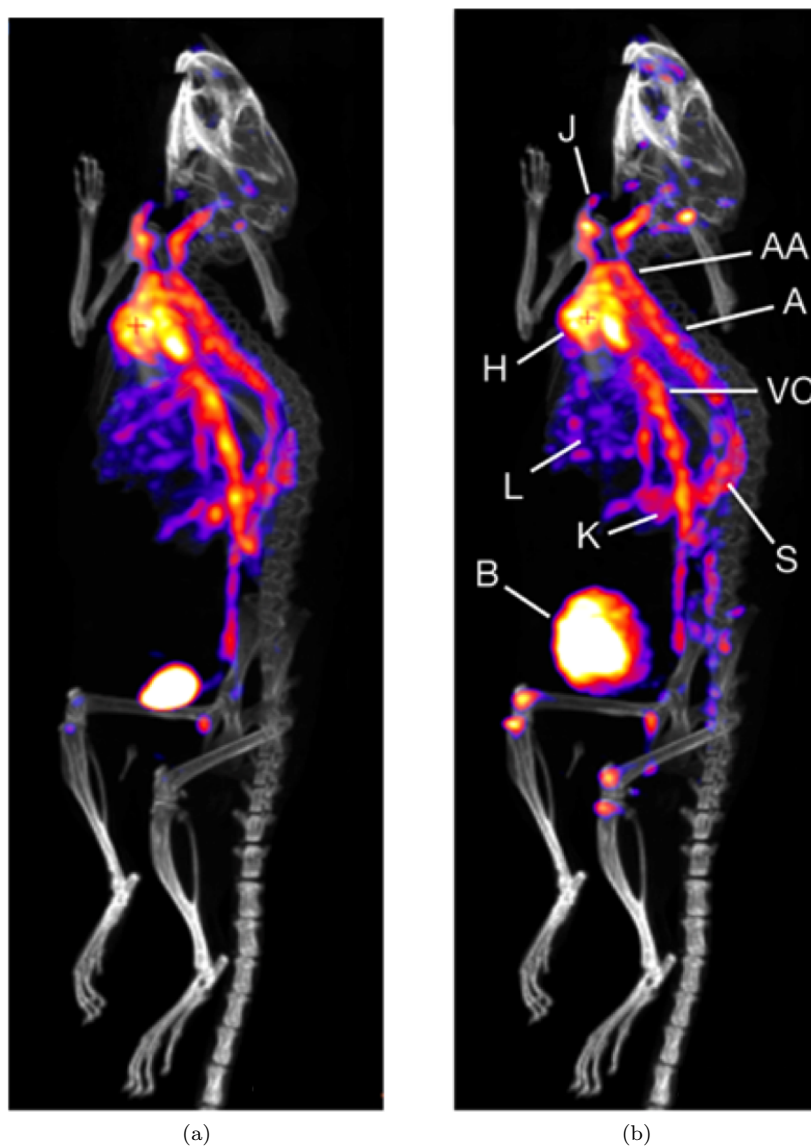
Figure 2.42: Maximum intensity projection SPECT-CT images (a) 40 min, and (b) 200 min post *iv* injection of radiolabelled USPIOs, colour bar for each image has the same minimum/maximum setting. Labels: H = heart, J = jugular vein, AA = aortic arch, A = aorta, VC = vena cava, L = liver, K = kidney, S = spleen, B = bladder.

The SPECT-CT images obtained confirm the behaviour seen in the MR imaging. It can clearly be seen that the majority of the radiolabelled particles remain in the bloodstream for at least 200 min as evidenced by no decrease in the signal intensity of the heart as well as major blood vessels and vascular organs. Figure 2.43 shows the pharmacokinetic profile obtained from the SPECT-CT imaging performed. It was observed that the signal of vascular organs reaches a maximum concentration before the first 45 min followed by an elimination phase after 80 min. However, it can also be seen there is a continuous signal increase in non-vascular organs such as the bladder and bones (knee). This is a result of free ^{99m}Tc-DPA-ale which is released during the decomposition of PEG(5)-BP-USPIOs (*vide infra*). Imaging at the first time point displayed a significant signal from the bladder which may be a consequence of a small number of USPIOs that had a small enough D_H to be excreted with the urine [50]. A second reason may be due to a large fraction of ^{99m}Tc-DPA-ale ($\sim$7 % ID) detaches soon after injection. There are some indications, however, that this option is less likely. It has been reported that injecting ^{99m}Tc-DPA-ale alone results in high bone uptake, which would be expected at the first time point if 7 % of the injected dose (% ID) suddenly detached from the iron oxide nanoparticles once in the bloodstream [82]. Furthermore, an immediate breaking of the BP-iron oxide bond after injection is not in agreement with the slow rate of BP release found throughout the rest of the study and the *in vitro* stability studies. A final argument is that there is a large proportion of non-specifically bound radiolabelled BP in the injected dose but this is unlikely after the extensive purification and characterisation experiments.

$$t_{1/2} = \frac{0.693}{\lambda_z} \tag{2.4}$$

where $t_{1/2}$ = elimination (blood) half-life (min)

λ_z = slope of the elimination phase

The blood half-life was calculated using the slope of the elimination phase in the heart (assuming first-order single compartment pharmacokinetics, equation 2.4 [99]) and was found to be 178 min (2.97 h). This long circulation time of the bimodal USPIOs is advantageous as it increases the probability of reaching the destination site (e.g. tumour) before clearance from the body [100]. Interestingly, there is no sign of significant accumulation in the liver. On the other hand, the T_2*-weighted MRI studies in figure 2.41 reveal signs of uptake in the liver. From reviewing previous studies, it is thought this is the result of a slow loss of
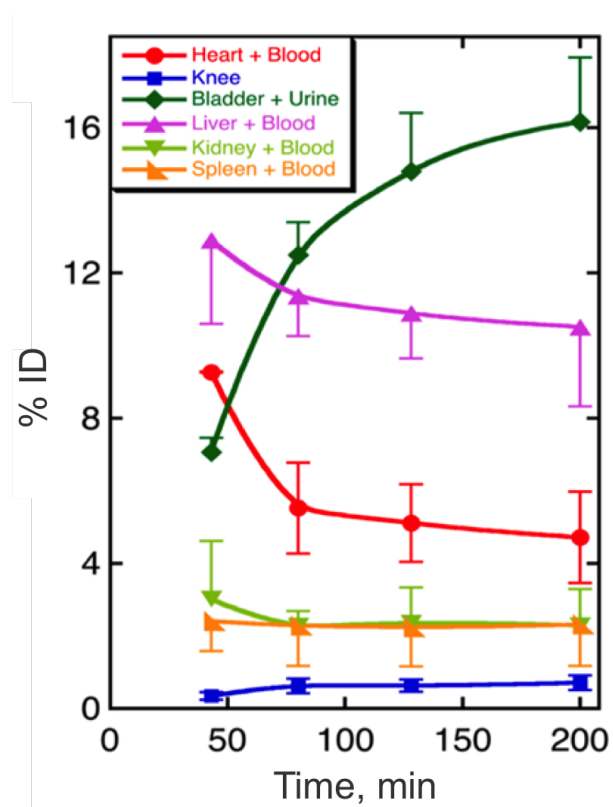
Figure 2.43: Pharmacokinetic profile as obtained by quantification of the signal from several tissues showing the changes in the % ID as a function of time. Data represents the mean ± SD (n = 2 mice).

the BP-based coating. The basis for this proposal is that throughout the duration of the SPECT study (3.3 h), the images show a gradual increase in bone uptake due to the release of ^{99m}Tc-DPA-ale into the bloodstream (figure 2.42b) [82]. Thus, as both PEG(5)-BP and ^{99m}Tc-DPA-ale share a BP anchoring group, it is reasonable to assume that PEG(5)-BP is also being released. This would then increase RES uptake of the USPIOs because of aggregation of the uncoated particles, which are only detectable by T_2*-weighted MRI, and not SPECT scanning. Interestingly, the *in vitro* stability studies in human serum revealed almost no degradation after 48 h at 37 °C (*vide supra*). This suggests that some action of soft tissues *in vivo* is occurring causing the slow release of the BP components. SPECT imaging also revealed substantial uptake in the kidneys, implying the BPs may detach from the USPIOs via functions of the kidneys. Figure 2.44 (in addition to figures 2.42 and 2.43) supports this statement as the SPECT images clearly show accumulation in the kidneys whereas no kidney retention is observed after injection of ^{99m}Tc-DPA-ale alone [82]. Additionally, during the experiment there was an increase in the radioactivity measured in the urine. Particles with a hydrodynamic diameter in the range 10-50 nm are known to be cleared through the renal system. There are two possible mechanisms by which this may occur, either by tubular excretion or glomerular filtration. The latter being the most ideal as particles are not metabolised internally. As this only happens for particles with a diameter of less than 6 nm, it is most likely the clearance mechanism in this case is via tubular excretion [19,101]. Further experiments are needed to clarify the role of the kidneys and other tissues in the excretion and metabolism of PEG(5)-BP-USPIO.
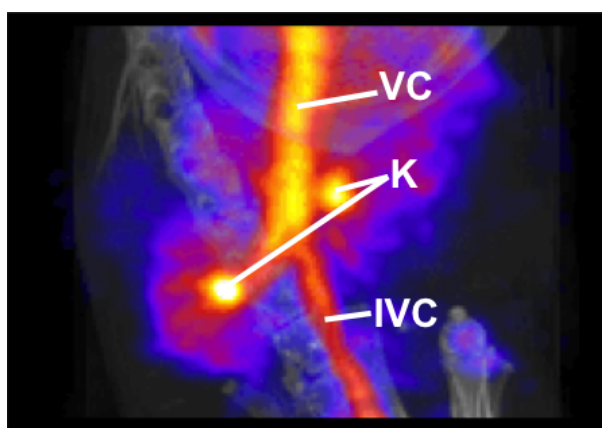
Figure 2.44: SPECT-CT images of a mouse injected with 20 MBq of radiolabelled PEG(5)-BP-USPIOs 40 min after injection. Close up of the abdominal area showing high signal in the kidneys. Labels: VC = vena cava, K = kidney, IVC = inferior vena cava.

2.7.3 Analysis of urine

Preliminary urine analysis with PEG(5)-BP-USPIOs was performed at the end of the SPECT imaging study in order to further investigate the excretion route of the radiolabelled particles (figures 2.45 and 2.46).

A sample of urine was collected following the 3.3 h *in vivo* study and passed through a size exclusion column (as before during purification after radiolabelling), figure 2.45. As can be seen most of the activity elutes as a broad peak in the small-molecule area. Studies using both TLC and hydroxyapatite-binding confirmed this band to correspond to ^{99m}Tc-DPA-ale. This indicates that if renal metabolism is taking place, it seems that a fraction of the radioactivity is excreted in the urine once the BPs are released, whilst another is recycled back into the bloodstream, where it binds to bone. This has previously been detailed for other BPs [102]. Interestingly, there is also a small but detectable peak that elutes at the same elution volume as radiolabelled PEG(5)-BP-USPIOs, suggesting a small fraction of particles of very small size are excreted intact. This results correlates with previous observations from the SPECT-CT imaging studies.

In addition to measuring the activity in each fraction eluted from the size exclusion column, the iron concentration for each elution volume was evaluated, figure 2.46. A presence of iron at 2 mL was found which corresponds to the radiolabelled NPs, as was seen previously. There is also a high concentration found at 5 mL. This may be due to some of the radiotracer being metabolised and therefore this peak represents smaller fragments of the probe.

2.7.4 Comparison with FeraSpin XS

Injection of radiolabelled FeraSpin XS revealed that the activity accumulated solely in the liver and bladder 50 min after injection (figure 2.47, imaging of earlier time points could not be achieved due to the low radiolabelling yields obtained). This is expected for FeraSpin XS and other dextran-coated USPIOs, as this polysaccharide is avidly taken by macrophages, providing a useful method to target these NPs to macrophage-rich tissues [103, 104]. This result was also consistent with the MRI experiments using Feraspin XS in which there was a 50 % reduction of signal from the blood in the first 30 min (*vide supra*). Other clinically approved dextran-coated USPIOs also display short blood half-lives in mice (*e.g.*, Sinerem,
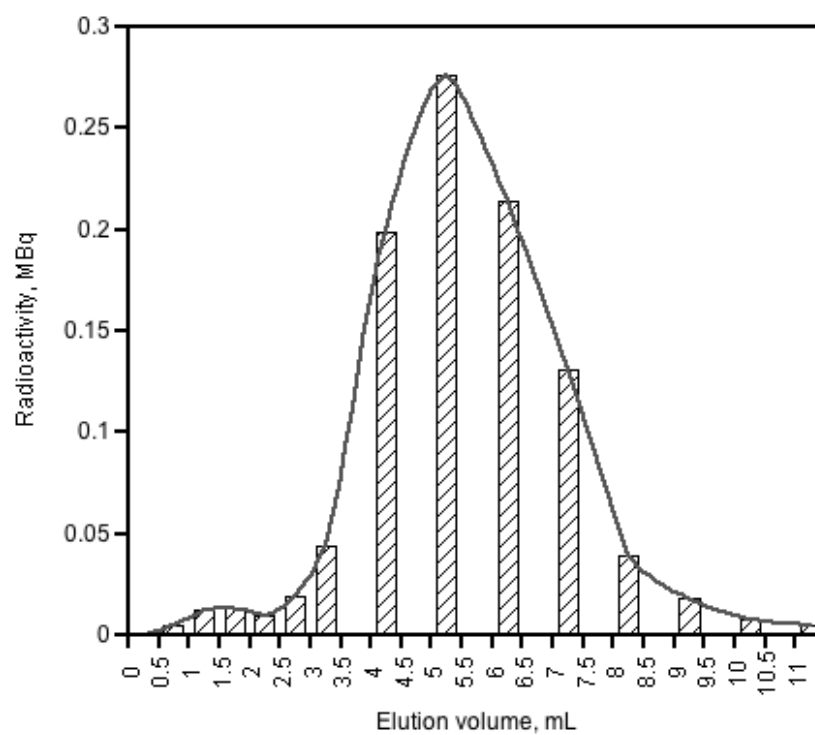
Figure 2.45: Characterisation of radiolabelled NPs: Size exclusion chromatogram of a urine sample after 3.3 h injection of PEG(5)-BP-USPIO (note that 0.5 mL fractions were collected until volume of 3 mL, whereas 1 mL fractions were collected thereafter). Most of the activity elutes as ^{99m}Tc-DPA-ale (peak at 5 mL) whereas a small radioactive peak at 1-1.5 mL suggests some PEG(5)-BP-USPIOs elute intact.
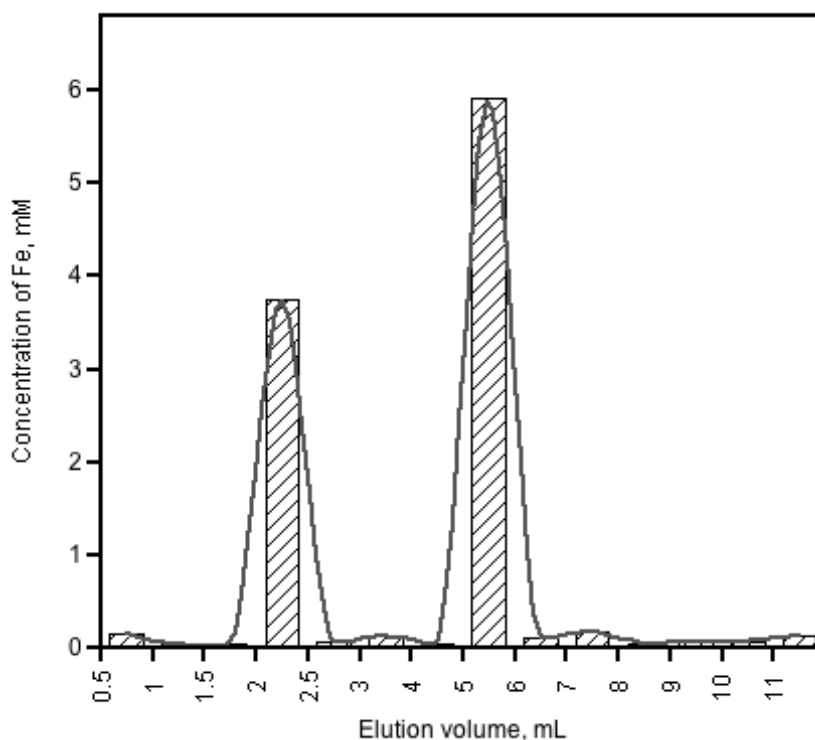
Figure 2.46: Characterisation of radiolabelled NPs: Iron concentration of each fraction collected from size exclusion column.

18 min) [77].

2.8   Targeting

The main focus of this work was vascular targets due to the long circulation time of the particles that had previously been established. In order to add targeting ability to the particles, it was necessary to introduce a group into the coating of the USPIOs which would allow conjugation of biomolecules. In this case, maleimide (figure 2.48a) was chosen due to its high stability in water and known binding to thiols which are present on the side chain of cysteine residues [105]. Recent reports have detailed the successful conjugation of antibodies to this imide for applications such as drug delivery as well as functionalisation of gold NPs for potential biological uses [106, 107, 109]. Figure 2.48b shows the structure of the maleimide-PEG-BP (mal-PEG(5)-BP, this has previously been shown to provide stable functionalisation for NPs [110]) used alongside the PEG(5)-BP in the phase transfer of the USPIOs. The method of PEGylation was identical to the previous scheme shown, with the slight alteration of a ratio of PEG(5)-BP to mal-PEG(5)-BP being used (as shown in scheme
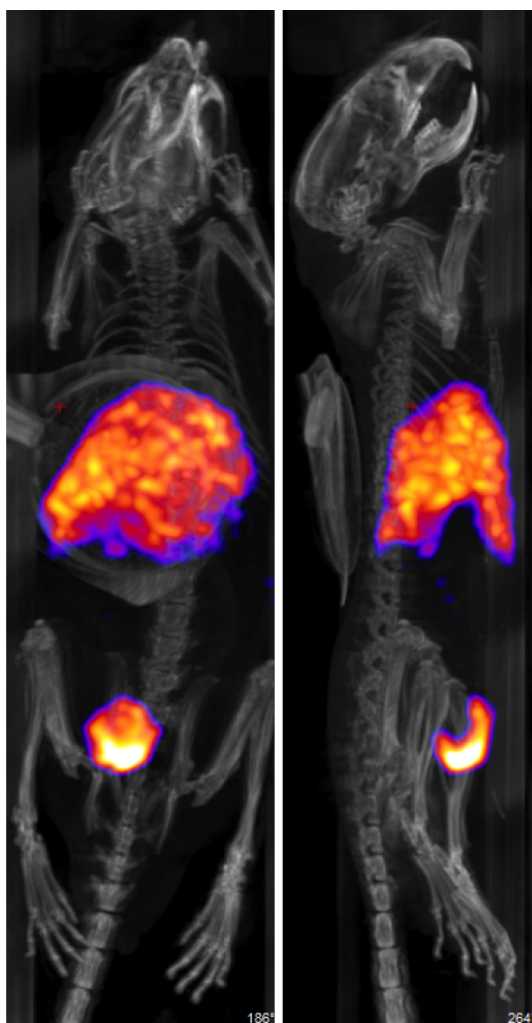
Figure 2.47: SPECT-CT images of a mouse injected with 3 MBq of radiolabelled FeraSpin XS 50 min after injection showing accumulation of particles in liver and the bladder. The USPIOs were radiolabelled using ^{99m}Tc-DPA-ale (30 min incubation at 37 °C followed by purification by size exclusion filtration, 10 kDa MWCO).

2.5).
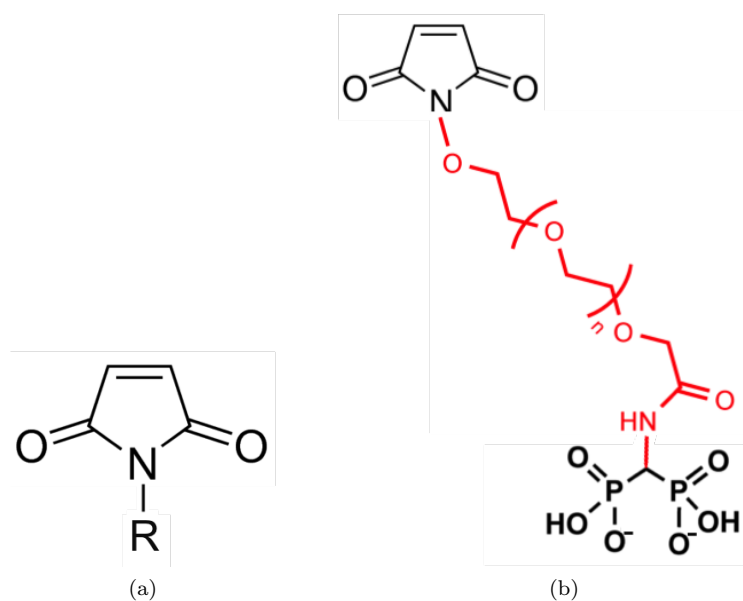
Figure 2.48: General structure of (a) maleimide, and (b) mal-PEG-BP.
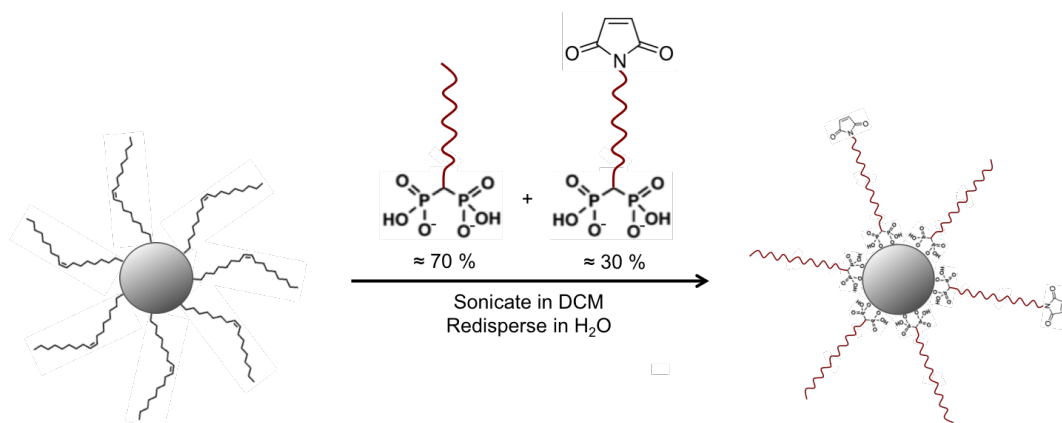
Scheme 2.5: Reaction scheme for the method of PEGylation of iron oxide NPs using both PEG(5)-BP and mal-PEG(5)-BP.

2.8.1 Characterisation of maleimide-polyethylene glycol-coated ultrasmall superparamagnetic iron oxide nanoparticles

Before conjugation to the targeting modality, it was necessary to ensure the introduction of the maleimide hadn't affected the properties of the particles. Figure 2.49 shows the TEM obtained of the mal-PEG(5)-BP-USPIOs and the particle size was measured to be 5.6 $\pm$ 0.8 nm (based on the measurement of 100 particles) showing no change in core size. IR spectroscopy was attempted, however the maleimide peak was not visible. This was possibly due to the low concentration of maleimide present in the sample, as well as the IR peaks

occurring in similar positions to those for PEG. Nonetheless, the mal-PEG(5)-BP-USPIOs reacted with a thiol-fluorophore, which demonstrated the presence of the maleimide group on the NP surface.
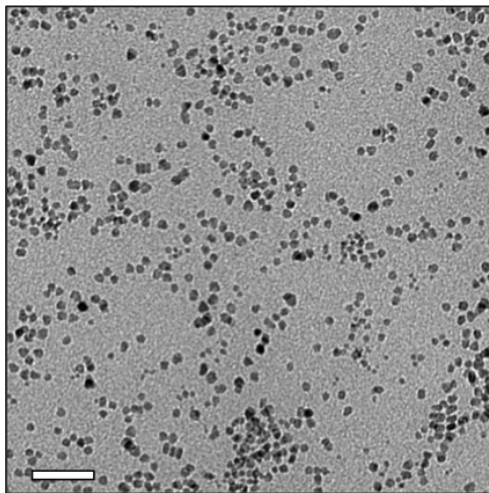
Figure 2.49: Characterisation of maleimide-PEGylated Fe_3O_4 NPs: TEM micrograph of a dispersion in water ($D_{TEM} = 5.6 \pm 0.8$ nm based on measurement of 100 particles). Scale bar is 50 nm.

Once it had been established that the introduction of the maleimide into the coating had no effect on the overall dimensions of the particles, relaxivity studies were performed to observe any variation in the potential MR properties. It was found that relaxation rates at both 26 °C and 37 °C were significantly lower than those found for PEG(5)-BP. Likewise, this was consistent across studies investigating concentration and field strength. This decrease could be explained by a difference of hydrophilicity. If the USPIOs were coated with a more hydrophobic molecule, the diffusion of water around the particle core would reduce resulting in lower values for r_1 and r_2 [111].

In order to determine if non-specific uptake occurred, before introducing a targeting moiety, the PEG(5)-BP-USPIOs and mal-PEG(5)-BP-USPIOs were incubated at 37 °C for 1 h with a breast cancer cell line, MDA-MB-435 (although recent reports debate whether this is the true tissue of origin for this cell line [112–115]). Both the PEGylated and maleimide-PEGylated particles had a fluorescent component (fluorescein-mal-PEG(5)-BP) added to the coating to allow for analysis via fluorescence-activated cell sorting (FACS). The FACS data collected is shown in figure 2.51. There was an observed shift once the cells were incubated with the fluorescent PEG(5)-BP-USPIOs corresponding to non-specific binding. This is most likely due to pinocytosis processes taking place [116–119]. A further shift was
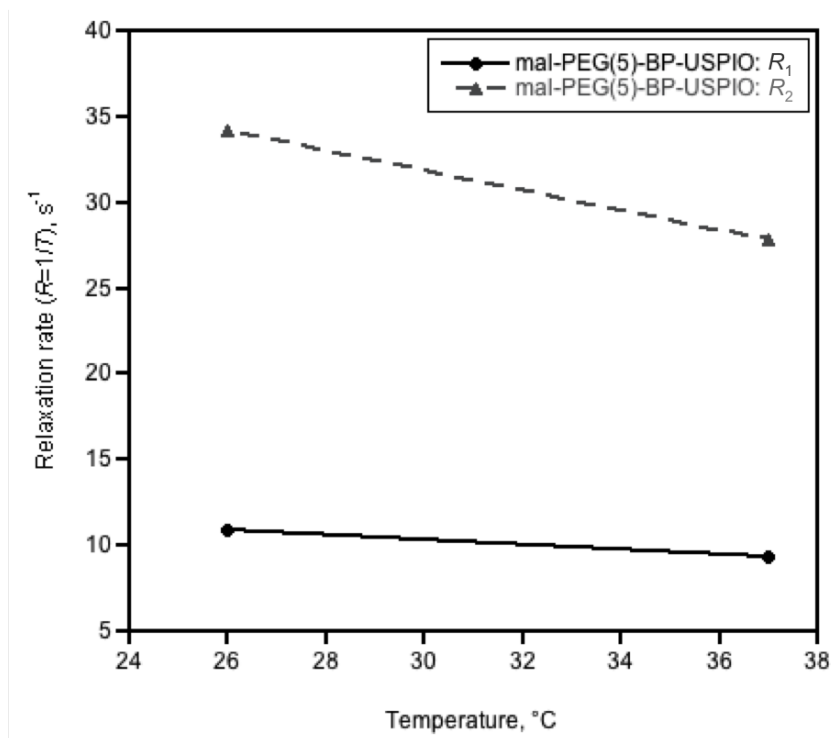
Figure 2.50: Relaxivity characterisation of mal-PEGylated Fe_3O_4 NPs: Variation of spin-lattice relaxation rate (R_1; solid black line) and spin-spin relaxation rate (R_2; dashed grey line) with temperature for mal-PEG(5)-BP-USPIOs.

detected when the cells were incubated with the mal-PEG(5)-BP-USPIOs (with the free maleimide groups on the surface), owing to binding with free thiols that are present on the cell membrane [120–122]. This result was further confirmed by fluorescence cell imaging, figure 2.52 displays the images captured, with figure 2.52a being MDA-MB-435's only, and figure 2.52b being the cells that were incubated with mal-PEG(5)-BP-USPIOs. The first image is the transmitted light (TRANS), the second is the 4',6-diamidino-2-phenylindole (DAPI) showing the nuclei of the cells and the third is the green fluorescent channel (GFC). The GFC images show that for the cells alone, no autofluorescence was revealed. However, for the cells which have been incubated with the maleimide-PEG coated particles, there is emission due to the fluorescein present. This agrees with the results found by FACS and verifies there is some binding to the surface of the cells.

2.8.2 Prostate-Specific Membrane Antigen

The first target to investigate was the prostate-specific membrane antigen (PSMA). This is a transmembrane protein expressed in all types of prostatic tissue with elevated expression
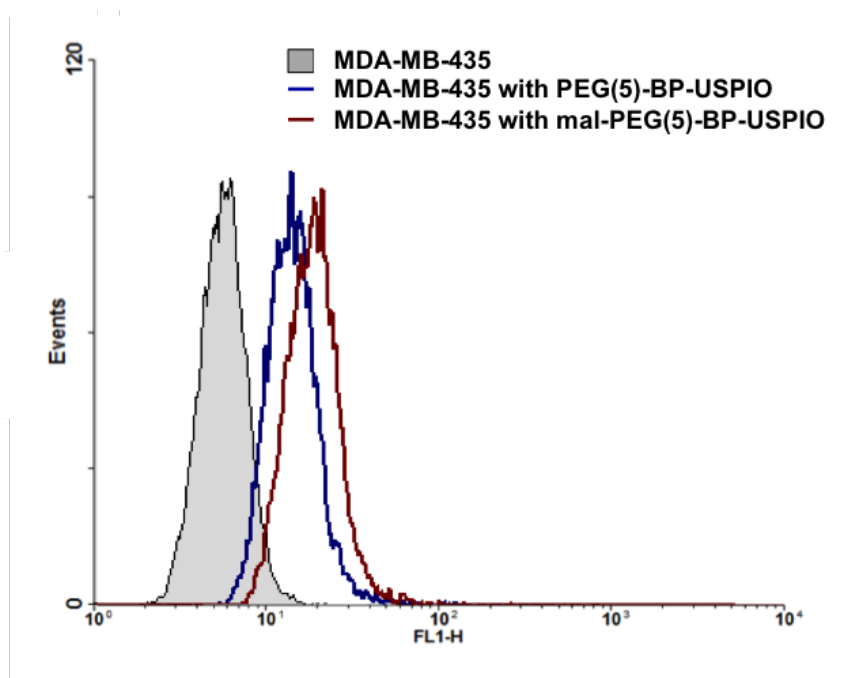
Figure 2.51: *In vitro* characterisation of PEGylated Fe_3O_4 NPs: FACS data showing binding of PEG(5)-BP-USPIOs and mal-PEG(5)-BP-USPIOs to MDA-MB-435 cells.
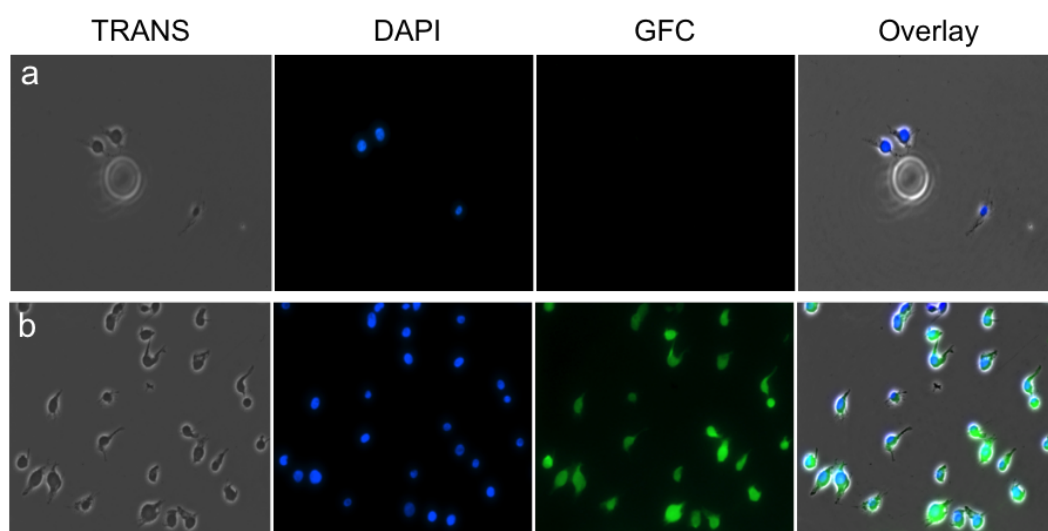
Figure 2.52: *In vitro* characterisation of PEGylated Fe_3O_4 NPs: Fluorescence microscopy images of (a) MDA-MB-435 cells only, and (b) MDA-MB-435 cells incubated with mal-PEG(5)-BP-USPIOs. All microscope/fluorescence settings were identical for both acquisitions.

found in all prostate cancers; the highest levels found in high-grade, hormone-refractory and metastatic disease [123–129]. Several groups have recently published high-contrast images of prostate cancer achieved using PSMA-targeted ligands [130, 131], and it has also been proposed that the degree of PSMA expression may be an indicator of disease outcome [132, 133]. In this case, a single chain variable fragment (scFv) was used, as depicted in figure 2.53. The basic structure consists of variable regions of the heavy chain (V_H) which link to variable regions of the light chain (V_L). The N-terminal at beginning of heavy chain is an amine group and the C-terminal at end of the light chain is a carboxylic acid. A fragment of the antibody J591 was used which has 6 consecutive histidines (a Histag) and a cysteine conjugated to the C-terminal. Previous work in several groups, including this group, has established the targeting ability of this antibody, and provided an ideal starting point to evaluate the possibility of targeting to specific cell-surface receptors (*i.e.* PSMA). [134–139].
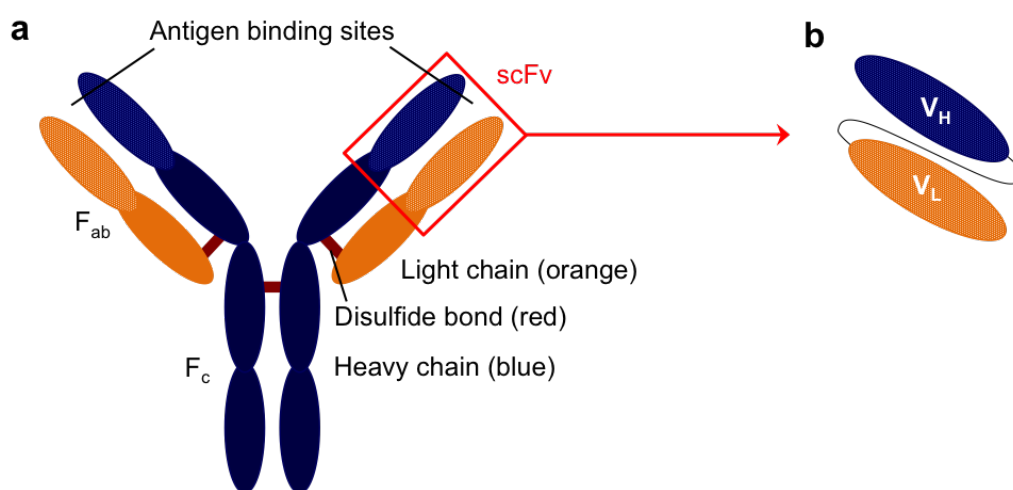
Figure 2.53: General structure of (a) an antibody, and (b) a scFv.

This conjugation was performed in two steps as shown in scheme 2.6. The first was to reduce J591 using dithiothreitol (DTT) in order to remove dimers which form due to disulfide bonds between two cysteines. This was then passed through a size exclusion column to remove excess DTT and the reduced J591 was eluted directly into the mal-PEG(5)-BP-USPIOs. The incubation period was 2 h at room temperature, after which purification occurred via an ÄKTA chromatography system (Superose 6, 10/300 GL Tricorn column). Figures 2.54 and 2.55 shows the size exclusion chromatograms for J591 in PBS, mal-PEG(5)-BP-USPIOs and also for the conjugation solution containing J591 and mal-PEG(5)-BP-USPIOs. It can be seen there is a good separation between the J591 conjugated USPIOs (first peak as known

from figure 2.54a) and the excess J591 (later peaks at 15 mL, 17 mL and 20 mL, known from figure 2.54b). This ensured there was no unbound scFv in the NP fractions. The elution volume for J591 is expected to be present at 17 mL. It is thought that the small peak observed at 15 mL is due a small population of reformed dimers, whereas the origin of the peak at 20 mL is unknown.
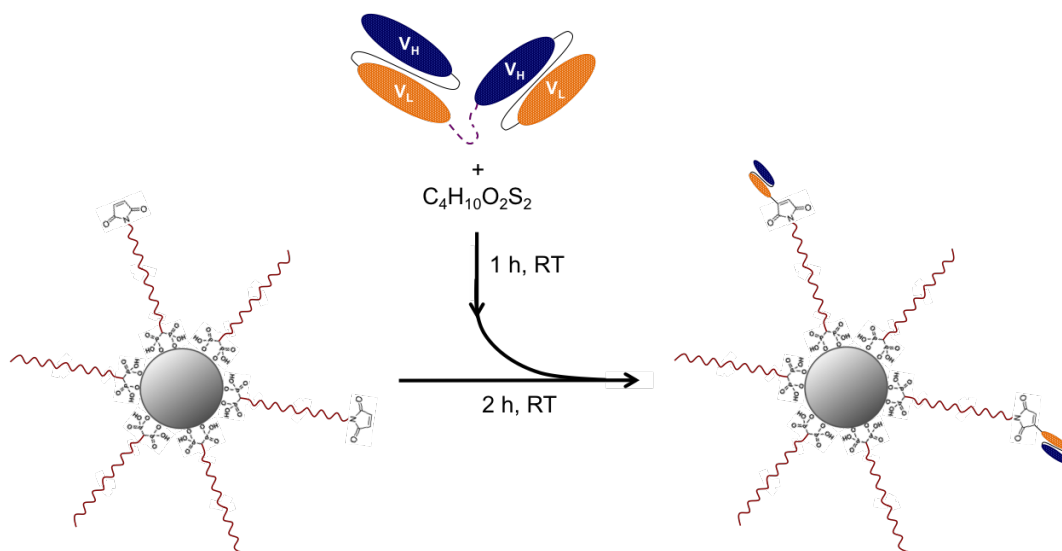
Scheme 2.6: Reaction scheme for the method of targeting of mal-PEG(5)-BP-USPIOs.

Cell binding was tested using two relevant cell lines. The cell line chosen was DU145 which are human prostate cancer cells [140]. The control run was the DU145 cells with no alterations, with the cells then used to examine the targeting properties of the USPIOs being DU145 transduced in order to express PSMA in high levels (DU145-PSMA). To measure binding, FACS was performed requiring the introduction of a fluorophore. The fluorophore was in the form of Penta·His Alexa Fluor 488, a secondary (2°) antibody that binds to the J591 conjugated to the NPs. Three samples of cells where prepared for each cell line to allow for the following to be run: (1) sample containing cells only, (2) sample containing cells incubated with the secondary antibody only, and (3) sample incubated with targeted USPIOs followed by the secondary antibody. The sample incubated with the secondary antibody only was to ensure any uptake observed wasn't from binding of the 2° antibody to PSMA. The FACS results can be seen in figure 2.56. In figure 2.56a, the cells incubated with the 2° antibody only exhibit a shift in signal from the cells background indicating some non-specific binding of Penta·His Alexa Fluor 488. The further shift with the sample containing both the targeting NPs and the 2° antibody again demonstrates non-specific binding, this time due to the USPIOs which is consistent as previously ascertained in figure 2.51. With the
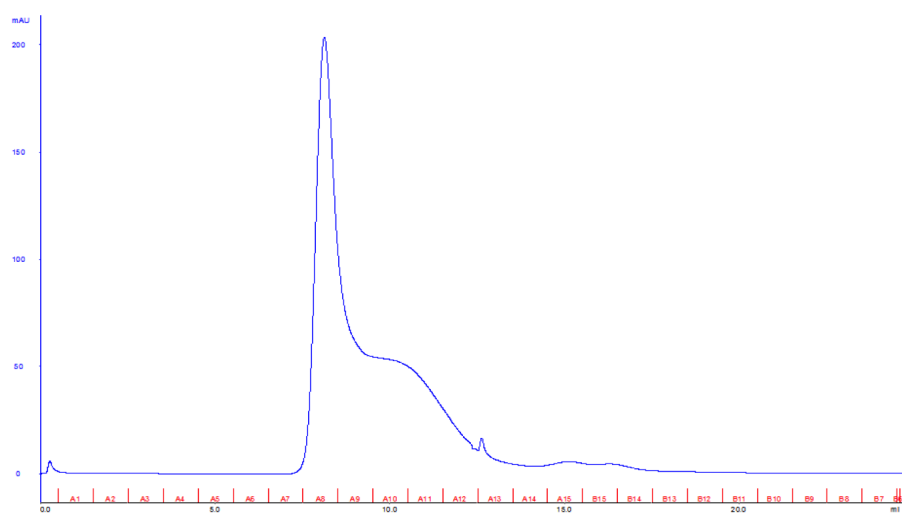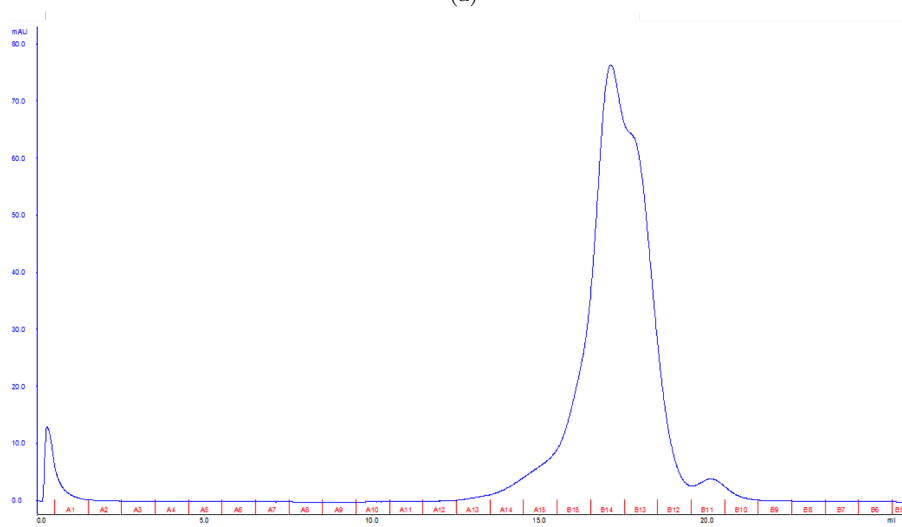
Figure 2.54: Characterisation of maleimide-PEGylated Fe_3O_4 NPs and J591: Size exclusion chromatogram (intensity plot) of (a) mal-PEG(5)-BP-USPIOs in PBS, and (b) J591 in PBS.
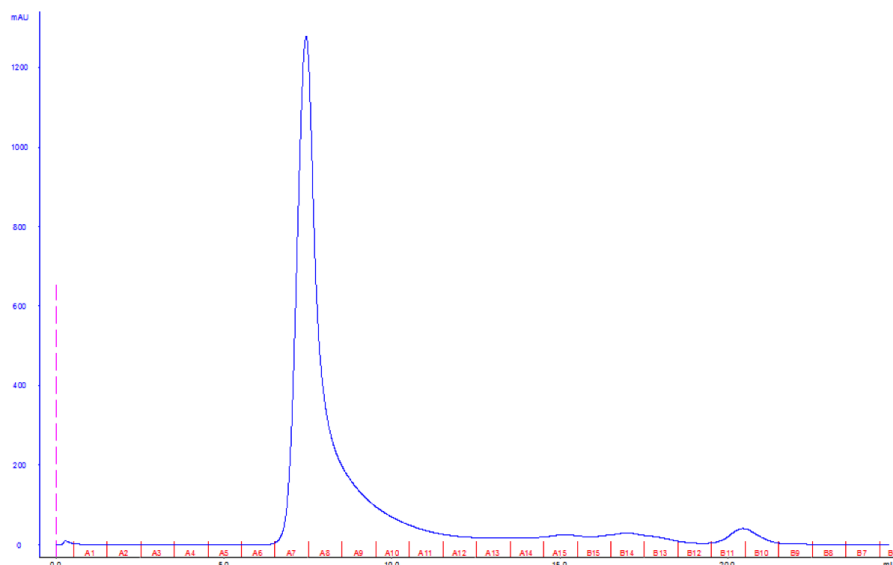
Figure 2.55: Characterisation of J591 targeted Fe_3O_4 NPs: Size exclusion chromatogram (intensity plot) of J591 conjugated to mal-PEG(5)-BP-USPIOs in PBS.

DU145-PSMA, it was hoped that there would be an increase in the shift of the signal for the J591-PEG(5)-BP-USPIOs. Focusing on figure 2.56b, it can be seen that there is again the nonspecific binding of the 2° antibody, but with the targeted USPIOs there is indeed a larger shift which is representative of binding. Note, the broad peak is due to the cells not possessing the same level of expression of the protein accounted for by the inefficiency of the transduction process, and this has also been observed when using J591 only [134]. This result confirms an increase in uptake of the USPIOs, hence proving the concept of targeting PSMA *in vitro*.

The initial approach for radiolabelling the targeted USPIOs was to use the His-tag sequences on the J591 to directly radiolabel (scheme 2.7a) with the technetium tricarbonyl as it is known that His-tags are excellent $[^{99m}Tc(CO)_3]^+$ coordinators [141, 142]. This was attempted alongside the radiolabelled BP method (scheme 2.7b) previously described. Both samples were incubated for 1 h at 37 °C (it was not possible to use the temperature gradient as before as higher temperatures would cause the protein to unfold and hence reduce binding capability). The particles were then purified as before using size exclusion columns, however a combination of a PD MiniTrap (Sephadex G-25 medium) was used followed by a PD MidiTrap (Sephadex G-25 medium) in order to acquire a more concentrated radiolabelled NP sample. Radiolabelling yields were poor for both, direct conjugation resulting in 1 % and BP conjugation gave 4 %, nonetheless this was sufficient enough to enable a cell binding assay to be performed to verify the targeted NPs were still active once the radionuclide had
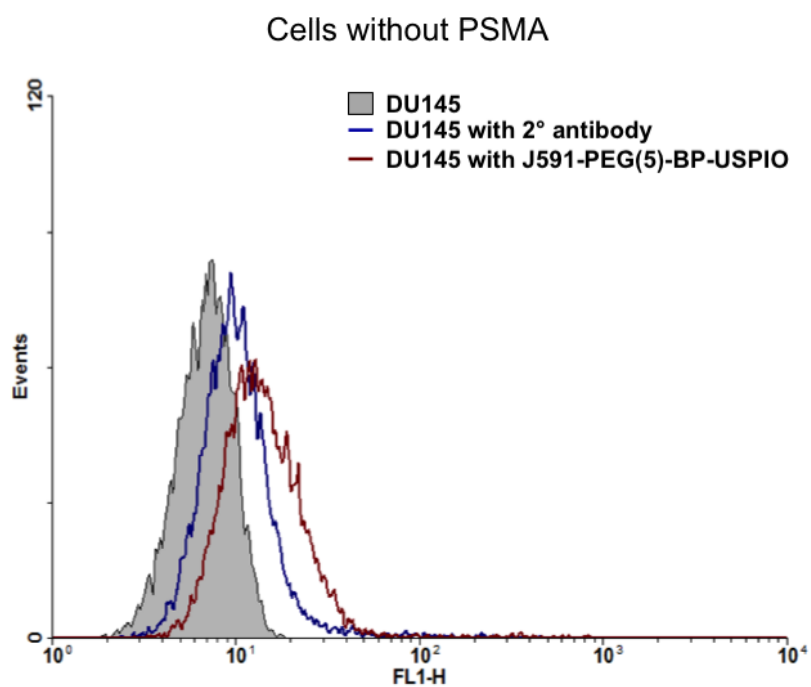
(a)
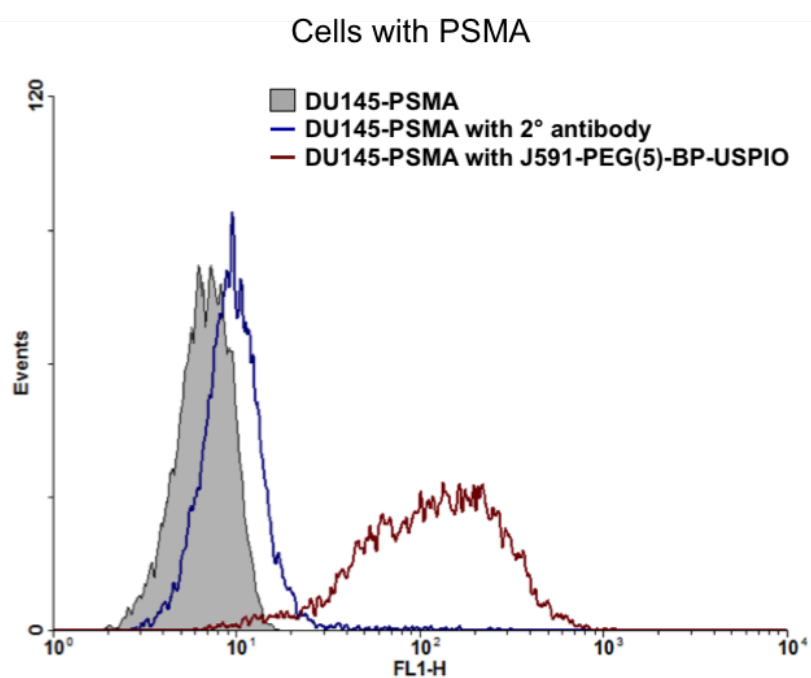
(b)

Figure 2.56: *In vitro* characterisation of J591 targeted Fe_3O_4 NPs: FACS data showing binding of J591-PEG(5)-BP-USPIOs to (a) DU145 cells, and (b) DU145 cells transduced to express PSMA.

been introduced.

(a)

(b)
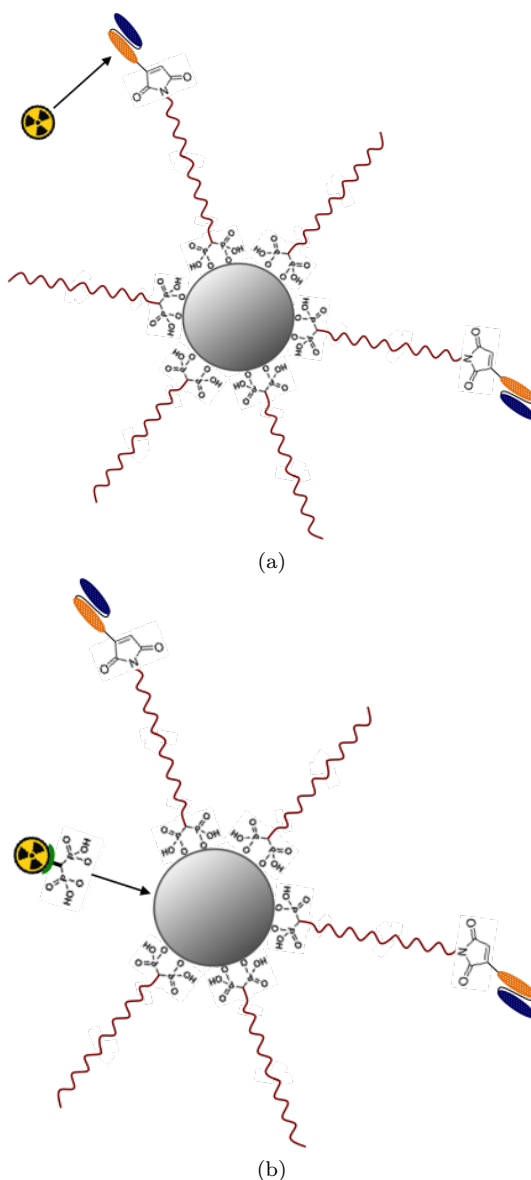
Scheme 2.7: Graphical representation for the methods of radiolabelling of targeted mal-PEG(5)-BP-USPIOs via (a) direct conjugation to Histags, and (b) conjugation using a BP.

The radiolabelled sample (using the BP method) was incubated with DU145 and DU145-PSMA cells, half at 37 °C and half on ice for same period of time. These temperatures were chosen so the binding of the particles to the cell membrane could be investigated (the sample on ice) as well as the binding at the physiological temperature (the sample at 37 °C). The plot in figure 2.57 shows higher activity present in the transduced cells, with increased uptake exhibited by the cells incubated with the NPs at 37 °C. This result was expected due to internalisation processes occurring.
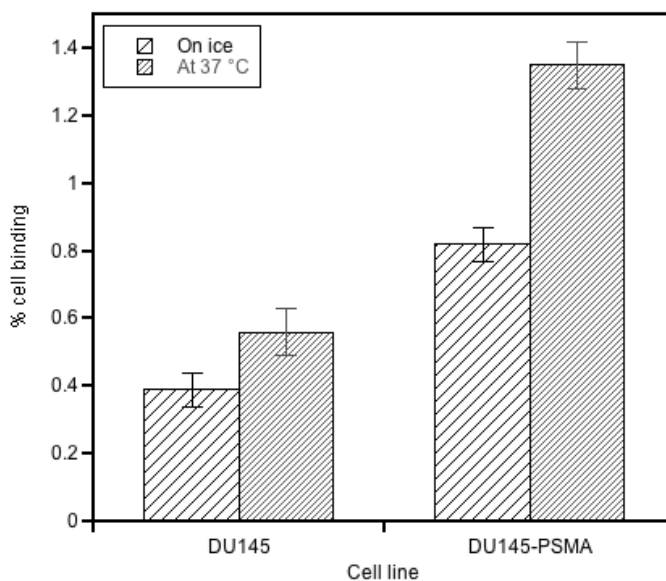
Figure 2.57: *In vitro* characterisation of radiolabelled J591 targeted Fe_3O_4 NPs: Cell binding of radiolabelled J591-PEG(5)-BP-USPIOs.

2.8.3 Vascular Cell Adhesion Protein 1

The next target to be investigated was vascular cell adhesion protein 1 (VCAM-1). This is expressed on activated endothelial cells and its role is to recruit lymphocytes and monocytes during the early stages of inflammation and atherogenesis, leading to plaque formation. This makes VCAM-1 an attractive target for early imaging and therapy of atherosclerosis [143–149]. The conjugation method was identical to that of PSMA (scheme 2.6), however in this case the antibody fragment used was called 6C7.1 [150]. Due to the successful separation of excess antibody fragment from the targeted USPIOs above, purification was performed using the ÄKTA. Again, two distinct peaks were observed very similar to previous observations, as can be seen in figure 2.58.

Cell binding studies were implemented in same way as for the PSMA studies. The cell line chosen was HEK 293T, a derivative of the human embryonic kidney 293 cells. One main reason this cell line was selected is due to the fact that they are highly transfectable [151] allowing for high levels of expression of VCAM-1 (this cell line has been labeled HEK 293T VCAM). As before, the samples run were (1) sample containing cells only, (2) sample containing cells incubated with the secondary antibody (as before) only, and (3) sample incubated with targeted USPIOs (6C7.1-PEG(5)-BP-USPIOs) followed by the secondary antibody. However, an additional control of the antibody fragment tagged with fluorescein
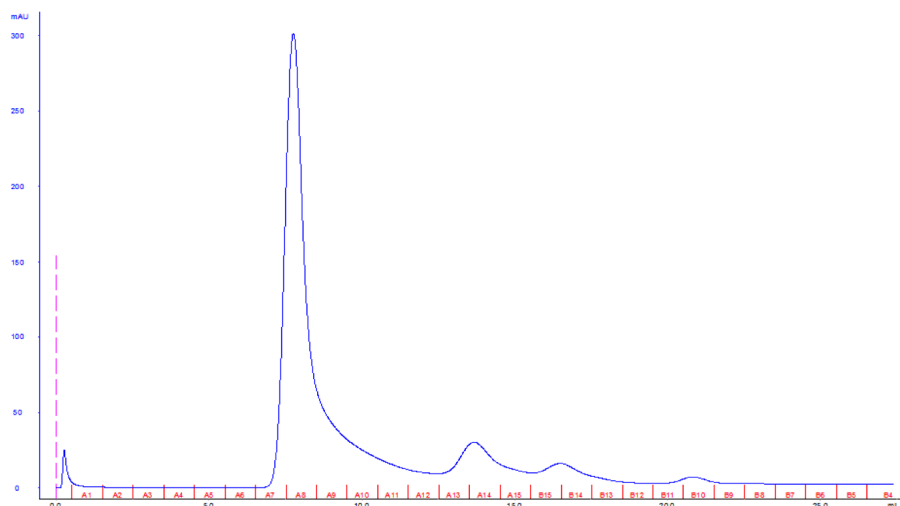
Figure 2.58: Characterisation of 6C7.1 targeted Fe$_3$O$_4$ NPs: Size exclusion chromatogram (intensity plot) of 6C7.1 conjugated to mal-PEG(5)-BP-USPIOs in PBS.

was conducted. This is known to target VCAM-1 from previous work in the group, and was used to verify any uptake detected was as a consequence of binding to the correct receptor.

Figure 2.59a displays some non-specific binding of both the 2° antibody and 6C7.1-PEG(5)-BP-USPIOs, yet no shift is observed for the fluorescein conjugated antibody fragment. Examining figure 2.59b reveals a significantly larger shift for both the targeted USPIOs and the fluorescein conjugated particles confirming targeted binding of the particles. The notably broad peak is due to the poor efficiency of transfection which leaves some cells expressing none of the receptor, and others expressing VCAM-1 to a higher degree. Again, this has been observed when using 6C7.1 only.

Once it was established that the targeting modality was successful, the next stage was to introduce the radionuclide. This time only the bisphosphonate method was carried out due to the slightly higher radiolabelling yield, again at 37 °C in order to prevent any damage to the antibody fragment. Once radiolabelling was complete, the particles were purified using the ÄKTA. Plot 2.60 shows two peaks, the first corresponds to radiolabelled NPs and the second to unbound radiolabelled BP. The fractions were collected and the activity counted (figure 2.61). It was found that the majority of the activity had not bound to the particles, in fact only 0.5 MBq (radiolabelling yield of 0.4 %) appeared to have associated with the USPIOs. It is assumed that this particularly low yield is a result of no longer being able to use a temperature gradient during the labelling procedure.
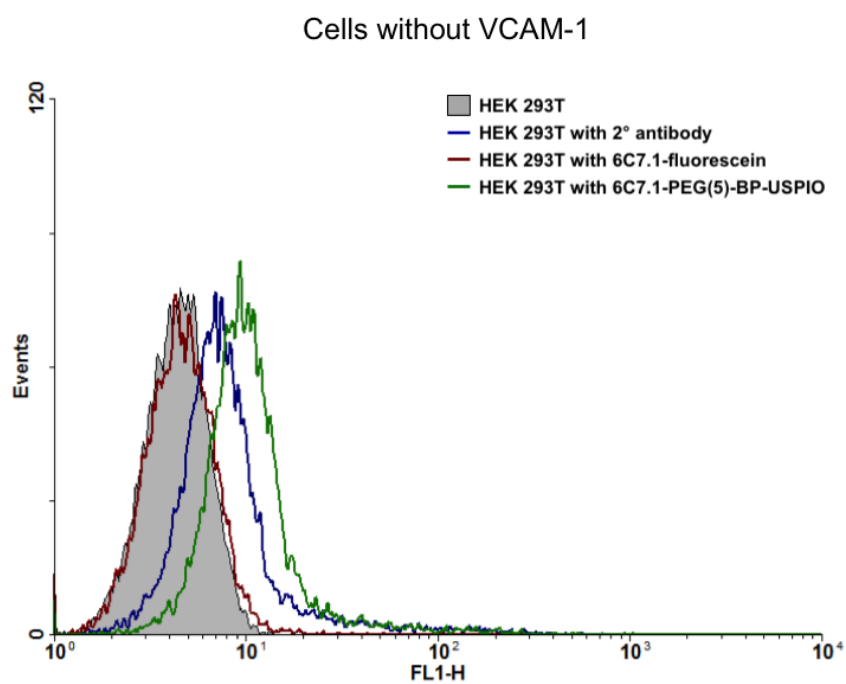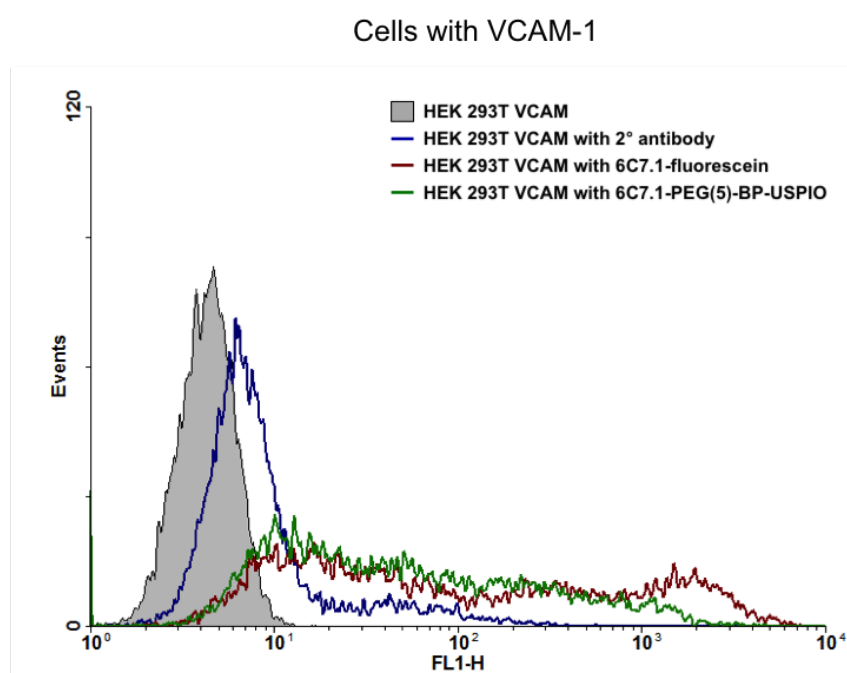
Figure 2.59: *In vitro* characterisation of 6C7.1 targeted Fe_3O_4 NPs: FACS data showing binding of 6C7.1-PEG(5)-BP-USPIOs to (a) HEK 293T cells, and (b) HEK 293T cells transfected to express VCAM-1.
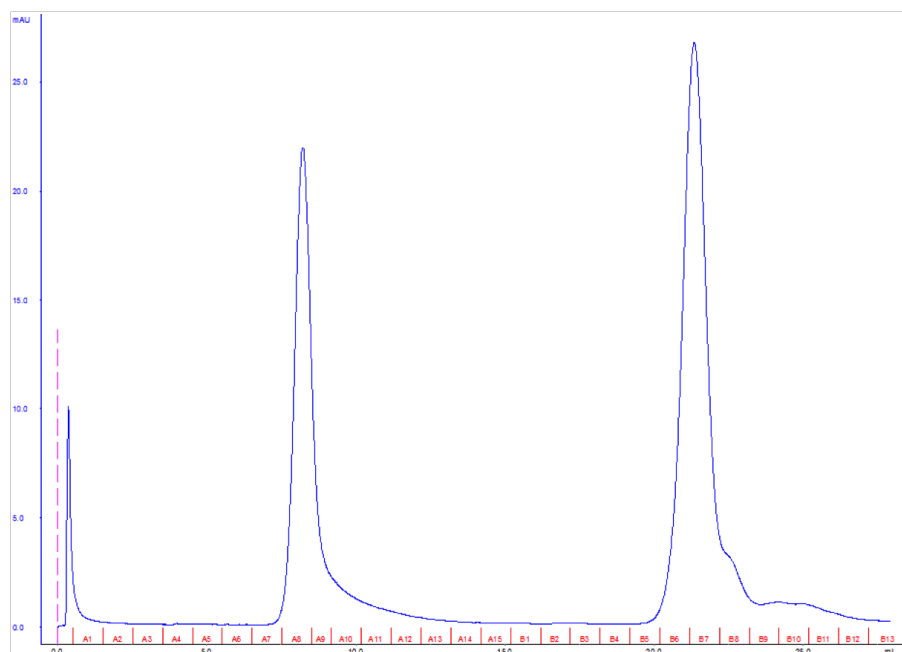
Figure 2.60: Characterisation of radiolabelled 6C7.1 targeted Fe_3O_4 NPs: Size exclusion chromatogram (intensity plot) of radiolabelled 6C7.1-PEG(5)-BP-USPIOs.
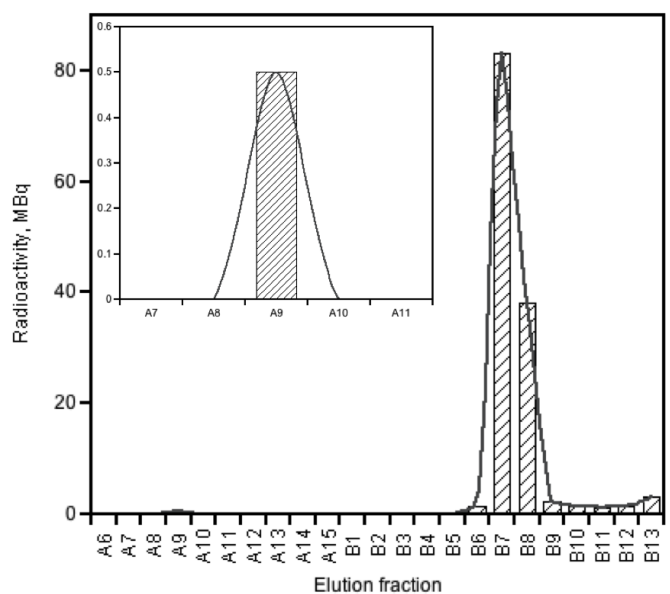
Figure 2.61: Characterisation of radiolabelled 6C7.1 targeted Fe_3O_4 NPs: Elution profile of radiolabelled 6C7.1-PEG(5)-BP-USPIOs

A cell binding experiment was performed thereafter with the radiolabelled NP fractions obtained (fraction A9 in figure 2.61), again to ensure the radiolabel was having no detrimental effect on the targeting abilities of the particles. As was confirmed with PSMA studies, introducing ^{99m}Tc did not impair VCAM-1 targeting. Figure 2.62 shows a higher count is present in the transfected cells, with some activity in the control cells due to nonspecific uptake which was previously established by FACS. This indicates the targeted USPIOs bind to the VCAM-1 positive cells to a far greater degree than to the VCAM-1 negative cells. The data collected here confirms that after radiolabelling, the targeting aspect of the USPIOs remains.
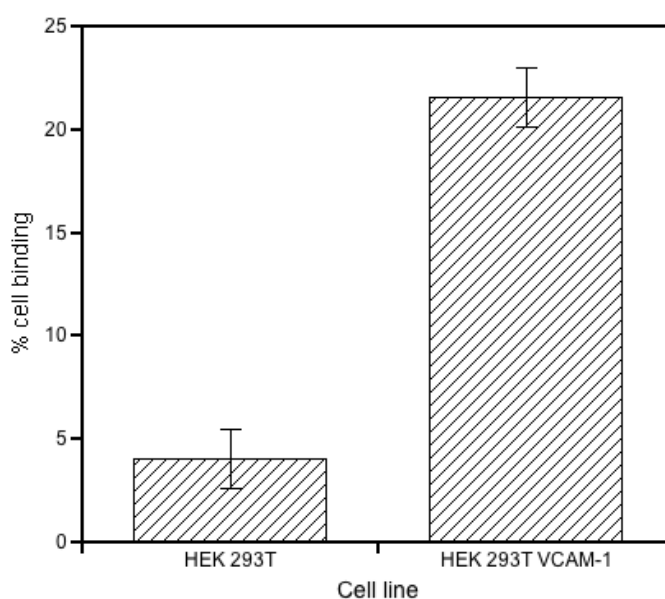
Figure 2.62: *In vitro* characterisation of radiolabelled 6C7.1 targeted Fe_3O_4 NPs: Cell binding of radiolabelled 6C7.1-PEG(5)-BP-USPIOs

Despite the poor efficient of the radiolabelling procedure, no further investigation into routes for improvement were conducted due to the limited quantities of the antibody fragment available.

2.8.4 p32 receptor

The next targeting moiety chosen was a 9-amino acid cyclic peptide called LyP-1 [152]. Previous studies on MDA-MB-435 cells has identified that LyP-1 binds to tumours, in particular the receptor p32 [153–155]. Human p32 (also known as SF2-associated p32, p32/TAP, and gC1qR) has a doughnut-shaped quaternary structure formed from three molecules re-

sulting in a considerable central channel and an asymmetric charge distribution on the surface [156]. This receptor is intracellular in normal cells but is extracellular and over expressed not only in the tumour but in several compartments, for example the lymphatics and tumour-associated macrophages [157, 158]. It has also been shown that LyP-1 has NP tumour penetrating properties [159–162].

The method used for conjugating the LyP-1 peptide to the USPIOs was similar to the previous two targeting functionalisations, however in this case the first step of reducing the disulphide bonds with DTT was not required. As before, purification was performed using the ÄKTA system. Figure 2.63 shows the profile of the eluted sample, with the distinct separation of the particles and peptide as expected.
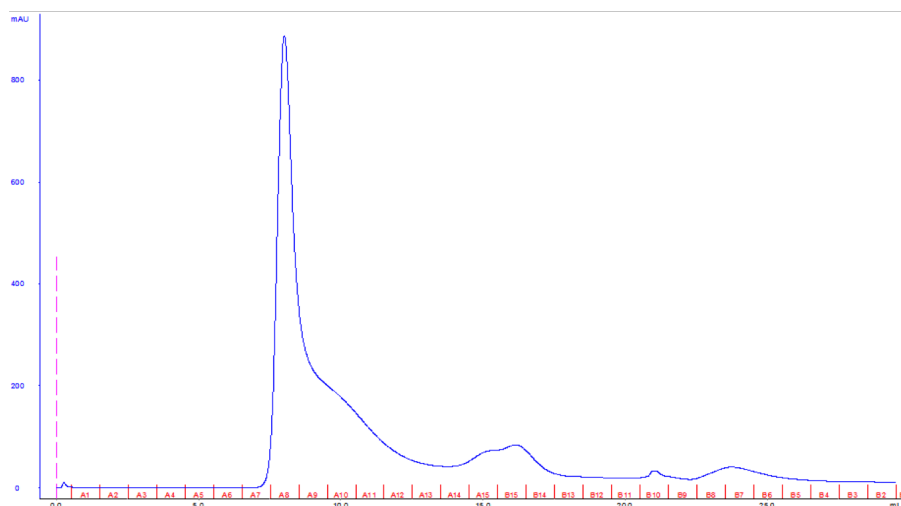
Figure 2.63: Characterisation of LyP-1 targeted Fe_3O_4 NPs: Size exclusion chromatogram (intensity plot) of LyP-1-PEG(5)-BP-USPIOs.

In order to ensure introduction of the peptide wasn't inducing particle core etching, TEM imaging was performed. Figure 2.64 shows LyP-1-PEG(5)-BP-USPIOs and it can be seen that there was no change in D_{TEM} (5.7 ± 0.8 nm based on the measurement of 100 particles).

Fogal *et al.* identified several cell lines expressing p32 on the surface, including MDA-MB-435, MDA-MB-231 and MCF7 (human breast cancer cell lines), and finally 4T1 (mouse breast cancer cells) [159]. Due to the highest uptake being observed with MDA-MB-435 cells, these were the focus of the cell binding analysis, which were performed in same way as for the PSMA and VCAM-1 studies. Several samples were run: (1) sample containing cells only, (2) sample containing cells incubated with LyP-1 tagged with a fluorescent
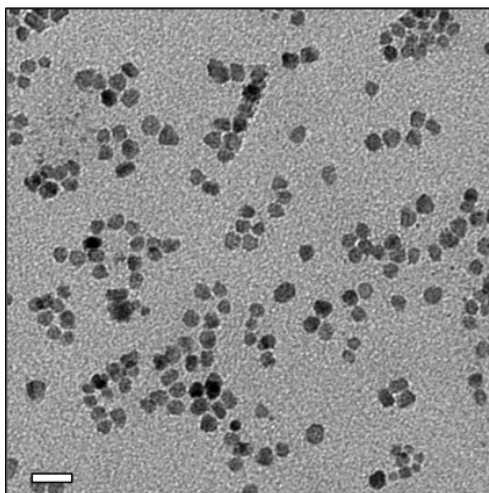
Figure 2.64: Characterisation of LyP-1 targeted Fe_3O_4 NPs: TEM micrograph of a dispersion in water ($D_{\text{TEM}} = 5.7 \pm 0.8$ nm based on measurement of 100 particles). Scale bar is 20 nm.

component (carboxytetramethylrhodamine; TAMRA), (3) sample incubated with targeted USPIOs (functionalised using the TAMRA tagged LyP-1), and (4) a blocking experiment whereby the cells were initially incubated with a non-fluorescent version of the LyP-1 peptide (85 μM) for 30 min at 37 °C, followed by incubation with the targeted NPs. The results revealed maximum uptake from the blocking experiment which appears to be equivalent to the shift detected with the targeted NPs plus the shift from the peptide only. The observed increase in accumulation may have been a result of the blocking peptide aiding in NP uptake. The FACS results were then corroborated using fluorescence microscopy. Images obtained are of cells only (figure 2.66a), blocking peptide and the targeted NPs (figure 2.66b), then two concentrations of targeted NPs, 25 μL (figure 2.66c) and 200 μL (figure 2.66d). The images gathered from the fluorescent peptide only were too bright to show. It can be seen that the microscopy confirms the results collected from FACS.

2.9 Conclusions

The phase transfer of a PEG polymer containing a bisphosphonate anchor for strong binding to the surface of iron oxide materials has been described, and is capable of generating hydrophilic USPIOs using a simple and fast method. Using this method, a colloidally stable PEGylated USPIO has been synthesised that can be stored as a dispersion in water or saline for several months without changes in D_{H}. PEG(5)-BP-USPIOs could be used as
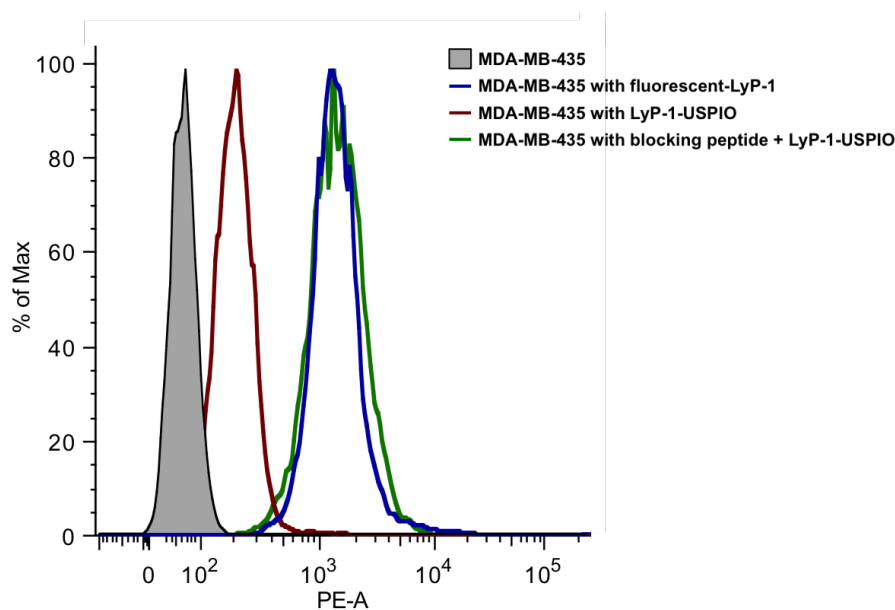
Figure 2.65: FACs data showing binding of LyP-1-PEG(5)-BP-USPIOs to MDA-MB-435 cells.

an effective contrast agent for T_1-weighted imaging, which is attributed to the high r_1 and low r_2 relaxivities, a result of the optimal size of the superparamagnetic iron oxide core and stable hydrophilic coating. From reviewing the literature it appears these may be the highest r_1 and lowest r_2/r_1 (2.97) reported to date at B_0 of 3 T. *In vivo* studies demonstrated the potential of PEG(5)-BP-USPIOs as a contrast agent for MRI angiography. After intravenous injection in mice, the signal in the blood increased 6-fold for the duration of the experiment at a lower dose (4-fold) of contrast agent compared to other USPIOs to obtain a similar signal enhancement. The MRI study revealed minor accumulation of USPIOs in the liver. PEG(5)-BP-USPIOs could also be radiolabelled using a BP, [99mTc]-DPA-ale, that allowed tracking of the NPs using SPECT imaging with high sensitivity and quantification capabilities. The *in vivo* imaging study confirmed the MRI results, showing long blood circulation times ($t_{1/2} = 2.97$ h). In addition, the SPECT study provided important information about the fate of PEG(5)-BP-USPIOs and its components. [99mTc]-DPA-ale was slowly released into the urine and the bloodstream and led to the hypothesis that the same maybe occurring to PEG(5)-BP. Interestingly, uptake in the kidneys suggested this organ is playing a role in the decomposition of PEG(5)-BP-USPIOs. Further studies, however, are warranted to understand its excretion properties. Targeting studies were performed to examine the ability to functionalise these particles in order to provide better detectability and quantification capabilities of vascular targets involved in cardiovascular and oncologic diseases. *In vitro* cell binding studies were performed on three individual targets, PSMA, VCAM-1 and p32,
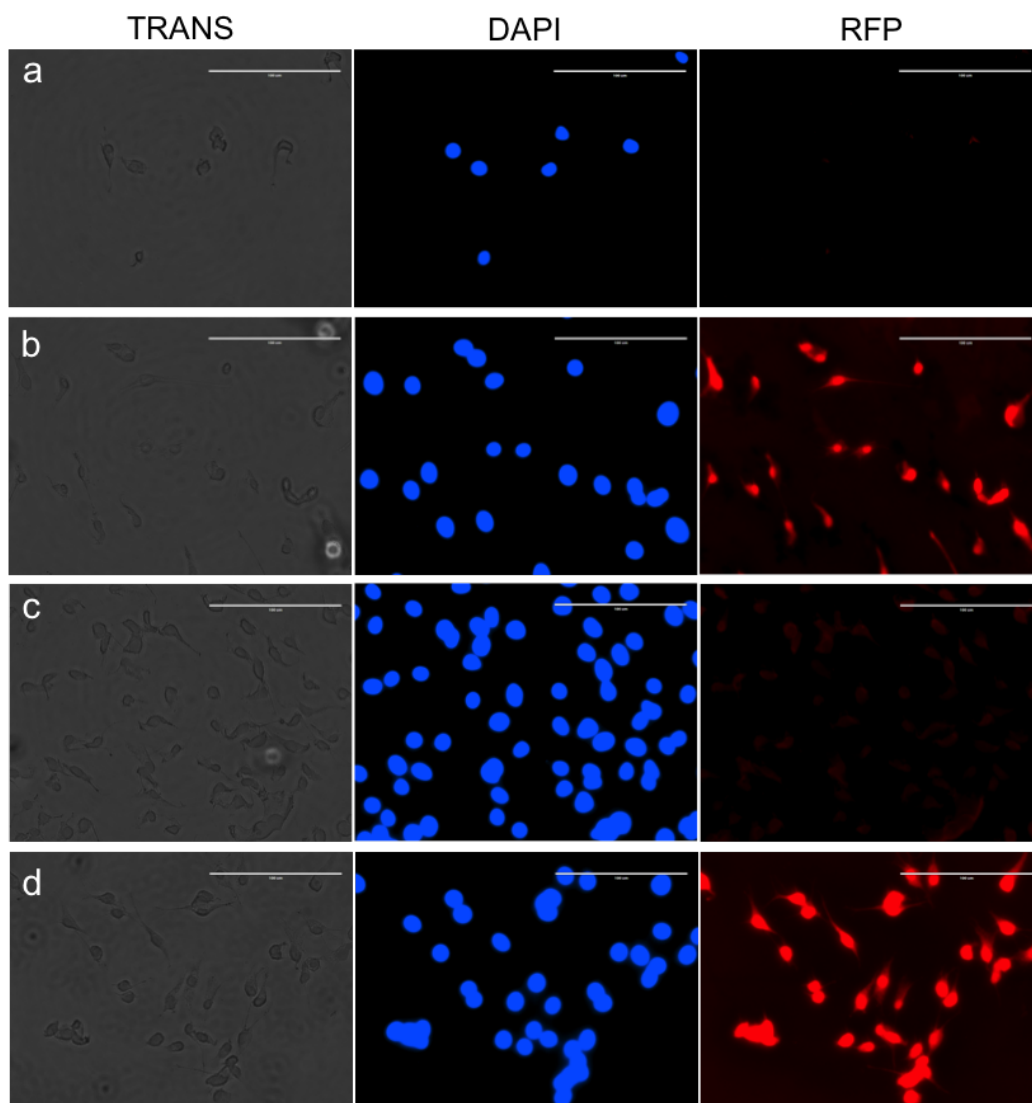
Figure 2.66: *In vitro* characterisation of LyP-1 targeted Fe_3O_4 NPs: Fluorescence microscopy images of (a) MDA-MB-435 cells only, (b) MDA-MB-435 cells incubated with blocking peptide followed by 200 μL of LyP-1-mal-PEG(5)-BP-USPIOs, (c) MDA-MB-435 cells incubated with 25 μL of LyP-1-PEG(5)-BP-USPIOs, and (d) MDA-MB-435 cells incubated with 200 μL of LyP-1-PEG(5)-BP-USPIOs.

and revealed successful binding in all cases as proved by FACS and fluorescence microscopy. In addition, once the radionuclide component had been introduced into the coating of the targeted particles, cell binding was still observed, demonstrating the potential of this probe to be used for targeted dual modality applications.

This work demonstrates that the surface functionalisation with PEG-BPs is an effective method for developing highly stable USPIOs with low RES uptake and long blood circulation times, which are the major limitations in the development of targeted USPIOs for biomedical imaging. Furthermore, PEG(5)-BP-USPIOs represent a promising platform for the development of agents for multimodal medical imaging and these compounds could find applications with the new generation of multimodal clinical scanners.

Bibliography

[1] S. Yu and G. M. Chow. Synthesis of Monodisperse Iron Oxide and Iron/Iron Oxide Core/Shell Nanoparticles via Iron-Oleylamine Complex. *J. Nanosci. Nanotechnol.*, 6: 2135–2140, **2006**.

[2] Y. Yu, W. Yang, X. Sun, W. Zhu, X-Z. Li, D. J. Sellmyer, and S. Sun. Monodisperse MPt (M = Fe, Co, Ni, Cu, Zn) Nanoparticles Prepared from a Facile Oleylamine Reduction of Metal Salts. *Nano Lett.*, 14: 2778–2782, **2014**.

[3] W. S. Seo, H. H. Jo, K. Lee, B. Kim, S. J. Oh, and J. T. Park. Size-Dependent Magnetic Properties of Colloidal Mn_3O_4 and MnO Nanoparticles. *Angew. Chem. Int. Ed.*, 43: 1115–1117, **2004**.

[4] W. S. Seo, J. H. Shim, S. J. Oh, E. K. Lee, N. H. Hur, and J. T. Park. Phase- and Size-Controlled Synthesis of Hexagonal and Cubic CoO Nanocrystals. *J. Am. Chem. Soc.*, 127: 6188–6189, **2005**.

[5] C. Wang, S. Peng, L-M. Lacroix, and S. Sun. Synthesis of High Magnetic Moment CoFe Nanoparticles via Interfacial Diffusion in Core/Shell Structured Co/Fe Nanoparticles. *Nano Res.*, 2: 380–385, **2009**.

[6] T. K. Jain, M. A. Morales, S. K. Sahoo, D. L. Leslie-Pelecky, and V. Labhasetwar. Iron Oxide Nanoparticles for Sustained Delivery of Anticancer Agents. *Mol. Pharmaceutics*, 2: 194–205, **2005**.

[7] L. Zhang, R. He, and H-C. Gu. Oleic Acid Coating on the Monodisperse Magnetite Nanoparticles. *Appl. Surf. Sci.*, 253: 2611–2617, **2006**.

[8] K. Woo, J. Hong, S. Choi, H-W. Lee, J-P. Ahn, C. S. Kim, and S. W. Lee. Easy Synthesis and Magnetic Properties of Iron Oxide Nanoparticles. *Chem. Mater.*, 16: 2814–2818, **2004**.

[9] N. Wu, L. Fu, M. Su, M. Aslam, K. C. Wong, and V. P. Dravid. Interaction of Fatty Acid Monolayers with Cobalt Nanoparticles. *Nano Lett.*, 4: 383–386, **2004**.

[10] G. Kataby, M. Cojocaru, R. Prozorov, and A. Gedanken. Coating Carboxylic Acids on Amorphous Iron Nanoparticles. *Langmuir*, 15: 1703–1708, **1999**.

[11] S. Mourdikoudis and L. M. Liz-Marzán. Oleylamine in Nanoparticle Synthesis. *Chem. Mater.*, 25: 1465–1476, **2013**.

[12] Y. Ma, J. Zeng, W. Li, M. McKiernan, Z. Xie, and Y. Xia. Seed-Mediated Synthesis of Truncated Gold Decahedrons with a AuCl/Oleylamine Complex as Precursor. *Adv. Mater.*, 22: 1930–1934, **2010**.

[13] X. Liu, M. Atwater, J. Wang, Q. Dai, J. Zou, J. P. Brennan, and Q. Huo. A Study on Gold Nanoparticle Synthesis Using Oleylamine as Both Reducing Agent and Protecting Ligand. *J. Nanosci. Nanotechnol.*, 7: 3126–3133, **2007**.

[14] K.M. Nam, J.H. Shim, H. Ki, S-I. Choi, G. Lee, J.K. Jang, Y. Jo, M-H. Jung, H. Song, and J.T. Park. Single-Crystalline Hollow Face-Centered-Cubic Cobalt Nanoparticles from Solid Face-Centered-Cubic Cobalt Oxide Nanoparticles. *Angew. Chem. Int. Ed.*, 47: 9504–9508, **2008**.

[15] M. Mohapatra and S. Anand. Synthesis and Applications of Nano-Structured Iron Oxides/Hydroxides – A Review. *Int. J. Eng. Sci Technol.*, 2: 127–146, **2010**.

[16] Z. Xu, C. Shen, Y. Hou, H. Gao, and S. Sun. Oleylamine as Both Reducing Agent and Stabilizer in a Facile Synthesis of Magnetite Nanoparticles. *Chem. Mater.*, 21: 1778–1780, **2009**.

[17] S. Sun and H. Zeng. Size-Controlled Synthesis of Magnetite Nanoparticles. *J. Am. Chem. Soc.*, 124: 8204–8205, **2002**.

[18] J. Park, K. An, Y. Hwang, J-G. Park, H-J. Noh, J-Y. Kim, J-H. Park, N-M. Hwang, and T. Hyeon. Ultra-Large-Scale Syntheses of Monodisperse Nanocrystals. *Nat. Mater.*, 3: 891–895, **2004**.

[19] E. Amstad, M. Textor, and E. Reimhult. Stabilization and Functionalization of Iron Oxide Nanoparticles for Biomedical Applications. *Nanoscale*, 3: 2819–2843, **2011**.

[20] C. Marianecci, M. Carafa, L. Di Marzio, F. Rinaldi, C. Di Meo, P. Matricardi, F. Alhaique, and T. Coviello. A New Vesicle-loaded Hydrogel System Suitable for Topical Applications: Preparation and Characterization. *J. Pharm. Pharmaceut. Sci.*, 14: 336–346, **2011**.

[21] J-Y. Kim, J-K. Kim, J-S. Park, Y. Byun, and C-K. Kim. The Use of PEGylated Liposomes to Prolong Circulation Lifetimes of Tissue Plasminogen Activator. *Biomaterials*, 30: 5751–5756, **2009**.

[22] D. D. Verma, S. Verma, G. Blume, and A. Fahr. Particle Size of Liposomes Influences Dermal Delivery of Substances into Skin. *Int. J. Pharm.*, 258: 141–151, **2003**.

[23] C. A. Crouse and A. R. Barron. Reagent Control Over the Size, Uniformity, and Composition of Co-Fe-O Nanoparticles. *J. Mater. Chem.*, 18: 4146–4153, **2008**.

[24] A. P. LaGrow, B. Ingham, M. F. Toney, and R. D. Tilley. Effect of Surfactant Concentration and Aggregation on the Growth Kinetics of Nickel Nanoparticles. *J. Phys. Chem. C*, 117: 16709–16718, **2013**.

[25] Y. C. Han, H. G. Cha, C. W. Kim, Y. H. Kim, and Y. S. Kang. Synthesis of Highly Magnetized Iron Nanoparticles by a Solventless Thermal Decomposition Method. *J. Phys. Chem. C*, 111: 6275–6280, **2007**.

[26] H. G. Cha, D. K. Lee, Y. H. Kim, C. W. Kim, C. S. Lee, and Y. S. Kang. Solventless Nanoparticles Synthesis under Low Pressure. *Inorg. Chem.*, 47: 121–127, **2008**.

[27] H. Cui, Y. Feng, W. Ren, T. Zeng, H. Lv, and Y. Pan. Strategies of Large Scale Synthesis of Monodisperse Nanoparticles. *Recent Pat. Nanotechnol.*, 3: 32–41, **2009**.

[28] C. C. Yec and H. C. Zeng. Synthesis of Complex Nanomaterials via Ostwald Ripening. *J. Mater. Chem. A*, 2: 4843–4851, **2014**.

[29] M. Nakaya, R. Nishida, and A. Muramatsu. Size Control of Magnetite Nanoparticles in Excess Ligands as a Function of Reaction Temperature and Time. *Molecules*, 19: 11395–11403, **2014**.

[30] D. Maity, J. Ding, and J-M. Xue. Synthesis of Magnetite Nanoparticles by Thermal Decomposition: Time, Temperature, Surfactant and Solvent Effects. *Funct. Mater. Lett.*, 01: 189–193, **2008**.

[31] T. Gelbrich, M. Feyen, and A. M. Schmidt. Magnetic Thermoresponsive Core-Shell Nanoparticles. *Macromolecules*, 39: 3469–3472, **2006**.

[32] U. I. Tromsdorf, O. T. Bruns, S. C. Salmen, U. Beisiegel, and H. Weller. A Highly Effective, Nontoxic T1 MR Contrast Agent Based on Ultrasmall PEGylated Iron Oxide Nanoparticles. *Nano. Lett.*, 9: 4434–4440, **2009**.

[33] A. Mori, A. L. Klibanov, V. P. Torchilin, and L. Huang. Influence of the Steric Barrier Activity of Amphipathic Poly(ethyleneglycol) and Ganglioside GM1 on the Circulation Time of Liposomes and on the Target Binding of Immunoliposomes *In Vivo*. *FEBS Lett.*, 284: 263–266, **1991**.

[34] E. Amstad, T. Gillich, I. Bilecka, M. Textor, and E. Reimhult. Ultrastable Iron Oxide Nanoparticle Colloidal Suspensions Using Dispersants with Catechol-Derived Anchor Groups. *Nano Lett.*, 9: 4042–4048, **2009**.

[35] B. H. Kim, N. Lee, H. Kim, K. An, Y. I. Park, Y. Choi, K. Shin, Y. Lee, S. G. Kwon, H. B. Na, J-G. Park, T-Y. Ahn, Y-W. Kim, W. K. Moon, S. H. Choi, and T. Hyeon. Large-Scale Synthesis of Uniform and Extremely Small-Sized Iron Oxide Nanoparticles for High-Resolution T1 Magnetic Resonance Imaging Contrast Agents. *J. Am. Chem. Soc.*, 133: 12624–12631, **2011**.

[36] F. Q. Hu, L. Wei, Z. Zhou, Y. L. Ran, Z. Li, and M. Y. Gao. Preparation of Biocompatible Magnetite Nanocrystals for *In Vivo* Magnetic Resonance Detection of Cancer.

Adv. Mater., 18: 2553–2556, **2006**.

[37] E. Amstad, A. U. Gehring, H. Fischer, V. V. Nagaiyanallur, G. Hähner, M. Textor, and E. Reimhult. Influence of Electronegative Substituents on the Binding Affinity of Catechol-Derived Anchors to Fe_3O_4 Nanoparticles. *J. Phys. Chem. C*, 115: 683–691, **2011**.

[38] A. K. L. Yuen, G. A. Hutton, A. F. Masters, and T. Maschmeyer. The Interplay of Catechol Ligands with Nanoparticulate Iron Oxides. *Dalton Trans.*, 41: 2545–2559, **2012**.

[39] M. D. Shultz, J. U. Reveles, S. N. Khanna, and E. E. Carpenter. Reactive Nature of Dopamine as a Surface Functionalization Agent in Iron Oxide Nanoparticles. *J. Am. Chem. Soc.*, 129: 2482–2487, **2007**.

[40] J. Xie, C. Xu, N. Kohler, Y. Hou, and S. Sun. Controlled PEGylation of Monodisperse Fe_3O_4 Nanoparticles for Reduced Non-Specific Uptake by Macrophage Cells. *Adv. Mater.*, 19: 3163–3166, **2007**.

[41] C. Allen, N. Dos Santos, R. Gallagher, G. N. C. Chiu, Y. Shu, W. M. Li, S. A. Johnstone, A. S. Janoff, L. D. Mayer, M. S. Webb, and M. B. Bally. Controlling the Physical Behavior and Biological Performance of Liposome Formulations Through Use of Surface Grafted Poly(ethylene glycol). *Biosci. Rep.*, 22: 225–250, **2002**.

[42] J. V. Jokerst, T. Lobovkina, R. N. Zare, and S. S. Gambhir. Nanoparticle PEGylation for Imaging and Therapy. *Nanomedicine*, 6: 715–728, **2011**.

[43] T. J. Daou, S. Buathong, D. Ung, B. Donnio, G. Pourroy, D. Guillon, and S. Bégin. Investigation of the Grafting Rate of Organic Molecules on the Surface of Magnetite Nanoparticles as a Function of the Coupling Agent. *Sensor. Actuat. B-Chem.*, 126: 159–162, **2007**.

[44] S. Sun, H. Zeng, D. B. Robinson, S. Raoux, P. M. Rice, S. X. Wang, and G. Li. Monodisperse MFe_2O_4 (M = Fe, Co, Mn) Nanoparticles. *J. Am. Chem. Soc.*, 126: 273–279, **2004**.

[45] H. El-Ghandoor, H. M. Zidan, M. M. H. Khalil, and M. I. M. Ismail. Synthesis and Some Physical Properties of Magnetite (Fe_3O_4) Nanoparticles. *Int. J. Electrochem. Sci.*, 7: 5734–5745, **2012**.

[46] W. Wu, X. Xiao, S. Zhang, H. Li, X. Zhou, and C. Jiang. One-Pot Reaction and Subsequent Annealing to Synthesis Hollow Spherical Magnetite and Maghemite Nanocages. *Nanoscale Research Letters*, 4(8):926–931, 2009.

[47] H. Yang, T. Ogawa, D. Hasegawa, and M. Takahashi. Synthesis and Magnetic Prop-

erties of Monodisperse Magnetite Nanocubes. *J. Appl. Phys.*, 103: 07D526, **2008**.

[48] X. Li, H. Si, J. Z. Niu, H. Shen, C. Zhou, H. Yuan, H. Wang, L. Ma, and L. S. Li. Size-Controlled Syntheses and Hydrophilic Surface Modification of Fe_3O_4, Ag, and Fe_3O_4/Ag Heterodimer Nanocrystals. *Dalton Trans.*, 39: 10984–10989, **2010**.

[49] S. V. Ganachari, V. K. Joshi, R. Bhat, R. Deshpande, B. Salimath, N. V. S. Rao, and A. Venkataraman. Large Scale Synthesis and Characterization of γ-Fe_2O_3 Nanoparticles by Self-Propagating Low Temperature Combustion Method. *Int. J. Sci. Res.*, 1: 77–79, **2012**.

[50] H. S. Choi, W. Liu, P. Misra, E. Tanaka, J. P. Zimmer, B. I. Ipe, M. G. Bawendi, and J. V. Frangioni. Renal Clearance of Quantum Dots. *Nat. Biotech.*, 25: 1165–1170, **2007**.

[51] S-D. Li and L. Huang. Pharmacokinetics and Biodistribution of Nanoparticles. *Mol. Pharm.*, 5: 496–504, **2008**.

[52] Y. Tian, B. Yu, X. Li, and K. Li. Facile Solvothermal Synthesis of Monodisperse Fe_3O_4 Nanocrystals with Precise Size Control of One Nanometre as Potential MRI Contrast Agents. *J. Mater. Chem.*, 21: 2476–2481, **2011**.

[53] E. K. U. Larsen, T. Nielsen, T. Wittenborn, H. Birkedal, T. Vorup-Jensen, M. H. Jakobsen, L. Østergaard, M. R. Horsman, F. Besenbacher, K. A. Howard, and J. Kjems. Size-Dependent Accumulation of PEGylated Silane-Coated Magnetic Iron Oxide Nanoparticles in Murine Tumors. *ACS Nano*, 3: 1947–1951, **2009**.

[54] V. DiNoto. A Novel Polymer Electrolyte Based on Oligo(ethylene glycol) 600, K_2PdCl_4, and $K_3Fe(CN)_6$. *J. Mater. Res.*, 12: 3393–3403, **1997**.

[55] B. Y. Yu and S-Y. Kwak. Assembly of Magnetite Nanocrystals into Spherical Mesoporous Aggregates with a 3-D Wormhole-Like Pore Structure. *J. Mater. Chem.*, 20: 8320–8328, **2010**.

[56] Q. Wang, Z. Dong, Y. Du, and J. F. Kennedy. Controlled Release of Ciprofloxacin Hydrochloride from Chitosan/Polyethylene Glycol Blend Films. *Carbohyd. Polym.*, 69: 336 – 343, **2007**.

[57] A. K. Yadav, P. Mishra, A. K. Mishra, P. Mishra, S. Jain, and G. P. Agrawal. Development and Characterization of Hyaluronic Acid–Anchored PLGA Nanoparticulate Carriers of Doxorubicin. *Nanomedicine: Nanotechnol. Biol. Med.*, 3: 246–257, **2007**.

[58] X. Cui, X. Liu, A. S. Tatton, S. P. Brown, H. Ye, and A. Marsh. Nanodiamond Promotes Surfactant-Mediated Triglyceride Removal from a Hydrophobic Surface at or Below Room Temperature. *ACS Appl. Mater. Interfaces*, 4: 3225–3232, **2012**.

[59] K. Wagener, C. Batich, B. Kirsch, and S. Wanigatunga. Chain Propagation/Step Propagation Polymerization. III. An XPS Investigation of Poly(oxyethylene)-b-poly(pivalolactone) Telechelomer. *J. Polym. Sci. Pol. Chem.*, 27: 2625–2631, **1989**.

[60] G. Beamson and D. Briggs. *High Resolution XPS of Organic Polymers, the Scienta ESCA300 Database.* Wiley, **1992**.

[61] I. Fishbein, I. S. Alferiev, O. Nyanguile, R. Gaster, J. M. Vohs, G. S. Wong, H. Felderman, I-W. Chen, H. Choi, R. L. Wilensky, and R. J. Levy. Bisphosphonate-Mediated Gene Vector Delivery from the Metal Surfaces of Stents. *PNAS*, 103: 159–164, **2006**.

[62] M. Das, D. Mishra, P. Dhak, S. Gupta, T. K. Maiti, A. Basak, and P. Pramanik. Biofunctionalized, Phosphonate-Grafted, Ultrasmall Iron Oxide Nanoparticles for Combined Targeted Cancer Therapy and Multimodal Imaging. *Small*, 5: 2883–2893, **2009**.

[63] T. J. Daou, J. M. Grenèche, G. Pourroy, S. Buathong, A. Derory, C. Ulhaq-Bouillet, B. Donnio, D. Guillon, and S. Begin-Colin. Coupling Agent Effect on Magnetic Properties of Functionalized Magnetite-Based Nanoparticles. *Chem. Mater.*, 20: 5869–5875, **2008**.

[64] Z. Ali, A. Z. Abbasi, F. Zhang, P. Arosio, A. Lascialfari, M. F. Casula, A. Wenk, W. Kreyling, R. Plapper, M. Seidel, R. Niessner, J. Knöll, A. Seubert, and W. J. Parak. Multifunctional Nanoparticles for Dual Imaging. *Anal. Chem.*, 83: 2877–2882, **2011**.

[65] N. Gehrke, A. Briel, F. Ludwig, H. Remmer, T. Wawrzik, and S. Wellert. *New Perspectives for MPI: A Toolbox for Tracer Research.* Springer Berlin Heidelberg, **2012**.

[66] G. A. Bain and J. F. Berry. Diamagnetic Corrections and Pascal's Constants. *J. Chem. Educ.*, 85: 532, **2008**.

[67] A. Bjørnerud and L. Johansson. The Utility of Superparamagnetic Contrast Agents in MRI: Theoretical Consideration and Applications in the Cardiovascular System. *NMR Biomed.*, 17: 465–477, **2004**.

[68] T. Kawaguchi, A. Yoshino, M. Hasegawa, T. Hanaichi, S. Maruno, and N. Adachi. Dextran-Magnetite Complex: Temperature Dependence of its NMR Relaxivity. *J. Mater. Sci. - Mater. M*, 13: 113–117, **2002**.

[69] Y. Gossuin, A. Roch, R. N. Muller, and P. Gillis. An Evaluation of the Contributions of Diffusion and Exchange in Relaxation Enhancement by MRI Contrast Agents. *J. Magn. Reson.*, 158: 36–42, **2002**.

[70] A. Roch, R. N. Muller, and P. Gillis. Theory of Proton Relaxation Induced by Superparamagnetic Particles. *J. Chem. Phys.*, 110: 5403–5411, **1999**.

[71] A. Roch, P. Gillis, and R. N. Muller. Proceedings of the 3rd Annual Meeting of the Society of Magnetic Resonance. volume 1447, pages 1094, **1995**.

[72] Y. Gossuin, P. Gillis, A. Hocq, Q. L. Vuong, and A. Roch. Magnetic Resonance Relaxation Properties of Superparamagnetic Particles. *Nanomed. Nanobiotechnol.*, 1: 299–310, **2009**.

[73] G. H. Simon, J. Bauer, O. Saborovski, Y. Fu, C. Corot, M. F. Wendland, and H. E. Daldrup-Link. T1 and T2 Relaxivity of Intracellular and Extracellular USPIO at 1.5 T and 3 T Clinical MR Scanning. *Eur. Radiol.*, 16: 738–745, **2006**.

[74] M. F. Casula, P. Floris, C. Innocenti, A. Lascialfari, M. Marinone, M. Corti, R. A. Sperling, W. J. Parak, and C. Sangregorio. Magnetic Resonance Imaging Contrast Agents Based on Iron Oxide Superparamagnetic Ferrofluids. *Chem. Mater.*, 22: 1739–1748, **2010**.

[75] R. Weissleder, G. Elizondo, J. Wittenberg, C. A. Rabito, H. H. Bengele, and L. Josephson. Ultrasmall Superparamagnetic Iron Oxide: Characterization of a New Class of Contrast Agents for MR Imaging. *Radiology*, 175: 489–493, **1990**.

[76] F. Hu, Q. Jia, Y. Li, and M. Gao. Facile Synthesis of Ultrasmall PEGylated Iron Oxide Nanoparticles for Dual-Contrast T1- and T2-Weighted Magnetic Resonance Imaging. *Nanotechnology*, 22: 245604, **2011**.

[77] M. M. J. Modo and J. W. M. Bulte. *Molecular and Cellular MR Imaging.* CRC Press, **2007**.

[78] M. Reiser, W. Semmler, and H. Hricak. *Magnetic Resonance Tomography.* Springer-Verlag Berlin Heidelberg, **2008**.

[79] J. Lodhia, G. Mandarano, N. J. Ferris, P. Eu, and S. F. Cowell. Development and Use of Iron Oxide Nanoparticles (Part 1): Synthesis of Iron Oxide Nanoparticles for MRI. *Biomed. Imaging Interv. J.*, 6: e12, **2010**.

[80] R. T. M. de Rosales, R. Tavaré, A. Glaria, G. Varma, A. Protti, and P. J. Blower. ^{99m}Tc-Bisphosphonate-Iron Oxide Nanoparticle Conjugates for Dual-Modality Biomedical Imaging. *Bioconjugate Chem.*, 22: 455–465, **2011**.

[81] R. T. M. de Rosales, R. Tavaré, R. L. Paul, M. Jauregui-Osoro, A. Protti, A. Glaria, G. Varma, I. Szanda, and P. J. Blower. Synthesis of ^{64}Cu(II)–Bis(dithiocarbamatebisphosphonate) and Its Conjugation with Superparamagnetic Iron Oxide Nanoparticles: *In Vivo* Evaluation as Dual-Modality PET–MRI Agent. *Angew. Chem. Int. Ed.*, 50: 5509–5513, **2011**.

[82] R. T. M. de Rosales, C. Finucane, S. J. Mather, and P. J. Blower. Bifunctional

Bisphosphonate Complexes for the Diagnosis and Therapy of Bone Metastases. *Chem. Commun.*, pages 4847–4849, **2009**.

[83] F. Benyettou, Y. Lalatonne, O. Sainte-Catherine, M. Monteil, and L. Motte. Superparamagnetic Nanovector with Anti-cancer Properties: γFe_2O_3@Zoledronate. *Int. J. Pharm.*, 379: 324–327, **2009**.

[84] A. Clearfield. Recent Advances in Metal Phosphonate Chemistry II. *Curr. Opin. Solid State Mater. Sci.*, 6: 495–506, **2002**.

[85] W. Gao, L. Dickinson, C. Grozinger, F. G. Morin, and L. Reven. Self-Assembled Monolayers of Alkylphosphonic Acids on Metal Oxides. *Langmuir*, 12: 6429–6435, **1996**.

[86] Y. Lalatonne, C. Paris, J. M. Serfaty, P. Weinmann, M. Lecouvey, and L. Motte. Bisphosphonates-Ultra Small Superparamagnetic Iron Oxide Nanoparticles: A Platform Towards Diagnosis and Therapy. *Chem. Commun.*, pages 2553–2555, **2008**.

[87] S. Mohapatra and P. Pramanik. Synthesis and Stability of Functionalized Iron Oxide Nanoparticles Using Organophosphorus Coupling Agents. *Colloids Surf., A: Physicochem. Eng. Aspects*, 339: 35–42, **2009**.

[88] D. Portet, B. Denizot, E. Rump, J. J. Lejeune, and P. Jallet. Nonpolymeric Coatings of Iron Oxide Colloids for Biological Use as Magnetic Resonance Imaging Contrast Agents. *J. Colloid Interface Sci.*, 238: 37–42, **2001**.

[89] R. D. Rutledge, C. L. Warner, J. W. Pittman, R. S. Addleman, M. Engelhard, W. Chouyyok, and M. G. Warner. Thiol-Ene Induced Diphosphonic Acid Functionalization of Superparamagnetic Iron Oxide Nanoparticles. *Langmuir*, 26: 12285–12292, **2010**.

[90] Y. Sahoo, H. Pizem, T. Fried, D. Golodnitsky, L. Burstein, C. N. Sukenik, and G. Markovich. Alkyl Phosphonate/Phosphate Coating on Magnetite Nanoparticles: A Comparison with Fatty Acids. *Langmuir*, 17: 7907–7911, **2001**.

[91] W. Li, S. Tutton, A. T. Vu, L. Pierchala, B. S.Y. Li, J. M. Lewis, P. V. Prasad, and R. R. Edelman. First-Pass Contrast-Enhanced Magnetic Resonance Angiography in Humans Using Ferumoxytol, a Novel Ultrasmall Superparamagnetic Iron Oxide (USPIO)-Based Blood Pool Agent. *J. Magn. Reson. Imaging*, 21: 46–52, **2005**.

[92] T. Allkemper, C. Bremer, L. Matuszewski, W. Ebert, and P. Reimer. Contrast-Enhanced Blood-Pool MR Angiography with Optimized Iron Oxides: Effect of Size and Dose on Vascular Contrast Enhancement in Rabbits. *Radiology*, 223: 432–438, **2002**.

[93] M. Wagner, S. Wagner, J. Schnorr, E. Schellenberger, D. Kivelitz, L. Krug, M. Dewey, M. Laule, B. Hamm, and M. Taupitz. Coronary MR Angiography Using Citrate-Coated Very Small Superparamagnetic Iron Oxide Particles as Blood-Pool Contrast Agent: Initial Experience in Humans. *J. Magn. Reson. Imaging*, 34: 816–823, **2011**.

[94] T. Persigehl, R. Bieker, L. Matuszewski, A. Wall, T. Kessler, H. Kooijman, N. Meier, W. Ebert, W. E. Berdel, W. Heindel, R. M. Mesters, and C. Bremer. Antiangiogenic Tumor Treatment: Early Noninvasive Monitoring with USPIO-Enhanced MR Imaging in Mice. *Radiology*, 244: 449–456, **2007**.

[95] D. W. McRobbie, E. A. Moore, M. J. Graves, and M. R. Prince. *MRI from Picture to Proton*. Cambridge University Press, Cambridge, 2nd edition, **2007**.

[96] C. J. Fretz, G. Elizondo, R. Weissleder, P. F. Hahn, D. D. Stark, and J. T. Ferrucci. Superparamagnetic Iron Oxide-Enhanced MR Imaging: Pulse Sequence Optimization for Detection of Liver Cancer. *Radiology*, 172: 393–397, **1989**.

[97] C. Chouly, D. Pouliquen, I. Lucet, J. J. Jeune, and P. Jallet. Development of Superparamagnetic Nanoparticles for MRI: Effect of Particle Size, Charge and Surface Nature on Biodistribution. *J. Microencapsul.*, 13: 245–255, **1996**.

[98] Y. X. J. Wang, S. M. Hussain, and G. P. Krestin. Superparamagnetic Iron Oxide Contrast Agents: Physicochemical Characteristics and Applications in MR Imaging. *Eur. Radiol.*, 11: 2319–2331, **2001**.

[99] P. L. Toutain and A. Bousquet-Mélou. Plasma Terminal Half-Life. *J. Vet. Pharmacol. Ther.*, 27: 427–439, **2004**.

[100] C. Xu and S. Sun. New Forms of Superparamagnetic Nanoparticles for Biomedical Applications. *Adv. Drug Deliver. Rev.*, 65: 732–743, **2013**.

[101] M. R. Longmire, M. Ogawa, P. L. Choyke, and H. Kobayashi. Biologically Optimized Nanosized Molecules and Particles: More than Just Size. *Bioconjugate Chem.*, 22: 993–1000, **2011**.

[102] P. D. Miller. The Kidney and Bisphosphonates. *Bone*, 49: 77–81, **2011**.

[103] E. J. Keliher, J. Yoo, M. Nahrendorf, J. S. Lewis, B. Marinelli, A. Newton, M. J. Pittet, and R. Weissleder. ^{89}Zr-Labeled Dextran Nanoparticles Allow *In Vivo* Macrophage Imaging. *Bioconjugate Chem.*, 22: 2383–2389, **2011**.

[104] Y. Chao, M. Makale, P. P. Karmali, Y. Sharikov, I. Tsigelny, S. Merkulov, S. Kesari, W. Wrasidlo, E. Ruoslahti, and D. Simberg. Recognition of Dextran–Superparamagnetic Iron Oxide Nanoparticle Conjugates (Feridex) via Macrophage Scavenger Receptor Charged Domains. *Bioconjugate Chem.*, 23: 1003–1009, **2012**.

[105] D. J. Nieves, N. S. Azmi, R. Xu, R. Levy, E. A. Yates, and D. G. Fernig. Monovalent Maleimide Functionalization of Gold Nanoparticles via Copper-Free Click Chemistry. *Chem. Commun.*, 50: 13157–13160, **2014**.

[106] J. Kalia and R. T. Raines. Catalysis of Imido Group Hydrolysis in a Maleimide Conjugate. *Bioorg. Med. Chem. Lett.*, 17: 6286–6289, **2007**.

[107] S. C. Alley, N. M. Okeley, and P. D. Senter. Antibody-Drug Conjugates: Targeted Drug Delivery for Cancer. *Curr. Opin. Chem. Biol.*, 14: 529–537, **2010**.

[108] F. F. Schumacher, V. A. Sanchania, B. Tolner, Z. V. F. Wright, C. P. Ryan, M. E. B. Smith, J. M. Ward, S. Caddick, C. W. M. Kay, G. Aeppli, K. A. Chester, and J. R. Baker. Homogeneous Antibody Fragment Conjugation by Disulfide Bridging Introduces 'Spinostics'. *Sci. Rep.*, 3: 1525, **2013**.

[109] J. Zhu, C. Waengler, R. B. Lennox, and R. Schirrmacher. Preparation of Water-Soluble Maleimide-Functionalized 3 nm Gold Nanoparticles: A New Bioconjugation Template. *Langmuir*, 28: 5508–5512, **2012**.

[110] E. Oh, K. Susumu, J. B. Blanco-Canosa, I. L. Medintz, P. E. Dawson, and H. Mattoussi. Preparation of Stable Maleimide-Functionalized Au Nanoparticles and Their Use in Counting Surface Ligands. *Small*, 6: 1273–1278, **2010**.

[111] H. Duan, M. Kuang, X. Wang, Y. A. Wang, H. Mao, and S. Nie. Reexamining the Effects of Particle Size and Surface Chemistry on the Magnetic Properties of Iron Oxide Nanocrystals: New Insights into Spin Disorder and Proton Relaxivity. *J. Phys. Chem. C*, 112: 8127–8131, **2008**.

[112] J. M. Rae, C. J. Creighton, J. M. Meck, B. R. Haddad, and M. D. Johnson. MDA-MB-435 Cells are Derived from M14 Melanoma Cells - A Loss for Breast Cancer, but a Boon for Melanoma Research. *Breast Cancer Res. Tr.*, 104: 13–19, **2007**.

[113] A. F. Chambers. MDA-MB-435 and M14 Cell Lines: Identical but not M14 Melanoma? *Cancer Res.*, 69: 5292–5293, **2009**.

[114] S. Sellappan, R. Grijalva, X. Zhou, W. Yang, M. B. Eli, G. B. Mills, and D. Yu. Lineage Infidelity of MDA-MB-435 Cells: Expression of Melanocyte Proteins in a Breast Cancer Cell Line. *Cancer Res.*, 64: 3479–3485, **2004**.

[115] D. T. Ross, U. Scherf, M. B. Eisen, C. M. Perou, C. Rees, P. Spellman, V. Iyer, S. S. Jeffrey, M. Van de Rijn, M. Waltham, A. Pergamenschikov, J. C. F. Lee, D. Lashkari, D. Shalon, T. G. Myers, J. N. Weinstein, D. Botstein, and P. O. Brown. Systematic Variation in Gene Expression Patterns in Human Cancer Cell Lines. *Nat. Genet.*, 24: 227–235, **2000**.

[116] N. Oh and J-H. Park. Endocytosis and Exocytosis of Nanoparticles in Mammalian Cells. *Int. J. Nanomedicine*, 9 (Suppl 1): 51–63, **2014**.

[117] J. A. Swanson and C. Watts. Macropinocytosis. *Trends Cell Biol.*, 5: 424–428, **1995**.

[118] C. Commisso, S. M. Davidson, R. G. Soydaner-Azeloglu, S. J. Parker, J. J. Kamphorst, S. Hackett, E. Grabocka, M. Nofal, J. A. Drebin, C. B. Thompson, J. D. Rabinowitz, C. M. Metallo, M. G. V. Heiden, and D. Bar-Sagi. Macropinocytosis of Protein is an Amino Acid Supply Route in Ras-Transformed Cells. *Nature*, 497: 633–637, **2013**.

[119] H. Gao, Z. Yang, S. Zhang, S. Cao, S. Shen, Z. Pang, and X. Jiang. Ligand Modified Nanoparticles Increases Cell Uptake, Alters Endocytosis and Elevates Glioma Distribution and Internalization. *Sci. Rep.*, 3: 2534, **2013**.

[120] J. Skalska, P. S. Brookes, S. M. Nadtochiy, S. P. Hilchey, C. T. Jordan, M. L. Guzman, S. B. Maggirwar, M. M. Briehl, and S. H. Bernstein. Modulation of Cell Surface Protein Free Thiols: A Potential Novel Mechanism of Action of the Sesquiterpene Lactone Parthenolide. *PLoS ONE*, 4: e8115, **2009**.

[121] T. Li and S. Takeoka. Enhanced Cellular Uptake of Maleimide-Modified Liposomes via Thiol-Mediated Transport. *Int. J. Nanomedicine*, 9: 2849–2861, **2014**.

[122] M. T. Stephan, J. J. Moon, S. H. Um, A. Bershteyn, and D. J. Irvine. Therapeutic Cell Engineering with Surface-Conjugated Synthetic Nanoparticles. *Nat. Med.*, 16: 1035–1041, **2010**.

[123] D. G. Bostwick, A. Pacelli, M. Blute, P. Roche, and G. P. Murphy. Prostate Specific Membrane Antigen Expression in Prostatic Intraepithelial Neoplasia and Adenocarcinoma: A Study of 184 Cases. *Cancer*, 82: 2256–2261, **1998**.

[124] S. S. Chang. Overview of Prostate-Specific Membrane Antigen. *Rev. Urol*, 6 (Suppl 10): S13–S18, **2004**.

[125] P. Mhawech-Fauceglia, S. Zhang, L. Terracciano, G. Sauter, A. Chadhuri, F. R. Herrmann, and R. Penetrante. Prostate-Specific Membrane Antigen (PSMA) Protein Expression in Normal and Neoplastic Tissues and its Sensitivity and Specificity in Prostate Adenocarcinoma: An Immunohistochemical Study Using Mutiple Tumour Tissue Microarray Technique. *Histopathology*, 50: 472–483, **2007**.

[126] J. R. Osborne, N. H. Akhtar, S. Vallabhajosula, A. Anand, K. Deh, and S. T. Tagawa. Prostate-Specific Membrane Antigen-Based Imaging. *Urol. Oncol. Semin. Ori.*, 31: 144–154, **2013**.

[127] D. A. Silver, I. Pellicer, W. R. Fair, W. D. Heston, and C. Cordon-Cardo. Prostate-Specific Membrane Antigen Expression in Normal and Malignant Human Tissues.

Clin. Cancer Res., 3: 81–85, **1997**.

[128] S. D. Sweat, A. Pacelli, G. P. Murphy, and D. G. Bostwick. Prostate-Specific Membrane Antigen Expression is Greatest in Prostate Adenocarcinoma and Lymph Node Metastases. *Urology*, 52: 637–640, **1998**.

[129] G. L. Wright Jr., C. Haley, M. L. Beckett, and P. F. Schellhammer. Expression of Prostate-Specific Membrane Antigen in Normal, Benign, and Malignant Prostate Tissues. *Urol. Oncol. Semin. Ori.*, 1: 18–28, **1995**.

[130] A. Afshar-Oromieh, A. Malcher, M. Eder, M. Eisenhut, H. G. Linhart, B. A. Hadaschik, T. Holland-Letz, F. L. Giesel, C. Kratochwil, S. Haufe, U. Haberkorn, and C. M. Zechmann. PET Imaging with a [^{68}Ga]Gallium-Labelled PSMA Ligand for the Diagnosis of Prostate Cancer: Biodistribution in Humans and First Evaluation of Tumour Lesions. *Eur. J. Nucl. Med. Mol. I.*, 40: 486–495, **2013**.

[131] S. Y. Cho, K. L. Gage, R. C. Mease, S. Senthamizhchelvan, D. P. Holt, A. Jeffrey-Kwanisai, C. J. Endres, R. F. Dannals, G. Sgouros, M. Lodge, M. A. Eisenberger, R. Rodriguez, M. A. Carducci, C. Rojas, B. S. Slusher, A. P. Kozikowski, and M. G. Pomper. Biodistribution, Tumor Detection, and Radiation Dosimetry of ^{18}F-DCFBC, a Low-Molecular-Weight Inhibitor of Prostate-Specific Membrane Antigen, in Patients with Metastatic Prostate Cancer. *J. Nucl. Med.*, 53: 1883–1891, **2012**.

[132] J. S. Ross, C. E. Sheehan, H. A. G. Fisher, R. P. Jr. Kaufman, P. Kaur, K. Gray, I. Webb, G. S. Gray, R. Mosher, and B. V. S. Kallakury. Correlation of Primary Tumor Prostate-Specific Membrane Antigen Expression with Disease Recurrence in Prostate Cancer. *Clin. Cancer Res.*, 9: 6357–6362, **2003**.

[133] S. Perner, M. D. Hofer, R. Kim, R. B. Shah, H. Li, P. Moller, R. E. Hautmann, J. E. Gschwend, R. Kuefer, and M. A. Rubin. Prostate-Specific Membrane Antigen Expression as a Predictor of Prostate Cancer Progression. *Hum. Pathol.*, 38: 696–701, **2007**.

[134] F. Kampmeier, J. D. Williams, J. Maher, G. E. Mullen, and P. J. Blower. Design and Preclinical Evaluation of a $^{99\mathrm{m}}$Tc-Labelled Diabody of mAb J591 for SPECT Imaging of Prostate-Specific Membrane Antigen (PSMA). *Eur. J. Nucl. Med. Mol. I. Res.*, 4: 13, **2014**.

[135] N. H. Bander, E. J. Trabulsi, L. Kostakoglu, D. Yao, S. Vallabhajosula, P. Smith-Jones, M. A. Joyce, M. Milowsky, D. M. Nanus, and S. J. Goldsmith. Targeting Metastatic Prostate Cancer with Radiolabeled Monoclonal Antibody J591 to the Extracellular Domain of Prostate Specific Membrane Antigen. *J. Urol.*, 170: 1717–1721, **2003**.

[136] M. J. Morris, C. R. Divgi, N. Pandit-Taskar, M. Batraki, N. Warren, A. Nacca, P. Smith-Jones, L. Schwartz, W. K. Kelly, S. Slovin, D. Solit, J. Halpern, A. Delacruz,

T. Curley, R. Finn, J. A. O'Donoghue, P. Livingston, S. Larson, and H. I. Scher. Pilot Trial of Unlabeled and Indium-111-Labeled Anti-Prostate-Specific Membrane Antigen Antibody J591 for Castrate Metastatic Prostate Cancer. *Clin. Cancer Res.*, 11: 7454–7461, **2005**.

[137] N. Pandit-Taskar, J. A. O'Donoghue, M. J. Morris, E. A. Wills, L. H. Schwartz, M. Gonen, H. I. Scher, S. M. Larson, and C. R. Divgi. Antibody Mass Escalation Study in Patients with Castration-Resistant Prostate Cancer using 111In-J591: Lesion Detectability and Dosimetric Projections for 90Y Radioimmunotherapy. *J. Nucl. Med.*, 49: 1066–1074, **2008**.

[138] M. J. Morris, N. Pandit-Taskar, C. R. Divgi, S. Bender, J. A. O'Donoghue, A. Nacca, P. Smith-Jones, L. Schwartz, S. Slovin, R. Finn, S. Larson, and H. I. Scher. Phase I Evaluation of J591 as a Vascular Targeting Agent in Progressive Solid Tumors. *Clin. Cancer Res.*, 13: 2707–2713, **2007**.

[139] S. T. Tagawa, M. I. Milowsky, M. Morris, S. Vallabhajosula, P. Christos, N. H. Akhtar, J. Osborne, S. J. Goldsmith, S. Larson, N. P. Taskar, H. I. Scher, N. H. Bander, and D. M. Nanus. Phase II Study of Lutetium-177-Labeled Anti-Prostate-Specific Membrane Antigen Monoclonal Antibody J591 for Metastatic Castration-Resistant Prostate Cancer. *Clin. Cancer Res.*, 19: 5182–5191, **2013**.

[140] A. Y. Liu. Differential Expression of Cell Surface Molecules in Prostate Cancer Cells. *Cancer Res.*, 60: 3429–3434, **2000**.

[141] R. Waibel, R. Alberto, J. Willuda, R. Finnern, R. Schibli, A. Stichelberger, A. Egli, U. Abram, J-P. Mach, A. Pluckthun, and P. A. Schubiger. Stable One-Step Technetium-99m Labeling of His-Tagged Recombinant Proteins with a Novel Tc(I)-Carbonyl Complex. *Nat. Biotechnol.*, 17: 897–901, **1999**.

[142] A. Badar, J. Williams, R. T. M. de Rosales, R. Tavaré, F. Kampmeier, P. J. Blower, and G. E. D. Mullen. Optimising the Radiolabelling Properties of Technetium Tricarbonyl and His-Tagged Proteins. *Eur. J. Nucl. Med. Mol. I.*, 4: 14–14, **2014**.

[143] K. A. Kelly, J. R. Allport, A. Tsourkas, V. R. Shinde-Patil, L. Josephson, and R. Weissleder. Detection of Vascular Adhesion Molecule-1 Expression Using a Novel Multimodal Nanoparticle. *Circ. Res.*, 96: 327–336, **2005**.

[144] K. A. Kelly, M. Nahrendorf, A. M. Yu, F. Reynolds, and R. Weissleder. *In Vivo* Phage Display Selection Yields Atherosclerotic Plaque Targeted Peptides for Imaging. *Mol. Imaging Biol.*, 8: 201–207, **2006**.

[145] P. Libby, P. M. Ridker, and A. Maseri. Inflammation and Atherosclerosis. *Circulation*, 105: 1135–1143, **2002**.

[146] P. Libby. Inflammation in Atherosclerosis. *Nature*, 420: 868–874, **2002**.

[147] M. Nahrendorf, F. A. Jaffer, K. A. Kelly, D. E. Sosnovik, E. Aikawa, P. Libby, and R. Weissleder. Noninvasive Vascular Cell Adhesion Molecule-1 Imaging Identifies Inflammatory Activation of Cells in Atherosclerosis. *Circulation*, 114: 1504–1511, **2006**.

[148] A. Broisat, S. Hernot, J. Toczek, J. De Vos, L. M. Riou, S. Martin, M. Ahmadi, N. Thielens, U. Wernery, V. Caveliers, S. Muyldermans, T. Lahoutte, D. Fagret, C. Ghezzi, and N. Devoogdt. Nanobodies Targeting Mouse/Human VCAM1 for the Nuclear Imaging of Atherosclerotic Lesions. *Circ. Res.*, 110: 927–937, **2012**.

[149] P. Libby. Inflammation and Cardiovascular Disease Mechanisms. *Am. J. Clin. Nutr.*, 83: 456S–460S, **2006**.

[150] N. Strebe, A. Guse, M. Schüngel, T. Schirrmann, M. Hafner, T. Jostock, M. Hust, W. Müller, and S. Dübel. Functional Knockdown of VCAM-1 at the Posttranslational Level with ER Retained Antibodies. *J. Immunol. Methods*, 341: 30–40, **2009**.

[151] V. Jäger, K. Büssow, A. Wagner, S. Weber, M. Hust, A. Frenzel, and T. Schirrmann. High Level Transient Production of Recombinant Antibodies and Antibody Fusion Proteins in HEK293 Cells. *BMC Biotechnol.*, 13: 52, **2013**.

[152] J. Hamzah, V. R. Kotamraju, J. W. Seo, L. Agemy, V. Fogal, L. M. Mahakian, D. Peters, L. Roth, M. K. J. Gagnon, K. W. Ferrara, and E. Ruoslahti. Specific Penetration and Accumulation of a Homing Peptide within Atherosclerotic Plaques of Apolipoprotein E-Deficient Mice. *Proc. Natl. Acad. Sci. USA*, 108: 7154–7159, **2011**.

[153] P. Laakkonen, K. Porkka, J. A. Hoffman, and E. Ruoslahti. A Tumor-Homing Peptide with a Targeting Specificity Related to Lymphatic Vessels. *Nat. Med.*, 8: 751–755, **2002**.

[154] P. Laakkonen, M. E. Akerman, H. Biliran, M. Yang, F. Ferrer, T. Karpanen, R. M. Hoffman, and E. Ruoslahti. Antitumor Activity of a Homing Peptide that Targets Tumor Lymphatics and Tumor Cells. *Proc. Natl. Acad. Sci. USA*, 101: 9381–9386, **2004**.

[155] J-H. Park, G. von Maltzahn, M. J. Xu, V. Fogal, V. R. Kotamraju, E. Ruoslahti, S. N. Bhatia, and M. J. Sailor. Cooperative Nanomaterial System to Sensitize, Target, and Treat Tumors. *Proc. Natl. Acad. Sci. USA*, 107: 981–986, **2010**.

[156] J. Jiang, Y. Zhang, A. R. Krainer, and R-M. Xu. Crystal Structure of Human p32, a Doughnut-Shaped Acidic Mitochondrial Matrix Protein. *Proc. Natl. Acad. Sci. USA*, 96: 3572–3577, **1999**.

[157] D. Sánchez-Martín, A. M. Cuesta, V. Fogal, E. Ruoslahti, and L. Álvarez-Vallina.

The Multicompartmental p32/gClqR as a New Target for Antibody-Based Tumor Targeting Strategies. *J. Biol. Chem.*, 286: 5197–5203, **2011**.

[158] L. Agemy, V. R. Kotamraju, D. Friedmann-Morvinski, S. Sharma, K. N. Sugahara, and E. Ruoslahti. Proapoptotic Peptide-Mediated Cancer Therapy Targeted to Cell Surface p32. *Mol. Ther.*, 21: 2195–2204, **2013**.

[159] V. Fogal, L. Zhang, S. Krajewski, and E. Ruoslahti. Mitochondrial/Cell Surface Protein p32/gC1qR as a Molecular Target in Tumor Cells and Tumor Stroma. *Cancer Res.*, 68: 7210–7218, **2008**.

[160] L. Roth, L. Agemy, V. R. Kotamraju, G. Braun, T. Teesalu, K. N. Sugahara, J. Hamzah, and E. Ruoslahti. Transtumoral Targeting Enabled by a Novel Neuropilin-Binding Peptide. *Oncogene*, 31: 3754–3763, **2012**.

[161] P. P. Karmali, V. R. Kotamraju, M. Kastantin, M. Black, D. Missirlis, M. Tirrell, and E. Ruoslahti. Targeting of Albumin-Embedded Paclitaxel Nanoparticles to Tumors. *Nanomedicine*, 5: 73–82, **2009**.

[162] Y. Ren, S. Hauert, J. H. Lo, and S. N. Bhatia. Identification and Characterization of Receptor-Specific Peptides for siRNA Delivery. *ACS Nano*, 6: 8620–8631, **2012**.

Chapter 3

Polyethylene glycol phase transfer of CdZnSeS alloyed quantum dots

3.1 Introduction

Once phase transfer of Fe_3O_4 NPs using PEG(5)-BP had been established and subsequent *in vivo* imaging was successful, studies into whether this method of PEGylation was possible with other materials, in particular CdZnSeS alloyed QDs, were performed. This particular material was chosen for several reasons, the principle being the longer wavelength red emission is beneficial in *in vivo* applications as biological autoflurorescence, absorbance and scattering is minimised in this region [1, 2]. In addition, tissue depth penetration is increased [3].

This chapter will describe the synthesis used to produce the red emitting QDs, followed by optical and size characterisation of the synthesised and PEGylated particles. Finally, preliminary macrophage cell studies will be described.

3.2 Synthesis of CdZnSeS alloyed quantum dots

The synthesis used to prepare the CdZnSeS alloyed QDs was a modification of a single-step method reported by Bae *et al.* which involved the thermolysis of precursor solutions containing Cd, Zn, Se and S [4]. The developed scheme was accomplished by a collaborator at the University of Oxford, and was chosen on account of previous results showing that this facile procedure produced monodisperse, bright red emitting nanocrystals [5]. From scheme 3.1 it can be seen that the synthesis involved preparation of a solution containing Cd and Zn, followed by injection of a S-Se TOP solution which was maintained at a high temperature for several minutes to allow for particle growth. The surfactant used in this synthesis was oleic acid, and figure 3.1 illustrates both the oleic acid coated QD produced and the binding of the molecule through the carboxyl group to the QD surface.

During the particle growth stage of the synthesis, aliquots of the reaction solution were obtained and can be seen in figure 3.2. The colour photo clearly demonstrated the prevalent size-tuneable fluorescent properties of semiconductor nanoparticles, ranging from $\sim$560 nm to $\sim$610 nm [6]. This was further confirmed by TEM with a particle size of 3.4 $\pm$ 0.4 nm (based on the measurement of 30 particles; figure 3.3a) measured for the aliquot taken at 2 min, and a final size of 4.2 $\pm$ 0.6 nm (based on the measurement of 86 particles; figure 3.3b).
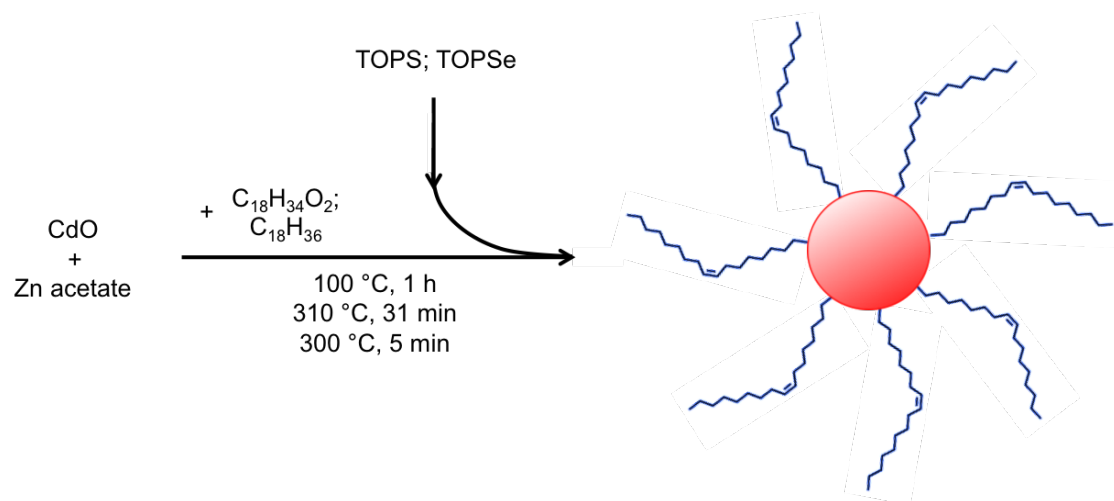
Scheme 3.1: Reaction scheme for the synthesis of CdZnSeS alloyed QDs [5].
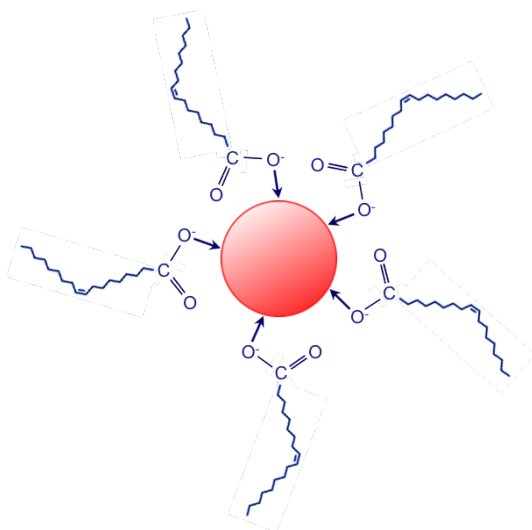
Figure 3.1: Schematic representation of oleic acid binding to a quantum dot via the carboxyl group.

It was not possible to perform DLS studies on the particles to determine the hydrodynamic diameters, presumably due to the similarity in emission wavelength of the QDs with the zetasizer light source (a He-Ne laser with a wavelength of 633 nm [7]) resulting in inference of the scattered laser beam and detection.

Figure 3.2: Aliquots of CdZnSeS alloyed QDs in hexane taken after injection of the selenium/sulphur precursor solution at time points of 30 sec, 1 min, and every min thereafter (vials arranged left to right).

(a)	(b)
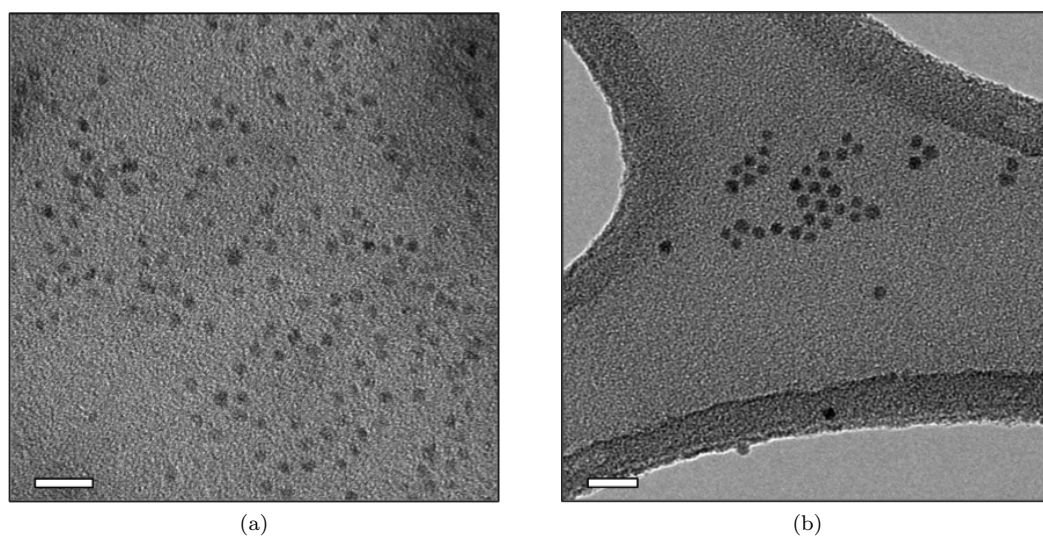
Figure 3.3: Characterisation of synthesised QDs: TEM micrograph of oleic acid coated CdZnSeS alloyed QDs in hexane after (a) 2 min ($D_{\text{TEM}} = 3.4 \pm 0.4$ nm based on the measurement of 25 particles), and (b) 5 min ($D_{\text{TEM}} = 4.2 \pm 0.6$ nm based on the measurement of 86 particles). Scale bars are 20 nm.

For the remainder of this study only the final aliquot was analysed in view of the reasons highlighted earlier related to emission wavelength. Figure 3.4 displays the absorption and emission profiles for CdZnSeS QDs, with emission at a wavelength of 604.0 nm.
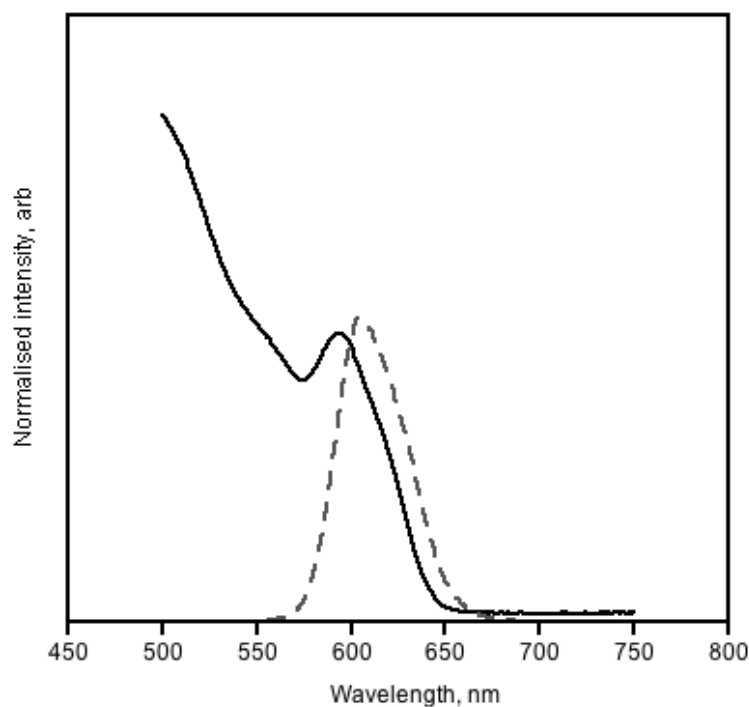
Figure 3.4: Characterisation of synthesised QDs: Absorption and emission spectra of CdZnSeS alloyed QDs in hexane (λ_{abs} = 593.5 nm, λ_{ems} = 604.0 nm).

3.3 Polyethylene glycol phase transfer of CdZnSeS alloyed quantum dots

The scheme employed to PEGylate the alloyed nanocrylates was different to that for the iron oxide NPs, and is represented in scheme 3.2. An immiscible mixture of QDs in hexane and PEG(5)-BP in water was formed and left stirring overnight, after which ligand exchange had occurred and the CdZnSeS particles were coated with PEG(5)-BP. This adjustment was made due to the QDs being dispersed in hexane after synthesis, rather than in a dried state as for the iron oxide. The molecular weight of the PEG-BP used was 5000 Da as before owing to the favourable properties bestowed to the magnetite NPs proceeding PEGylation. Figure 3.5 confirms PEGylation was successful. The vial on the left contains the alloyed particles in hexane, and the vial on the right contains the particles in water. It is apparent that the particles transferred to water displayed no significant shift in either absorption or emission wavelengths with some reduction in the quantum yield. Optical characterisation, figure 3.6, verified this finding (λ_{abs} = 592.0 nm, λ_{ems} = 606.0 nm). Finally, TEM analysis of the PEGylated quantum dots was performed and displayed no change in the core size with the sample remaining spherical and monodispersed (figure 3.7).
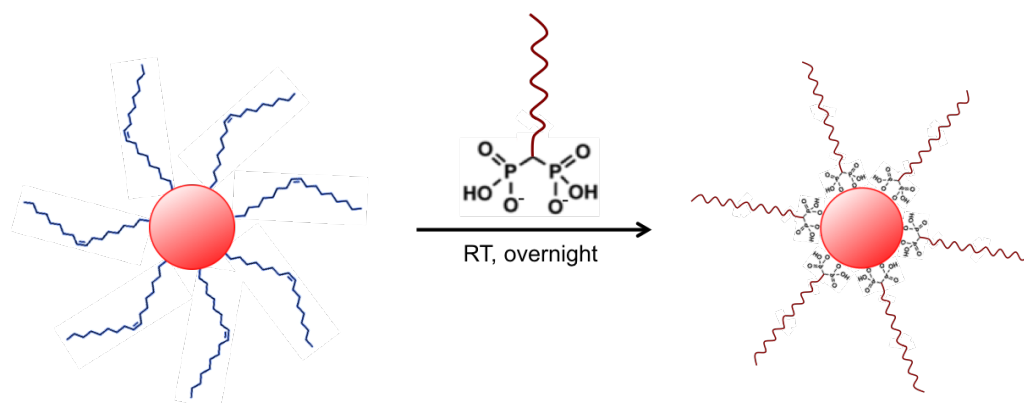
Scheme 3.2: Reaction scheme for the the method of PEGylation of CdZnSeS alloyed QDs using DCM.

(a)   (b)
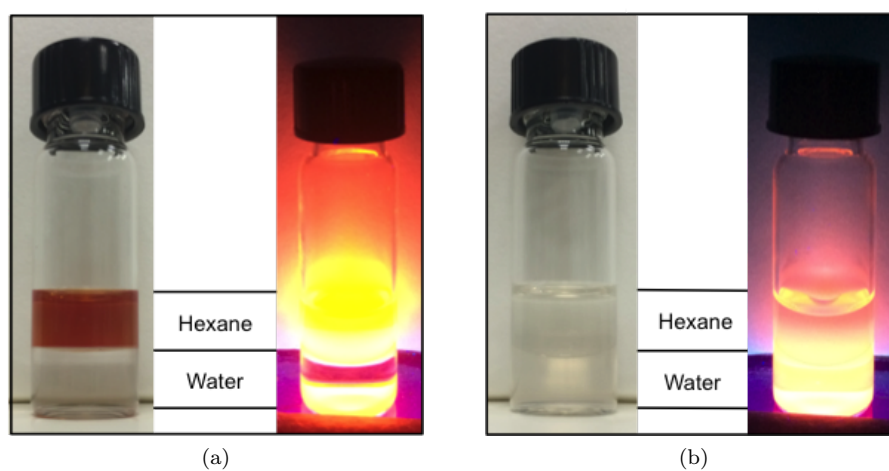
Figure 3.5: Photograph of (a) CdZnSeS alloyed QDs coated with oleic acid in hexane (right vial is photo excited at 365 nm in the dark), and (b) PEG(5)-BP coated CdZnSeS alloyed QDs in water (right vial is photo excited at 365 nm in the dark).
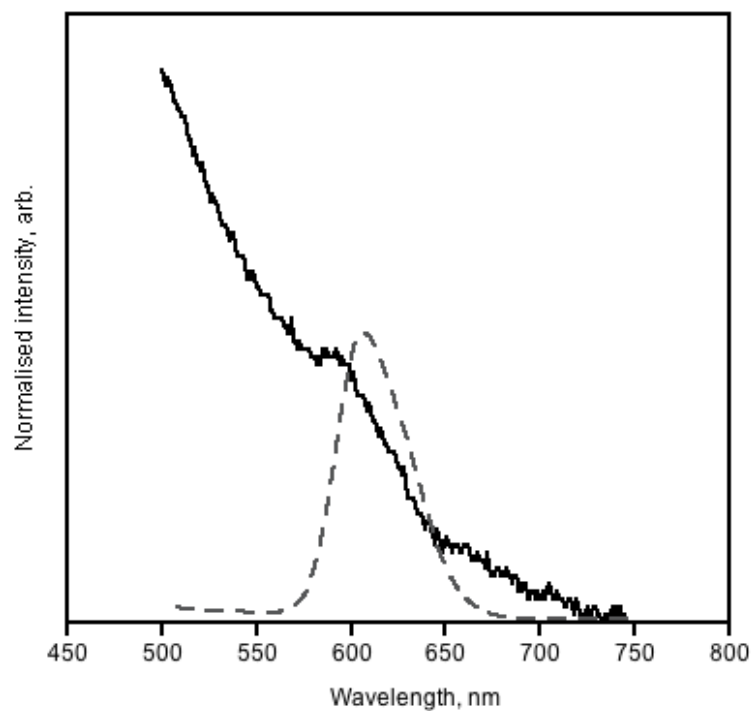
Figure 3.6: Characterisation of PEGylated QDs: Absorption and emission spectra of PEG(5)-BP coated CdZnSeS alloyed QDs in water (λ_{abs} = 592.0 nm, λ_{ems} = 606.0 nm).
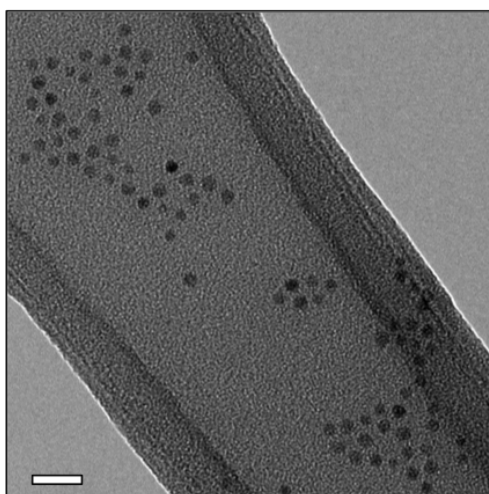
Figure 3.7: Characterisation of PEGylated QDs: TEM micrograph of PEG(5)-BP coated CdZnSeS alloyed QDs in water (D_{TEM} = 4.4 ± 0.5 nm based on the measurement of 100 particles). Scale bar is 20 nm.

3.4 *In vitro* cell uptake study

Once PEGylation of the CdZnSeS alloyed QDs had been established, *in vitro* confocal studies with J774 murine macrophage cells were performed in order to determine the stability of the particles in a biological environment. This study was performed in collaboration with Dr. Lea Ann Dailey in the Institute of Pharmaceutical Science at Kings College London. As it can be seen from figure 3.8, there is a certain measure of accumulation of the PEG(5)-BP-QDs in the cells, with the z-stack image revealing some internalisation, suggested by the bottom image of figure 3.8b which looks to show QDs throughout cells. Although PEGylation of nanoparticles is well-known to reduce macrophage uptake, there will always be a small degree of uptake [8–10]. This study confirmed the bond between the QD surface and BP was stable in cell media. If PEG(5)-BP had detached from the particle surface, aggregation would have occurred, resulting in all QDs being removed during the sample preparation for confocal microscopy.

3.5 Introduction of maleimide-polyethylene glycol into coating

To allow for potential targeted bioapplications, mal-PEG(5)-BP was introduced into the phase transfer in the manner as the PEGylation in scheme 3.2, with the same ratio as used for the iron oxide particles. The transfer of the QDs into an aqueous phase with the combination of PEG molecules appeared to result in full dispersion in water. However, no further characterisation was performed.

3.6 Conclusions

In conclusion, the simple method of PEGylation described in chapter 2 has been successfully applied to alloyed quantum dots. The emission profile of the particles remained largely unchanged, with some reduction in the quantum yield. TEM characterisation of the resulting water-soluble NPs displayed no change in morphology or core size. *In vitro* studies revealed the stability of the PEG(5)-BP-coated CdZnSeS QDs in a biological environment at
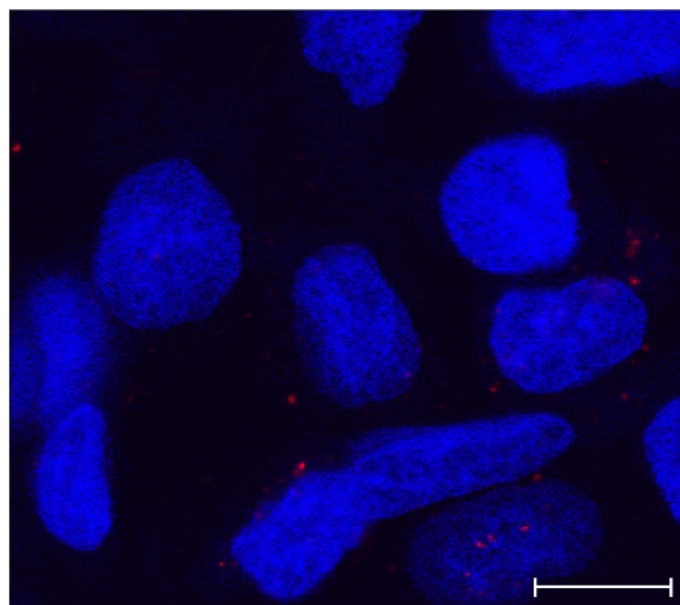
(a)
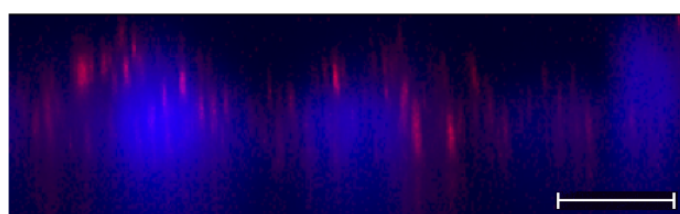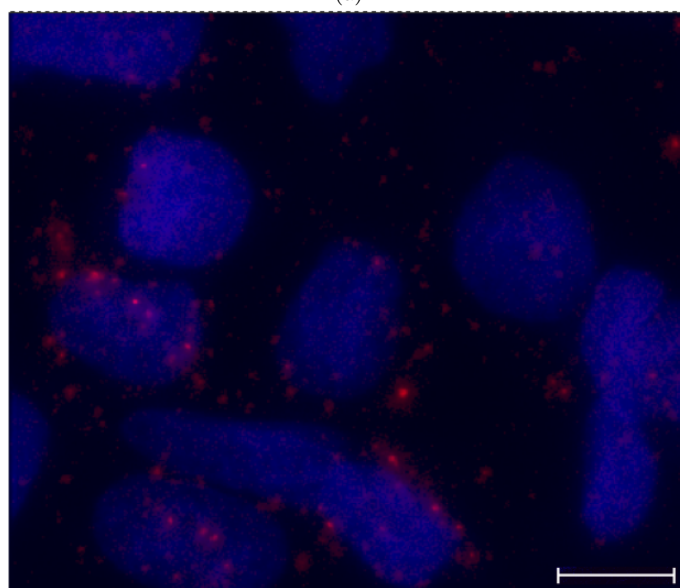
(b)

Figure 3.8: *In vitro* characterisation of PEGylated QDs: Confocal imaging of J774 murine macrophage cells incubated with PEG(5)-BP coated CdZnSeS alloyed QDs, with (a) showing a top view, and (b) showing a top view and the corresponding z-stack. Scale bar is 11.9 µm.

physiological temperature, with some macrophage cell uptake observed. In addition, the introduction of the maleimide-PEG(5)-BP into the coating allows for the possibility of further functionalisation by the addition of biomarkers.

Bibliography

[1] A. M. Smith, S. Dave, S. Nie, L. True, and X. Gao. Multicolor Quantum Dots for Molecular Diagnostics of Cancer. *Expert Rev. Mol. Diagn.*, 6: 231–244, **2006**.

[2] T. Jamieson, R. Bakhshi, D. Petrova, R. Pocock, M. Imani, and A. M. Seifalian. Biological Applications of Quantum Dots. *Biomaterials*, 28: 4717–4732, **2007**.

[3] E. Z. Chong, D. R. Matthews, H. D. Summers, K. L. Njoh, R. J. Errington, and P. J. Smith. Development of FRET-Based Assays in the Far-Red Using CdTe Quantum Dots. *J. Biomed. Biotechnol.*, 2007: 54169, **2007**.

[4] W. K. Bae, K. Char, H. Hur, and S. Lee. Single-Step Synthesis of Quantum Dots with Chemical Composition Gradients. *Chem. Mater.*, 20: 531–539, **2008**.

[5] S. Fairclough. *Carrier Dynamics within Semiconductor Nanocrystals*. PhD thesis, Mansfield College, University of Oxford, **2014**.

[6] I. L. Medintz, H. Mattoussi, and A. R. Clapp. Potential Clinical Applications of Quantum Dots. *Int. J. Nanomedicine*, 3: 151–167, **2008**.

[7] Malvern. http://www.malvern.com/en/products/product-range/zetasizer-range/zetasizer-nano-range/zetasizer-nano-zs/default.aspx, March 2015.

[8] M. L. Schipper, G. Iyer, A. L. Koh, Z. Cheng, Y. Ebenstein, A. Aharoni, S. Keren, L. A. Bentolila, J. Li, J. Rao, X. Chen, U. Banin, A. M. Wu, R. Sinclair, S. Weiss, and S. S. Gambhir. Particle Size, Surface Coating, and PEGylation Influence the Biodistribution of Quantum Dots in Living Mice. *Small*, 5: 126–134, **2009**.

[9] M. M. Barroso. Quantum Dots in Cell Biology. *J. Histochem. Cytochem.*, 59: 237–251, **2011**.

[10] B. Ballou, B. C. Lagerholm, L. A. Ernst, M. P. Bruchez, and A. S. Waggoner. Noninvasive Imaging of Quantum Dots in Mice. *Bioconjugate Chem.*, 15: 79–86, **2004**.

Chapter 4

Hydrophobin phase transfer of inorganic nanoparticles

4.1 Introduction

Once phase transfer and surface modification of Fe_3O_4 NPs and CdZnSeS alloyed QDs had been accomplished, further investigation into an alternative coating was performed in the hope that a simple method of functionalisation would be achieved involving a naturally occurring amphiphile. In order to do this, a recombinant protein named H*Protein B (BASF) which consists of the class I hydrophobin DewA (from the filamentous fungi *A. nidulans*) and 40 N-terminal amino acids of the *Bacillus subtilis* protein yaaD, with a molecular weight of 18.8 kDa and a size of *ca.* 1.2 nm [1,2] was used (for more details on hydrophobins see page 42 of the introduction). This particular protein was chosen due to its high stability [3] and several reports stating that hydrophobins have previously been utilised to stabilise particles of different materials, for example boehmite and silicon [4–6].

This chapter will describe the hydrophobin encapsulation of inorganic NPs with all associated optical and size characterisation. The *in vitro* and *in vivo* studies performed will be detailed, concluding with the radiolabelling of the protein-coated QDs.

4.1.1 Protein passivation of nanoparticles

Several inorganic nanoparticles were used during this study, namely CdSe/ZnS core-shell QDs coated with hexadecylamine (HDA; Lumidot 590) or HDA/TOPO (prepared in-house using methods described by Qu *et al.* [7] and Talapin *et al.* [8]), CdSeS/ZnS core-shell QDs coated with oleic acid and Fe_3O_4 coated with oleylamine (synthesised using the method described in chapter 2). The previously synthesised CdZnSeS alloyed QDs were attempted several times unsuccessfully, the reason for which is unknown. The phase transfer to water involved a simple technique shown in scheme 4.1, and prior to this, the hydrophobin solution was diluted in water and left standing to prevent self-assembly of the protein which has previously been proved to occur (figure 4.1; for further details see experimental). To this was added a non-polar organic solution of particles followed by sonication, producing a cloudy emulsion. After a brief storage period at low temperature and filtration, centrifugal concentration and further dilution with water, a transparent aqueous solution of particles was obtained. Centrifugal concentration was found to be essential, as this step removed excess protein and significantly increased cell viability when the particles were used in imaging

applications. It is believed the amphiphilic nature of the protein was exploited by inter-digitating the aliphatic chain of the protein with the hydrophobic capping agent of the quantum dot, leaving the cysteine-rich hydrophilic region exposed to solution, making the composite water-soluble and stable in a range of buffer solutions. Hydrophobins are known to be robust and it is unlikely that sonication affected the structure. For example, it is suggested that class II hydrophobins keep their secondary and ternary structure after exposure to sodium dodecylsulphate, a compound routinely used to denature proteins [9]. In addition, ultrasound treatment has been applied in some phase transfer reactions, showing no evidence of protein unfolding [10].
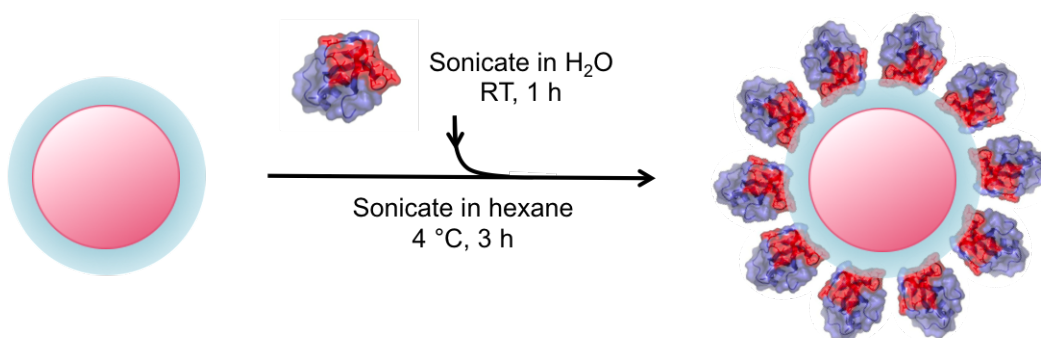
Scheme 4.1: Reaction scheme for the method of encapsulation of particles with hydrophobin.
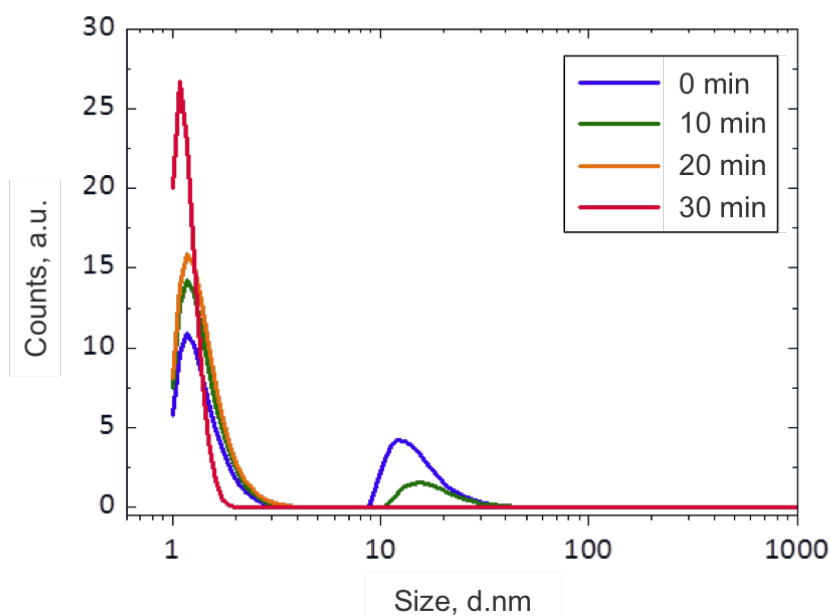
Figure 4.1: Characterisation of hydrophobin: DLS number distributions of 150 µL of H*Protein B diluted with 3 mL of water. Measurements taken at 0 min (blue), 10 min (green), 20 min (orange), and 30 min (red) after dilution [2].

4.1.2 Characterisation

Optical properties

Once phase transfer was achieved, analysis of the resulting water-soluble QDs (in particular CdSe/ZnS and CdSeS/ZnS) was performed to ensure there was no considerable change in the optical properties. A typical example is shown in figure 4.2 and it is evident that the particles transferred to water displayed no significant shift in either absorption or emission wavelengths. Although generally the emission quantum yield was reduced by up to 50 % due to a small degree of degradation of the surface, the solution still emitted brightly under 365 nm excitation (figure 4.3b).
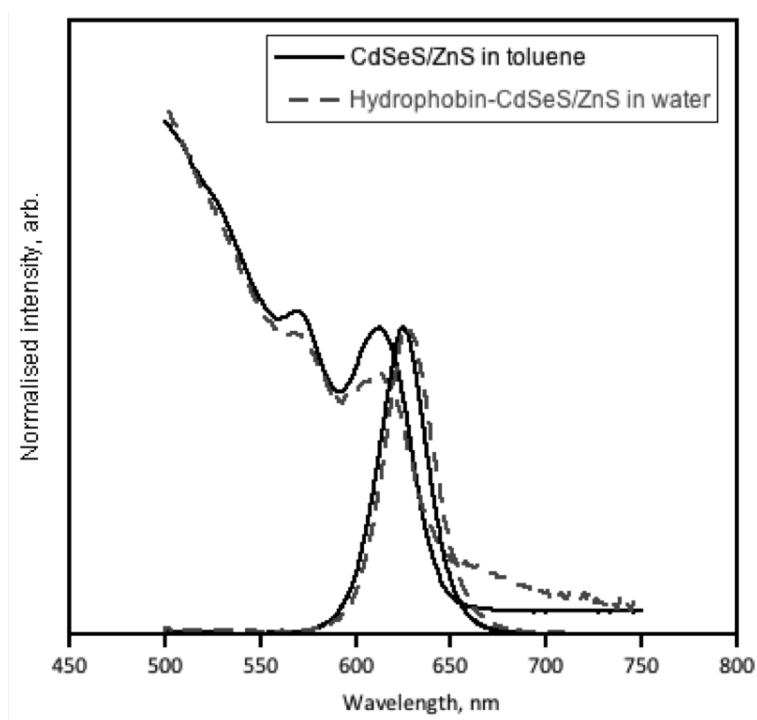
Figure 4.2: Characterisation of hydrophobin-QDs: Absorption and emission spectra of CdSeS/ZnS QDs before phase transfer in toluene (black solid line; λ_{abs} = 613.0 nm, λ_{ems} = 625.5 nm), and after phase transfer with H*Protein B in water (grey dashed line; λ_{abs} = 613.0 nm, λ_{ems} = 627.5 nm).

Transmission electron microscopy and dynamic light scattering

Once it had been established that there was no shift in emission wavelength once encapsulation had occurred, the size of the particles needed to be determined. TEM revealed a high proportion of the CdSeS/ZnS quantum dots remained as discreet individual particles after phase transfer with no change in core size (figure 4.4b), although they were occasionally

(a)   (b)
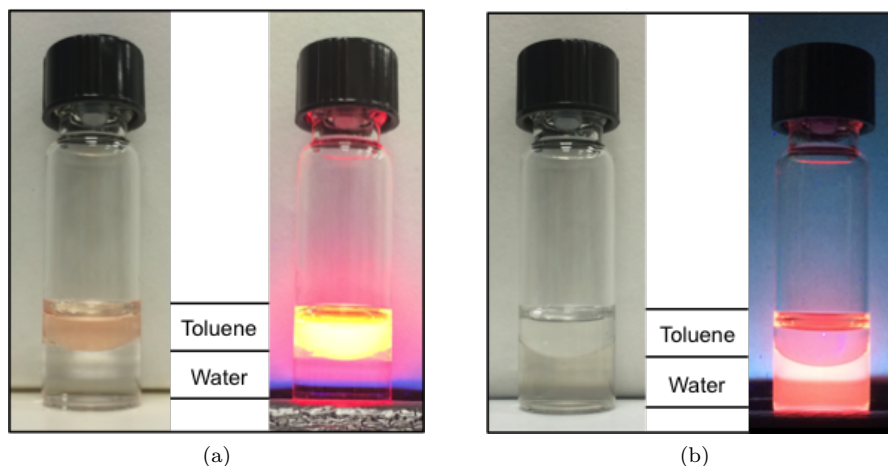
Figure 4.3: Photograph of (a) CdSeS/ZnS QDs coated with oleic acid in toluene (right vial is photo excited at 365 nm in the dark), (b) H*Protein B coated CdSeS/ZnS QDs in water (right vial is photo excited at 365 nm in the dark).

observed to cluster (figure 4.4c). This was attributed to the hydrophobin encapsulating multiple quantum dots into aggregates as shown in figure 4.5. In addition, encapsulation of Fe_3O_4 NPs was performed, and it can be seen from figure 4.4d that again, some agglomerates were formed but most particles continued to exist separately. DLS studies suggested that the CdSeS/ZnS particles, 4.6 ± 0.8 nm in diameter as determined by electron microscopy (based on the measurement of 50 particles), had an initial D_H of 42.4 ± 24.9 nm (with a PDI of 0.22) once coated, however it was observed that this value dropped to 14.2 ± 2.7 nm (PDI of 0.25) after 2 months with no aggregation occurring. The reason for this is unknown. For hydrophobin-coated CdSe/ZnS QDs (core size of *ca.* 5 nm), the D_H was found to be *ca.* 9 nm although diameters of up to *ca.* 60 nm were occasionally observed, attributed to clustering in solution or free protein agglomerates.

Zeta potential

The zeta potential of the hydrophobin-capped quantum dots was -42.8 ± 8.8 mV, which is in agreement with the charge expected of a protein and confirms good colloidal stability due to the high degree of electrostatic repulsion [11].

Analytical ultracentrifugation

Hydrophobin-stabilised QDs (CdSe/ZnS) were subjected to analytical ultracentrifugation (AUC) in order to compare the conjugates to freely dissolved hydrophobins [1]. This study was performed by collaborators at BASF. It was found that the distribution of sedimentation
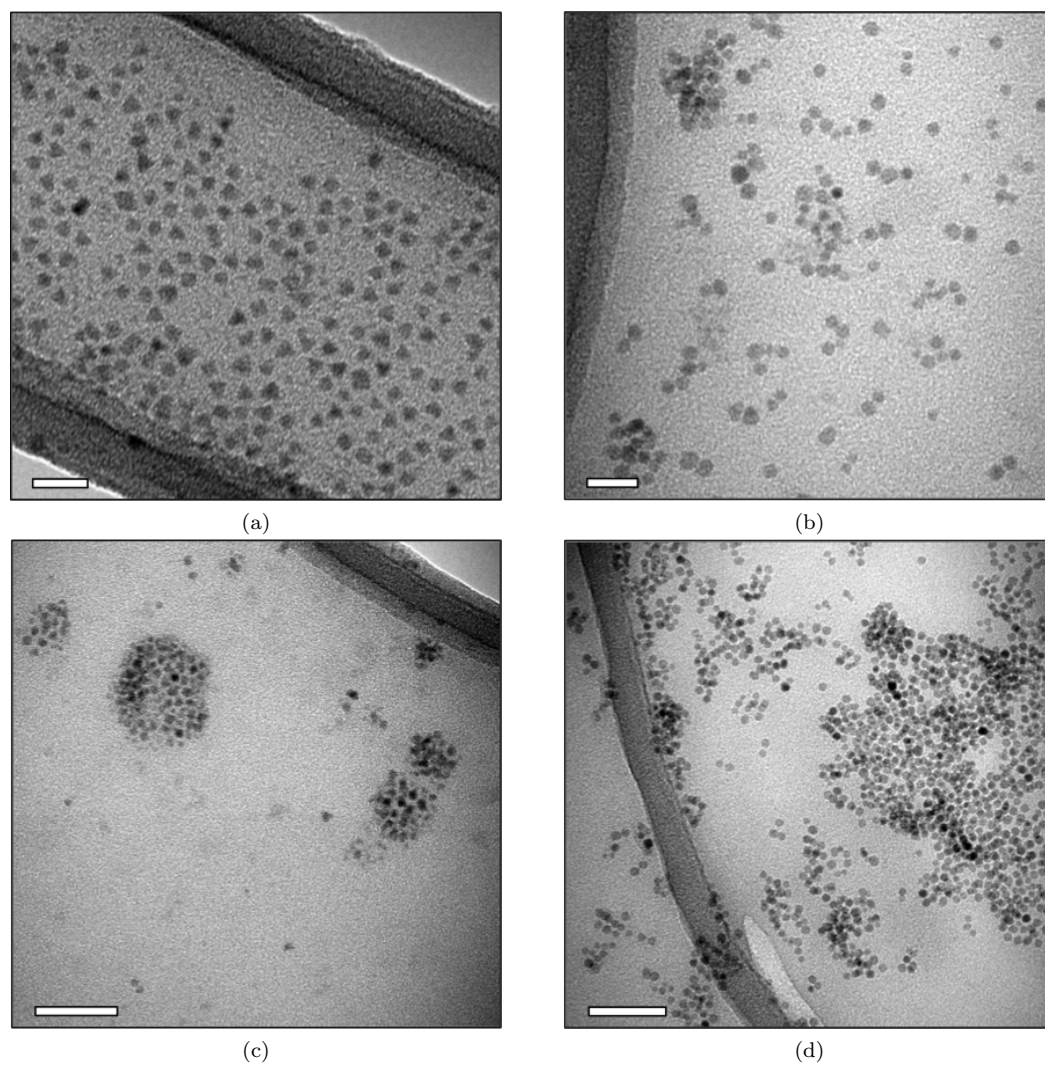
Figure 4.4: Characterisation of hydrophobin-QDs: TEM micrograph of (a) CdSeS/ZnS QDs coated with oleic acid in toluene ($D_{\mathrm{TEM}} = 4.6 \pm 0.8$ nm based on the measurement of 50 particles), (b) H*Protein B coated CdSeS/ZnS QDs in water ($D_{\mathrm{TEM}} = 4.9 \pm 0.8$ nm based on the measurement of 70 particles), (c) H*Protein B coated CdSeS/ZnS QDs in water showing evidence of clustering on the grid, and (d) H*Protein B coated Fe_3O_4 NPs in water ($D_{\mathrm{TEM}} = 4.9 \pm 0.5$ nm based on the measurement of 80 particles). Scale bars are 20 nm for (a,b) and 50 nm for (c,d).
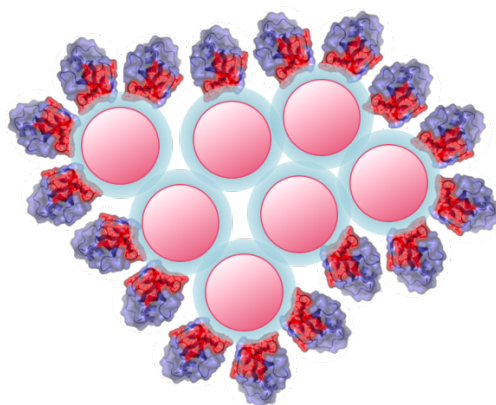
Figure 4.5: Schematic representation of hydrophobin encapsulation of multiple nanoparticles.

coefficients was bimodal with a very small shoulder/feature at the lowest sedimentation coefficients (figure 4.6). This shoulder corresponded to about 0.01 mg/mL of non-adsorbed protein, as quantified by the refractive index detector during fractionation. The molar mass of this fraction (as derived from the distribution of sedimentation coefficients) ranged from 50 kDa to 150 kDa and was hence comparable with free hydrophobin aggregates. Evaluating the main peak of the distribution of sedimentation coefficients, a diameter distribution with $D_{50} = 4.2$ nm, $D_{90} = 9.7$ nm was obtained (figure 4.7). An independent experiment with a UV/VIS detector synchronised to the centrifuge, tuned to 520 nm, confirmed that this distribution was selective for the QDs and did not contain signal from any macromolecules. Since the hydrodynamic diameter values matched the diameters from TEM and dynamic light scattering data, we can conclude that the QDs are extremely well-dispersed in water without measurable agglomeration (<5 %). Using a refractive index increment of $dn/dc = 0.163$ mL/mg, we determined the actual dispersed concentration of QDs was 0.45 mg/mL represented by the distribution shown in figure 4.7.

Secondary-ion mass spectrometry

Further, the stabilised QDs were also analysed by secondary-ion mass spectrometry (SIMS; technique by which the mass/charge ratios of secondary ions ejected from a specimen sputtered by a primary ion beam are measured), in order to compare their surface to free quantum dots and hydrophobins [12]. Apart from sodium salts, only traces of cadmium, zinc and selenium were detected. However, significant and characteristic even-numbered protein peaks were found in both positive and negative ion spectra (marked as blue dots in figure 4.8), which are characteristic of the hydrophobin [12]. Therefore, it is concluded that the
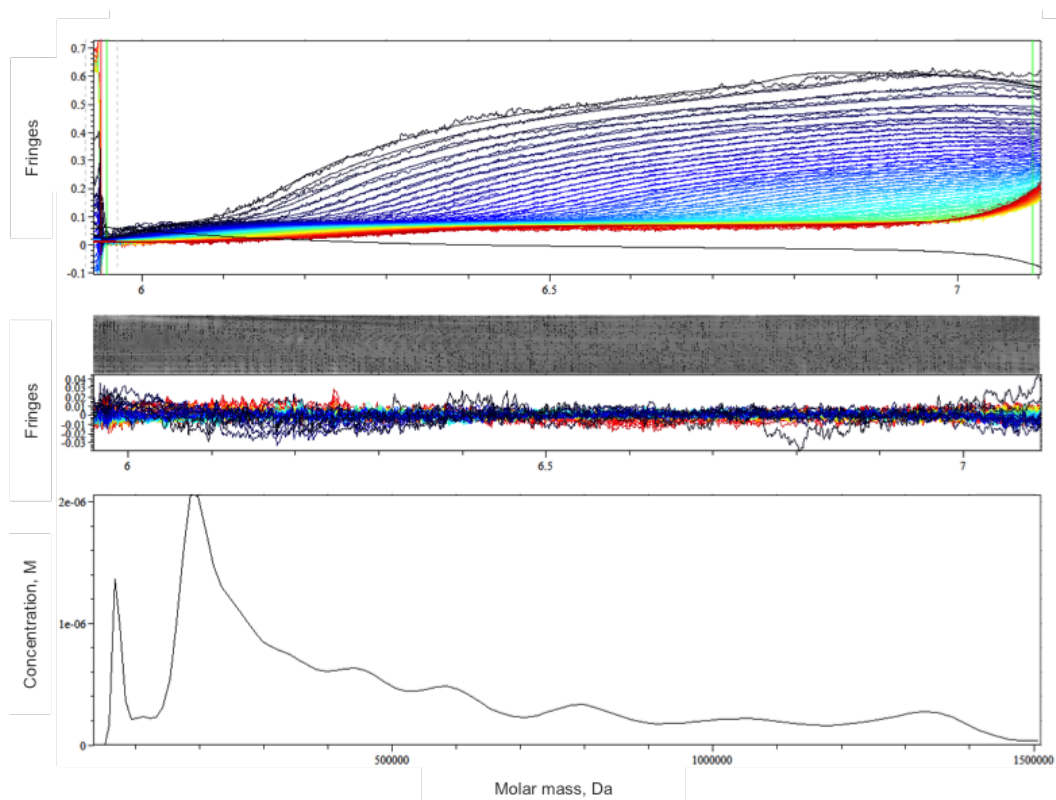
Figure 4.6: Characterisation of hydrophobin-QDs: Raw data and fit of AUC of the QD suspension after phase transfer, showing the bimodality of a small peak of slowly sedimenting organics, identified by their molar mass as non-bound H*Protein B, and the main peak of H*Protein B coated CdSeS/ZnS QDs.
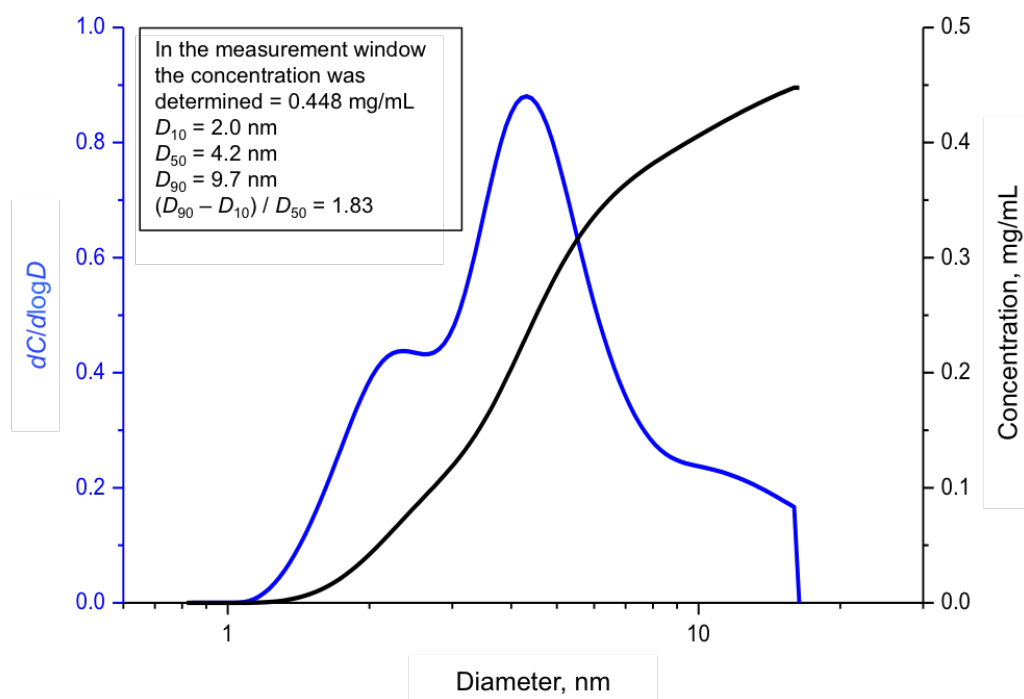
Figure 4.7: Characterisation of hydrophobin-QDs: Volume distribution of H*Protein B coated CdSeS/ZnS QDs as derived from AUC (raw data shown in figure 4.6).

QDs are effectively covered by hydrophobins, with vanishing physiological visibility of the inorganic core.
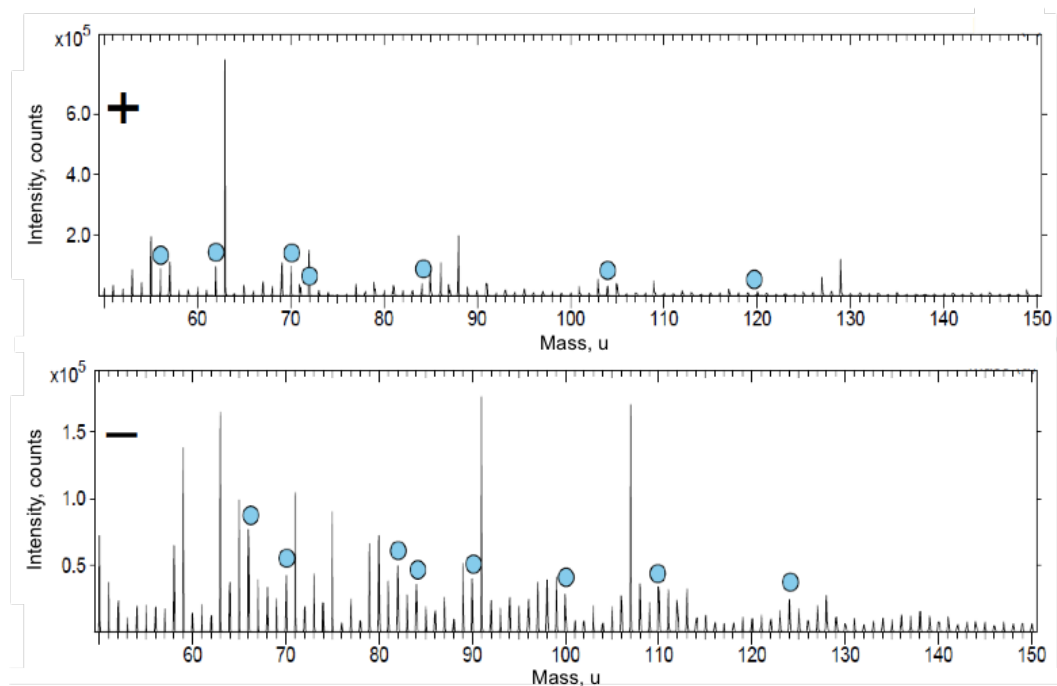
Figure 4.8: Characterisation of hydrophobin-QDs: SIMS of H*Protein B coated CdSeS/ZnS QDs after washing. Blue dots identify the characteristic hydrophobin ions (positive: 56 u, 62 u, 70 u, 72 u, 84 u, 104 u, 120 u; negative: 66 u, 70 u, 82 u, 84 u, 90 u, 100 u, 110 u, 124 u) [12].

4.2 *In vitro/vivo* studies

Hydrophobin-capped QDs were then used in labelling experiments in order to establish the potential for using this system in *in vivo* applications such as imaging and drug delivery.

4.2.1 Ovarian and breast cancer cells

In vitro labelling was explored by incubating the hydrophobin-CdSe/ZnS QDs with ovarian cancer cells (IGROV-1; figure 4.9), whilst *in vitro* labelling of breast cancer (MDA-MB-231 cells) was carried out alongside *in vivo* imaging of intratumourly injected particles administered to a live mouse model (figures 4.10 and 4.11). These studies were performed in collaboration with Dr. Maya Thanou in the Institute of Pharmaceutical Science at King's

College London. In both cases, successful endocytosis of the particles was observed, with strong QD emission clearly visible from the biological tissues. In the *in vivo* study, the particles were clearly observed 3 hours post-injection but found to largely clear from the tumour site after a further 24 hours, potentially via the lymphatic system as indicated by possible popliteal lymph node uptake. A scab was observed (96 hours post-injection) on the surface of the tumour that still exhibited a profile consistent with the presence of luminescent quantum dots.
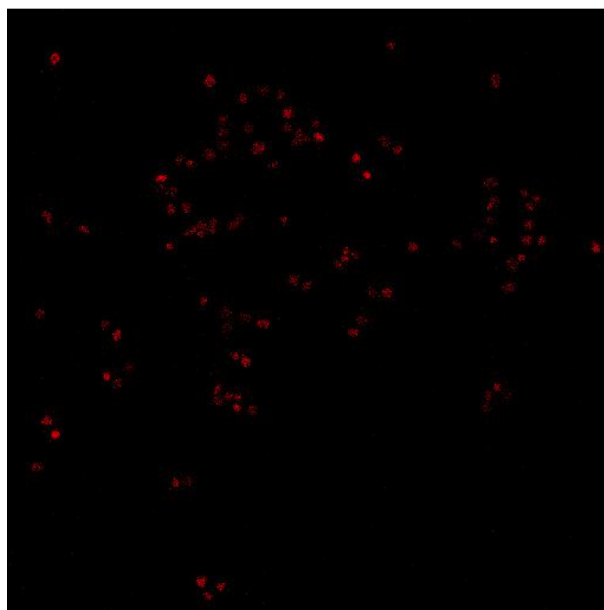
Figure 4.9: *In vitro* characterisation of hydrophobin-QDs: Ovarian cancer cells (IRGOV-1) incubated with H*Protein B coated CdSe/ZnS QDs for 1 h.

4.2.2 HeLa cells

Crosslinking

It was found that in some cases, the simple hydrophobin-QD (CdSeS/ZnS) conjugates were not stable in cell culture medium (in particular that used with HeLa cells), and this was overcome by crosslinking the hydrophobins whilst on the surface of the QD with glutaraldehyde (an amine-reactive crosslinker [13]). This resulted in a stable protein shell on the surface of the QDs which could withstand further processing, in a similar manner to the crosslinking of amphiphilic shells of polymers on quantum dots [14, 15]. The method used to crosslink the hydrophobin on to the QDs is shown in scheme 4.2 and involved simply stirring the hydrophobin QDs with a glutaraldehyde solution for 1 h at room temperature.
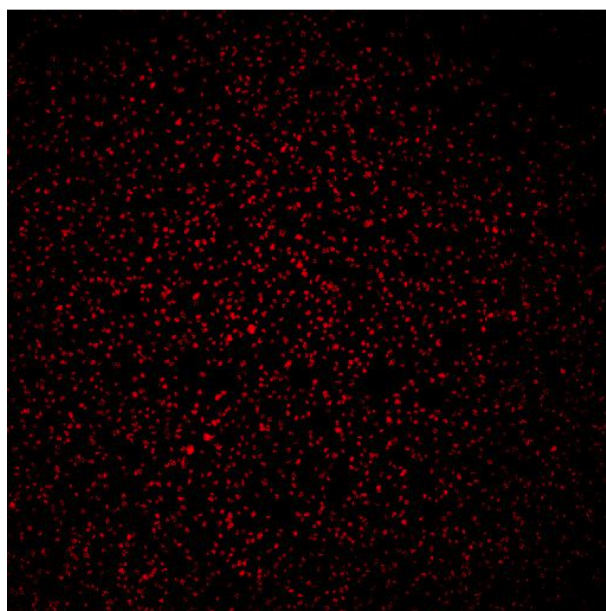
Figure 4.10: *In vitro* characterisation of hydrophobin-QDs: Breast cancer cells (MDA-MB-231) incubated with H*Protein B coated CdSe/ZnS QDs for 1 h.
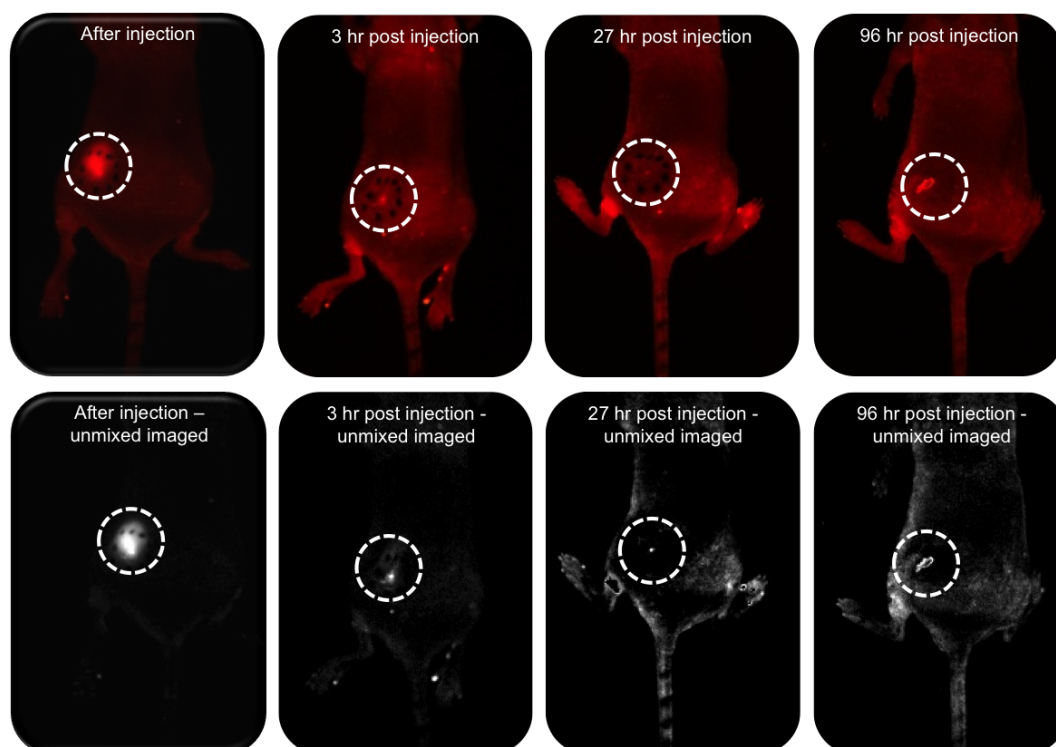
Figure 4.11: *In vivo* characterisation of hydrophobin-QDs: Time series images of H*Protein B coated CdSe/ZnS QDs injected intratumourly in a mouse.

The particles were then purified using a PD-10 column, and analysis of the brightest eluted fraction performed. The emission profile (figure 4.12) clearly shows a peak corresponding to gluataraldehyde present in the QD sample, with a smaller peak correlates to the found of the hydrophobin-QDs in figure 4.2. TEM revealed no change in particle core size, while DLS showed a slight increase and a shift of 20 mV in zeta potential was measured. All observations led to the conclusion that the glutaraldehyde was present on the surface of the protein coated QDs.
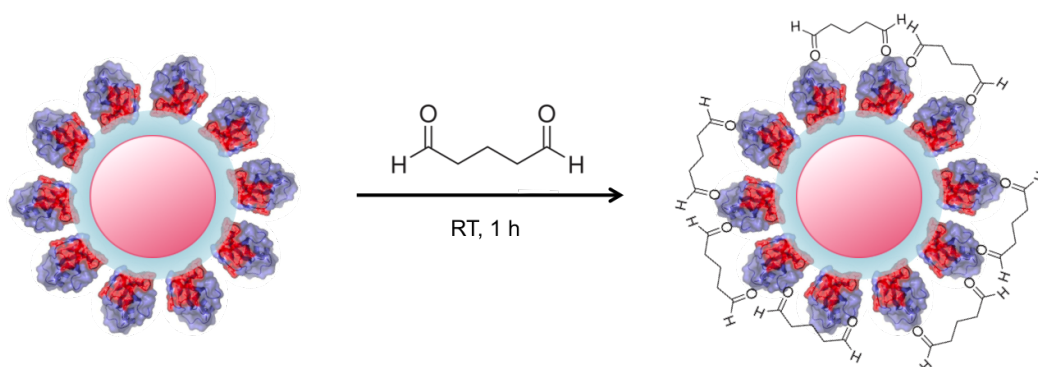
Scheme 4.2: Reaction scheme for the method of cross linking the hydrophobin on the surface of the QDs.
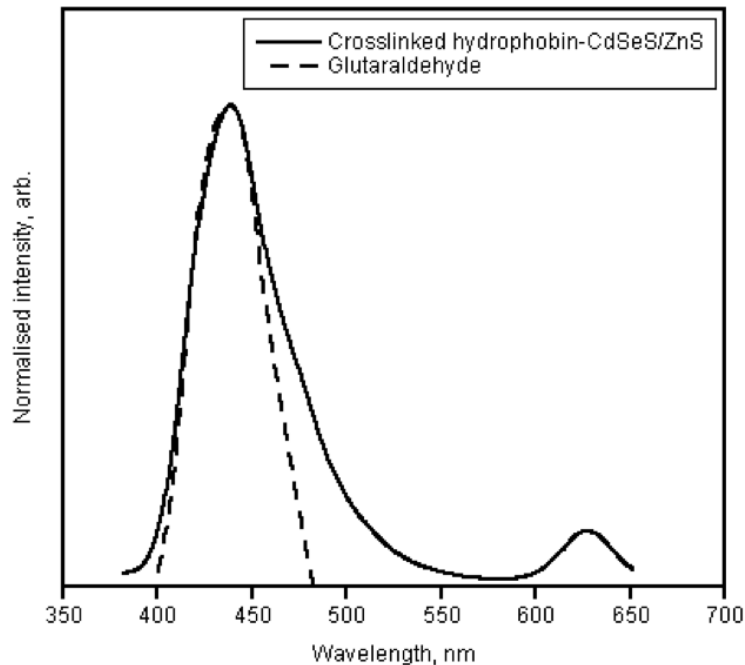
Figure 4.12: Characterisation of crosslinked hydrophobin-QDs: Emission spectra of H*Protein B coated CdSeS/ZnS QDs crosslinked with glutaraldehyde in water (black solid line; λ_{ems} = 439.0 nm and 627.5 nm), and glutaraldehyde only in water (grey dashed line; λ_{ems} = 438.5 nm).
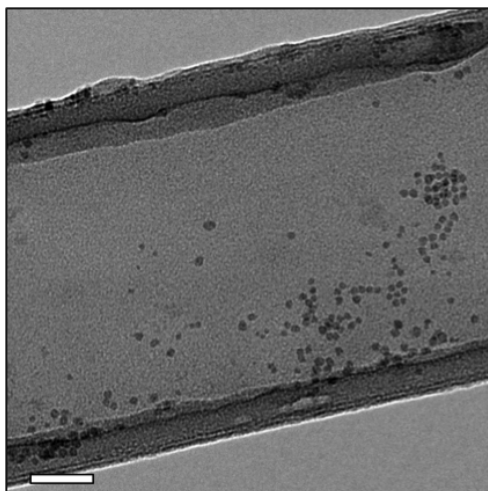
Figure 4.13: Characterisation of crosslinked hydrophobin-QDs: TEM micrograph of H*Protein B coated CdSeS/ZnS QDs crosslinked with glutaraldehyde in water ($D_{\text{TEM}} = 4.5 \pm 0.8$ nm based on the measurement of 40 particles). Scale bar is 50 nm.

Fluorescence imaging

Samples of crosslinked hydrophobin-QDs were used in the labelling of live HeLa cells. These studies were performed in collaboration with Dr. Dylan Owen in the Department of Physics at King's College London. Cells were stained and imaged using a spectral detector and 561 nm laser excitation. Fluorescence was collected over the range 570 nm to 740 nm. Figure 4.14a shows a composite fluorescence image of HeLa cells generated by summing all fluorescence channels. From this image, two points were selected. The first (blue) show the spectrum of cellular autofluorescence only, whereas the second (red) shows the additional fluorescence signal from QDs emitting in the 600 nm range which were also evident in the fluorescence image. Figure 4.14b shows the normalised fluorescence spectrum from the two regions of interest in figure 4.14a. Figure 4.14c shows an overlay of a fluorescence (610-650 nm) and bright-field image of HeLa cells incubated with hydrophobin coated QDs.

4.3 Functionalisation

The ability to add a further functionality to the hydrophobin-capped QDs then needed to be proved, allowing for potential targeting or multimodal imaging applications. Previous work by several groups has shown the feasibility of conjugating additional compounds to these proteins, for example Valo *et al.* reported the introduction of mercaptosuccinic acid
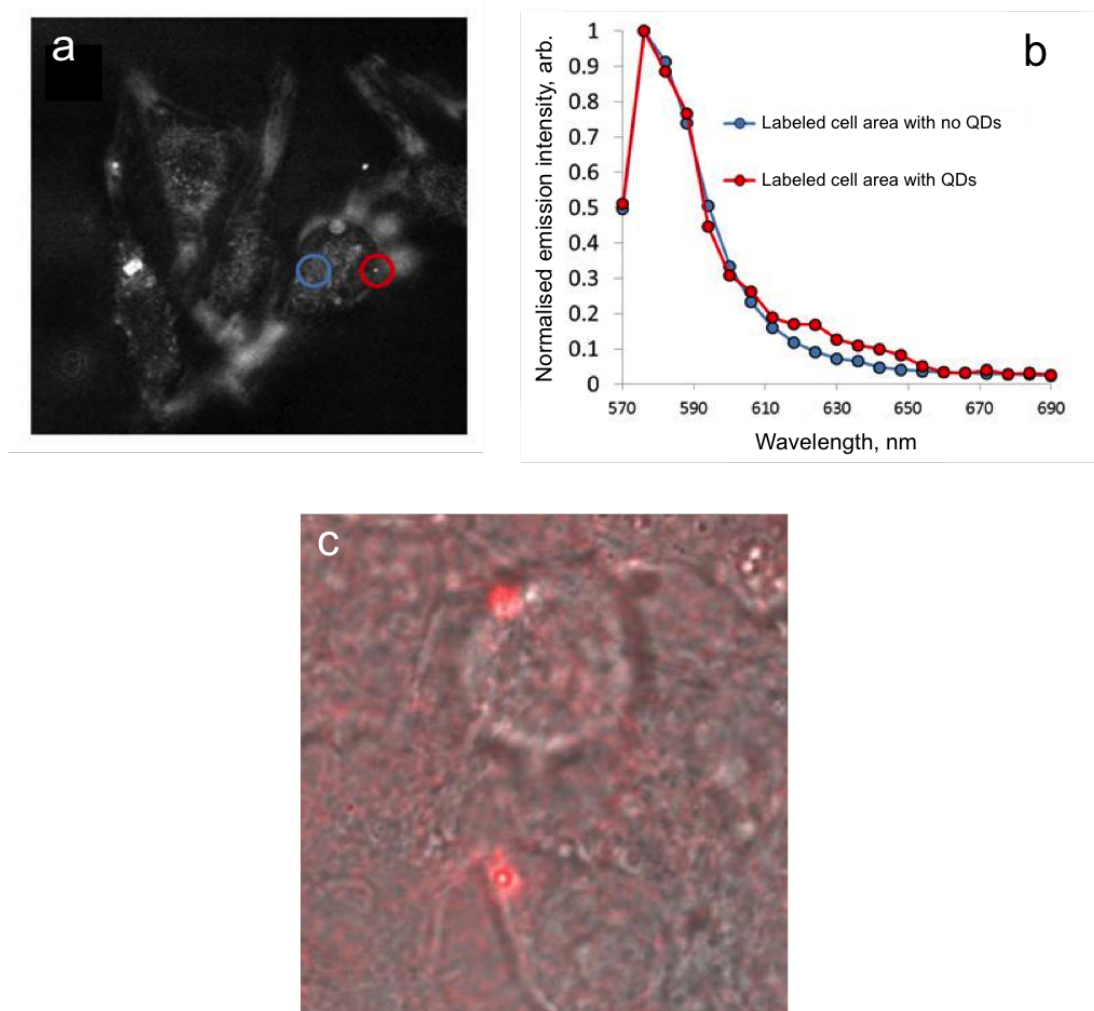
Figure 4.14: *In vivo* characterisation of hydrophobin-QDs: (a) Fluorescence image of live HeLa cells stained with H*Protein B coated CdSeS/ZnS QDs. Fluorescence was collected over the range 570 - 690 nm; (b) Normalised fluorescence emission spectrum from the two regions of interest shown in (a). The bright punctate structure in the red region shows the characteristic fluorescence signature of the nanoparticles in the 610 - 650 nm range, as compared to the blue region which exhibits only autofluorescence; (c) Fluorescence image collected in the 610-650 nm (red) range overlaid with a bright-field image of live HeLa cells showing uptake of the nanoparticles.

(MSA)-coated gold NPs on to the surface of hydrophobin coated beclomethasone dipropionate (BDP) particles which could allow for improved localisation of the drug NPs in electron microscopy [16]. Furthermore, Sarparanta *et al.* have described the successful ^{18}F radiolabelling of hydrophobin coated porous silicon NPs enabling PET imaging of the particle distribution and easy quantification of NPs in tissues [17].

4.3.1   Radiolabelling

To demonstrate the suitability of hydrophobin-QDs (in particular CdSeS/ZnS) for further conjugation, the exposed tyrosine residues on the exposed portion of the hydrophobin were radiolabelled with iodine-131, ^{131}I, (a well known radioiodination procedure [18, 19]) with no detrimental effect on the optical properties, proving the availability of the amino acid and incidentally resulting in a multimodal imaging agent. This was achieved by simple incubation of the hydrophobin-QD conjugates with ^{131}I, followed by TLC to give an initial indication that radiolabelling was successful (figures 4.15 and 4.16; table 4.1). Prior to purification, the % labelling efficiency was 36 %.
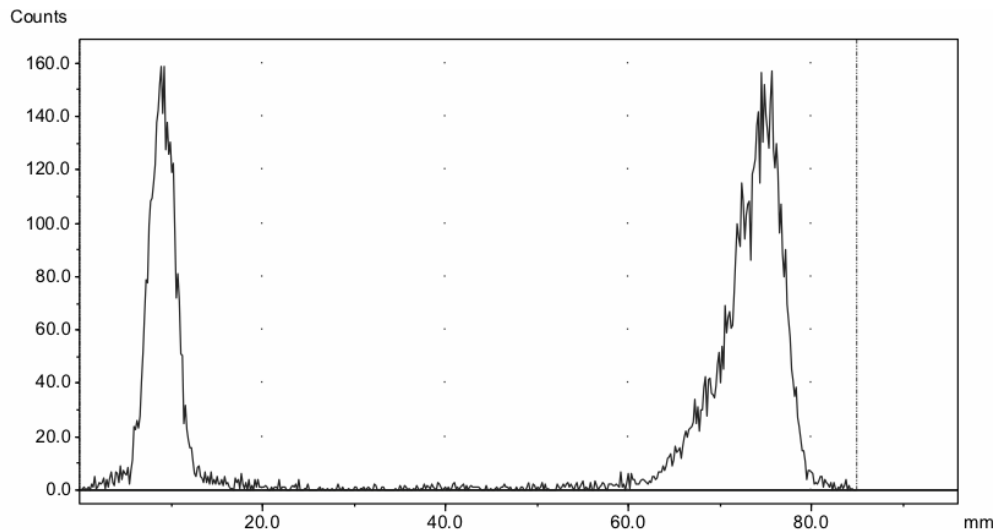
Figure 4.15: TLC characterisation of radiolabelled hydrophobin-QDs: Graphical representation of the TLC plate before purification (not integrated). The first peak corresponds to radiolabelled H*Protein B coated CdSe/ZnS QDs, the second peak corresponds to unreacted ^{131}I.

Purification through a PD-10 column was then performed, and it was found that isolated samples were clearly both luminescent and radioactive (activity in each collected fraction is given in table 4.2), confirming conjugation of the iodine to the free amino acid.
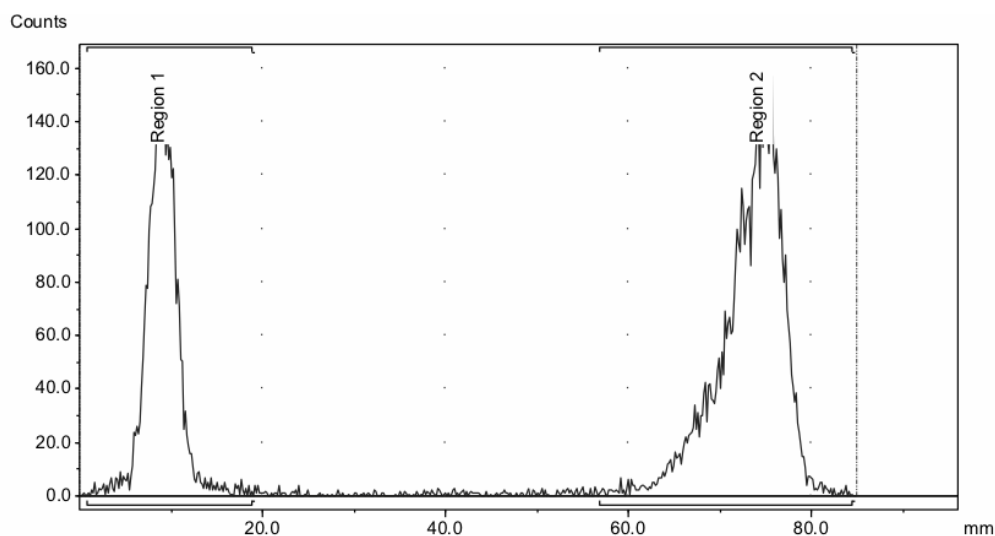
Figure 4.16: TLC characterisation of radiolabelled hydrophobin-QDs: Graphical representation of the TLC plate before purification (integrated). Region 1 corresponds to radiolabelled H*Protein B coated CdSeS/ZnS QDs, region 2 corresponds to unreacted ^{131}I.

Region	Rf	% Total	% ROI
1	0.155	35.26	35.95
2	0.882	62.81	64.05

Table 4.1: TLC characterisation of radiolabelled hydrophobin-QDs: Rf values for each region of the TLC plate before purification (integrated). Region 1 corresponds to radiolabelled H*Protein B coated CdSeS/ZnS QDs, region 2 corresponds to unreacted ^{131}I.

Fraction	Activity, MBq
1	0
2	0.7
3	3.6
4	1.7
5	0.5
Column	6.8

Table 4.2: PD-10 characterisation of radiolabelled hydrophobin-QDs: Activity measured in each radiolabelled H*Protein B coated CdSeS/ZnS QDs fraction after purification using a PD-10 column.

The purified fractions containing the majority of the activity were analysed by radio-TLC (figures 4.17 and 4.19) as before. The most active fraction was fraction 3, consistent with the size of the quantum dots. The counts were too low for detailed analysis on the TLC scanner so both fraction plates were cut into 9 equal parts and each section counted in the gamma counter, the results of which are shown in figures 4.18 and 4.20. The slight discrepancy between the two strips is most probably due to slight differences in the running of the strips as well as how they were cut, but essentially all activity is at the origin and none at the solvent front, which would be expected if there was free ^{131}I.
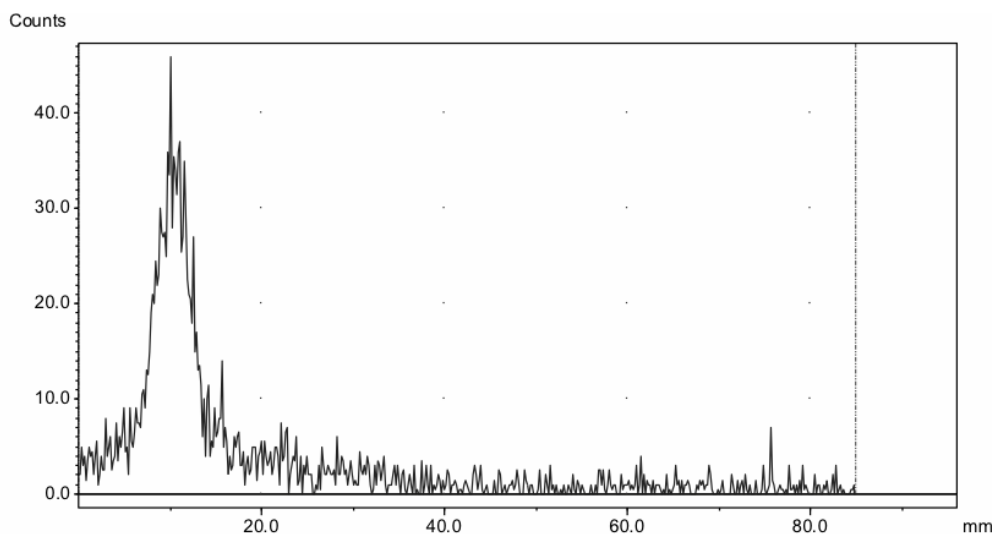
Figure 4.17: Radio-TLC characterisation of radiolabelled hydrophobin-QDs: Graphical representation of the TLC plate on fraction 3 after purification using a PD-10 column. The peak corresponds to radiolabelled H*Protein B coated CdSeS/ZnS QDs.

4.4 Conclusions

In conclusion, the simple encapsulation and phase transfer of quantum dots has been demonstrated using a commercially-available amphiphilic protein. The particles retained a significant amount of their emissive characteristics with no significant shift in the emission wavelength (625.5 nm before phase transfer, 627.5 nm after). TEM analysis confirmed encapsulation had no detrimental effect on the morphology and size of the QDs, however it was found that encapsulation of multiple particles into larger aggregates did occur occasionally. *In vitro* and *in vivo* studies revealed the potential use of these QDs in imaging with emission detected 24 h post injection. Finally, successful radiolabelling with ^{131}I confirmed the possibility of simply utilising residues on the hydrophobin surface for further
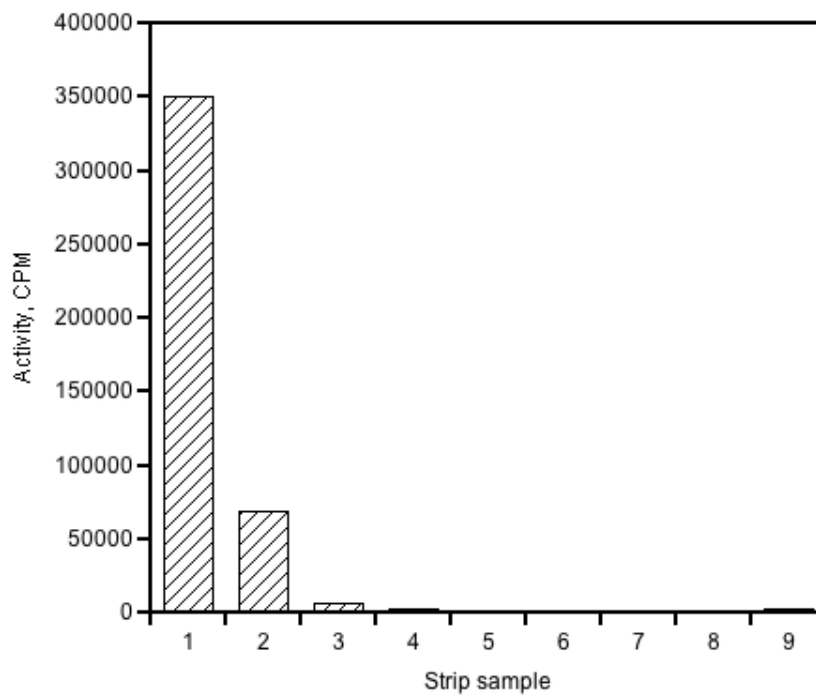
Figure 4.18: TLC characterisation of radiolabelled hydrophobin-QDs: Activity measured in each part of the strip for fraction 3 (radiolabelled H*Protein B coated CdSeS/ZnS QDs = 99 %, free ^{131}I = 1 %).
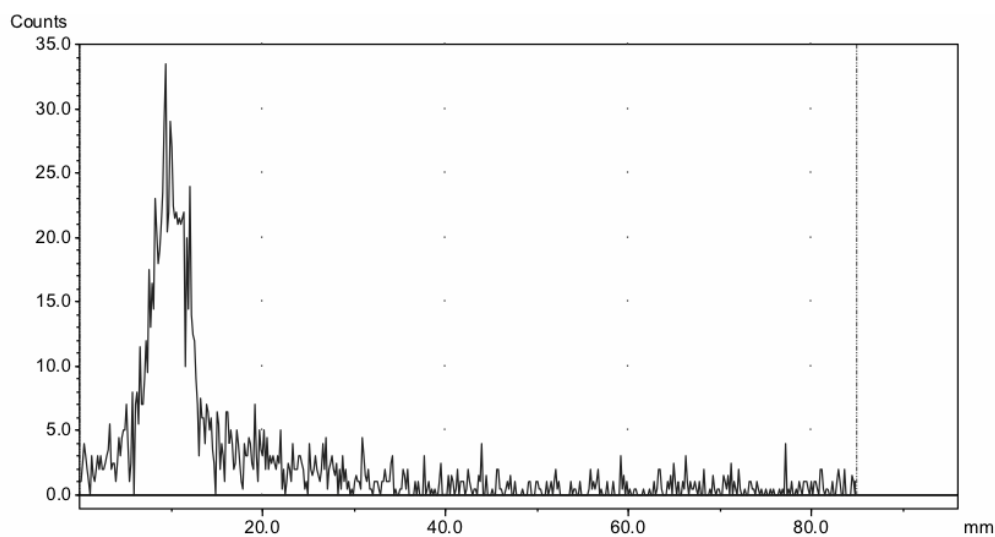
Figure 4.19: TLC characterisation of radiolabelled hydrophobin-QDs: Graphical representation of the TLC plate on fraction 4 after purification using a PD-10 column. The peak corresponds to radiolabelled H*Protein B coated CdSeS/ZnS QDs.
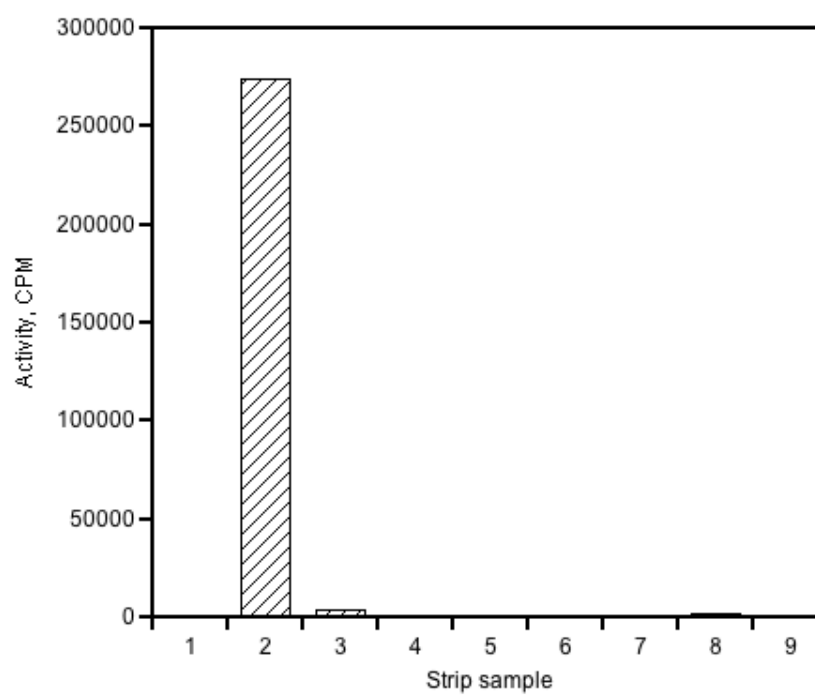
Figure 4.20: TLC characterisation of radiolabelled hydrophobin-QDs: Activity measured in each part of the strip for fraction 4 (radiolabelled H*Protein B coated CdSeS/ZnS QDs = 98.6 %, free ^{131}I = 1.4 %).

functionalisation.

Bibliography

[1] W. Wohlleben, T. Subkowski, C. Bollschweiler, B. von Vacano, Y. Liu, W. Schrepp, and U. Baus. Recombinantly Produced Hydrophobins from Fungal Analogues as Highly Surface-Active Performance Proteins. *Eur. Biophys. J.*, 39: 457–468, **2010**.

[2] S. Taniguchi. *The Synthesis of CdTe-Based Quantum Dots*. PhD thesis, King's College London, **2012**.

[3] M. Reger, T. Sekine, and H. Hoffmann. Boosting the Stability of Protein Emulsions by the Synergistic Use of Proteins and Clays. *Colloid Polym. Sci.*, 290: 631–640, **2012**.

[4] L. M. Bimbo, E. Mäkilä, J. Raula, T. Laaksonen, P. Laaksonen, K. Strommer, E. I. Kauppinen, J. Salonen, M. B. Linder, J. Hirvonen, and H. A. Santos. Functional Hydrophobin-Coating of Thermally Hydrocarbonized Porous Silicon Microparticles. *Biomaterials*, 32: 9089–9099, **2011**.

[5] M. Reger and H. Hoffmann. Hydrophobin Coated Boehmite Nanoparticles Stabilizing Oil in Water Emulsions. *J. Colloid Interface Sci.*, 368: 378–386, **2012**.

[6] G. Fang, B. Tang, Z. Liu, J. Gou, Y. Zhang, H. Xu, and X. Tang. Novel Hydrophobin-Coated Docetaxel Nanoparticles for Intravenous Delivery: *In Vitro* Characteristics and *In Vivo* Performance. *Eur. J. Pharm. Sci.*, 60: 1–9, **2014**.

[7] L. Qu, Z. A. Peng, and X. Peng. Alternative Routes toward High Quality CdSe Nanocrystals. *Nano Lett.*, 1: 333–337, **2001**.

[8] D. V. Talapin, A. L. Rogach, A. Kornowski, M. Haase, and H. Weller. Highly Luminescent Monodisperse CdSe and CdSe/ZnS Nanocrystals Synthesized in a HexadecylamineTrioctylphosphine OxideTrioctylphospine Mixture. *Nano Lett.*, 1: 207–211, **2001**.

[9] X. L. Zhang, J. Penfold, R. K. Thomas, I. M. Tucker, J. T. Petkov, J. Bent, A. Cox, and I. Grillo. Self-Assembly of Hydrophobin and Hydrophobin/Surfactant Mixtures in Aqueous Solution. *Langmuir*, 27: 10514–10522, **2011**.

[10] K. Kurppa, H. Jiang, G. R. Szilvay, A. G. Nasibulin, E. I. Kauppinen, and M. B. Linder. Controlled Hybrid Nanostructures through Protein-Mediated Noncovalent Functionalization of Carbon Nanotubes. *Angew. Chem. Int. Ed.*, 46: 6446–6449, **2007**.

[11] M. Reger, T. Sekine, T. Okamoto, and H. Hoffmann. Unique Emulsions Based on Biotechnically Produced Hydrophobins. *Soft Matter*, 7: 8248–8257, **2011**.

[12] B. von Vacano, R. Xu, S. Hirth, I. Herzenstiel, M. Rückel, T. Subkowski, and U. Baus. Hydrophobin can Prevent Secondary Protein Adsorption on Hydrophobic Substrates Without Exchange. *Anal. Bioanal. Chem.*, 400: 2031–2040, **2011**.

[13] I. Migneault, C. Dartiguenave, M. J. Bertrand, and K. C. Waldron. Glutaraldehyde: Behavior in Aqueous Solution, Reaction with Proteins, and Application to Enzyme Crosslinking. *BioTechniques*, 37: 790–796, **2004**.

[14] X. Wu, H. Liu, J. Liu, K. N. Haley, J. A. Treadway, J. P. Larson, N. Ge, F. Peale, and M. P. Bruchez. Immunofluorescent Labeling of Cancer Marker Her2 and Other Cellular Targets with Semiconductor Quantum Dots. *Nat. Biotech.*, 21: 41–46, **2003**.

[15] T. Pellegrino, L. Manna, S. Kudera, T. Liedl, D. Koktysh, A. L. Rogach, S. Keller, J. Rädler, G. Natile, and W. J. Parak. Hydrophobic Nanocrystals Coated with an Amphiphilic Polymer Shell: A General Route to Water Soluble Nanocrystals. *Nano Lett.*, 4: 703–707, **2004**.

[16] H. K. Valo, P. H. Laaksonen, L. J. Peltonen, M. B. Linder, J. T. Hirvonen, and T. J. Laaksonen. Multifunctional Hydrophobin: Toward Functional Coatings for Drug Nanoparticles. *ACS Nano*, 4: 1750–1758, **2010**.

[17] M. Sarparanta, L. M. Bimbo, J. Rytkönen, E. Mäkilä, T. J. Laaksonen, P. Laaksonen, M. Nyman, J. Salonen, M. B. Linder, J. Hirvonen, H. A. Santos, and A. J. Airaksinen. Intravenous Delivery of Hydrophobin-Functionalized Porous Silicon Nanoparticles: Stability, Plasma Protein Adsorption and Biodistribution. *Mol. Pharm.*, 9: 654–663, **2012**.

[18] S-L. Karonen. Developments in Techniques for Radioiodination of Peptide Hormones and Other Proteins. *Scand. J. Clin. Lab. Inv.*, 201: 135–138, **1990**.

[19] K. K. Bhargava and S. A. Acharya. Labeling of Monoclonal Antibodies with Radionuclides. *Semin. Nucl. Med.*, 19: 187–201, **1989**.

Chapter 5

Future work

5.1 Ultrasmall superparamagnetic iron oxide nanoparticles

Using this concept, multimodal USPIOs have been generated with exceptional imaging properties such as the lowest r_2/r_1 ratio reported to date at 3 T and long blood circulation times. These USPIOs are now being further evaluated for enhanced MR angiography using T_1-weighted sequences. Nonetheless, further work is required towards improving the targeting properties. *In vitro* cell studies have confirmed specific binding to PSMA and VCAM-1 via conjugation of single chain antibody fragments, but additional FACS studies are needed in order to fully understand the mechanisms taking place during uptake involving the LyP-1 peptide. Initially, the results obtained will need to be repeated alongside a control cell line in order to ensure that the uptake observed is a result of receptor-mediated endocytosis. From here, investigation into the dependency of targeted USPIO uptake on blocking peptide concentration could be performed, providing new data which may allow for a more thorough understanding of the processes occurring.

Moreover, analysis and quantification of the surface composition of the targeted-NPs is necessary but will pose certain challenges. One potential technique that would allow for evaluation of the individual components would be high performance liquid chromatography (HPLC).

Furthermore, development of the radionuclide conjugation procedure is necessary, as the radiolabelling yield is currently particularly low. A possible route to optimising the amount of activity bound to the particles is to introduce a BP-anchored chelator for binding radiometals into the initial phase transfer coating to which ^{99m}Tc can bind.

Finally, *in vivo* characterisation of the targeted USPIOs using the mouse models previously investigated will need to be performed in order to complete a full picture of the potential of these particles for molecular imaging *in vivo*. Obtaining images using a PET-MR instrument would also be a favourable addition to this work.

5.2 Polyethylene glycol phase transfer of CdZnSeS alloyed quantum dots

For the PEGylated QDs, it was found that the simple method of PEGylation previously described allowed for the successful dispersion of these semiconductor nanoparticles in water with few changes in the optical properties. However, a detailed analysis of the water-soluble particles is required. The presence of PEG(5)-BP needs to be confirmed using a combination of techniques, including IR spectroscopy, EDX and XPS. In addition, the amount of PEG(5)-BP bound to the surface of the QDs should be quantified as it was for the PEG(5)-BP-USPIOs, using TGA. Measurements for the quantum yield will also need to be performed in order to deduce the reduction in optical emission after ligand exchange has occurred.

Once the PEG-coated QDs have been fully characterised, the same techniques should be performed using the maleimide-PEGylated particles in order to determine the proportion of mal-PEG(5)-BP to PEG(5)-BP conjugated to the surface.

5.3 Hydrophobin phase transfer of inorganic nanoparticles

The objective of showing that an amphiphilic protein, a hydrophobin, could be used to successfully produce water-soluble QDs has been demonstrated. Further work on the synthesis is required to fully understand the mechanisms taking place in order to improve the yield of hydrophobin-QDs. Quantification of amount of protein encapsulating the quantum dots is necessary, and as it was shown that using tyrosine residues on the exposed region of the hydrophobin allows for further functionalisation, more detail on the availability of these regions is needed.

Once the above has been achieved, the next stage of this study will be to conjugate a targeting molecule to the exposed residues and perform *in vitro* cell studies as has been accomplished with targeted USPIOs. Potentially, this could be achieved using the biomarkers previously investigated during the iron oxide particle research.

Chapter 6

Experimental

6.1 Materials

6.1.1 General

Reagent grade ethanol, hexane, methanol, DCM, dimethylformamide (DMF) and nitric acid (TraceSelect Ultra) were purchased from commercial sources and used as received. Water (type I, 18.2 MΩ·cm) was obtained from an ELGA Purelab Option-Q system, or a Millipore, Direct-Q 3 UV Water Purification System. DMEM, Opti-MEM, and RPMI-1640 media (Gibco, UK) were used for cell culture. For TLC studies, silica gel 60 F254 glass plates (2.5 cm x 7 cm, Merck KGaA, Germany) were used. Size-exclusion filters (Vivaspin) and columns (PD-10, PD MidiTrap and PD MiniTrap) were obtained from GE Healthcare, UK. For cell studies, 16- and 24-well plates were obtained from Thermo Scientific. Millex IC 0.22 μm hydrophilic 13 mm polytetrafluoroethylene (PTFE) filters (Millipore, USA) and 0.2 μm 25 mm cellulose acetate filters (VWR, USA) were used throughout this study.

6.1.2 Ultrasmall superparamagnetic iron oxide nanoparticles

Iron(III) acetylacetonate, $Fe(acac)_3$, (97 %), oleylamine (70 %), and benzyl ether (98 %) were purchased from Sigma Aldrich. PEG-BP and mal-PEG-BP were prepared in-house by Dr. Rafael Torres Martin de Rosales. $Na[^{99m}TcO_4]$ in physiological saline was obtained from a $^{99}Mo/^{99m}Tc$ generator at the Radiopharmacy at Guy's and St Thomas' Hospital NHS Trust, London, UK. $[^{99m}Tc(CO)_3(H_2O)_3]^+$ was synthesised using Isolink kits (Mallinckrodt Medical B.V., St. Louis, MO, USA). DPA-ale and ^{99m}Tc-DPA-ale were synthesised as previously reported [1]. USPIO-1 particles were prepared in-house by Dr. Rafael Torres Martin de Rosales. Human serum from human male AB plasma was obtained from Sigma Aldrich. 5-((2-(and-3)-*S*-(acetylmercapto) succinoyl) amino) (SAMSA) fluorescein was purchased from Life Technologies. Dialysis cassettes with a 2 kDa MWCO were purchased from Fisher Scientific Ltd. J591, 6C7.1, and 6C7.1-fluorescein were prepared in-house by Dr. Florian Kampmeier, and LyP-1 (fluorescent and non-fluorescent) was purchased from ProteoGenix SAS, France. Penta · His Alexa Fluor 488 was purchased from Life Technologies. Transfection DNA (pCMV-SPORT6 mouse VCAM-1, maxi prep DNA, 2.764 μg/μL in 10 mM Tris pH 8.5) was purchased from Life Technologies and Lipofectamine 2000 reagent was obtained from Invitrogen.

6.1.3 Polyethylene glycol phase transfer of CdZnSeS alloyed quantum dots

Selenium powder (99.8 %), sulfur powder (99.5 %), trioctylphosphine (TOP, 90 %), cadmium oxide (CdO, 99.5 %), zinc acetate (analytical reagent grade), oleic acid (90 %), and 1-octadecene (ODE, 90 %) were obtained from Sigma Aldrich.

6.1.4 Hydrophobin phase transfer of inorganic nanoparticles

CdSe/ZnS (Lumidot 590) and CdSeS/ZnS quantum dots (QDs) were purchased from Sigma Aldrich and used as received. CdSe/ZnS was also prepared in-house by Dr. Shohei Taniguchi; the cores (CdSe) were prepared whilst referring to Qu *et al.* [2], whilst the ZnS shells were deposited using the method described by Talapin *et al.* [3]. Fe_3O_4 particles were prepared as described below. Hydrophobins (H*Protein B, 50 mg/mL) was obtained from BASF and used as received. ^{131}I was obtained from Perkin Elmer. Sodium phosphate buffer solution (for HPCE, pH 7.0) and 5.6 M glutaraldehyde solution (technical grade) were purchased from Sigma Aldrich.

6.2 Instrumentation

6.2.1 General

Samples for TEM were prepared by evaporation of a drop of the aqueous colloidal suspensions in ambient conditions onto a carbon-coated 3.05 mm copper grid (200 mesh, Agar Scientific, UK or holey 300 mesh, TAAB Laboratories Equipment Ltd., UK). TEM was obtained from a Tecnai T20 instrument (FEI, USA) with a LaB6 filament operating at 200 kV, or a Tecnai F20 200 kV FEGTEM fitted with an Orius SC600 CCD camera (Gatan, USA) and an 80 mm^2 X-Max SDD EDX detector (Oxford Instruments, UK). DLS and zeta potential were performed with a Zetasizer Nano ZS instrument (Malvern Instruments, UK) at 25 °C. TLC plates were scanned with a Mini-Scan TLC scanner equipped with a FC3600 detector of γ photons (Lablogic, UK). Radioactivity in samples was measured with a CRC-25R dose calibrator (Capintec, USA) or a 1282 CompuGamma gamma counter (LKB Wallac,

Finland). Absorption spectroscopy measurements were taken using a Hitachi U-4100 UV-Visible-NIR spectrophotometer in a 1 cm path length quartz cuvette. Emission spectra were obtained using a Perkin Elmer LS 50B spectrometer.

6.2.2 Ultrasmall superparamagnetic iron oxide nanoparticles

Final synthesis of USPIOs performed using a 250 mL heating mantle connected to a digital temperature monitor (J-KEM Scientific, USA). Lattice fringe spacing measurements made using ImageJ. IR studies were performed with a Spectrum 100 spectrometer (Perkin-Elmer, USA) equipped with a universal attenuated total reflection (ATR) sampling accessory. The concentrations of iron in the dispersions of SPIO nanoparticles were calculated by ICP-MS (Mass Spectrometry Service, King's College London) after digestion in nitric acid for 16 h. EDX was obtained from a Tecnai T20 instrument (FEI, USA) with a LaB6 filament operating at 200 kV and equipped with a Genesis system EDAX spectrometer (EDAX, USA). XPS were recorded using a Kratos AXIS ULTRA with monochromated Al KR radiation (10 kV anode potential, 15 A emission current) in fixed analyser transmission mode (80 eV pass energy). TGA was performed under N_2 flow (60 mL/min) with a heating rate of 10 °C/min using a TA SDT-600 thermogravimetric analyser. XRD was recorded on a Bruker D8 Advance powder diffractometer with a Cu KR X-ray source ($\lambda = 1.54058$ Å) operating at 40 kV and 40 mA and a Sol-X detector. Magnetisation data was obtained with a MPMS SQUID-VSM instrument by Quantum Design (San Diego, USA), or a Mini High-Field VSM (Cryogenics, UK), at 300 K. Relaxivity measurements were performed using a minispec mq20 NMR analyser operating at 20 MHz (Bruker, Germany), a minispec mq60 NMR analyser operating at 60 MHz (Bruker, Germany), a Spin Track analyser operating at 29 MHz and 39 MHz (Process NMR Associates, USA), an AMX 300 MHz (Bruker, Germany), and a Spinmaster fast field cycling relaxometer operating from 0.015 MHz up to 40 MHz (STELAR, Italy). Phantom relaxivity calculations were performed using a 3 T Philips Achieva MR scanner (Philips Healthcare, Best, The Netherlands) equipped with a clinical gradient system (30 mTm^{-1}, 200 mT/m/ms) and a single-loop surface coil (diameter = 47 mm). NMR spectrum was obtained using a Bruker Avance 400 at 20 °C in Deuterated chloroform,$CDCl_3$, (Cambridge Isotope Laboratories). ^{1}H resonances were referenced to the residual protic impurity of the solvent (δH 7.26 ppm). Purification of targeted particles was performed using an ÄKTA FPLC system (GE Healthcare, UK). FACS data was obtained

using a FACSCalibur with Cellquest software (BD Biosciences UK), or a BD FACSAria III cell sorter (BD Biosciences, UK).

6.2.3 Polyethylene glycol phase transfer of CdZnSeS alloyed quantum dots

Microscopy was performed using a Leica confocal microscope (Leica Microsystems, UK).

6.2.4 Hydrophobin phase transfer of inorganic nanoparticles

DLS measurements of hydrophobins only were performed by Dr. Shohei Taniguchi using Delsa Nano C Particle Analyser using 1 cm path length quartz cuvettes.

6.3 Ultrasmall superparamagnetic iron oxide nanoparticles procedures

6.3.1 Synthesis of ultrasmall superparamagnetic iron oxide nanoparticles

6.3.1.1 Initial synthetic method

Oleylamine-coated USPIOs were synthesised using a slight variation of the method of Xu *et al.* [4]. Fe(acac)$_3$ (1.042 g) was added to a mixture 15 mL of oleylamine and 15 mL of benzyl ether, and was stirred using a magnetic stirrer. The solution was then dehydrated at 170 °C for 1 h under a N$_2$ flow followed by a temperature increase to 260 °C over a period of 15 min, after which the heating appliance was removed. The solution was left to cool to room temperature and the iron oxide NPs precipitated upon the addition of 24 mL of ethanol, followed by centrifugation at 7000 rpm for 4 min. The supernatant was discarded and the process repeated with another 20 mL of ethanol, then a further 48 mL.

6.3.1.2 Development of synthesis

Fe(acac)$_3$ (1.042 g) was added to a mixture 15 mL of oleylamine and 15 mL of benzyl ether, and was stirred using a magnetic stirrer. The solution was then heated to 128 °C at a rate of 363.5 °C/h under a N$_2$ flow followed by a temperature increase to 180 °C over a period of 1 h, and finally heating to 260 °C at a ramping rate of 396 °C/h after which the heating appliance was removed. The solution was left to cool to room temperature and the iron oxide NPs precipitated upon the addition of 24 mL of ethanol, followed by centrifugation at 7000 rpm for 4 min. The supernatant was discarded and the process repeated with another 20 mL of ethanol, then a further 48 mL.

6.3.1.3 Changing ramping rate

Doubling ramping rate

Fe(acac)$_3$ (1.060 g) was added to a mixture 15 mL of oleylamine and 15 mL of benzyl ether, and was stirred using a magnetic stirrer rotating at 550 rpm. The solution was then heated to 128 °C at a rate of 727 °C/h under a N$_2$ flow followed by a temperature increase to 180 °C over a period of 30 min, and finally heating to 260 °C at a ramping rate of 792 °C/h after which the heating appliance was removed. The solution was left to cool to room temperature and the iron oxide NPs precipitated upon the addition of 35 mL of ethanol, followed by centrifugation at 7000 rpm for 4 min. The supernatant was discarded and the process repeated with another 40 mL of ethanol, then a further 56 mL.

Halving ramping rate

Fe(acac)$_3$ (1.055 g) was added to a mixture 15 mL of oleylamine and 15 mL of benzyl ether, and was stirred using a magnetic stirrer rotating at 550 rpm. The solution was then heated to 128 °C at a rate of 181.75 °C/h under a N$_2$ flow followed by a temperature increase to 180 °C over a period of 2 h, and finally heating to 265 °C at a ramping rate of 198 °C/h after which the heating appliance was removed. The solution was left to cool to room temperature and the iron oxide NPs precipitated upon the addition of 35 mL of ethanol, followed by centrifugation at 7000 rpm for 4 min. The supernatant was discarded and the process repeated with another 40 mL of ethanol, then a further 56 mL.

6.3.1.4 Changing precursor ratio

2:1 Oleylamine to benzyl ether

Fe(acac)$_3$ (1.058 g) was added to a mixture 20 mL of oleylamine and 10 mL of benzyl ether, and was stirred using a magnetic stirrer. The solution was then heated to 128 °C at a rate of 363.5 °C/h under a N$_2$ flow followed by a temperature increase to 180 °C over a period of 1 h, and finally heating to 270 °C at a ramping rate of 396 °C/h after which the heating appliance was removed. The solution was left to cool to room temperature and the iron oxide NPs precipitated upon the addition of 35 mL of ethanol, followed by centrifugation at 7000 rpm for 4 min. The supernatant was discarded and the process repeated with another 42 mL of ethanol, then a further 56 mL.

Oleylamine only

Fe(acac)$_3$ (1.042 g) was added to 30 mL of oleylamine, and was stirred using a magnetic stirrer rotating at 550 rpm. The solution was then heated to 128 °C at a rate of 345.9 °C/h under a N$_2$ flow followed by a temperature increase to 180 °C over a period of 1 h, and finally heating to 270 °C at a ramping rate of 396 °C/h after which the heating appliance was removed. The solution was left to cool to room temperature and the iron oxide NPs precipitated upon the addition of 30 mL of ethanol, followed by centrifugation at 7000 rpm for 4 min. The supernatant was discarded and the process repeated with another 35 mL of ethanol, then a further 56 mL.

6.3.1.5 Final synthetic method

Fe(acac)$_3$ (1.042 g) was added to 30 mL of oleylamine, and was stirred using a magnetic stirrer rotating at 550 rpm. The solution was then heated to 128 °C at a rate of 363.5 °C/h under a N$_2$ flow followed by a temperature increase to 180 °C over a period of 1 h, and finally heating to 270 °C at a ramping rate of 396 °C/h after which the heating appliance was removed. The solution was left to cool to room temperature and the iron oxide NPs precipitated upon the addition of 30 mL of ethanol, followed by centrifugation at 7000 rpm for 4 min. The supernatant was discarded and the process repeated with another 35 mL of ethanol, then a further 56 mL.

6.3.2 Polyethylene glycol phase transfer of ultrasmall superparamagnetic iron oxide nanoparticles

6.3.2.1 Initial synthetic method

Oleylamine-coated USPIOs (5.4 mg) and PEG(2)-BP (10 mg) were added to 3 mL of H_2O in an open glass vial, and the mixture was sonicated for $\sim$15 min. The solution was left at room temperature for 3 days, after which a pale brown dispersion remained with a small amount of precipitate settled on the bottom of the vial. The solution was centrifuged at 4000 rpm for 10 min to remove the solid.

6.3.2.2 Final synthetic method

Oleylamine-coated USPIOs (1 mg) and PEG(5)-BP (10 mg) were added to 1 mL of DCM in an open glass vial, and the mixture was sonicated until the solvent evaporated ($\sim$15 min). To the remaining residue was added 2 mL of water resulting in a clear brown solution. This mixture was washed with 2 mL of hexanes to remove the oleylamine. This process was repeated two more times followed by removal of hexanes by evaporation under a N_2 flow. The final mixture was filtered through a 0.2 μm hydrophilic PTFE filter, followed by several cycles of washing/concentrating using a Vivaspin 2 centrifugal filter (30 kDa MWCO) using water to remove excess PEG(5)-BP. The washings collected during this purification stage were dried to measure the mass of PEG(5)-BP bound. The final amber solution was removed from the filter and stored at 4 °C in a glass vial.

6.3.3 Radiolabelling

6.3.4 Conjugation of ^{99m}Tc to dipicolylamine-alendronate

DPA-ale (1 mg) was added to 1 mL of a 100 mM carbonyl buffer (pH 9), and 100 μL of this solution was the diluted up to 1 mL with 100 mM carbonyl buffer (pH 9). To prepare the radiolabel, ^{99m}TcO$_4^-$ was added to an Isolink kit and heated for 30 min at 100 °C, which produced $[^{99m}$Tc(CO)$_3$(OH$_2$)$_3]^+$ with a pH of 9-10. TLC was used to confirm this using a

mobile phase of 1 % HCl in methanol. 120 μL of 1 M HCl was used to lower the pH to 7. 500 μL of the DPA-ale solution was added to 500 μL of $[^{99m}Tc(CO)_3(OH_2)_3]^+$ (pH 7), and then heated for 30 min at 90 °C. TLC was then re run as before to confirm formation of ^{99m}Tc-DPA-ale.

6.3.4.1 Radiolabelling yield dependence on molecular weight and mass of polyethylene glycol

To a dispersion of PEG-BP-USPIOs (100 μL of solution containing 4 μmol Fe for USPIO-1 samples, 100 μL of solution containing 0.2 μmol of Fe for USPIO-2 sample) in saline was added to ∼2 MBq of ^{99m}Tc-DPA-ale in 20 μL. The mixture was mixed and incubated at room temperature at pH 7 in a sealed vial for 30 min. The contents were then washed by centrifugation with 100 μL saline at 10000 rpm for 1.5 min using a Vivaspin 500 with a 10 kDa MWCO. This cycle was repeated several times.

6.3.4.2 Radiolabelling yield dependence on reaction time

To a dispersion of PEG-BP-USPIOs (10 μL of solution containing 0.3 μmol Fe) in saline was added to ∼0.5 MBq of ^{99m}Tc-DPA-ale in 30 μL. The mixture was mixed and was either washed immediately, or incubated at room temperature at pH 7 in a sealed vial for 30 min. The contents were washed by centrifugation with 100-200 μL saline at 10000 rpm for 3 min using a Vivaspin 500 with a 10 kDa MWCO. This cycle was repeated several times.

6.3.4.3 Radiolabelling yield dependence on heating

To a dispersion of PEG-BP-USPIOs (20 μL of solution containing 0.6 μmol Fe) in saline was added to ∼7 MBq of ^{99m}Tc-DPA-ale in 100 μL. The mixture was mixed and was incubated at 37 °C at pH 7 in a sealed vial for 10 min, or heated from 25 °C to 90 °C during 10 min at pH 7. The reaction solution was cooled to room temperature and the contents were then washed by centrifugation with 200 μL saline at 10000 rpm for 3 min using a Vivaspin 500 with a 10 kDa MWCO. This cycle was repeated several times.

6.3.4.4   Radiolabelling yield dependence on filter

To a dispersion of PEG-BP-USPIOs (20 µL of solution containing 0.6 µmol Fe) in saline was added to ~0.5 MBq of ^{99m}Tc-DPA-ale in 100 µL. The mixture was mixed and was heated from 25 °C to 90 °C during 10 min at pH 7. The reaction solution was cooled to room temperature and the contents were then washed by centrifugation with 100 µL saline at 10000 rpm for 3 min using either a Vivaspin 500 with a 10 kDa MWCO, or a Vivaspin 2 with a 3 kDa MWCO. This cycle was repeated several times.

6.3.4.5   Radiolabelling yield dependence on purification method

To a dispersion of PEG-BP-USPIOs (50 µL of solution containing 1.5 µmol Fe) in saline was added to ~500 MBq of ^{99m}Tc-DPA-ale in 1 mL. The mixture was mixed and was heated from 25 °C to 90 °C during 10 min at pH 7. The reaction solution was cooled to room temperature and the contents were then washed by centrifugation with 200 µL saline at 10000 rpm for 3 min using either a Vivaspin 500 with a 10 kDa MWCO. This cycle was repeated several times. Once the excess unbound ^{99m}Tc-DPA-ale had been removed, the remaining radiolabelled NP solution was passed through a PD-10 desalting column with saline as the eluent in 0.5 mL fractions. The fraction containing the NPs was then centrifuged further as before to ensure all free radiolabel had been removed.

6.3.4.6   Finalised standard radiolabelling method

To a dispersion of PEG(5)-BP-USPIOs (20 µL of solution containing 0.6 µmol Fe) in saline was added to 1000 MBq of ^{99m}Tc-DPA-ale in 600 µL. The mixture was mixed and heated from 25 °C to 90 °C during 10 min at pH 7. The reaction solution was cooled to room temperature, and the contents were separated using two PD-10 columns with saline as the eluent in 0.5 mL fractions.

6.3.4.7 Characterisation of radiolabelled ultrasmall superparamagnetic iron oxide nanoparticles

To assess the *in vitro* stability of radiolabelled PEG(5)-BP-USPIOs in human serum, a 20 μL aliquot containing approximately 100 kBq of ^{99m}Tc in saline was incubated in human serum (500 μL) at 37 °C and constant shaking for 48 h. At the end of the experiment, the samples were filtered using the size-exclusion filters (MWCO of 10 kDa) and the radioactivity of the filtrate and retentate measured in a gamma-counter. Thus, if ^{99m}Tc-DPA-ale dissociated from the USPIOs, it would elute with the filtrate.

6.3.5 *In vivo* studies

In vivo studies were carried out in accordance with British Home Office regulations governing animal experimentation. Male BALB/c mice (8-10 weeks old) were used. Before the imaging procedure and contrast agent administration, mice were anesthetised with isoflurane and kept under its influence for the duration of the experiment (maximum 4 h) and culled by cervical dislocation at the end of the imaging session. The contrast agents used were injected intravenously through the tail vein using 0.5 mL insulin syringes. The doses used in these studies were 10 μmol Fe/kg (20 MBq of ^{99m}Tc) in 100 μL saline (PEG(5)-BP-USPIOs) or 40 μmol Fe/kg (3 MBq of ^{99m}Tc) in 100 μL saline (Feraspin XS).

6.3.5.1 Magnetic resonance imaging

In vivo MR imaging was performed using a 3 T Philips Achieva MR scanner (Philips Healthcare, Best, The Netherlands) equipped with a clinical gradient system (30 mTm^{-1}, 200 mT/m/ms) and a single-loop surface coil (diameter = 47 mm). Anesthesia was induced with 5 % and maintained with 12 % isoflurane during the MRI experiments. Mice were imaged in prone position. Dynamic contrast enhanced (DCE) magnetic resonance angiography (MRA), and T_1 and $T_2{}^*$ mapping protocols were acquired before and after injection of the nanoparticles. Following a 3D GRE scout scan, coronal 3D fast-field echo DCE-MRA images were acquired with TR = 10 ms, TE = 4.2 ms, flip angle = 40 °, FOV = 40 x 36 x 12 mm^3, acquired matrix = 160 x 144, slice thickness = 0.5 mm, resolution = 0.25 mm x 0.25 mm, reconstructed resolution = 0.1 mm x 0.1 mm, slice number = 25, averages = 1,

temporal resolution = 20 s, number of dynamic scans = 20, duration = 6.7 min.

T_1 mapping was performed using a sequence that employs two nonselective inversion pulses with inversion times ranging from 20 to 2000 ms, followed by eight segmented readouts for eight individual images. The two imaging trains result in a set of 16 images per slice with increasing inversion times. For T_1 mapping the acquisition parameters were: TR = 5.8 ms, TE = 2.7 ms, flip angle = 10 °, FOV = 31 x 31 x 13mm^3, acquired matrix = 80 x 77, measured slice thickness = 0.5 mm, acquired resolution = 0.4 mm x 0.4 mm, reconstructed resolution = 0.12 mm x 0.12 mm, slices = 26, averages = 1.

$T_2{}^*$ mapping was performed using a 3D fast-field echo sequence. Coronal images were acquired with TR = 248 ms, TE = 4.6 ms, echo spacing = 6.9 ms, six echoes, flip angle = 25 °, FOV = 31 x 31 x 13 mm^3, acquired matrix = 77 x 77, acquired resolution = 0.41 mm x 0.41 mm, reconstructed resolution = 0.11 mm x 0.11 mm, slice thickness = 0.5 mm, slices = 26, averages = 1. Similar acquisition protocols were used to scan vials containing different concentrations of the nanoparticles to calculate the r_1 and r_2 relaxivities.

MR images were analysed using the software OsiriX (OsiriX Foundation, Geneva, Switzerland). The dynamic contrast enhanced magnetic resonance angiogram (DCE-MRA) images were used to monitor the changes in the signal intensity of blood before and after injection of the nanoparticles. A region of interest (ROI) was manually drawn in the inferior vena cava and propagated over the different time points. T_1 mapping images were used to calculate the relaxation rate (R_1) of the liver and blood on a pixel-by-pixel basis using in house software (Matlab, Natick, MA) [5]. Similarly, the T_2^* mapping images were used to calculate the relaxation rate (R_2^*) of the corresponding tissues.

6.3.5.2 Single photon emission computed tomography-computed tomography imaging

SPECT-CT images were obtained with a NanoSPECT/CT PLUS preclinical animal scanner (Mediso, Hungary) equipped with four heads, each with nine 1 mm pinhole collimators, in helical scanning mode in 20 projections over 20 min. The CT images were obtained with a 45 kV X-ray source, 1000 ms exposure time in 180 projections over 10 min. Images were reconstructed in a 256 x 256 matrix using the HiSPECT (Scivis GmbH) reconstruction software

package, and fused using InVivoScope (IVS) software (Bioscan, France). Quantification was performed by selecting the desired organs as ROIs using the quantification tool of the IVS software.

6.3.6 Targeting

6.3.6.1 Maleimide-polyethylene glycol phase transfer of ultrasmall superparamagnetic iron oxide nanoparticles

Oleylamine-coated USPIOs (1.1 mg), PEG(5)-BP (7.2 mg) and mal-PEG(5)-BP (3.8 mg) were added to 1 mL of DCM in an open glass vial, and the mixture was sonicated until the solvent evaporated. To the remaining residue was added 1 mL of water resulting in a clear brown solution. This mixture was washed with 2 mL of hexanes to remove the oleylamine. This process was repeated two more times followed by removal of hexanes by evaporation under a N_2 flow. The final mixture was filtered through a 0.2 μm hydrophilic PTFE filter, followed by several cycles of washing/concentrating using a Vivaspin 2 centrifugal filter (30 kDa MWCO) using water to remove excess PEG(5)-BP and mal-PEG(5)-BP. The final amber solution was removed from the filter for use in targeting studies.

6.3.6.2 Characterisation of maleimide-polyethylene glycol-coated ultrasmall superparamagnetic iron oxide nanoparticles

Preparation of fluorescent component

Fluorescein-mal-PEG(5)-BP was synthesised by dissolving SAMSA fluorescein (22.329 mg) in 1.19 mL of 0.1 M NaOH and incubating for 15 min at room temperature. The solution was neutralised with ∼15 μL of concentrated HCl. Meanwhile, mal-PEG(5)-BP (8 mg) was dissolved in 5.952 mL of Tris buffer (0.5 M) at pH 6.8. The fluorescein solution was incubated with the mal-PEG(5)-BP solution for 2 h at room temperature, and then overnight at 4 °C. The reaction solution was then purified for 36 h at 4 °C using a dialysis cassette with a 2 kDa MWCO. The contents were then freeze dried.

Preparation of fluorescent polyethylene glycol-coated and maleimide-polyethylene glycol-coated ultrasmall superparamagnetic iron oxide nanoparticles

For cell studies, two samples were prepared. For PEG(5)-BP-USPIOs, oleylamine-coated USPIOs (1.5 mg) and PEG(5)-BP (9 mg) were added to 0.5 mL of DCM in an open glass vial. Fluorescein-mal-PEG(5)-BP (0.5 mg) was dissolved in 40 µL of dimethylformamide (DMF) and 0.5 mL of DCM. Both solutions were mixed an sonicated until all the solvent had evaporated. For mal-PEG(5)-BP-USPIOs, oleylamine-coated USPIOs (1.7 mg), PEG(5)-BP (7 mg) and mal-PEG(5)-BP (3 mg) were added to 0.5 mL of DCM in an open glass vial. Fluorescein-mal-PEG(5)-BP (0.5 mg) was dissolved in 40 µL of DMF and 0.5 mL of DCM. Both solutions were mixed an sonicated until all the solvent had evaporated. The washings steps were the same for both phase transfers. To the remaining residue was added 1 mL of water resulting in a yellow-brown solution. This mixture was washed with 2 mL of hexanes to remove the oleylamine. This process was repeated two more times followed by removal of hexanes by evaporation under a N_2 flow. The final mixture was filtered through a 0.2 µm hydrophilic PTFE filter, followed by several cycles of washing/concentrating using a Vivaspin 2 centrifugal filter (30 kDa MWCO) using water to remove excess PEG(5)-BP and mal-PEG(5)-BP. The final solution was removed from the filter for use in cell studies.

Fluorescence-activated cell sorting study

Samples of ∼400,000 MDA-MB-435 cells were prepared. The following specimens were investigated: (1) cells only, (2) cells incubated with fluorescent PEG(5)-BP-USPIOs, and (3) cells incubated with fluorescent mal-PEG(5)-BP-USPIOs. The volume for each sample was kept at 250 µL, and initially 250 µL of 0.1 % medium was added to all three samples, 2 µL of fluorescent PEG(5)-BP-USPIOs was added to (2), and 2 µL of fluorescent mal-PEG(5)-BP-USPIOs was added to (3). All samples were incubated for 1 h at 37 °C and shaken at 20 min intervals. After which time, each sample was washed by the addition of 2 mL of cold PBS, followed by centrifugation at 350 rcf for 3 min and removal of the supernatant. This process was repeated a further 2 times. The samples were then redispersed in 250 µL of cold PBS and kept on ice for performance of FACS.

Microscopy study

For microscopy studies, 5 μL of Hoechst 33342 was diluted up to 5 mL using PBS, and 100 μL of this solution was added to each of the above samples. These were then left for 15 min at room temperature. Washing was performed three times using 2 mL of cold PBS followed by centrifugation at 350 rcf for 3 min. The samples were redispersed in 100 μL PBS, and 10 μL of each was dropped on to a microscope slide. A cover slip was then fixed over the sample once dried.

6.3.6.3 Prostate-Specific Membrane Antigen

J591 conjugation

Oleylamine-coated USPIOs (1.1 mg), PEG(5)-BP (3.4 mg) and mal-PEG(5)-BP (2.1 mg) were added to 1 mL of DCM in an open glass vial, and the mixture was sonicated until the solvent evaporated. To the remaining residue was added 1 mL of water resulting in a clear brown solution. This mixture was washed with 2 mL of hexanes to remove the oleylamine. This process was repeated two more times followed by removal of hexanes by evaporation under a N_2 flow. The final mixture was filtered through a 0.2 μm hydrophilic PTFE filter, followed by several cycles of washing/concentrating using a Vivaspin 2 centrifugal filter (30 kDa MWCO) using water to remove excess PEG(5)-BP and mal-PEG(5)-BP. Meanwhile J591 was reduced. DTT (15.4 mg) was added to 1 mL of water and to achieve a 20 molar excess, 3.46 μL of this solution was added to 320 μL of J591 (21.6 nM) and left for 1 h at room temperature. The mixture was purified using a PD MiniTrap column followed by a PD MidiTrap column, both equilibrated with 2 mM ethylenediaminetetraacetic acid (EDTA) in PBS. J591 was eluted in a 1 mL fraction directly into 250 μL of the above mal-PEG(5)-BP-USPIOs, and left to react for 2 h at room temperature. The reaction solution was then purified using an ÄKTA chromatography system previously equilibrated for at least 1 h with PBS. Fractions of 1 mL were collected.

Fluorescence-activated cell sorting study

Samples of ∼500,000 DU145 and DU145-PSMA cells were prepared. For each cell line, the following specimens were investigated: (1) cells only, (2) cells incubated with 2° antibody,

and (3) cells incubated with J591-PEG(5)-BP-USPIOs followed by 2° antibody. The volume for each sample was kept at 250 μL, and initially 250 μL of PBS was added to (1), 250 μL of PBS was added to (2), and a mixture of 100 μL of J591-PEG(5)-BP-USPIOs and 150 μL of PBS was added to (3). All samples were incubated for 30 min on ice, followed by the addition of 2 mL of cold PBS, followed by centrifugation at 350 rcf for 3 min and removal of the supernatant. This process was repeated a further 2 times. 250 μL of PBS was then added to (1), with 1 μL of 2° antibody and 250 μL of PBS added to (2) and (3). All samples were incubated for 30 min on ice, followed by the addition of 2 mL of cold PBS, followed by centrifugation three times as before. The samples were then redispersed in 250 μL of cold PBS and kept on ice for performance of FACS.

Radiolabelling study

$[^{99m}\text{Tc}(\text{CO})_3(\text{OH}_2)_3]^+$ and ^{99m}-DPA-ale prepared as previously described. For the directly labeled particles, 15 μL of the $[^{99m}\text{Tc}(\text{CO})_3(\text{OH}_2)_3]^+$ stock solution ($\sim$40 MBq) was added to 100 μL of J591-PEG(5)-BP-USPIOs. For the particles labeled via the BP, 45 μL of ^{99m}-DPA-ale ($\sim$70 MBq) was added to 300 μL of J591-PEG(5)-BP-USPIOs. Both samples were incubated for 75 min at 37 °C whilst shaking at 450 rpm. Purification was performed using a PD MiniTrap column followed by a PD MidiTrap column.

Cell studies were performed using the particles radiolabelled via the BP only. Samples of $\sim$1,900,000 DU145 and DU145-PSMA cells were prepared. For each cell line, the following specimens were investigated: (1) cells incubated with radiolabelled J591-PEG(5)-BP-USPIOs on ice, and (2) cells incubated with radiolabelled J591-PEG(5)-BP-USPIOs at 37 °C, both performed in triplicate. To each cell sample, 116 μL of radiolabelled J591-PEG(5)-BP-USPIOs was added, followed by incubation for 45 min at the appropriate temperature. All samples were washed by the addition of 2 mL of cold PBS, followed by centrifugation at 350 rcf for 3 min. This process was repeated a further 2 times and each time the supernatant was kept. The remaining pellet and collected supernatant were then gamma counted.

6.3.6.4   Vascular Cell Adhesion Protein 1

6C7.1 conjugation

Oleylamine-coated USPIOs (1.4 mg), PEG(5)-BP (6.9 mg) and mal-PEG(5)-BP (3.8 mg) were added to 1 mL of DCM in an open glass vial, and the mixture was sonicated until the solvent evaporated. To the remaining residue was added 1 mL of water resulting in a clear brown solution. This mixture was washed with 2 mL of hexanes to remove the oleylamine. This process was repeated two more times followed by removal of hexanes by evaporation under a N_2 flow. The final mixture was filtered through a 0.2 μm hydrophilic PTFE filter, followed by several cycles of washing/concentrating using a Vivaspin 2 centrifugal filter (30 kDa MWCO) using water to remove excess PEG(5)-BP and mal-PEG(5)-BP. Meanwhile 6C7.1 was reduced. DTT (15.4 mg) was added to 1 mL of water and to achieve a 20 molar excess, 3.99 μL of this solution was added to 360 μL of 6C7.1 (1.6 mg/mL) and left for 1 h at room temperature. The mixture was purified using a PD MiniTrap column followed by a PD MidiTrap column, both equilibrated with 2 mM ethylenediaminetetraacetic acid (EDTA) in PBS. 6C7.1 was eluted in a 1 mL fraction directly into 250 μL of the above mal-PEG(5)-BP-USPIOs, and left to react for 2 h at room temperature. The reaction solution was then purified using an ÄKTA chromatography system previously equilibrated for at least 1 h with PBS. Fractions of 1 mL were collected.

Transfection of cell line

To transfect HEK 293T cells to express high levels of VCAM-1, 7.2 μL of DNA (20 μg) was diluted in 1.5 mL of Opti-MEM and 50 μL of Lipofectamine 2000 reagent was diluted in 1.5 mL of Opti-MEM. The two solutions were then mixed and left for 20 min at room temperature. This solution was made up to 8 mL with Opti-MEM. The HEK 293T cells were washed with Opti-MEM by centrifugation at 350 rcf for 3 min. The DNA/Lipofectamine solution was then incubated with the cells for ∼3.5 h at 37 °C, after which the cell media was replaced with normal media.

Fluorescence-activated cell sorting study

Samples of ∼500,000 HEK 293T and HEK 293T VCAM cells were prepared. For each cell line, the following specimens were investigated: (1) cells only, (2) cells incubated with 2°

antibody, (3) cells incubated with 6C7.1-fluorescein, and (4) cells incubated with 6C7.1-PEG(5)-BP-USPIOs followed by 2° antibody. The volume for each sample was kept at 250 μL, and initially 250 μL of PBS was added to (1), 250 μL of PBS was added to (2), a mixture of 1 μL of 6C7.1-fluorescein and 249 μL of PBS was added to (3), and a mixture of 200 μL of 6C7.1-PEG(5)-BP-USPIOs and 50 μL of PBS was added to (4). All samples were incubated for 30 min on ice, followed by the addition of 2 mL of cold PBS, followed by centrifugation at 350 rcf for 3 min and removal of the supernatant. This process was repeated a further 2 times. 250 μL of PBS was then added to (1) and (3), with 1 μL of 2° antibody and 250 μL of PBS added to (2) and (4). All samples were incubated for 30 min on ice, followed by the addition of 2 mL of cold PBS, followed by centrifugation three times as before. The samples were then redispersed in 250 μL of cold PBS and kept on ice for performance of FACS.

Radiolabelling study

^{99m}Tc-DPA-ale prepared as previously described. a small amount of ^{99m}Tc-DPA-ale was added to the 6C7.1-PEG(5)-BP-USPIOs. The sample was incubated for 75 min at 37 °C whilst shaking at 450 rpm. Purification was performed using the ÄKTA chromatography system.

Samples of ∼2,000,000 HEK 293T and HEK 293T VCAM cells were prepared. For each cell line, the cells incubated with radiolabelled 6C7.1-PEG(5)-BP-USPIOs at 37 °C performed in triplicate was investigated. To each cell sample, 166 μL of radiolabelled 6C7.1-PEG(5)-BP-USPIOs was added, followed by incubation for 45 min at 37 °C. All samples were washed by the addition of 2 mL of cold PBS, followed by centrifugation at 350 rcf for 3 min. This process was repeated a further 2 times and each time the supernatant was kept. The remaining pellet and collected supernatant were then gamma counted.

6.3.6.5   p32 receptor

LyP-1 conjugation

Oleylamine-coated USPIOs (1.2 mg), PEG(5)-BP (7.2 mg) and mal-PEG(5)-BP (3.8 mg) were added to 1 mL of DCM in an open glass vial, and the mixture was sonicated until the

solvent evaporated. To the remaining residue was added 1 mL of water resulting in a clear brown solution. This mixture was washed with 2 mL of hexanes to remove the oleylamine. This process was repeated two more times followed by removal of hexanes by evaporation under a N_2 flow. The final mixture was filtered through a 0.2 µm hydrophilic PTFE filter, followed by several cycles of washing/concentrating using a Vivaspin 2 centrifugal filter (30 kDa MWCO) using water to remove excess PEG(5)-BP and mal-PEG(5)-BP. 250 µL HEPES buffer was added to 250 µL of mal-PEG(5)-BP-USPIOs. To this NP solution, 20 µL of fluorescent LyP-1 in degassed water (200 µg) was added and left for 2 h at room temperature. The reaction solution was then purified using an ÄKTA chromatography system previously equilibrated for at least 1 h with 0.9 % saline. Fractions of 1 mL were collected.

Fluorescence-activated cell sorting study

Samples of ∼3,100,000 MDA-MB-435 cells were prepared. The following specimens were investigated: (1) cells only, (2) cells incubated with LyP-1-PEG(5)-BP-USPIOs, (3) cells incubated with a blocking peptide followed by LyP-1-PEG(5)-BP-USPIOs, (4) cells incubated with mal-PEG(5)-BP-USPIOs, and (5) cells incubated with LyP-1. The volume for each sample was kept at 250 µL, and initially 250 µL of PBS was added to (1), (2), (4) and (5), and a mixture of 27 µL of blocking peptide (non-fluorescent LyP-1; 85 µM) and 223 µL of PBS was added to (3). All samples were incubated for 30 min at 37 °, followed by the addition of 2 mL of PBS and centrifugation at 350 rcf for 3 min and removal of the supernatant. This process was repeated a further 2 times. 250 µL of PBS was then added to (1), 150 µL of LyP-1-PEG(5)-BP-USPIOs and 100 µL of PBS added to (2) and (3), 20 µL of mal-PEG(5)-BP-USPIOs and 230 µL of PBS added to (4), and a mixture of 0.5 µL of LyP-1 (5 µg) and 249.5 µL of PBS was added to (5). All samples were incubated for 1 h at 37 °, followed by the addition of 2 mL of PBS, followed by centrifugation three times as before. The samples were then redispersed in 250 µL of PBS and kept on ice for performance of FACS.

Microscope study

Cell samples containing 100,000 cells were prepared on to cover slips in a 24 well plate. The samples were rinsed with PBS at room temperature and fixed using 0.5 mL of 4 % FA for 15 min at room temperature, followed by three rinses with 0.5 mL of glycerine in PBS

(100 mM). Each well was covered with 500 μL of NaBH$_4$ solution (1 mg/mL) for 5 mins, and then rinsed twice with PBS. This was followed by incubation with 400 μL of blocking solution (1 % bovine serum albumin, BSA, in 25 mM Tris-buffered saline) for 15 min at room temperature. The following specimens were investigated: (1) cells only, (2) cells incubated with a blocking peptide (non-fluorescent LyP-1) followed by LyP-1-PEG(5)-BP-USPIOs, (3) cells incubated with a low concentration of LyP-1-PEG(5)-BP-USPIOs, and (4) cells incubated with a high concentration of LyP-1-PEG(5)-BP-USPIOs. The volume for each sample was kept at 250 μL, and initially 250 μL of PBS was added to (1), (3) and (4), and a mixture of 27 μL of blocking peptide (85 μM) and 223 μL of PBS was added to (2). All samples were incubated for 30 min at 37 °C, followed by three rinses with PBS. 250 μL of PBS was then added to (1), 25 μL of LyP-1-PEG(5)-BP-USPIOs and 225 μL of PBS added to (3), and a mixture of 200 μL of LyP-1-PEG(5)-BP-USPIOs and 50 μL of PBS was added to (2) and (4). All samples were incubated for 1 h at 37 °C, followed by three rinses with PBS. Each well was rinsed with water twice, and then the cover slips were fixed to a slide using 6.5 μL of Fluoroshield.

6.4 Polyethylene glycol phase transfer of CdZnSeS alloyed quantum dots procedures

6.4.1 Synthesis of CdZnSeS alloyed quantum dots

QDs were synthesised using a modified version of the synthesis by Bae *et al.* [6]. Se (7.9 mg) and S (3.3 mg) were dissolved in 3 mL TOP and stirred overnight under N$_2$ at 600 rpm. CdO (51.4 mg) and Zn acetate (733.9 mg) were added to a mixture of 5.6 mL of oleic acid and 20 mL ODE (90 %) and stirred at 550 rpm. This solution was degassed at for ∼1 h at 100 °C under vacuum. The solution was then placed under N$_2$ and heated to 310 ° at a ramping rate of 400 °C/h. Once at this temperature, 3 mL of the S-Se TOP solution was injected and the temperature was kept at 300 °C for 5 min. The heating appliance was removed and the reaction solution was left to cool to room temperature. The QDs were extracted by dispersing the cooled solution in 8 mL of chloroform and excess acetone, followed by centrifugation at 4000 rpm for 10 min. 2 mL of hexane and 2 mL of a hexane/methanol solution was added, and the solution was again centrifuged as before. This process was

repeated a further two times.

6.4.2   Polyethylene glycol phase transfer of CdZnSeS alloyed quantum dots

500 μL oleic acid-coated QDs in hexane was added to PEG(5)-BP (2.4 mg) and mal-PEG(5)-BP (1.1 mg) in 2 mL water. The solution was left stirring for 48 h at room temperature. The remaining solution was centrifuged at 4000 rpm for 5 min using a Vivaspin 2 centrifugal filter (30 kDa MWCO). 0.5 mL of water was added and the centrifugation process was repeated. This process was performed several times more. The final mixture was filtered through a 0.2 μm hydrophilic PTFE filter and stored at 4 °C.

6.4.3   *In vitro* study

This study was performed in collaboration with Dr. Lea Ann Dailey. J774 murine macrophage cells were incubated with PEG(5)-BP-QDs at 37 °C, and imaging was performed using a confocal microscope.

6.4.4   Introduction of maleimide component into coating

500 μL oleic acid-coated QDs in hexane was added to PEG(5)-BP (1.8 mg) and mal-PEG(5)-BP (1.1 mg) in 2 mL water. The solution was left stirring for 48 h at room temperature. The remaining solution was centrifuged at 4000 rpm for 5 min using a Vivaspin 2 centrifugal filter (30 kDa MWCO). 0.5 mL of water was added and the centrifugation process was repeated. This process was performed several times more. The final mixture was filtered through a 0.2 μm hydrophilic PTFE filter and stored at 4 °C.

6.5 Hydrophobin phase transfer of inorganic nanoparticles procedures

6.5.1 Protein passivation of nanoparticles

In a typical reaction, 100 µL of as-received H*Protein B (50 mg/mL) was dissolved in 2 mL water, and the mixture was sonicated for 15 min to ensure that the hydrophobins were dispersed in the solution. This mixture was then left for 1 h at room temperature. To the hydrophobin solution, 50 µL of QDs/hexane solution (5 µM) was added and the solution was sonicated for 30 min, resulting in a cloudy emulsion. After storing the emulsion for at least 3 h at 4 °C, the solution was centrifuged at 4,000 rpm for 2 min, resulting in two phases: a relatively clear solution phase and a turbid foam. The solution layer was taken and filtered through a filter paper (particle retention of 11 µm) and was then charged in a Vivaspin 4 centrifugal concentrator with a 100 kDa MWCO. After which the solution was centrifuged at 4,000 rpm for 5 min, separating a few mL of the solvent from the solution. The centrifugation process was repeated until the solution volume reduced to 200 µL in the centrifugal concentrator. The concentrated solution was diluted with 3.5 mL water and the concentration process was repeated again, resulting in brown solution with a slight turbidity. The solution was then filtered through a 0.2 µm cellulose acetate syringe filter.

6.5.2 Analytical ultracentrifugation

AUC was performed by BASF. The particle size distribution was determined by AUC using ~500 µL of the QD-hydrophobin solution. Simultaneous detection by synchronised interference optics (Beckmann, model XLI) quantified the amount and the diameter of each fraction independently from 1 nm up to several microns in diameter [7].

6.5.3 Secondary-ion mass spectrometry

Static TOF-SIMS spectra were recorded using a TOF-SIMS V spectrometer (Iontof GmbH, Germany) by BASF. A pulsed mass-filtered primary ion beam of 25 keV singly charged bismuth (Bi^+) was used. This primary ion beam, resulting in a spot size of typically 5 µm

on the sample surface, was raster scanned over an area of 250 x 250 μm to record spectra of positive and negative secondary ions. The rastered area integrates over more than 10^6 particles. The primary ion dose density was always kept well below 10-12 ions cm^2 and thus in the static SIMS regime. To prevent charging of the sample surface, a low-electron energy flood gun was used. The sample particle sediments were prepared for SIMS analysis by their placing on clean silicon wafers.

6.5.4 *In vitro/vivo* studies

6.5.4.1 Ovarian and breast cancer cells

These cell studies were performed by Dr. Maya Thanou. Ovarian carcinoma, IGROV-1 cells were propagated in RPMI-1640 media supplemented with 10 % FBS and antibiotics (1 % penicillin/streptomycin) and maintained under standard conditions, 37 °C with 5 % CO_2. On the day prior to the experiment the cells were plated in 16 well glass chamber slides at a density of 30,000 cells/well. The slide had been coated with gelatin by incubation overnight at 4 °C with 1 % gelatin in PBS. On the day of the experiment the media was replaced with Opti-MEM with or without QDs at a concentration of 0.3 μM. After 1 h incubation at 37 °C, the media was removed; cells were washed three times with PBS with Ca^{2+}/Mg^{2+}, fixed with 1 % paraformaldehyde (FA) for 15 min at room temperature, washed and incubated with DAPI for 10 min at room temperature for nuclei staining. Imaging of cells was done using a Leica TCS SP2 confocal microscope with a spectral detector. Images were adjusted for contrast and brightness using Image J software and each image was modified with the same settings. Each sample was performed in duplicates.

6.5.4.2 HeLa cells

Crosslinking

QD/hydrophobins (1 mg) were washed with 1 mL 10 mM sodium phosphate buffer at pH 7 three times (centrifuged at 3000 rpm for 1 min each time). The reaction solution was then made up to 500 μL with buffer containing 1 % glutaraldehyde. This was allowed to react for 1 h at room temperature whilst stirring. The solution was then purified using a PD-10

column (that had been blocked by washing with 0.5 mL of 1 % BSA), collecting 0.5 mL fractions with 10 mM sodium phosphate buffer as the eluent. The crosslinked QDs eluted in fractions 1, 2 and 3, with the strongest emission from fraction 2.

Fluorescence imaging

This cell study was performed by Dr. Dylan Owen. HeLa cells were cultured in DMEM media supplemented with 10 % FBS and maintained under standard conditions, 37 °C with 5 % CO_2 before being plated into Lab-Tek 8-well coverslip-bottomed dishes. Cells were incubated with QDs for 30 min prior to imaging. Imaging of cells was done using a Nikon AR-1 confocal microscope with a spectral detector and 561 nm laser excitation and a X63 objective lens. Imaging was performed at 37 °C.

6.6   *In vivo* imaging

This *in vivo* study was perfomed by Dr. Maya Thanou. All experiments were performed in accordance with the local ethical regulation of Kings College and the UK Home Office Animals Scientific Procedures Act, 1986. Xenografts were generated in BALB/c nude athymic mice (Harlan) by subcutaneous injection of MDA-MB-231 cells (3×10^{10} cells mixed with Geltrex 1:1 ratio). Three to four weeks later when the tumours reached sizes of approximately 50 mm^3, QDs were injected intratumourly. The distribution of the dots was monitored using *in vivo* imager, Maestro (Caliper). Images were collected at four time points: right after injection, 3, 27 and 96 h post injection. Images were acquired with Maestro Imaging System (Caliper) using the NIR filter setting. To separate the background signal from the QD signal the images were unmixed using previously defined spectra.

6.6.1   Functionalisation

6.6.1.1   Radiolabelling

Radiolabelling was performed by Dr. Margaret Cooper. 500 µL of the hydrophobin-QDs were placed in an Iodogen tube and ^{131}I (14 MBq in 10 µL) was added. The reaction was allowed to proceed at room temperature for 15 min with mixing. TLC was carried out using

ITLC-SG as the solid phase and 85 % aqueous methanol as the mobile phase. The TLC plate was scanned on a TLC scanner and the areas under the curve determined. Purification was carried out using a PD-10 column (that had been blocked by washing with 0.5 mL 1 % BSA) which was eluted with 5 x 0.5 mL PBS at pH 7.

The labelled QDs were also put down a BioSep-SEC-S 2000 HPLC size exclusion column with 0.1 M phosphate buffer as the mobile phase and no activity was observed.

Bibliography

[1] R. T. M. de Rosales, C. Finucane, S. J. Mather, and P. J. Blower. Bifunctional Bisphosphonate Complexes for the Diagnosis and Therapy of Bone Metastases. *Chem. Commun.*, pages 4847–4849, **2009**.

[2] L. Qu, Z. A. Peng, and X. Peng. Alternative Routes toward High Quality CdSe Nanocrystals. *Nano Lett.*, 1: 333–337, **2001**.

[3] D. V. Talapin, A. L. Rogach, A. Kornowski, M. Haase, and H. Weller. Highly Luminescent Monodisperse CdSe and CdSe/ZnS Nanocrystals Synthesized in a Hexadecylamine-Trioctylphosphine Oxide-Trioctylphospine Mixture. *Nano Lett.*, 1: 207–211, **2001**.

[4] Z. Xu, C. Shen, Y. Hou, H. Gao, and S. Sun. Oleylamine as Both Reducing Agent and Stabilizer in a Facile Synthesis of Magnetite Nanoparticles. *Chem. Mater.*, 21: 1778–1780, **2009**.

[5] M. R. Makowski, A. J. Wiethoff, U. Blume, F. Cuello, A. Warley, C. H. P. Jansen, E. Nagel, R. Razavi, D. C. Onthank, R. R. Cesati, M. S. Marber, T. Schaeffter, A. Smith, S. P. Robinson, and R. M. Botnar. Assessment of Atherosclerotic Plaque Burden with an Elastin-Specific Magnetic Resonance Contrast Agent. *Nat. Med.*, 17: 383–388, **2011**.

[6] W. K. Bae, K. Char, H. Hur, and S. Lee. Single-Step Synthesis of Quantum Dots with Chemical Composition Gradients. *Chem. Mater.*, 20: 531–539, **2008**.

[7] K. L. Planken and H. Colfen. Analytical Ultracentrifugation of Colloids. *Nanoscale*, 2: 1849–1869, **2010**.

Appendices

Appendix A

Ultrasmall superparamagnetic iron oxide nanoparticles

A.1 Developed oleylamine-coated Fe_3O_4 nanoparticle synthesis
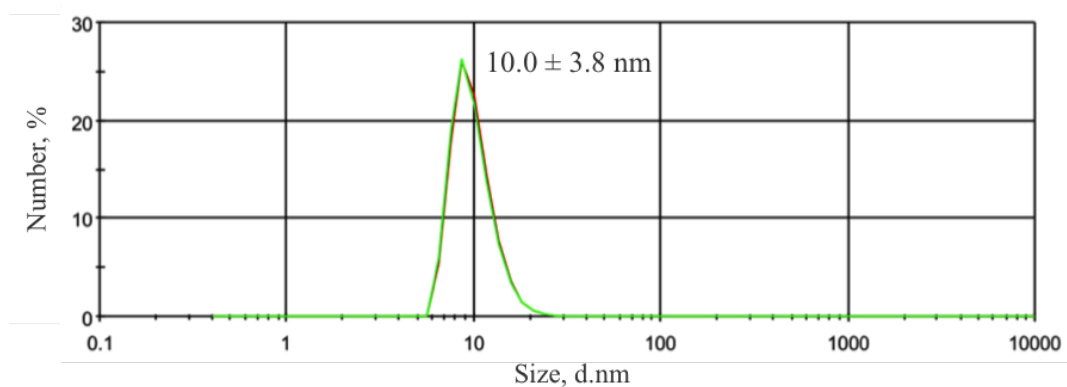
Figure A.1: DLS number-weighted size distribution of oleylamine coated Fe_3O_4 NPs in DCM synthesised by heating across three different stages followed by ageing at a lower temperature.
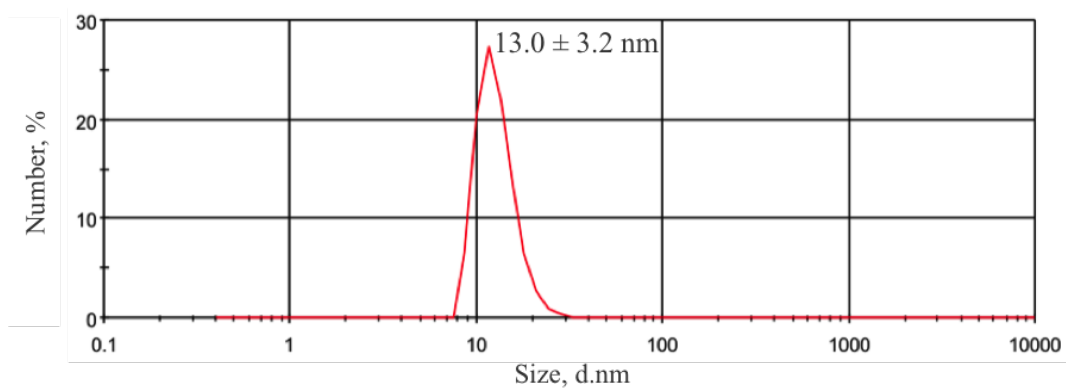
Figure A.2: DLS number-weighted size distribution of oleylamine coated Fe_3O_4 NPs in DCM synthesised using the final developed method.

A.2 Final synthetic oleylamine-coated Fe_3O_4 nanoparticle method

A.3 Stability studies of polyethylene glycol-coated Fe_3O_4 nanoparticles
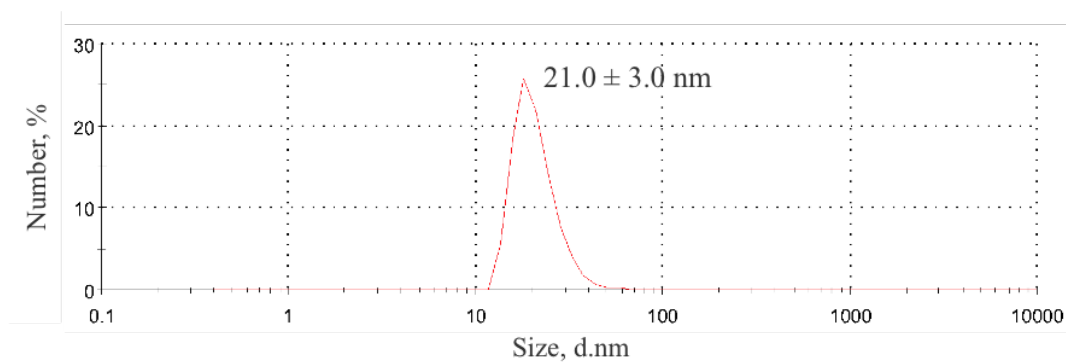
Figure A.3: DLS number-weighted size distribution of PEGylated Fe_3O_4 NPs stored in water for several months.
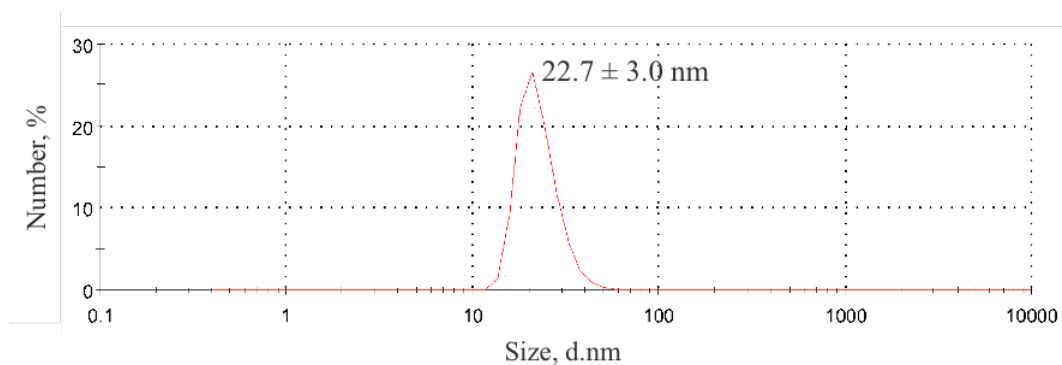
Figure A.4: DLS number-weighted size distribution of PEGylated Fe_3O_4 NPs stored in saline for several months.
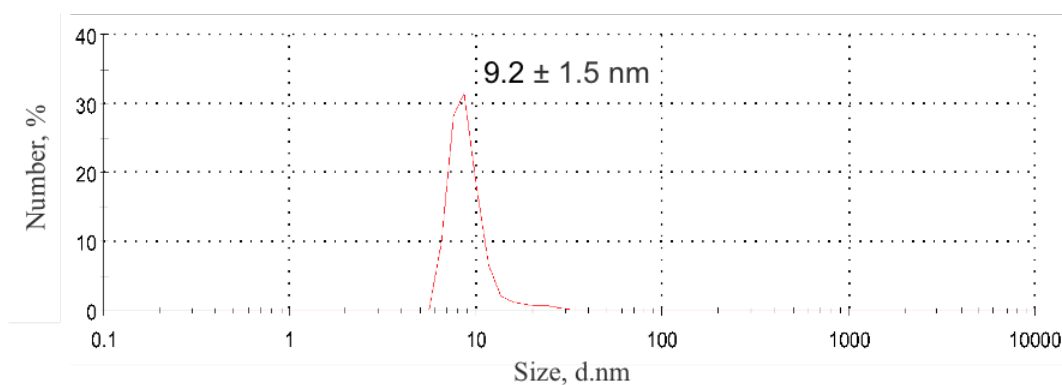
Figure A.5: DLS number-weighted size distribution of PEGylated Fe_3O_4 NPs in 10 % human serum.
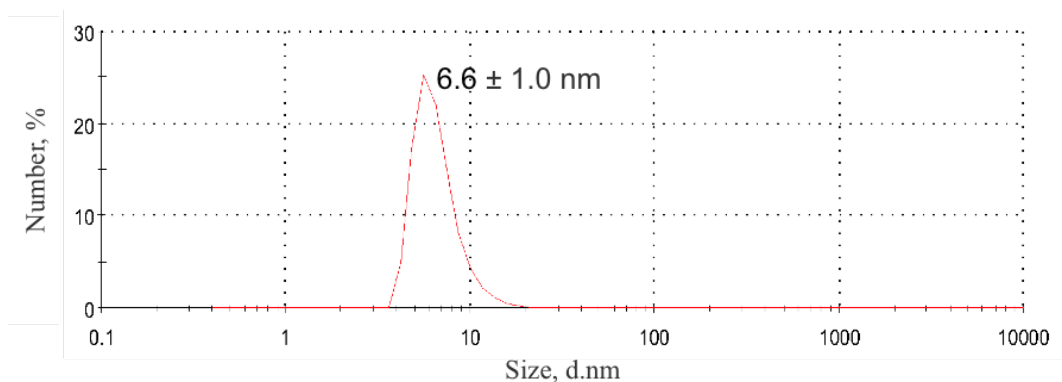
Figure A.6: DLS number-weighted size distribution of PEGylated Fe_3O_4 NPs in 10 % human serum after incubation at 37 °C for 1 h.
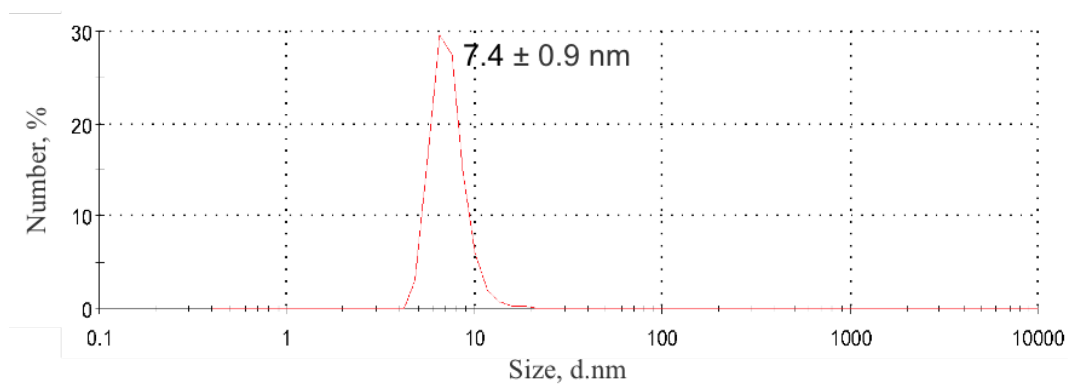
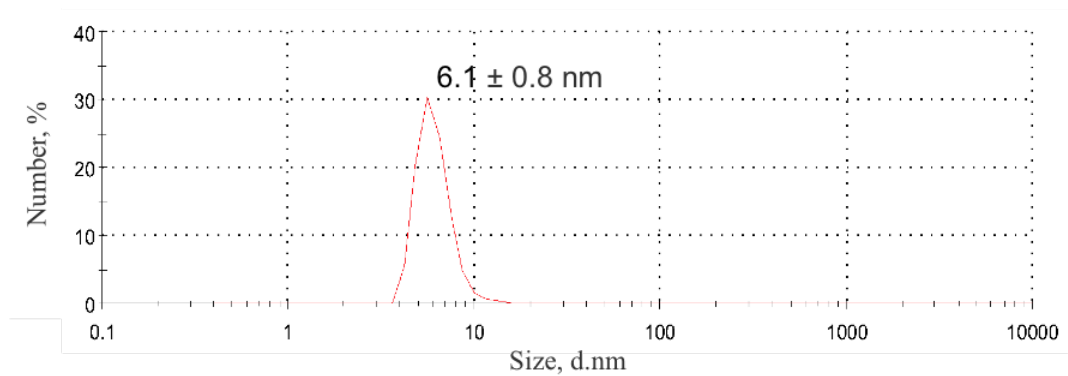Figure A.7: DLS number-weighted size distribution of PEGylated Fe_3O_4 NPs in 10 % human serum after incubation at 37 °C for 24 h.

Figure A.8: DLS number-weighted size distribution of PEGylated Fe_3O_4 NPs in 10 % human serum after incubation at 37 °C for 48 h.

A.4 Radiolabelled polyethylene glycol-coated Fe$_3$O$_4$ nanoparticles
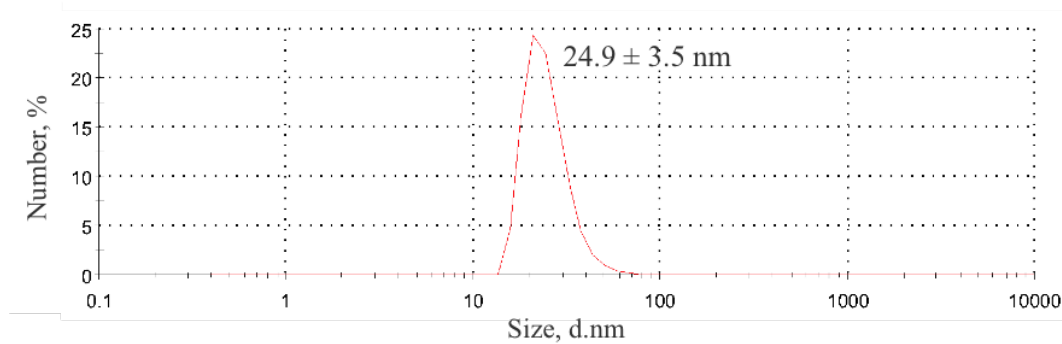
Figure A.9: DLS number-weighted size distribution of radiolabelled PEGylated Fe$_3$O$_4$ NPs in water.

Appendix B

Hydrophobin phase transfer of inorganic nanoparticles

B.1 Hydrophobin-coated CdSeS/ZnS quantum dots
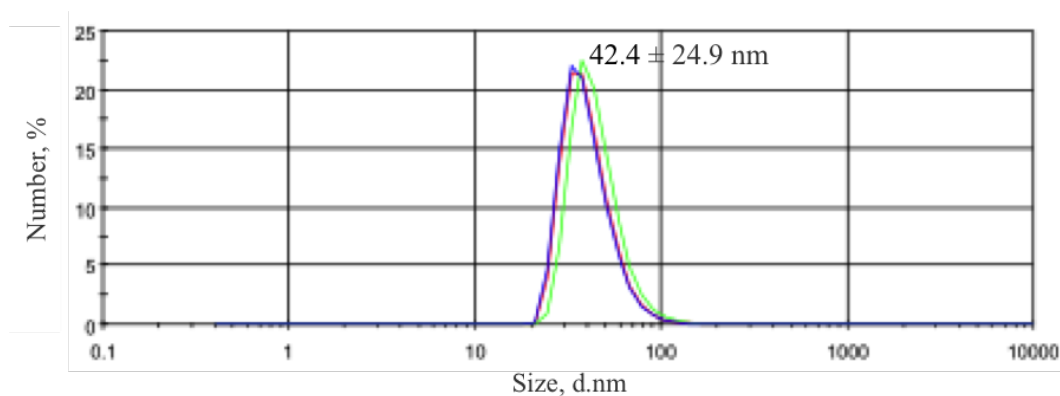
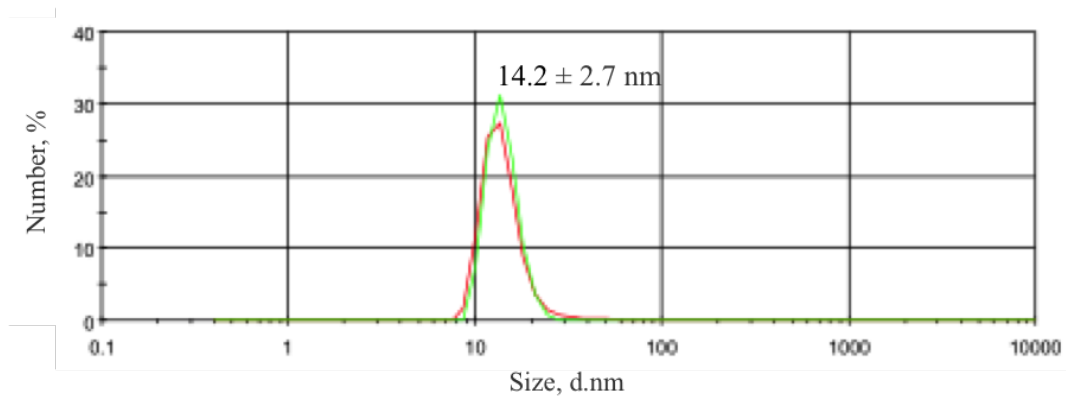Figure B.1: DLS number-weighted size distribution of hydrophobin-coated CdSeS/ZnS QDs in water.

Figure B.2: DLS number-weighted size distribution of hydrophobin-coated CdSeS/ZnS QDs stored in water for two months.
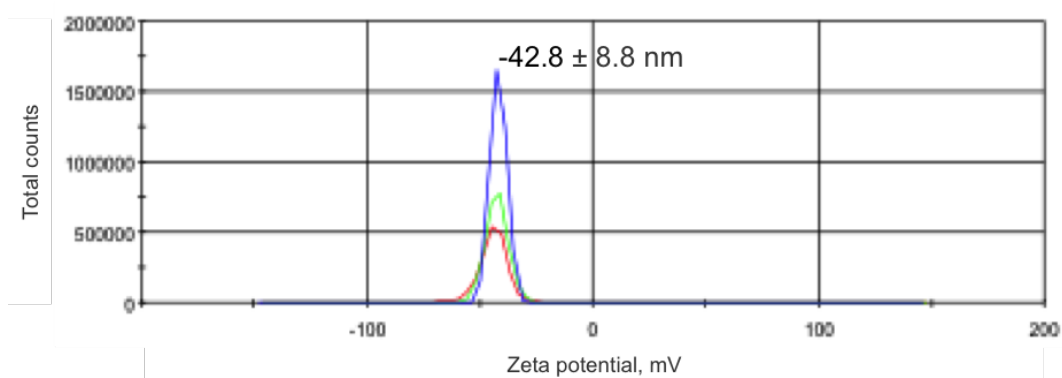

Figure B.3: Zeta potential distribution of hydrophobin-coated CdSeS/ZnS QDs in water.

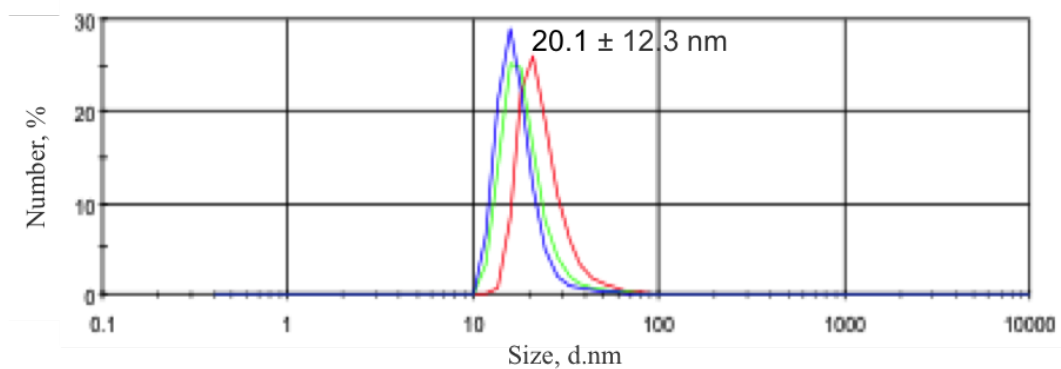## B.2 Crosslinked hydrophobin-coated CdSeS/ZnS quantum dots

Figure B.4: DLS number-weighted size distribution of crosslinked hydrophobin-coated CdSeS/ZnS QDs in water.
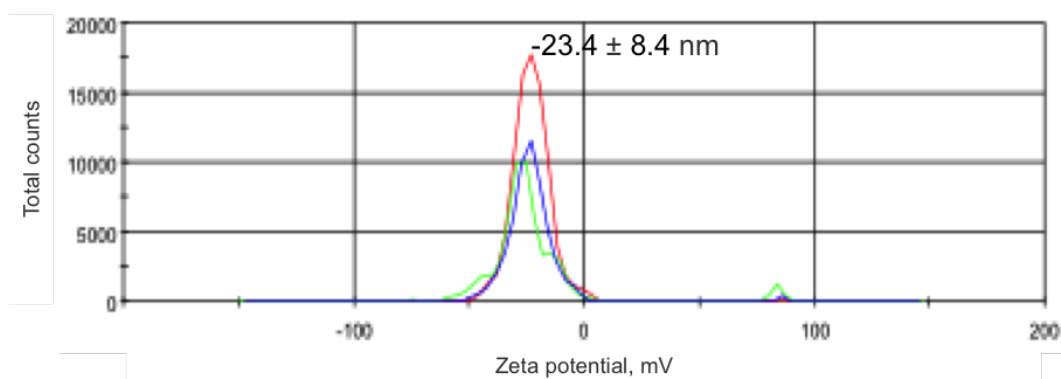

Figure B.5: Zeta potential distribution of crosslinked hydrophobin-coated CdSeS/ZnS QDs in water.